Crystal growth and structural aspects of alkali iridates and ruthenates of lithium and sodium

INAUGURAL-DISSERTATION

zur

Erlangung des Doktorgrades

der Mathematisch-Naturwissenschaftlichen Fakultät

der Universität zu Köln

vorgelegt von

Linda Kerkhoff, geb. Hollenbeck
aus Düsseldorf

Köln 2021

Berichterstatter/in: Prof. Dr. Petra Becker-Bohatý
Prof. Dr. Thomas Lorenz

Tag der mündlichen Prüfung: 23.04.2021

Abstract

The aim of the present investigation of alkali iridates and ruthenates of lithium and sodium is to achieve insights into their growth mechanisms, structural properties, and thermal behaviour. In recent times, these compounds as part of the Alkali Platinum-Group Metal Oxides (APGMO) family attracted considerable attention due to their unconventional magnetic properties. Here, four systems of different chemical composition were investigated: the *Li-Ir-O system* (α- and β-Li_2IrO_3), the *Li-Ru-O system* (Li_2RuO_3; Li_3RuO_4), the *Li-Ir-Ru-O system* ($Li_2Ir_{1-x}Ru_xO_3$), and the *Na-Ru-O system* ($Na_{3-x}Ru_4O_9$; $Na_{27}Ru_{14}O_{48}$).

Single crystals were grown by the Chemical Vapour Transport Reaction (CVTR) method and the solid-state reaction method. The former method was performed using an Al_2O_3 setup with separated educts and distinct crystallisation sites. Growth conditions were determined based on thermodynamic considerations of assumed chemical reactions. Thorough investigations demonstrate that the growth from the gaseous phase is not only possible for systems with similar partial pressures of gaseous components (Li_2IrO_3) but also for systems with different partial pressures (Li_2RuO_3 and $Li_2Ir_{1-x}Ru_xO_3$). In the *Li-Ir-Ru-O system* yielding $Li_2Ir_{1-x}Ru_xO_3$, the crystal symmetry of the end members α-Li_2IrO_3 and Li_2RuO_3 reveal a solid-solution series only at growth temperature. At room temperature, the phases are heterostructural ($C2/m$ and $P2_1/m$, respectively), which complicates the growth process. For $Na_{3-x}Ru_4O_9$ and $Na_{27}Ru_{14}O_{48}$, the solid-state reaction is the more suitable growth method due to the isolation of educts (Na_2CO_3 and RuO_2) and the prevented escape of volatiles during growth. The investigation of chemical instability of all grown compounds demonstrates a hygroscopic behaviour for sodium ruthenates and an instability against ethanol for lithium iridates and ruthenates. For both growth methods, comparable examinations of growth results, Energy-Dispersive X-ray Spectroscopy, and X-ray diffraction show that the amount, size, and morphology of crystals depend on many parameters such as the growth temperature and duration, educt type and ratio, arrangement of setup parts, and partial pressures of gaseous phases. To correctly assign the influence of these parameters on the structure of grown crystals, structural investigations based on X-ray diffraction were performed.

The common structural feature are the edge-sharing AO_6 and MO_6 octahedra (A = Li; Na and M = Ir; Ru). The majority of compounds is found in the Li_2MO_3 type characterised by honeycomb structures. Structural and thermal investigations reveal that the α-Li_2IrO_3 modification ($C2/m$) is

formed at lower temperatures than β- Li_2IrO_3 (*Fddd*) and both modifications are connected via a phase transition. For Li_2RuO_3, the room-temperature phase is confirmed, which crystallises in $P2_1/m$ symmetry and which is characterised by its Ru-Ru dimers in the two-dimensional honeycomb network. A phase transition to the high-temperature $C2/m$ phase is not observed by thermal analysis. In accordance, powder X-ray diffraction measurements on $Li_2Ir_{1-x}Ru_xO_3$ in a temperature range between 12 K and 310 K demonstrate that at a high relative Ir amount the $C2/m$ modification, which consists of non-dimerised honeycombs, is stable and does not undergo a phase transition. At a high relative Ru amount, the $P2_1/m$ modification is determined, implying the presence of the dimerised honeycomb structure and a phase transition between growth temperature and 310 K. This indicates a favoured dimerisation of Ru than of Ir, which is explained by a slightly smaller ionic radius of Ru^{4+} compared to Ir^{4+}. Overall, structural investigations of $Li_2Ir_{1-x}Ru_xO_3$ compounds point towards a limit between the stability areas of the non-dimerised $C2/m$ and the dimerised $P2_1/m$ phase at room temperature close to a relative Ir amount of 0.4 - 0.5.

Structural investigations of $Na_{27}Ru_{14}O_{48}$ reveal the occurrence of stacking faults and their influence on the unit-cell choice and Na stoichiometry. However, a dependence of the incidence of stacking faults on growth conditions is not found. In the tunnel-like structure of $Na_{3-x}Ru_4O_9$, a dependence of Na stoichiometry on the growth method is shown. Here, the Na stoichiometric amount is higher for a sample grown from the gaseous phase than for one grown by the solid-state reaction method. Further, the anisotropic refinement of atomic displacement parameters resulted in elongated displacement ellipsoids of Na in the direction of the tunnels, which indicates a mobility of Na atoms and, hence, suggested conducting behaviour in $Na_{3-x}Ru_4O_9$.

Kurzzusammenfassung

Das Ziel der vorliegenden Untersuchung von Alkaliiridaten und -ruthenaten des Lithiums und Natriums ist es, Einblicke in deren Wachstumsmechanismen, strukturelle Eigenschaften und thermische Verhalten zu erlangen. Die untersuchten Verbindungen haben aufgrund ihrer unkonventionellen magnetischen Eigenschaften große Aufmerksamkeit auf sich gezogen. In dieser Arbeit wurden vier Systeme untersucht: *Li-Ir-O* (α- und β-Li_2IrO_3), *Li-Ru-O* (Li_2RuO_3; Li_3RuO_4), *Li-Ir-Ru-O* ($Li_2Ir_{1-x}Ru_xO_3$) und *Na-Ru-O* ($Na_{3-x}Ru_4O_9$; $Na_{27}Ru_{14}O_{48}$).

Einkristalle wurden mittels Chemischer Transportreaktion und Festkörperreaktion gezüchtet. Für die Durchführung der ersten Methode wurde ein Al_2O_3-Aufbau verwendet, welcher sich durch getrennte Edukte und Kristallisationsstellen auszeichnet. Die Züchtungsbedingungen wurden auf Grundlage thermodynamischer Überlegungen der anzunehmenden chemischen Reaktionen bestimmt. Detaillierte Untersuchungen zeigen, dass die Züchtung aus der Gasphase nicht nur für Systeme mit ähnlichen Partialdrücken der gasförmigen Komponenten bei der Züchtungstemperatur möglich ist (Li_2IrO_3), sondern auch bei unterschiedlichen Partialdrücken (Li_2RuO_3 und $Li_2Ir_{1-x}Ru_xO_3$). Für das *Li-Ir-Ru-O-System* ergibt sich eine erweiterte Komplexität durch unterschiedliche Kristallsymmetrien von $Li_2Ir_{1-x}Ru_xO_3$ bei Züchtungs- und Raumtemperatur. Während die Endglieder α-Li_2IrO_3 und Li_2RuO_3 nur bei Züchtungstemperatur eine Mischkristallreihe mit $C2/m$ Symmetrie bilden, sind diese Phasen bei Raumtemperatur heterostrukturell ($C2/m$ und $P2_1/m$). Im *Na-Ru-O-System* zeigt sich für $Na_{3-x}Ru_4O_9$ und $Na_{27}Ru_{14}O_{48}$, dass, aufgrund der Isolierung der Edukte (Na_2CO_3 und RuO_2) und der geminderten Verflüchtigung von gasförmigen Komponenten während der Züchtung, die Festkörperreaktion die bevorzugte Züchtungsmethode ist. Desweiteren wurde für Natriumruthenate ein hygroskopisches Verhalten festgestellt. Dahingegen zeigen Lithiumiridate und -ruthenate eine Instabilität gegenüber Ethanol. Für beide Züchtungsmethoden ergaben vergleichende Untersuchungen der Züchtungsergebnisse, der energie-dispersiven Röntgenspektroskopie und der Röntgenbeugung, dass die Menge, Größe und Morphologie der Kristalle von einer Vielzahl von Parametern wie der Züchtungstemperatur und -dauer, Eduktart und -verhältnis, der Anordnung des Aufbaus und den Partialdrücken der Gasphasen abhängig ist. Um den Einfluss dieser Parameter auf die Struktur der gewachsenen Kristalle einzuordnen, wurden Strukturuntersuchungen auf Basis der Röntgenbeugung durchgeführt.

Das gemeinsame Strukturmerkmal der untersuchten Verbindungen sind die kantenverknüpften AO_6 und MO_6-Oktaeder (A = Li; Na und M = Ir; Ru). Die Mehrzahl der Verbindungen tritt im Li_2MO_3-Typ mit Honigwaben-Strukturen auf. Strukturelle und thermische Untersuchungen zeigen, dass sich die α-Li_2IrO_3-Modifikation ($C2/m$) bei niedrigeren Temperaturen bildet als β- Li_2IrO_3 ($Fddd$) und beide Modifikationen über einen Phasenübergang verbunden sind. Li_2RuO_3 wurde in der Raumtemperatur-Phase verfeinert, welche in $P2_1/m$-Symmetrie kristallisiert und durch Ru-Ru-Dimere im zweidimensionalen Honigwabennetzwerk gekennzeichnet ist. Ein Phasenübergang zur Hochtemperatur-Phase mit $C2/m$ Symmetrie ist in der Thermoanalyse nicht zu beobachten. In Übereinstimmung damit zeigen Pulver-Röntgenbeugungsmessungen an $Li_2Ir_{1-x}Ru_xO_3$-Verbindungen zwischen 12 K und 310 K, dass bei hohen relativen Ir-Anteilen die $C2/m$-Phase mit einer nicht-dimerisierten Honigwabenstruktur stabil ist und keinen Phasenübergang erfährt. Bei hohen relativen Ru-Anteilen kann die Struktur in $P2_1/m$-Symmetrie verfeinert werden, die eine dimerisierte Honigwabenstruktur beschreibt und einen Phasenübergang zwischen Züchtungstemperatur und 310 K impliziert. Dies deutet auf eine bevorzugte Dimerisierung von Ru gegenüber Ir hin und wird durch einen kleineren Ionenradius von Ru^{4+} im Vergleich zu Ir^{4+} erklärt. Insgesamt zeigen die Strukturuntersuchungen der $Li_2Ir_{1-x}Ru_xO_3$-Verbindungen, dass bei Raumtemperatur die Grenze zwischen den Stabilitätsbereichen der nicht-dimerisierten $C2/m$- und der dimerisierten $P2_1/m$-Phase nahe einer relativen Ir-Menge von 0,4 - 0,5 liegt.

Strukturelle Untersuchungen an $Na_{27}Ru_{14}O_{48}$ zeigen das Auftreten von Stapelfehlern und deren Einfluss auf die Stöchiometrie von Na und die Wahl der Einheitszelle. Eine Abhängigkeit der Häufigkeit von Stapelfehlern von den Züchtungsbedingungen ist nicht vorzufinden. In der tunnelartigen Struktur von $Na_{3-x}Ru_4O_9$ hingegen wird eine Abhängigkeit der Na-Stöchiometrie von der Züchtungsmethode aufgezeigt. Bei einer aus der Gasphase gewachsenen Probe ist die stöchiometrische Menge von Na höher als bei einer durch Festkörperreaktion gewachsenen Probe. Weiterhin ergab die anisotrope Verfeinerung der atomaren Auslenkungsparameter langgestreckte Auslenkungsellipsoide von Na in Richtung der Tunnels. Dies deutet auf eine Beweglichkeit der Na-Atome hin und damit auf ein leitendes Verhalten in $Na_{3-x}Ru_4O_9$.

Acknowledgements

I would like to begin by acknowledging the great support, engagement, and help from my supervisor Prof. Dr. Petra Becker-Bohatý. I would like to thank her for making this project possible, for introducing her great knowledge on crystal growth to the project, and for organising fruitful collaborations with other research groups. I would also like to acknowledge Prof. Dr. Thomas Lorenz for taking the role of the second supervisor and thus demonstrating the collaboration with the Institute of Physics II within the CRC1238.

I would also like to acknowledge Prof. Dr. Ladislav Bohatý for his enlightening hours on group theory and his excitement for symmetry. I thank Prof. Dr. Sandro Jahn for his support in the field of thermodynamics. I thank Maria for hours of excitement during LT P-XRD measurements and discussions on structural aspects of the Li_2IrO_3 modifications, and Christoph for supporting Raman spectroscopic measurements. Many thanks to Gunther for repairing an endless amount of heating elements, to Steffi for organising the lab, to Hanna for introducing me to EDX measurements, and to Katrin for her great efforts on finding the ideal polishing method.

In November 2019, I had the great opportunity to work in the laboratory of Prof. Ivan Neměc at the Charles University in Prague. I really enjoyed the time and felt extremely welcomed. Special thanks go to Dr. Ivana Císařová for sharing her knowledge with me on performing ideal SC-XRD experiments and analysing the data, for always being patient, and for trusting in me.

This work would not have been possible without Laura and Johannes, my dearest PhD colleagues. Very soon, colleagues became friends and together we have gone through ups and downs. Thank you for encouraging and supporting, for spontaneous trips to the ice-cream parlour, relaxed evenings and the surviving with me on way too hot summer days in the office. Very special thanks to Antje, who invested time and energy in proof reading of the thesis and taught me the correct usage of hyphens.

I would like to thank some (former) PhD students from the CRC1238, above all Tobias and Sebastian, but also to David, Andrea, and Daniel. I immediately felt warmly welcome in the CRC, even though I am not from physics but from the other side of the Grüngürtel.

Since the beginning of my Master's, my research was always accompanied by the Young Crystallographers of Deutsche Gesellschaft für Kristallographie. I thank all my team members for the great time of collaboration and organisation of meetings and conferences. This voluntary work was always a matter close to my heart.
I am very much thankful for my great friends in Köln and, back at home, in Bottrop. They have always supported and encouraged me, and organised feel-good hours after stressful working days. Thank you for always being there - even if we rarely see each other.

At the end, I would like to thank my family. To my parents and my brother: Thank you for understanding me, supporting me, and always giving me confidence in difficult times: I look up to you. My biggest thanks go to my husband Steffen, who is my best friend and my biggest fan, and has given me the best possible support during the thesis by listening to me, encouraging me, and sharing his life with me.

Contents

Abstract i

Kurzzusammenfassung iii

List of Abbreviations xi

List of Figures xiii

List of Tables xvii

1 Alkali Platinum-Group Metal Oxides 1

1.1 Structural aspects and synthesis methods . . . 2

1.1.1 Lithium iridates . . . 2

1.1.1.1 α-Li_2IrO_3 . . . 2

1.1.1.2 β-Li_2IrO_3 . . . 5

1.1.1.3 γ-Li_2IrO_3 . . . 7

1.1.2 Lithium ruthenates . . . 8

1.1.2.1 Li_2RuO_3 . . . 8

1.1.2.2 Li_3RuO_4 . . . 11

1.1.3 Lithium iridate-ruthenates . . . 13

1.1.4 Sodium ruthenates . . . 15

1.1.4.1 $Na_{3-x}Ru_4O_9$ . . . 15

1.1.4.2 $Na_{27}Ru_{14}O_{48}$ . . . 18

1.2 Magnetic properties . . . 19

1.2.1 Alkali iridates . . . 19

1.2.2 Lithium ruthenates . . . 21

1.2.3 Lithium iridate-ruthenates . . . 22

1.2.4 Sodium ruthenates . . . 22

1.3 Electronic properties . . . 23

1.4 Motivation . . . 23

2 Principles and techniques of single-crystal growth 25
2.1 Introduction to single-crystal growth . . . 25
2.2 Chemical Vapour Transport Reaction . . . 26
2.2.1 Thermodynamic fundamentals . . . 28
2.2.2 Experimental setup . . . 33
2.2.3 Preparation methods . . . 34
2.2.4 External factors influencing the growth process . . . 36
2.3 Solid-state reaction method . . . 39
2.4 Laboratory chemicals . . . 40

3 Methods of characterisation 41
3.1 Structural analysis . . . 41
3.1.1 Instruments . . . 45
3.1.1.1 Powder X-ray diffraction . . . 45
3.1.1.2 Single-crystal X-ray diffraction . . . 45
3.2 Thermal analysis . . . 46
3.3 Spectroscopic analysis . . . 47
3.3.1 Energy Dispersive X-Ray Spectroscopy . . . 47
3.3.2 Raman Spectroscopy . . . 48

4 Li-Ir-O system 51
4.1 Crystal-growth investigations . . . 51
4.1.1 Thermodynamic considerations . . . 51
4.1.2 General observations . . . 54
4.1.3 α-Li_2IrO_3 . . . 59
4.1.4 β-Li_2IrO_3 . . . 61
4.1.5 γ-Li_2IrO_3 . . . 62
4.1.6 Time-dependent crystallisation process . . . 63
4.1.7 Bottom-body formation process . . . 65
4.2 Material characterisation . . . 66
4.2.1 Structural aspects . . . 66
4.2.1.1 α-Li_2IrO_3 . . . 67
4.2.1.2 β-Li_2IrO_3 . . . 70
4.2.1.3 γ-Li_2IrO_3 . . . 73
4.2.2 Chemical instability . . . 75
4.2.3 Elemental analysis . . . 76
4.2.3.1 α-Li_2IrO_3 . . . 76
4.2.3.2 β-Li_2IrO_3 . . . 79
4.2.4 Thermal analysis . . . 80

4.2.4.1 Decomposition reactions of α- and β-Li_2IrO_3 . . . 80
4.2.4.2 Phase transition between α- and β-Li_2IrO_3 . . . 81

5 Li-Ru-O system 83
5.1 Crystal-growth investigations . . . 83
5.1.1 Thermodynamic considerations . . . 83
5.1.2 Li_2RuO_3 . . . 88
5.1.3 Li_3RuO_4 . . . 91
5.1.4 Bottom-body formation process . . . 93
5.2 Material characterisation . . . 93
5.2.1 Structural aspects . . . 93
5.2.1.1 Li_2RuO_3 . . . 93
5.2.1.2 Li_3RuO_4 . . . 96
5.2.2 Chemical instability . . . 98
5.2.3 Elemental analysis . . . 99
5.2.3.1 Li_2RuO_3 . . . 99
5.2.3.2 Li_3RuO_4 . . . 100
5.2.4 Thermal analysis . . . 101
5.2.4.1 Decomposition reaction of Li_3RuO_4 . . . 101
5.2.4.2 Thermal behaviour of Li_2RuO_3 . . . 101

6 Li-Ir-Ru-O system 103
6.1 Crystal-growth investigations . . . 103
6.1.1 Thermodynamic considerations . . . 103
6.1.2 $Li_2Ir_{1-x}Ru_xO_3$ . . . 105
6.2 Material characterisation . . . 106
6.2.1 Elemental analysis . . . 106
6.2.2 Structural aspects . . . 110
6.2.2.1 Room-temperature measurements . . . 110
6.2.2.2 Low-temperature measurements . . . 119

7 Na-Ru-O system 125
7.1 Crystal-growth investigations . . . 125
7.1.1 Thermodynamic considerations . . . 125
7.1.2 $Na_{3-x}Ru_4O_9$ . . . 129
7.1.3 $Na_{27}Ru_{14}O_{48}$ . . . 132
7.2 Material characterisation . . . 133
7.2.1 Structural aspects . . . 133
7.2.1.1 $Na_{3-x}Ru_4O_9$ . . . 133
7.2.1.2 $Na_{27}Ru_{14}O_{48}$ . . . 139

7.2.2 Chemical instability 147
7.2.3 Elemental analysis 147
7.2.4 Thermal analysis 149

8 Conclusion and Outlook **151**

Appendix A Li-Ir-O system **157**

Appendix B Li-Ru-O system **177**

Appendix C Li-Ir-Ru-O system **191**

Appendix D Na-Ru-O system **203**

Bibliography **217**

Erklärung **225**

List of Abbreviations

The following abbreviations are used within the text and the captions of tables and figures as shown in the List of Tables and List of Figures.

a, b, c, α, β, γ	lattice parameters of structural models
A	alkali metal
APGMO	Alkali Platinum-Group Metal Oxides
ADP	atomic displacement parameter
BVS	Bond-valence sum
BVT	Bond-valence theory
CVTR	Chemical Vapour Transport Reaction
C_T^0	heat capacity as a function of temperature
$\Delta_R G$	Gibbs free energy
ΔH^0	standard enthalpy of formation
$\Delta_R H$	enthalpy of reaction
$\Delta_R S$	entropy of reaction
ΔS^0	standard entropy of formation
ΔT	temperature change
DFT	Density-functional theory
DSC	Differential Scanning Calorimetry
DTA	Differential Thermal Analysis
EDX	Energy Dispersive X-ray Spectroscopy
GOF	Quality indicator of structural refinement: Goodness of fit
HT	high temperature
K_p	equilibrium constant
LT	low temperature
M	platinum-group metal
μ	absorption coefficient
$p(i)$	partial pressure of compound i
P-ND	powder neutron diffraction
P-XRD	powder X-ray diffraction
ρ_{calc}	calculated density

R	ideal gas constant
R_{int}	Quality indicator of structural refinement: internal R-value
R_1	Quality indicator of structural refinement: unweighted R-value
w_{R2}	Quality indicator of structural refinement: weighted R-value
RT	room temperature
SC-XRD	Single-crystal X-ray diffraction
SEM	Scanning Electron Microscopy
TG	Thermogravimetry
T_{opt}	optimum transport temperature
V	unit cell volume
x, y, z	fractional coordinates of atomic positions
$x_{d,max}$	maximum relative difference of x_m between highest and lowest stair
x_{in}	weighed relative amount of Ru
x_m	measured relative amount of Ru via EDX
$\bar{x}_m$	averaged x_m of a sample
XRD	X-ray diffraction
2D	two-dimensional
3D	three-dimensional

List of Figures

Alkali Platinum-Group Metal Oxides

1.1 Crystal structure of α-Li_2IrO_3, after O'Malley et al. [90]. 3
1.2 Crystal-growth setup for Chemical Vapour Transport Reaction experiments. 4
1.3 Crystal structure of β-Li_2IrO_3, after Biffin et al. [11]. 6
1.4 Crystal structure of γ-Li_2IrO_3, after Modic et al. [77]. 8
1.5 *hkl* reflections of calculated P-XRD patterns of Li_2RuO_3. 10
1.6 Depiction of the dimerisation phenomenon in Li_2RuO_3, after Miura et al. [76]. 11
1.7 Crystal structure of Li_3RuO_4, after Alexander et al. [2]. 12
1.8 Crystal structure of $Na_{3-x}Ru_4O_9$, after Darriet [29]. 16
1.9 Crystal structure of $Na_{27}Ru_{14}O_{48}$, after Allred et al. [3]. 19

Principles and techniques of single-crystal growth

2.1 Chemical Vapour Transport Reaction in a closed system. 28
2.2 Experimental setup for Chemical Vapour Transport Reactions. 34
2.3 Constituent Al_2O_3 parts of the CVTR setup. 35
2.4 Prepared crucible for N_2 insertion. 36
2.5 Horizontal and vertical temperature profiles of the muffle furnace. 37
2.6 Temperature and relative humidity conditions of the laboratory. 38
2.7 Closed conic crucible for solid-state reaction experiments. 39

Li-Ir-O system

4.1 Temperature-dependent progress of $p(i)$ of IrO_2(g), IrO_3(g), and LiOH(g). 52
4.2 Reaction cycle for the growth of Li_2IrO_3. 54
4.3 Single crystals of α-Li_2IrO_3 obtained in the present work by CVTR. 59
4.4 Morphology of α-Li_2IrO_3 single crystals. 60
4.5 Single crystals of β-Li_2IrO_3 obtained in the present work by CVTR. 62
4.6 Time-dependent crystallisation process of Li_2IrO_3. 64
4.7 Solidified part of the bottom body consisting of α- and β-Li_2IrO_3 crystals. 65
4.8 Comparison of calculated P-XRD patterns of α-, β-, and γ-Li_2IrO_3. 66
4.9 Ir-Ir distances in α-Li_2IrO_3. 67

4.10 Ir-Ir distances in β-Li_2IrO_3. 71
4.11 Li positions in the γ-Li_2IrO_3 structure, after Analytis [4]. 75
4.12 Chemical instability of Li_2IrO_3. 76
4.13 Element distribution of Ir and O in isometric α-Li_2IrO_3. 77
4.14 Element distribution of Ir and O in platy α-Li_2IrO_3. 78
4.15 Element distribution of Ir and O in dendritic α-Li_2IrO_3. 79
4.16 Element distribution of Ir and O in β-Li_2IrO_3. 79
4.17 DTA measurements of α- and β-Li_2IrO_3. 80

Li-Ru-O system

5.1 Temperature-dependent progress of $p(i)$ of RuO_3(g) and LiOH(g). 84
5.2 Reaction cycle for the growth of Li_2RuO_3 and Li_3RuO_4. 85
5.3 Morphology of isometric and platy Li_2RuO_3 crystals. 89
5.4 Time-dependent crystallisation process of Li_2RuO_3. 90
5.5 Modified setup for the growth of Li_3RuO_4. 92
5.6 Crystal structure of Li_2RuO_3. 95
5.7 Refined P-XRD pattern of Li_3RuO_4. 98
5.8 Element distribution of Ru and O in isometric and platy Li_2RuO_3. 99
5.9 Element distribution of Ru and O in platy Li_2RuO_3. 100
5.10 Element distribution of Ru and O in Li_3RuO_4. 100
5.11 DTA measurement of Li_3RuO_4. 101

Li-Ir-Ru-O system

6.1 Reaction cycle for the growth of $Li_2Ir_{1-x}Ru_xO_3$. 104
6.2 Single crystals of $Li_2Ir_{1-x}Ru_xO_3$ obtained in the present work by CVTR. 105
6.3 Elemental composition of $Li_2Ir_{1-x}Ru_xO_3$ crystals depending on the growth position. 108
6.4 Element distribution of Ir and Ru in $Li_2Ir_{1-x}Ru_xO_3$. 109
6.5 Indexed P-XRD pattern of $Li_2Ir_{1-x}Ru_xO_3$ with $\bar{x}_m = 0.28(2)$. 111
6.6 Indexed P-XRD pattern of $Li_2Ir_{1-x}Ru_xO_3$ with $\bar{x}_m = 0.93(1)$. 112
6.7 Indexed P-XRD pattern of $Li_2Ir_{1-x}Ru_xO_3$ with $\bar{x}_m = 0.71(3)$. 113
6.8 RT P-XRD patterns of $Li_2Ir_{1-x}Ru_xO_3$. 114
6.9 Progression of lattice parameters of $Li_2Ir_{1-x}Ru_xO_3$. 118
6.10 LT P-XRD measurements of $Li_2Ir_{1-x}Ru_xO_3$ with $\bar{x}_m = 0.87(3)$. 120
6.11 LT P-XRD measurements of $Li_2Ir_{1-x}Ru_xO_3$ with $\bar{x}_m = 0.24(2)$. 121
6.12 LT P-XRD measurements of $Li_2Ir_{1-x}Ru_xO_3$ with $\bar{x}_m = 0.60(3)$. 122

Na-Ru-O system

7.1 Reaction cycle for the growth of $Na_{3-x}Ru_4O_9$ by CVTR. 127
7.2 Single crystals of $Na_{3-x}Ru_4O_9$ obtained in the present work by CVTR. 129
7.3 Single crystals of $Na_{3-x}Ru_4O_9$ obtained in the present work by solid-state reaction. . 130

7.4 DSC/TG measurement of a mixture of Na_2CO_3 and RuO_2. 131
7.5 Single crystals of $Na_{27}Ru_{14}O_{48}$ obtained in the present work by solid-state reaction. . 132
7.6 Thermal displacement ellipsoids of Na in $Na_{3-x}Ru_4O_9$. 137
7.7 Clusters in the $Na_{27}Ru_{14}O_{48}$ structure. 142
7.8 Position of partially occupied Na^+ ions in the first $Na_{27}Ru_{14}O_{48}$ structure. 143
7.9 Comparison of unit cells of $Na_{27}Ru_{14}O_{48}$. 144
7.10 Orientation of clusters in the second $Na_{27}Ru_{14}O_{48}$ structure. 145
7.11 Comparison of Na^+ positions in the structural models of $Na_{27}Ru_{14}O_{48}$. 146
7.12 Element distribution of Na and Ru in $Na_{3-x}Ru_4O_9$. 148
7.13 DTA measurement of $Na_{3-x}Ru_4O_9$. 149
7.14 DSC/TG measurement of $Na_{3-x}Ru_4O_9$. 150

Appendix A: Li-Ir-O system

A.1 Raman spectrum of chemically instable α-Li_2IrO_3. 158

Appendix C: Li-Ir-Ru-O system

C.1 LT P-XRD measurements of $Li_2Ir_{1-x}Ru_xO_3$ with $\bar{x}_m = 0.13(2)$. 198
C.2 LT P-XRD measurements of $Li_2Ir_{1-x}Ru_xO_3$ with $\bar{x}_m = 0.31(3)$. 199
C.3 LT P-XRD measurements of $Li_2Ir_{1-x}Ru_xO_3$ with $\bar{x}_m = 0.45(2)$. 200
C.4 LT P-XRD measurements of $Li_2Ir_{1-x}Ru_xO_3$ with $\bar{x}_m = 0.70(3)$. 201
C.5 LT P-XRD measurements of $Li_2Ir_{1-x}Ru_xO_3$ with $\bar{x}_m = 0.87(3)$. 202

List of Tables

Alkali Platinum-Group Metal Oxides

1.1 Comparison of lattice parameters and GII of Li_2RuO_3. 9
1.2 Lattice parameters of Li_2MO_3 (M = Ir; Ru) with $C2/m$ and $P2_1/m$ symmetry. 14

Principles and techniques of single-crystal growth

2.1 Sizes of the constituent parts of the CVTR setup. 35
2.2 Laboratory chemicals used in the present work. 40

Li-Ir-O system

4.1 Growth experiments in the Li-Ir-O system. 56
4.2 Structural model of α-Li_2IrO_3 of the present work. 68
4.3 Comparison of lattice parameters and GII of structural models of α-Li_2IrO_3. 69
4.4 Comparison of lattice parameters and GII of structural models of β-Li_2IrO_3. 71
4.5 Structural model of β-Li_2IrO_3 of the present work. 72
4.6 Comparison of interatomic distances in α- and β-Li_2IrO_3. 73
4.7 Results from DTA measurements of α- and β-Li_2IrO_3. 80

Li-Ru-O system

5.1 Growth experiments in the Li-Ru-O system. 86
5.2 Structural model of Li_2RuO_3 of the present work 94
5.3 Comparison of lattice parameters, GII, and Ru-Ru distances of Li_2RuO_3. 96
5.4 Comparison of lattice parameters and GII of Li_3RuO_4. 97

Li-Ir-Ru-O system

6.1 Growth experiments in the Li-Ir-Ru-O system. 107

Na-Ru-O system

7.1 Growth experiments in the Na-Ru-O system. 128
7.2 Comparison of lattice parameters and GII of structural models of $Na_{3-x}Ru_4O_9$. . . . 133
7.3 Structural model of $Na_{2.55(8)}Ru_4O_9$ of the present work (CVTR). 134
7.4 Structural model of $Na_{2.36(3)}Ru_4O_9$ of the present work (solid-state reaction). 135

7.5 Structural model of $Na_{25.7(1)}Ru_{14}O_{48}$. 139
7.6 Comparison of lattice parameters and GII of $Na_{27}Ru_{14}O_{48}$ structural models. 141

Appendix A: Li-Ir-O system

A.1 Compounds in the Li-Ir-O system. 157
A.2 Calculated temperature-dependent ΔH_T^0, ΔS_T^0, and C_p of Li_2IrO_3. 157
A.3 Calculated temperature-dependent ΔH_R and ΔS_R of Li_2IrO_3. 158
A.4 ADPs of α-Li_2IrO_3 of the present work. 159
A.5 Selected bond angles of α-Li_2IrO_3 of the present work. 159
A.6 Averaged bond lengths and BVS of α-Li_2IrO_3 of the present work. 160
A.7 Structural model of α-Li_2IrO_3 of Freund et al. [35]. 161
A.8 Structural model of α-Li_2IrO_3 of O'Malley et al. [90]. 162
A.9 Averaged bond lengths and BVS of α-Li_2IrO_3 of Freund et al. [35]. 163
A.10 Averaged bond lengths and BVS of α-Li_2IrO_3 of O'Malley et al. [90]. 164
A.11 ADPs of β-Li_2IrO_3 of the present work. 165
A.12 Selected bond angles of β-Li_2IrO_3 of the present work. 165
A.13 Averaged bond lengths and BVS of β-Li_2IrO_3 of the present work. 166
A.14 Structural model of β-Li_2IrO_3 of Biffin et al. [11]. 167
A.15 Averaged bond lengths and BVS of β-Li_2IrO_3 of Biffin et al. [11]. 168
A.16 Structural model of γ-Li_2IrO_3 from .cif file of Modic et al. [77]. 169
A.17 Structural model of γ-Li_2IrO_3 from supplementary material of Modic et al. [77] . . . 170
A.18 Structural model of γ-Li_2IrO_3 of Analytis [4]. 171
A.19 Averaged bond lengths and BVS of γ-Li_2IrO_3 from .cif file of Modic et al. [77]. . . . 172
A.20 Averaged bond lengths and BVS of γ-Li_2IrO_3 from suppl. material of Modic et al. [77]. 173
A.21 Averaged bond lengths and BVS of γ-Li_2IrO_3 of Analytis [4]. 174
A.22 Selected bond angles of γ-Li_2IrO_3 of Analytis [4]. 175

Appendix B: Li-Ru-O system

B.1 Compounds in the Li-Ru-O system. 177
B.2 Calculated temperature-dependent ΔH_T^0, ΔS_T^0, and C_p of Li_2RuO_3. 178
B.3 Calculated temperature-dependent ΔH_R and ΔS_R of Li_2RuO_3. 178
B.4 Calculated temperature-dependent ΔH_T^0, ΔS_T^0, and C_p of Li_3RuO_4. 179
B.5 Calculated temperature-dependent ΔH_R and ΔS_R of Li_3RuO_4. 179
B.6 Structural model of Li_2RuO_3 ($C2/c$) of Ramesha et al. [101]. 180
B.7 Structural model of Li_2RuO_3 ($C2/m$) of Miura et al. [76] 180
B.8 Structural model of Li_2RuO_3 ($P2_1/m$) of Miura et al. [76] 181
B.9 Averaged bond lengths and BVS of Li_2RuO_3 ($C2/c$) of Ramesha et al. [101]. 182
B.10 Averaged bond lengths and BVS of Li_2RuO_3 ($C2/m$) of Miura et al. [76] 183
B.11 Averaged bond lengths and BVS of Li_2RuO_3 ($P2_1/m$) of Miura et al. [76]. 184

B.12 ADPs of Li_2RuO_3 ($P2_1/m$) of the present work. 185
B.13 Averaged bond lengths and BVS of Li_2RuO_3 ($P2_1/m$) of the present work. 185
B.14 Structural model of $Li_{2.81(2)}Ru_{1.04(2)}O_4$ of Alexander et al. [2]. 186
B.15 Structural model of Li_3RuO_4 of Jacquet et al. [43]. 187
B.16 Averaged bond lengths and BVS of Li_3RuO_4 of Jacquet et al. [43]. 187
B.17 Averaged bond lengths and BVS of Li_3RuO_4 of Alexander et al. [2]. 188
B.18 Structural model of Li_3RuO_4 of the present work. 189
B.19 Averaged bond lengths and BVS of Li_3RuO_4. 190
B.20 Comparison of Ru-Ru distances in structural models of Li_3RuO_4. 190

Appendix C: Li-Ir-Ru-O system

C.1 Calculated temperature-dependent ΔH_T^0, ΔS_T^0, ΔH_R, ΔS_R, and C_p of $Li_2Ir_{1-x}Ru_xO_3$. . 191
C.2 Transformed structural model of Li_2RuO_3 ($C2/m$). 196
C.3 Transformed structural model of Li_2RuO_3 ($P2_1/m$). 196
C.4 Lattice parameters of $C2/m$ and $P2_1/m$ phases of $Li_2Ir_{1-x}Ru_xO_3$. 197

Appendix D: Na-Ru-O system

D.1 Compounds in the Na-Ru-O system. 203
D.2 Calculated temperature-dependent ΔH_T^0, ΔS_T^0, and C_p of $Na_3Ru_4O_9$. 204
D.3 Calculated temperature-dependent ΔH_R and ΔS_R of $Na_3Ru_4O_9$. 204
D.4 Bond lengths and BVS of $Na_{2.55(8)}Ru_4O_9$ grown by CVTR. 205
D.5 ADPs of $Na_{2.55(8)}Ru_4O_9$ grown by CVTR. 206
D.6 Bond lengths and BVS of $Na_{2.36(3)}Ru_4O_9$ grown by solid-state reaction. 207
D.7 ADPs of $Na_{2.36(3)}Ru_4O_9$ grown by solid-state reaction. 208
D.8 Structural model of $Na_{2.1}Ru_4O_9$ of Darriet [29]. 209
D.9 Structural model of $Na_{2.73}Ru_4O_9$ of Regan et al. [103]. 210
D.10 BVS of $Na_{2.1}Ru_4O_9$ of Darriet [29], including Ru^{3+}. 211
D.11 BVS of $Na_{2.73(4)}Ru_4O_9$ of Regan et al. [103], including Ru^{3+}. 211
D.12 BVS of $Na_{2.1}Ru_4O_9$of Darriet [29], including Ru^{3+} and Ru^{4+}. 212
D.13 BVS of $Na_{2.73(4)}Ru_4O_9$ of Regan et al. [103], including Ru^{3+} and Ru^{4+} 212
D.14 Structural model of $Na_{27}Ru_{14}O_{48}$ of Allred et al. [3]. 213
D.15 Stacking faults in $Na_{27}Ru_{14}O_{48}$. 214
D.16 Structural model of $Na_{37.1(4)}Ru_{21}O_{72}$ of the present work. 214

Chapter 1

Alkali Platinum-Group Metal Oxides

Alkali iridates and ruthenates of lithium and sodium are part of the Alkali Platinum-Group Metal Oxides (APGMO). These compounds cover a large variety of oxidic structures and are characterised by incorporating an alkali metal A and a platinum-group metal M. The diversity of M is large and includes ruthenium (Ru), rhodium (Rh), palladium (Pd), osmium (Os), iridium (Ir), and platinum (Pt). The superior group of AGPMO compounds are the platinum-group metal oxocompounds, which are not restricted to incorporate an alkali metal but other elements. Due to variations in stoichiometry and oxidation states, a large variety of compounds is known. An extensive overview is given by a series of review articles of Müller-Buschbaum [83–88].

The present work is focussed on APGMO compounds including the alkali metals sodium and lithium. With respecting the crystal chemistry, typical stoichiometries are *e.g.* A_2MO_3 [4, 11, 26, 33, 35, 44, 60, 62, 64, 65, 67, 72, 76–78, 90, 96, 99, 101, 124, 126, 128, 136], A_3MO_4 [2, 21, 43], $A_{3-x}M_4O_9$ [22, 29, 103, 113, 137], and $A_{27}M_{14}O_{48}$ [3] with A = Li; Na. Some further APGMO compounds with other stoichiometry are known in literature but will not be considered in the present work. The common structural feature of the compounds of interest is the octahedral coordination of the platinum-group metal M, forming MO_6 octahedra. In the present work, the focus is set on M = Ir; Ru. In the investigated crystal structures, the oxidation state of M varies. A_2MO_3 and A_3MO_4 compounds incorporate M with one oxidation state, M^{4+} or M^{5+}, respectively. Contrarily, in the $A_{3-x}M_4O_9$ and $A_{27}M_{14}O_{48}$ compounds M exhibit different oxidation states: M^{3+}, M^{4+}, and M^{5+}.

The present work aims the investigation of alkali iridates and ruthenates of lithium and sodium and focuses on the above stoichiometries. In the following, the current state of research on these compounds is presented and includes their crystal structures, synthesis conditions, and most important physical properties.

1.1 Structural aspects and synthesis methods

The description of crystal structures and synthesis methods of alkali iridates and ruthenates of lithium and sodium is divided into sections regarding their chemical composition. In each section, the literature review is complemented by the discussion of further structurally related APGMO compounds.

1.1.1 Lithium iridates

In the family of APGMO, the lithium iridate compounds Li_2IrO_3 [11, 77, 90] and Li_8IrO_6 [63] are known (appendix table A.1). In the present work, the focus lies on lithium iridates with the chemical composition Li_2IrO_3, which are characterised by their honeycomb-related crystal structures. Li_2IrO_3 compounds incorporate Ir^{4+} and crystallise in three symmetries, forming α-Li_2IrO_3 ($C2/m$ [35, 90]), β-Li_2IrO_3 (*Fddd* [11, 124]), and γ-Li_2IrO_3 (*Cccm* [4, 77]).
The fundamental framework of the Li_2IrO_3 modifications is derived from a face-centred-cubic lattice, in which O atoms are cubic-close packed and Li and Ir atoms occupy the octahedral positions. With this, an arrangement of edge-sharing IrO_6- and LiO_6-octahedra is formed. In both, monoclinic and orthorhombic symmetry, a honeycomb network of edge-sharing IrO_6 octahedra is established. Depending on the crystal symmetry and, hence, the distribution of Li and Ir atoms on the octahedral positions, two-dimensional (2D) and three-dimensional (3D) honeycomb structures are formed.

1.1.1.1 α-Li_2IrO_3

The crystal structure of monoclinic α-Li_2IrO_3 ($C2/m$) [90] is derived from the Li_2MnO_3 structure type [123]. In the literature, different cell symmetries for the Li_2MnO_3 structure were reported. After stating an orthorhombic [66], monoclinic [45], cubic, or hexagonal symmetry [74], Strobel and Lambert-Andron [123] presented a monoclinic $C2/m$ cell symmetry, which was solved based on a single-crystal study of synthesised Li_2MnO_3 crystals.
In accordance with the Li_2MnO_3 structure [123], the crystal structure of α-Li_2IrO_3 can be derived from a cubic-closed packing of O^{2-} ions. Li^+ and Ir^{4+} are situated on octahedral sites and form edge-sharing LiO_6 and IrO_6 octahedra [90]. In direction of the *c*-axis, a mixed metal $LiIr_2$ layer and a Li layer are alternatingly stacked. In the mixed metal layer, a 2D honeycomb structure is formed parallel to (001). The center of each honeycomb is filled up by one Li atom, Li2 (figure 1.1a). The Li layer consists of Li3/Li4 atoms (figure 1.1b). There is no shift between adjacent layers. Due to almost equal Ir-Ir distances, a nearly hexagonal honeycomb network is realised [90].

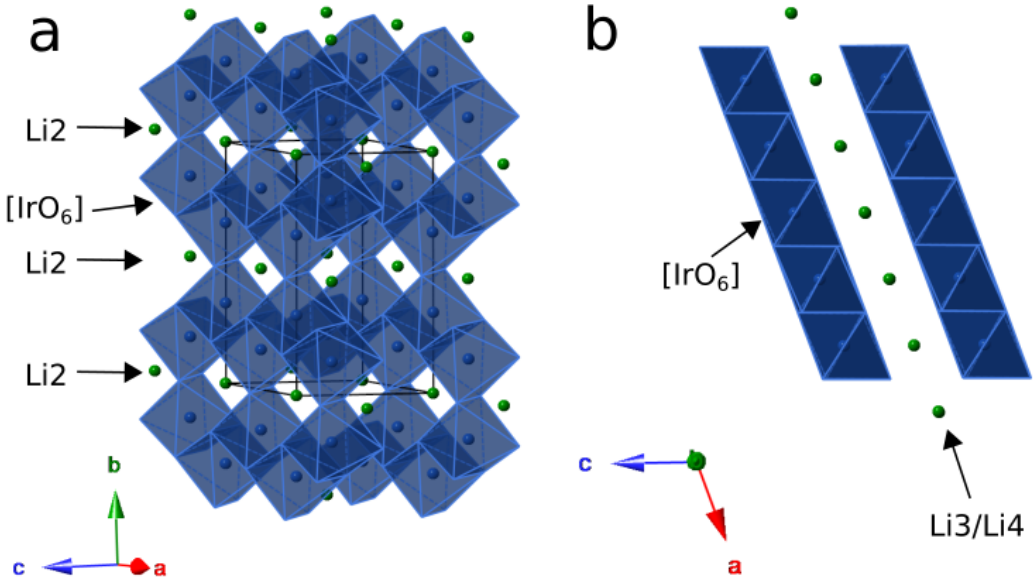

Figure 1.1: Crystal structure of α-Li_2IrO_3, after O'Malley et al. [90]. (a) Edge-sharing IrO_6 octahedra (dark blue) build up the 2D honeycomb structure of α-Li_2IrO_3. In each honeycomb center Li2 atoms (green) are situated. (b) In between the mixed metal layers, Li3/Li4 atoms (green) form a Li atomic layer. The simplified structural visualisations neglect the depiction of the atomic O positions and LiO_6 octahedra.

In a study of Freund et al. [35], three different types of twinning of α-Li_2IrO_3 were reported. The most common twinning type results from a rotation by $\pm$ 120° around [001]. This twinning phenomenon is favoured due to the nearly three-fold symmetry of the honeycomb layers and the group-subgroup relation between six-fold and three-fold rotation. Here, due to a rotation of subsequent layers by $\pm$ 120° the loss of the three-fold symmetry must lead to a triplet formation. Another type of twinning is caused by the rotation by 180° around [101], which exchanges the *a*- and *c*-axis. This twinning is favoured due to the almost similar lengths of *a* and *c*. The third type of twinning occurs due to a rotation by $\pm$ 90° around $[\bar{1}01]$. These structural investigations on α-Li_2IrO_3 showed that its crystal structure is dominated by a variety of crystal defects [35].

Pressure-dependent structural investigations of α-Li_2IrO_3 revealed a pressure-induced structural phase transition from the $C2/m$ to a $P\bar{1}$ structure at a critical pressure of P_c = 3.8 GPa [39]. This phase transition mainly affects the 2D honeycomb network in the *ab* plane. According to Hermann et al. [39], equally long Ir-Ir distances (2.9787(18) Å and 2.979(4) Å) are shortened or elongated and lead to an Ir dimerisation phenomenon which affects two Ir-Ir distances within the honeycomb ring. One Ir-Ir distance is elongated by around 1.7 %, whereas a second Ir-Ir distance is significantly shortened by around 8.8 %. Thus, the two-fold symmetry axis is not preserved, which leads to the $P\bar{1}$ symmetry and a halfed unit-cell volume. During the phase transition, the Ir^{4+} oxidation state is maintained [39].

First polycrystalline samples of α-Li_2IrO_3 were obtained by Kobayashi et al. [61] by heating mixtures of Li_2CO_3 and IrO_2 to 923 K-1323 K. Similarly, O'Malley et al. [90] performed the solid-state reaction method by preparing stoichiometric mixtures of Li_2CO_3 and Ir with 5 % excess of Li_2CO_3 to compensate for the high-temperature (HT) volatility of lithium compounds. Subsequently, the homogenised mixture was heated in air with 10 K/min to reach 1025 K and held for 12 h before cooling with a rate of 10 K/min. Pure phases were obtained due to successive heating cycles up to 1325 K. Another comparable approach for obtaining polycrystalline samples was performed by Takayama et al. [124]. First single crystals of α-Li_2IrO_3 were obtained by Freund et al. [35] by conducting Chemical Vapour Transport Reaction experiments (CVTR) with separated educts (figure 1.2). In the growth setup, two educts are situated in a crucible but separated by rings with spikes forming a spiral staircase. During the growth experiment, crystallisation took place on these spikes, which act as preferred crystallisation sites [35].

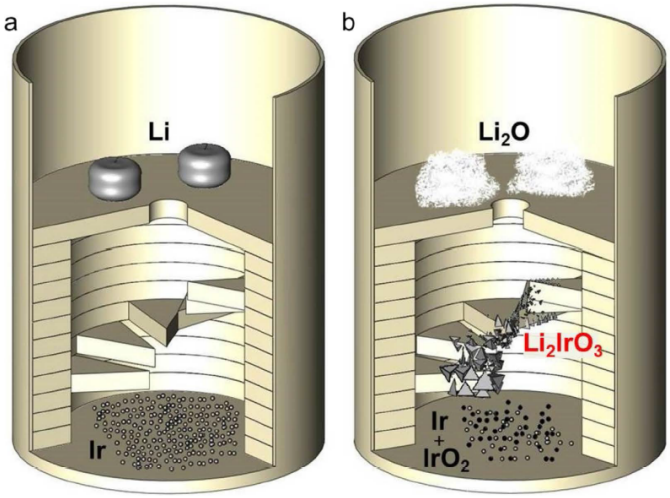

Figure 1.2: Crystal-growth setup for performing Chemical Vapour Transport Reaction experiments. (a) The educts Li and Ir are separated from each other by rings with spikes forming a spiral staircase. (b) Crystallisation of Li_2IrO_3 takes place on these spikes, whereas the educts oxidise and form Li_2O and IrO_2. Adapted from Freund et al. [35].

Structural solutions from both, powder and single-crystal X-ray diffraction (P-XRD, SC-XRD, appendix tables A.8) [90] and A.7) [35], show fully occupied atomic positions. In contrast to Freund et al. [35], O'Malley et al. [90] proposed a shared occupancy of Li and Ir atomic positions: Ir1/Li1 and Li2/Ir2. They reported that Ir1 is mainly occupied by Ir (Ir1: 90.2(2) %; 9.8(2) %), whereas the Li2 atomic position is mainly occupied by Li (Li2: 80.4(3) %; Ir2: 19.6(3) %) [90]. By considering the multiplicity of the different atomic sites, the overall proposed stoichiometry Li_2IrO_3 is still maintained [90]. This different structural solution might be explained by structural disorder in powder samples of α-Li_2IrO_3 [90]. In this study, stacking faults were described as shifts between $LiIr_2$ layers. Hence, O'Malley et al. [90] reported that P-XRD patterns of α-Li_2IrO_3 are influenced by a classic Warren lineshape, which results in non-ideal curve fitting in the range from 19° to

30° 2Θ. Therefore, the shared occupancy of both, Ir1 and Li2 positions, in α-Li_2IrO_3 is interpreted as a result of difficulties in curve fitting due to structural disorder in powder samples of α-Li_2IrO_3 [90].

Further compounds with two-dimensional honeycomb structure (C2/m)

Next to α-Li_2IrO_3, further AGPMO compounds are based on the Li_2MnO_3 structure type ($C2/m$) and already known in the literature: Li_2PdO_3 [65], Li_2PtO_3 [90], and Li_2RhO_3 [126]. For Na_2IrO_3, first structural solutions reported a $C2/c$ cell symmetry [118]. In a later publication of Choi et al. [26] the $C2/c$ symmetry was rejected and revised to space group $C2/m$ by describing the $C2/c$ structure as a ′supercell′ of the $C2/m$ structure, which was caused by small atomic displacements and led to a doubled unit cell. Since no superlattice peaks could be observed, $C2/m$ is considered as the most suitable solution for Na_2IrO_3 [26]. According to Singh and Gegenwart [118] and Krizan et al. [62], polycrystalline samples of Na_2IrO_3 were obtained by annealing pellets of stoichiometric mixtures of Na_2CO_3 and Ir or anhydrous IrO_2 with an excess of 5 % Na_2CO_3 to compensate for Na volatility during the synthesis at 1073-1173 K for 48 h. Single crystals could be obtained after regrinding and pelletising the material by treating the pellet at 1323 K for 72 h and quenching it in air after cooling it to 1173 K [118]. Samples of Na_2IrO_3 are sensitive to moisture [62]. Polycrystalline samples of Li_2PdO_3 were prepared from a mixture of Li_2CO_3 and PdO in a ratio of 1:1, which was heated to 873 K for 48 h and slowly cooled to room temperature (RT) [65]. Subsequently, the result was pressed into pellets and heated at 873 K for 70 h under an oxygen pressure of 161 bar. Structural solution was derived from P-XRD data [65]. Polycrystalline samples of Li_2RhO_3 were prepared using stoichiometric mixtures of RhO_2 and LiOH with a subsequent heat treatment at 1123 K for 48 h in an oxygen flow [126]. The structure was solved by P-XRD [126]. Another compound with 2D honeycomb structure is Li_2PtO_3 [90]. Polycrystalline samples were prepared by reacting stoichiometric mixtures of Li_2CO_3 and Pt with 5 % excess of Li_2CO_3 to compensate for Li volatility at HT. The homogenised mixtures were heated in air at 1025 K for 12 hours before cooling them to RT. The heating and cooling rates were 10 K/h. To obtain pure Li_2PtO_3 samples, successive heating cycles were performed with increasing temperature up to 1325 K [90].

1.1.1.2 β-Li_2IrO_3

β-Li_2IrO_3 crystallises in space group *Fddd* [124] on the basis of the Ba_3SiI_2 structure type [131]. The Ba_3SiI_2 structure itself is derived from the rock-salt structure and can be described as a weakly distorted cubic-closed packing of iodide and silicon anions [131]. The main structural feature of the orthorhombic *Fddd* cell is the packing of $SiBa_6$ octahedra, which are connected with three neighbouring octahedra via their edges forming two interlacing layers. These layers are rotated by $\approx 70.6°$ around the c-axis and, therefore, run along the $a \pm b$ diagonals. In between this 3D network of $SiBa_6$ octahedra, iodide anions occupy all octahedral sites.

The crystal structure of β-Li_2IrO_3 was first observed by Biffin et al. [11] and solved from both powder neutron diffraction (P-ND) and SC-XRD data. Shortly afterwards, the crystal structure was

confirmed by Takayama et al. [124]. β-Li_2IrO_3 is classified as a related Ba_3SiI_2 structure, in which the cation and anion distribution is inverted. In β-Li_2IrO_3, edge-sharing IrO_6 octahedra build the 3D honeycomb network and form partially opened honeycomb rings (figure 1.3a). In between this network, Li2/Li3 atoms are situated on the octahedral sites [11]. As in Ba_3SiI_2, the 3D honeycomb network is characterised by two layers, which are rotated by $\approx 70^\circ$ around the c-axis and, hence, run along the $a \pm b$ diagonals (figure 1.3b). Along these diagonals, zig-zag chains of edge-connected IrO_6 octahedra run. Each IrO_6 octahedron is edge-connected with three neighbouring IrO_6 octahedra. With this, the local environment of the Ir atoms in β-Li_2IrO_3 [11] is close to the one in α-Li_2IrO_3 [90]. As a consequence, the structure of β-Li_2IrO_3 is described as a 3D 'hyper'-honeycomb structure [124]. In contrast to the shared occupancy of Li and Ir atomic positions in α-Li_2IrO_3 [90], the sharing of atomic positions in β-Li_2IrO_3 was not observed [11]. In accordance with α-Li_2IrO_3 [90], the oxidation state of iridium is Ir^{4+} with electronic configuration $5d^5$. At ambient conditions, the interatomic Ir-Ir distances are almost similar [11].

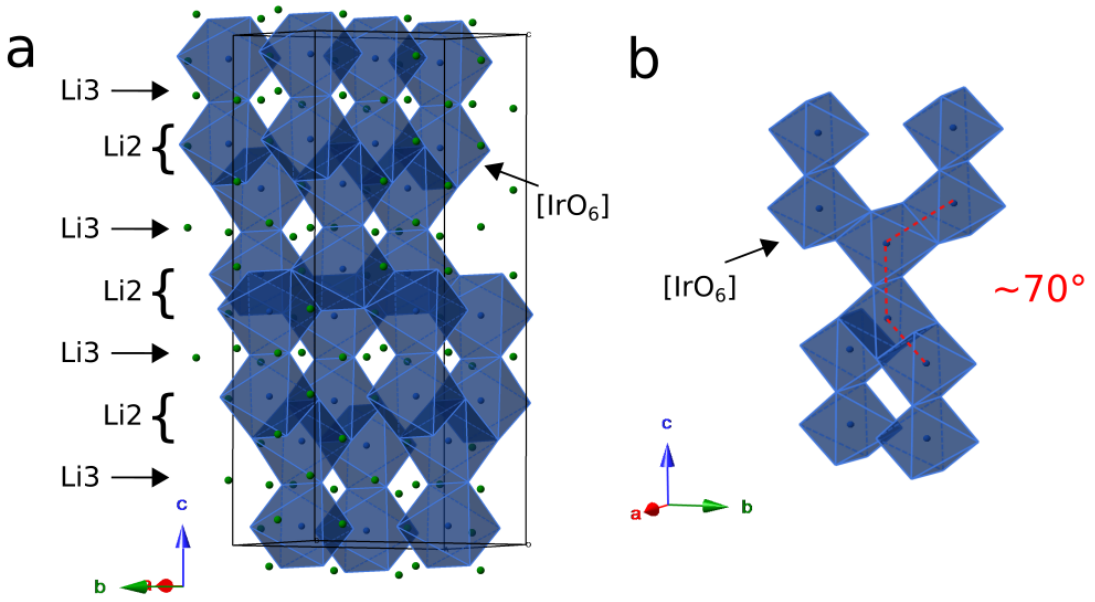

Figure 1.3: The 3D hyper-honeycomb structure of β-Li_2IrO_3, after Biffin et al. [11]. (a) The structure is build up by edge-sharing IrO_6 octahedra (dark blue). In between these layers, Li2/Li3 atoms (green) are situated and built up edge-sharing LiO_6 octahedra. The simplified structure neglects the depiction of the atomic O positions and LiO_6 octahedra. (b) Two layers of edge-sharing IrO_6 octahedra are rotated by $\approx 70^\circ$ around the c-axis and, hence, run along the $a \pm b$ diagonals.

Different approaches were realised to obtain polycrystalline and single crystalline samples of β-Li_2IrO_3 [11, 35, 124]. First polycrystalline samples were obtained by performing a solid-state reaction using Li_2CO_3, IrO_2, and LiCl in a molar ratio of 10 : 1 : 100 [124]. After pelletising the

mixture, it was heated at 1373 K for 24 h, cooled to 973 K with 30 K/h, and finally cooled to RT inside the furnace. To remove excess of LiCl, the sample was rinsed with distilled water. Following this approach, impurities of IrO_2 were found. Single-crystalline samples of 50 µm were taken out of the polycrystalline product and used for SC-XRD [124]. Biffin et al. [11] prepared polycrystalline material of β-Li_2IrO_3 by a repetitive annealing of α-Li_2IrO_3 at 1373 K. Like in Takayama et al. [124], single crystals were extracted from the polycrystalline material. Ruiz et al. [106] used amounts of Ir and Li_2CO_3 to produce pellets, which were heated in an alumina crucible at 1323 K for 12 h and then cooled to 1123 K at 2 K/h. With this method, a powder sample of β-Li_2IrO_3 with small single crystals of 105 µm x 105 µm x 300 µm was obtained [106]. Furthermore, single crystals of β-Li_2IrO_3 were grown by the CVTR method [35].

1.1.1.3 γ-Li_2IrO_3

γ-Li_2IrO_3 crystallises in the orthorombic system with space group *Cccm* [77]. The structure of γ-Li_2IrO_3 is a unique structure and no other compounds of this structure type are known in literature. As for α- and β-Li_2IrO_3, the fundamental framework of γ-Li_2IrO_3 is derived from a cubic-close packed arrangement of O atoms with Li and Ir atoms on the octahedral sites. As in α-Li_2IrO_3 (2D honeycomb) and β-Li_2IrO_3 (3D hyper-honeycomb), edge-sharing IrO_6 octahedra build up the main structural feature (figure 1.4). In accordance with the crystal structure of β-Li_2IrO_3, IrO_6 octahedra form two interlacing layers, which are rotated by $\approx 69.9^\circ$ around the *c*-axis and, therefore, run parallel the $a \pm b$ diagonals. In γ-Li_2IrO_3, the two interlacing layers consist of fully closed honeycomb rings compared to the open honeycomb structure in β-Li_2IrO_3. Hence, γ-Li_2IrO_3 is described as a 3D honeycomb structure as well. Its additional designation being a 'stripy'-honeycomb structure is explained by the alignment of magnetic spins forming a stripy magnetic lattice [56].
Structure solution was based on SC-XRD data [77]. In contrast to the shared occupancy of atomic Li and Ir positions in α-Li_2IrO_3 [90], but in accordance with the structural solution of β-Li_2IrO_3 [11], in γ-Li_2IrO_3 the atomic positions are fully occupied [77]. Similar to both, α-Li_2IrO_3 [90] and β-Li_2IrO_3 [11], the oxidation state of Ir is +4 with the electronic configuration $5d^5$. According to [77], the interatomic Ir-Ir distances are almost similar.
Modic et al. [77] reported the growth of single crystalline γ-Li_2IrO_3 using the flux-growth method. IrO_2 and Li_2CO_3 were reacted in a ratio of 1 : 1.05 at 1273 K, reground, pelletised, heated to 1373 K, and cooled slowly to 1073 K. Subsequently, the pellets were melted with LiOH in a ratio of 1 : 100 between 973 K-1073 K. By applying a cooling rate of 5 K/h, single crystals with a size of 100 µm x 100 µm x 200 µm were obtained [77].

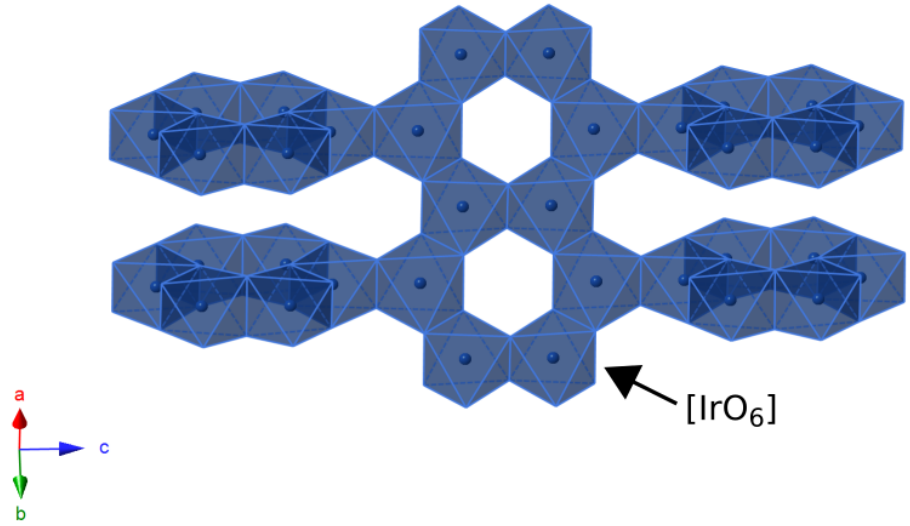

Figure 1.4: Crystal structure of γ-Li_2IrO_3, after Modic et al. [77]. Edge-sharing IrO_6 octahedra (dark blue) build up the 3D honeycomb structure, which consists of two layers, which are rotated around the *c*-axis. The simplified structure neglects the depiction of the atomic O and Li positions.

1.1.2 Lithium ruthenates

In the family of APGMO, a variety of lithium ruthenate compounds is known in the literature (appendix table B.1). Their common structural feature are the edge-sharing RuO_6 octahedra. In the present work, the focus is set on the investigation of Li_2RuO_3 and Li_3RuO_4. Whilst for Li_2RuO_3 opposing structural solutions were reported [33, 44, 60, 76, 101], the two similar structural models of Li_3RuO_4 only show deviations in site occupancies [2, 43].

1.1.2.1 Li_2RuO_3

In the literature, opposing structural solutions for Li_2RuO_3 were published and suggested a $C2/c$, $C2/m$ or $P2_1/m$ symmetry. The three structure types are derived from a cubic-closed packing of O^{2-} ions and characterised as 2D honeycomb structures, which are build up by edge-sharing RuO_6 octahedra. In accordance with the α-Li_2IrO_3 structure, a mixed metal $LiRu_2$ layer and a Li layer are formed. In the mixed metal layer, a 2D honeycomb structure is realised parallel to (001). In the center of each honeycomb a Li atom is situated. Differences between the structural models are mainly due to Ru-Ru distances in the 2D honeycomb rings.
First reports on polycrystalline samples of Li_2RuO_3 suggested a $C2/c$ structure [33, 44, 101]. In contrast, Miura et al. [76] reported a structural phase transition near 540 K from a high-temperature (HT) structure with $C2/m$ symmetry to a low-temperature (LT) structure with $P2_1/m$ symmetry. In table 1.1, the structural parameters, Goodness of Fit (GOF) of structural refinement and calculated

global instability indices (GII) of the three structural solutions with space groups $C2/c$, $C2/m$, and $P2_1/m$ are compared.

Table 1.1: Structural parameters (a, b, c, β, V), Goodness of Fit (GOF) of structural refinement, and global instability indices (GII) of published Li_2RuO_3 structures with space groups $C2/c$, $C2/m$ and $P2_1/m$ [76, 101].

Space group	Li_2RuO_3 $C2/c$ Ramesha et al. [101]	Li_2RuO_3 $P2_1/m$ Miura et al. [76]	Li_2RuO_3 $C2/m$ Miura et al. [76]
a / Å	4.914(1)	4.9210(2)	5.0466(3)
b / Å	8.763(2)	8.7829(2)	8.7649(2)
c / Å	9.859(2)	5.8941(2)	5.9417(3)
β / °	100.08(1)	124.342(2)	124.495(4)
V / Å^3	417.99	210.34	216.61
GOF	2.44	1.36	1.41
GII	0.183	0.206	0.160

In the $C2/m$ and $C2/c$ structures the honeycomb rings are nearly perfect with almost equal Ru-Ru distances with a maximum deviation of only 2.5 % [76] and 3.9 % [101], respectively. In contrast, the honeycomb rings in the $P2_1/m$ structure are mainly characterised by their unequal Ru-Ru distances yielding Ru dimerisation [76, 97].

In the literature, first structural investigations of Li_2RuO_3 were all based on powder diffraction methods and revealed the $C2/c$ structure [33, 44, 60, 101]. By comparing the calculated P-XRD patterns of the three structural models, a high conformity between the ones of the $C2/c$ and the $P2_1/m$ phase is found, whereas the calculated P-XRD pattern of the $C2/m$ phase is clearly distinguishable. The differences between the calculated P-XRD patterns of the $C2/c$ [101] and the $P2_1/m$ structure [76] are explained by systematic absences (figure 1.5). In $P2_1/m$, the only present reflection condition is for $0k0$ reflections with $k = 2n$ due to the screw axis 2_1. In contrast, in $C2/c$, a variety of reflection conditions are derived from the C lattice and the c glide plane: hkl: $h+k = 2n$, $h0l$: $l = 2n; h = 2n$, $0k0$: $k = 2n$. Due to a special position of the Li1 atom in the $C2/c$ structure ($4d$, appendix table B.6) the additional reflection conditions are present for hkl: $k+l = 2n$; $l+h = 2n$. In figure 1.5, the differences between the calculated P-XRD patterns of the $C2/c$ and the $P2_1/m$ structure are emphasised with arrows pointing to reflections, which are only allowed in $P2_1/m$. These reflections have weak relative intensities of maximum 2 %. Exemplary, the $(10\bar{1})$ reflection at 19.00° 2Θ as well as the $(10\bar{2})$ reflection at 30.41° 2Θ do not fulfil the requirements $l = 2n; h = 2n$ for $h0l$ reflections in $C2/c$. Next to $h0l$ reflections, the hkl reflection $(12\bar{1})$ at 27.90° 2Θ is not allowed since not all sums of two Miller indices are even. In addition, the $(h00)$ reflections also mark a difference between the calculated P-XRD patterns. In $P2_1/m$, (100) is allowed, whereas in $C2/c$ only even h values are allowed, *e.g.* (200) at 37.14° 2Θ.

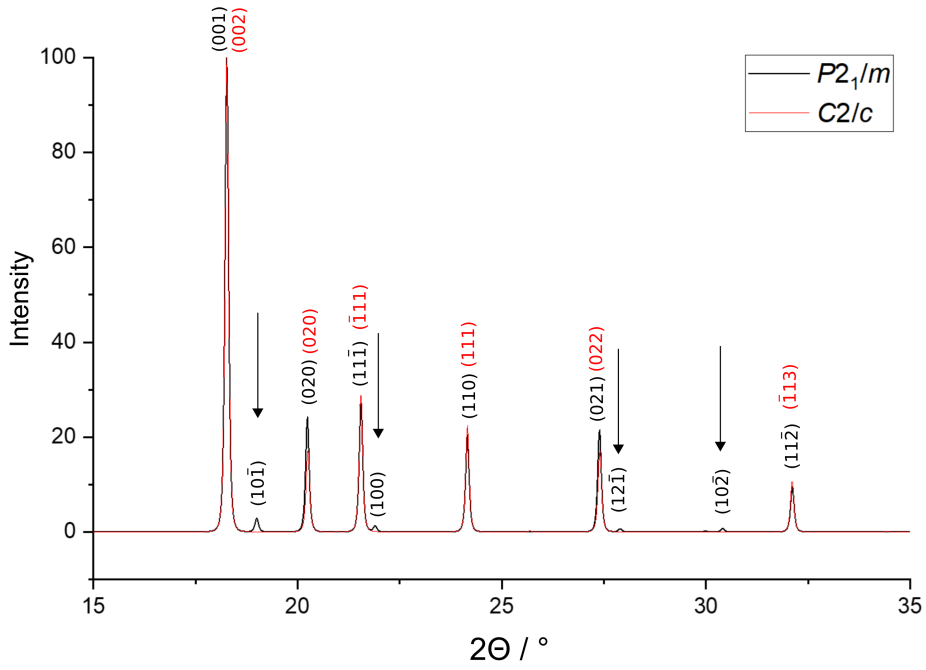

Figure 1.5: Calculated P-XRD patterns with indexed *hkl* reflections of the crystal structures of Li_2RuO_3 with space groups $C2/c$ (red) [101] and $P2_1/m$ (black) [76] in the 2Θ range between 15° and 35°.

The studies, which reported Li_2RuO_3 to show $C2/c$ symmetry after a synthesis at 1273 K, were based on polycrystalline samples and structural solution from P-XRD or P-ND data [33, 44, 60, 101]. In a figure published by Kobayashi et al. [60], at 19.00° 2Θ a reflection is notable and coincides with the ($\bar{1}$01) reflection, which is allowed for $P2_1/m$ but not for $C2/c$ symmetry. Ramesha et al. [101] compared between different structural solutions while reaching a GOF of 2.44 and resulting in a significant difference curve at low 2Θ values, where one would expect *e.g.* the ($\bar{1}$01) reflection (figure 1.5). Based on these considerations, in the present work the structural solution of Li_2RuO_3 with space group $C2/c$ is assumed to have limited plausibility. Further, the requirement of high-quality SC-XRD data to obtain a plausible structural solution of Li_2RuO_3 is emphasised.

The comparison of Li_2RuO_3 structural models of the non-dimerised $C2/m$ phase (HT) and the dimerised $P2_1/m$ phase (LT) mainly reveals a loss of face centring of the monoclinic plane and a changing arrangement of Ru cations in the honeycomb ring while maintaining the Ru^{4+} oxidation state [76] (figure 1.6). In the HT phase ($C2/m$), an almost ideal honeycomb structure with similar Ru-Ru distances occurs and a small deviation of 2.5 % between the distances a_1 and a_2 (figure 1.6a). In the LT phase ($P2_1/m$), one Ru-Ru distance is shortened by 13 % (figure 1.6b). Due to this, the nearly ideal hexagonal symmetry of the Ru honeycomb ring is broken and, therefore, shows a high level of distortion. This effect is described as Ru dimerisation [76, 97].

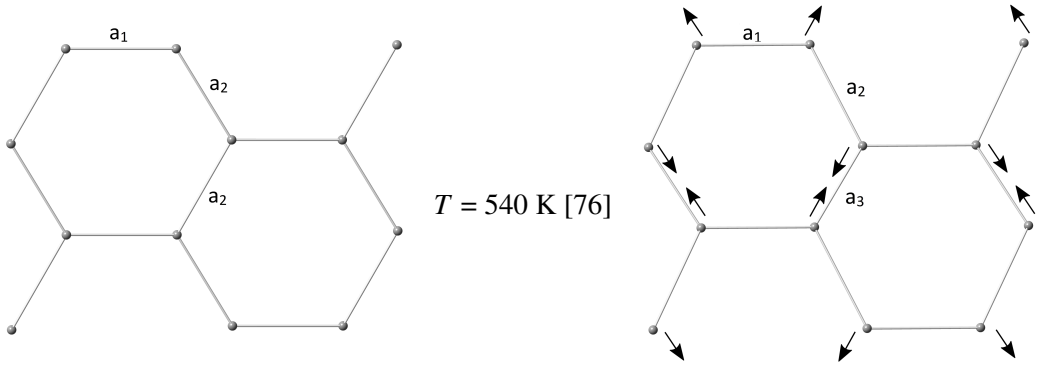

(a) HT-phase, $C2/m$ [76]

(b) LT-phase, $P2_1/m$ [76]

Figure 1.6: Depiction of the dimerisation phenomenon in Li_2RuO_3. During a structural phase transition at 540 K, changes in the Ru-Ru distances a_1, a_2, and a_3 in honeycomb skeletons cause a change from (a) the HT non-dimerised $C2/m$ phase to (b) the LT dimerised $P2_1/m$ phase. Modified after Miura et al. [76].

In the study by Miura et al. [76], the phase transition was characterised as of second-order type. However, Jimenez-Segura et al. [47] and Terasaki et al. [125] found indications for a first-order structural phase transition by observing a finite jump in magnetisation and a clear peak in differential thermal analysis at transition temperature. A further study by Wang et al. [130] showed that single crystalline Li_2RuO_3 either crystallised in $C2/m$ or $P2_1/m$ symmetry, whereas a structural phase transition between both phases could not be detected. The difference in behaviour between polycrystalline and single crystalline Li_2RuO_3 was assumed to depend on the different synthesis conditions. According to Wang et al. [130], especially in single crystals the control of stoichiometry and the prevention of lattice defects is more challenging than in polycrystalline samples which might explain the absence of the structural phase transition in such samples.

Polycrystalline samples of Li_2RuO_3 were obtained by solid-state reaction [33, 44, 47, 60, 76, 97, 101]. Here, stoichiometric mixtures of predried Li_2CO_3 and RuO_2 were heated at 1273 K for 24 h. Kobayashi et al. [60] and Ramesha et al. [101] complemented this synthesis procedure with pelletisations and regrindings of the samples. Park et al. [97] performed a final sintering of the pellet at 1273 K for up to 200 h with intermediate grindings. Single crystalline Li_2RuO_3 was obtained by Wang et al. [130] by starting from off-stoichiometric mixtures of Li_2CO_3 and RuO_2. The chemically homogenised sample was heated to 1523 K, cooled to 1173 K at 2 K/h, and finally cooled to RT at 5 K/h [130].

1.1.2.2 Li_3RuO_4

In the monoclinic Li_3RuO_4 compound with space group $P2/a$, the oxidation state of Ru is 5+. The structure of Li_3RuO_4 is a unique structure and no other compound of this composition is known in the literature [2, 43]. The existence of Li_3RuO_4 was first predicted based on *ab initio* calculations by Bush et al. [21]. Subsequently. first experimental data was published by Alexander et al. [2].

The structure of Li_3RuO_4 is described as an ordered rock-salt structure with edge-sharing LiO_6 and RuO_6 octahedra (figure 1.7). Along the *c*-axis, layers of LiO_6 octahedra alternate with layers that are described as mixed metal layers consisting of LiO_6 and RuO_6 octahedra. In the mixed metal layer, zig-zag chains of either edge-sharing LiO_6 or RuO_6 octahedra run along the [100] direction, which results in a homogeneously alternating stacking sequence of zig-zag chains along the [010] direction [2]. Hence, the structure is characterised by their isolated zig-zag chains of edge-sharing RuO_6 octahedra along [100]. The structure of Li_3RuO_4 is closely related to the previously published structure of Na_3BiO_4, which shows a similar space group and atomic arrangement, but a deviating orientation of zig-zag chains with isolated BiO_6 chains along the *c*-axis [112].

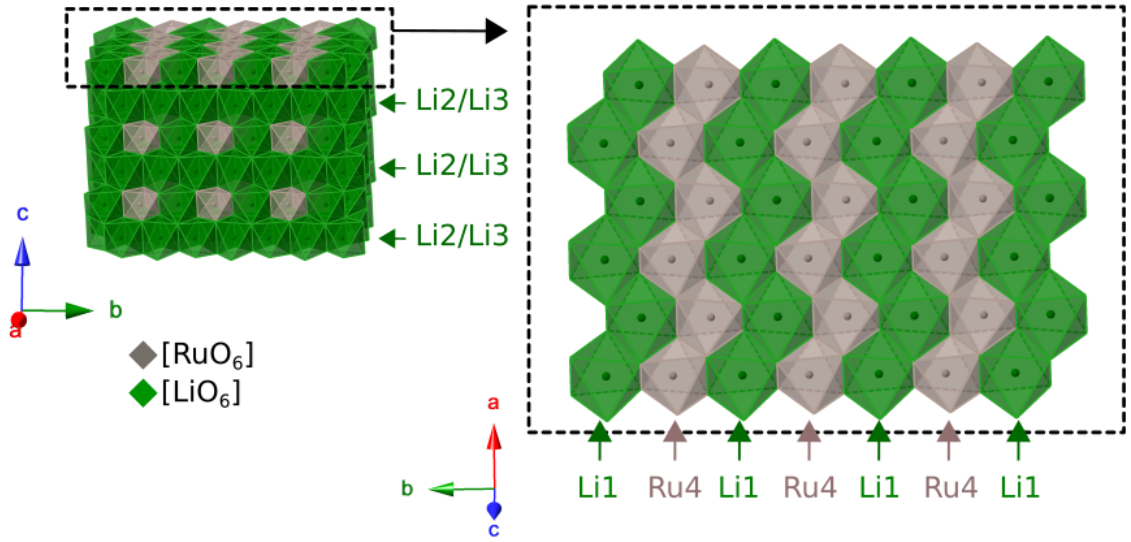

Figure 1.7: Crystal structure of Li_3RuO_4, after Alexander et al. [2]. The structure is mainly characterised by zig-zag chains of edge-sharing RuO_6 octahedra of Ru4 (grey) running along the *a*-axis, which are embedded in a matrix of edge-sharing LiO_6 octahedra (green). In direction of the *c*-axis, two layers are alternating, whereas one layer consists of pristine LiO_6 octahedra of Li2/Li3 and the other mixed metal layers consists of zig-zag chains of both, edge-sharing RuO_6 and LiO_6 octahedra (dashed box, Ru4 and Li1). The simplified structural visualisations neglect the depiction of the atomic O positions.

First structural data of Li_3RuO_4 were published by Alexander et al. [2] on the basis of P-ND measurements and revealed Li defiencies as well as Li/Ru mixing. According to Alexander et al. [2], three Li atomic positions share occupancies with Ru. Further Li deficiencies resulted in an overall chemical composition of $Li_{2.81(2)}Ru_{1.04(2)}O_4$ and a refinement result with GOF = 1.672 [2]. Later on, Jacquet et al. [43] published a closely related structural model of Li_3RuO_4. in this study, they neither showed Li/Ru mixing nor Li deficiencies, which led to a composition of Li_3RuO_4 and a refinement result with GOF = 2.20 [43]. Structural investigations based on SC-XRD were not published until now which is explained by a lack of single crystals of this compound. In the proposed structural model of Alexander et al. [2], Ru-Ru distances differ depending on their positions in the structure. The shortest Ru-Ru distance (2.990(5) Å) is found intrachain between two neighbouring and edge-sharing

RuO_6 octahedra in the zig-zag chain along the [100] direction. Slightly longer Ru-Ru distances are found interchain in the *ab* plane (4.999(9) Å), whereas longest Ru-Ru distances are located intrachain between next-neighbour RuO_6 octahedra (5.10570(11) Å) and interchain along the [001] direction (5.10620(11) Å). Along these Ru-Ru distances of different lengths, the interplay of magnetic interactions shape the magnetic behaviour of Li_3RuO_4 compound (section 1.2.2) [70, 121].
First polycrystalline material of Li_3RuO_4 was prepared by Bush et al. [21] by heating a 3:1 mixture of Li_2CO_3 and dried RuO_2 in air at 1273 K using an excess of Li_2CO_3 to compensate for Li volatilisation during the heat treatment. Alexander et al. [2] and Jacquet et al. [43] performed the same synthesis approach. In contrast, Soma and Sato [120] used a hydrothermal approach. For this, Li_2O_2 and RuO_2 were sealed in a gold capsule with added amount of H_2O and put into a test-tube type autoclave. By heating the autoclave to 923 K, a hydrostatic pressure of 150 MPa was obtained. However, none of these synthesis approaches led to single crystals of Li_3RuO_4.

1.1.3 Lithium iridate-ruthenates

Due to the broad interest in 2D honeycomb structures with a composition of Li_2MO_3 (M = Ir; Ru), the structural investigation of $Li_2Ir_{1-x}Ru_xO_3$ was aimed [67]. As discussed in the previous sections, both end members α-Li_2IrO_3 and Li_2RuO_3 are isostructural at HT and crystallise in the $C2/m$ structure with non-dimerised honeycombs [76, 90]. During cooling, Li_2RuO_3 undergoes a phase transition and changes to a structure, which is characterised by Ru-Ru dimers ($P2_1/m$). Therefore, only at HT forms a solid-solution series of $Li_2Ir_{1-x}Ru_xO_3$ is formed, whereas at LT both end members are heterostructural. Despite the structural aspects, the end members α-Li_2IrO_3 and Li_2RuO_3 follow the *Hume-Rothery rules* of a solid-solution series [28, p.192]. The ionic radii of solute and solvent atoms, here Ir and Ru, do not differ by more than 15%. Further, the atoms have the same valency and a similar electronegativity. This allows for substitutional disorder in $Li_2Ir_{1-x}Ru_xO_3$ crystals. Lei et al. [67] tried to force the Ir dimerisation in α-Li_2IrO_3 by substituting specific amounts of Ru.
For the $C2/m$ and $P2_1/m$ phases, different unit-cell choices were reported in the literature. However, by transforming the unit cells these are comparable (table 1.2). For $C2/m$, the uni-cell choice of α-Li_2IrO_3 is yielded (appendix tableA.8). The linear transformation -a, $-b$. $a+c$ of the non-dimerised HT Li_2RuO_3 structure ($C2/m$ [76]) yields similar atomic positions with variations on mostly the third decimal place and only small differences in lattice parameters in comparison to α-Li_2IrO_3. These small differences in lattice parameters are explained by different areas of stability of both phases. Hence, both structures are considered as isostructural. The original crystal structure of the non-dimerised HT Li_2RuO_3 phase by Miura et al. [76] is given in appendix table B.7 and the transformed structure is listed in appendix table C.2. Using the same unit-cell transformation, the unit-cells of the Li_2RuO_3 structure ($P2_1/m$, LT), which were given by Miura et al. [76] and Lei et al. [67], are comparable and considered as isostructural as well (table 1.2).

Table 1.2: Comparison of lattice parameters (a, b, c, β) and unit-cell volume V of Li_2MO_3 phases (M = Ir;Ru) with space group $C2/m$ and $P2_1/m$ [67, 76]. For comparison, the structures of Miura et al. [76] were transformed by applying the linear transformation: $-a$, $-b$, $a+c$.

	α-Li_2IrO_3 O'Malley et al. [90]	Li_2RuO_3 Miura et al. [76] transformed	Li_2RuO_3 Lei et al. [67]	Li_2RuO_3 Miura et al. [76] transformed
Space group	$C2/m$	$C2/m$	$P2_1/m$	$P2_1/m$
a / Å	5.1633(2)	5.0466(3)	4.9213(6)	4.9210(2)
b / Å	8.9294(3)	8.7649(2)	8.7632(6)	8.7829(2)
c / Å	5.1219(2)	5.1777(3)	5.1163(6)	5.1217(2)
β / °	109.759(2)	108.952(4)	108.21(5)	108.16(2)
V / Å^3	222.24(4)	216.61	209.59(6)	210.34

Polycrystalline samples of $Li_2Ir_{1-x}Ru_xO_3$ were obtained by performing a solid-state reaction of stoichiometric mixtures of preheated RuO_2, anhydrous IrO_2, and Li_2CO_3. Samples were homogenised, pelletised, and sintered at 1248 K for 24 h. By mixing a total excess of 5 % of Li_2CO_3, Li volatility during heat treatments was compensated. Various heat treatments were repeated, leading to pure $Li_2Ir_{1-x}Ru_xO_3$ samples. In total, six samples were synthesised from $x = 0$ to $x = 1$ with an increment of 0.2 [67]. On the basis of P-XRD analyses, structure refinement after Rietveld was performed to determine the crystal structure of each synthesis approach. Each P-XRD pattern was refined starting from the structure of the compositionally closest end member. Lattice parameters and atomic positions were refined from P-XRD patterns. Evaluations of the results were carried out on the basis of R-values. In the supplementary material, the P-XRD patterns were presented and show poorly fitted data. Hence, the refined atomic positions and the illustrated progression of metal-metal distances should be considered with care. However, Lei et al. [67] could assign the $P2_1/m$ phase at high relative amounts of Ru and the $C2/m$ phase at high relative amounts of Ru and proposed a crossover from $P2_1/m$ to $C2/m$ at $x = 0.5-0.6$ at RT. Further, they showed an increase of unit-cell volume with increasing amount of Ru. However, they assigned each measurement to a relative Ru amount x based on the growth approaches but did not give a proof of the elemental composition of the synthesised samples based on an elemental analysis method. Therefore, the investigation of $Li_2Ir_{1-x}Ru_xO_3$ reveals some gaps, which should be filled.

Further solid-solution series with two-dimensional honeycomb structure

To investigate the influence of substitutional effects on crystal structures, the examinations of further solid-solution series with 2D honeycomb structure of type A_2MO_3 were reported in the literature [72, 73, 23, 64]. In $(Li_{1-x}Na_x)_2RuO_3$, a change in dimerisation was observed by substituting 5 % of Na leading to four short and two long Ru-Ru distances [73]. Other investigations on 2D honeycomb structures mainly revealed a change in lattice parameters. A complete single-crystal study of $(Na_{1-x}Li_x)_2IrO_3$ ($C2/m$) showed a monotonically decrease of the lattice parameters with increasing

Li content, which is explained by the smaller ionic radius of Li compared to that of Na [23]. Due to the difference in ionic radii of Ir and Rh, in $Li_2Ir_{1-x}Rh_xO_3$ ($C2/m$) the lattice parameters decrease marginally with increasing Rh content following Vegard's rule [64]. In difference to this, the structural change in $Na_2Ir_{1-x}Ru_xO_3$ is not clearly understood [72]. Here, a complete miscibility could not be observed and an exchange at $x > 0.5$ caused the formation of two separate phases, Na_2RuO_3 and Na_2IrO_3 by retaining the space group $C2/m$. Likewise to $Li_2Ir_{1-x}Ru_xO_3$, these structural investigations emphasise that substitutional effects can have an influence on the lattice parameters but also on the structural aspects of compounds due to *e.g.* ionic radii of substitutional elements.

1.1.4 Sodium ruthenates

In the group of sodium ruthenates of the APGMO family, a variety of compounds are known (appendix table D.1). In the present work, the focus is set on the compounds $Na_{3-x}Ru_4O_9$ and $Na_{27}Ru_{14}O_{48}$ [3, 29]. For both, no other compound of this stoichiometry is known.

1.1.4.1 $Na_{3-x}Ru_4O_9$

The first investigation of the monoclinic $Na_{3-x}Ru_4O_9$ compound with space group $C2/m$ was published by Darriet [29]. Further examinations were given by Cao et al. [22], Regan et al. [103], and Yogi et al. [137]. In $Na_{3-x}Ru_4O_9$ with $0 \leq x \leq 1$, Ru can possess an average oxidation state from $M^{3.75+}$ for $x = 0$ up to M^{4+} for $x = 1$.

The crystal structure of $Na_{3-x}Ru_4O_9$ can be described as a tunnel-type structure with single, double, and triple groups of edge-sharing RuO_6 octahedra (figure 1.8). A single group consists of a RuO_6 octahedron of the Ru1 atom, a double group of RuO_6 octahedra of Ru4, and the triple groups of those of Ru2 and Ru3. These groups are interconnected via common oxygen ligands and build two different chains parallel the *c*-axis. One type of chain is composed of single and triple groups, whereas the other type of chain consists of double groups. Both chain types are alternating in direction of the *a*-axis. The large cavities between them, that form a tunnel-type structure along the *b*-axis, are filled with chains of three crystallographic inequivalent Na atoms, Na1-Na3 (figure 1.8). The RuO_6 octahedra are strongly distorted [103]. In the triple chain, the edge-sharing of RuO_6 octahedra results in a Ru-Ru distance of 3.129(8) Å with a Ru-O-Ru angle of 100.7°, which is in contrast to the ideal 90° angle. In a double chain, the Ru-Ru distances of edge-sharing RuO_6 are slightly smaller (3.063(12) Å). The angle between corner-connected double chains is 135° and, hence, deviates strongly from an ideal angle of 180° [103]. The Ru-Ru distances of corner-connected RuO_6 octahedra are almost similar for interconnected double (3.645(11) Å) or triple/single chains (3.633(7) Å), but smaller between the different types of chains (3.514(10) Å).

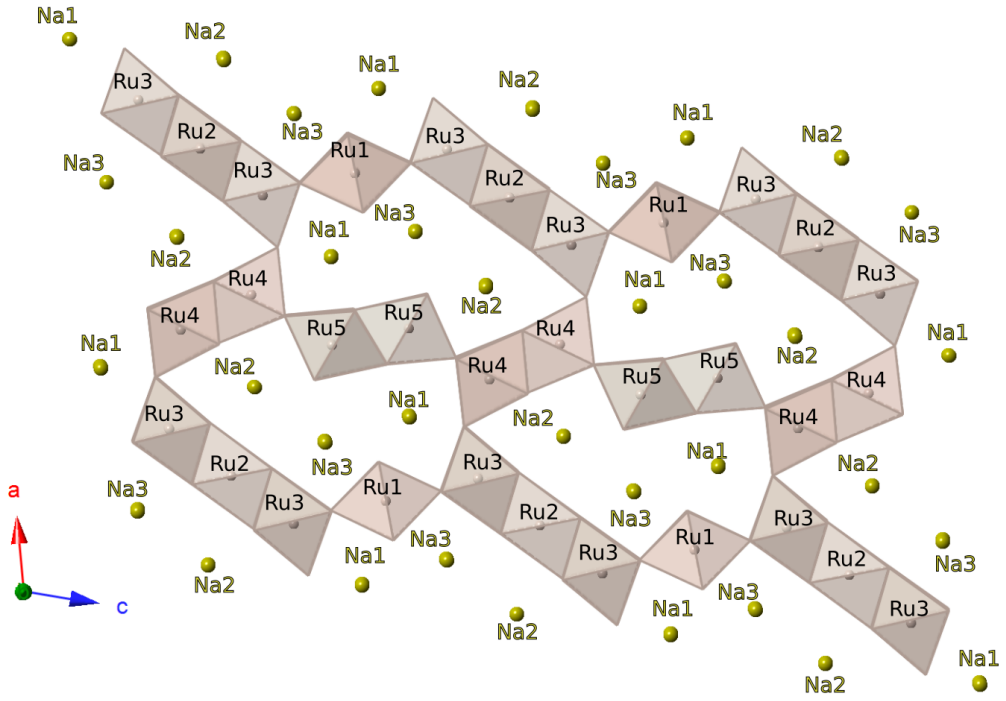

Figure 1.8: Crystal structure of $Na_{3-x}Ru_4O_9$, after Darriet [29]. Single, double, and triple groups of edge-sharing RuO_6 octahedra (grey; Ru1-Ru5) are corner-connected along the *c*-axis. Between the groups, large cavities accommodate Na cations (yellow; Na1-Na3) and represent a tunnel-like structure along the *b*-axis.

The structural models of $Na_{3-x}Ru_4O_9$ mostly result from different site occupancies of the three distinct Na atom sites. The structure of $Na_{2.1}Ru_4O_9$ of Darriet [29] was solved from SC-XRD and describes three Na positions, which are not fully occupied (Na1: 0.95; Na2: 0.76; Na3: 0.39). Shaplygin and Lazarev [113] and Cao et al. [22] described the composition $Na_2Ru_4O_9$. Contrastingly, both stated to be in excellent accordance with Darriet [29] but did not give detailed information on the Na positions and their occupancies. Regan et al. [103] solved the structure from P-ND data and reported the composition $Na_{2.73}Ru_4O_9$ with fully occupied Na1 and Na2 and an occupation of Na3 of 0.73, which results in a higher Na amount in the unit cell compared to results of Darriet [29]. Regan et al. [103] stated that no variation in composition is possible and, hence, give contradictory results to the previously reported data.

In accordance with Regan et al. [103], Yogi et al. [137] reported a similar composition: $Na_{2.7}Ru_4O_9$. They observed a phase transition in electrical-resistivity and heat-capacity measurements, which led to a detailed investigation of the compound by multiple diffraction experiments on single- and polycrystalline $Na_{2.7}Ru_4O_9$. Based on SC-XRD data, Yogi et al. [137] found various superlattice peaks emerging at the phase-transition temperatures $T_{C1} = 630\,\mathrm{K}$ and $T_{C2} = 370\,\mathrm{K}$. These superlattice reflections were not observed in P-XRD patterns by Regan et al. [103], which was explained by

their weak intensity [137]. In accordance with Yogi et al. [137], Onoda et al. [91] observed motional averaging of Na^+ sites at 390 K, probably due to ionic motion in the crystal structure.
According to Yogi et al. [137], the prototype HT phase of $Na_{2.7}Ru_4O_9$ has $C2/m$ symmetry [137], which is similar to the structure given by Regan et al. [103]. At $T_{C1} = 630$ K, a phase transition takes place and forms an intermediate phase with space group symmetry $P2/m$ ($365\,\text{K} \geq T \geq 630\,\text{K}$) and similar atomic positions as in the prototype phase. Due to the loss of face centring, the unit cell is doubled. Bond-valence calculations of Yogi et al. [137] showed that due to a dynamical change in the Ru – O bond length, the Ru valence states are clearly segregated in Ru^{3+} and Ru^{4+} [137]. With further cooling, Yogi et al. [137] reported a first-order phase transition at $T_{C2} = 370$ K, forming a unit cell with space group symmetry $P\bar{1}$, which is 18 times larger than the protoype unit cell [137]. In contrast to a charge ratio of 3 Ru^{3+} : 1 Ru^{4+} in the intermediate phase, the charge ratio of the LT phase changes drastically to 1:1. This phenomenon is described as an unconventional charge ordering of $Na_{2.7}Ru_4O_9$ without loss of metallicity at RT [137] and is further described in section 1.2.4.
The results of Yogi et al. [137] deviate from the published structural models of Darriet [29] and Regan et al. [103]. Next to exceptionally high R-values for the structure refinement based on SC-XRD data (300K: 0.16; 450K: 0.114) [137], both structural models reveal structural instabilities. For the 450K phase, $P2/m$, with a doubled unit cell, the calculated GII is 0.27 and, therefore, in the range of structural instability (section 3.1). Moreover, the interatomic distances between Ru atoms are inappropriately too short (*e.g.* Ru7-Ru9: 1.4355 Å; Ru7-Ru8: 1.46849 Å). Further, for the 300K phase with a 18 times larger unit cell [137], the implementation of bond-valence calculations was not feasible in the present work due to 12 out of 15 Ru atoms, which were considered as uncoordinated. Consequently, the structural stability of these temperature-dependent phases is questioned in the present work.

A variety of synthesis methods was performed to obtain polycrystalline and single crystalline samples of $Na_{3-x}Ru_4O_9$ compounds with $x = 0.23$ [102, 137], $x = 0.9$ [29], and $x = 1$ [113, 22], but also of deoxygenated $Na_2Ru_4O_{9-\delta}$ [22]. Darriet [29] synthesised polycrystalline samples by reacting Na_2RuO_4, RuO_2, and Ru in sealed Au tubes at 773 K-873 K. The reaction product was ground and heated at 1223 K. The resulting compounds had the composition $Na_{3-x}Ru_4O_9$ with $0 \leq x \leq 0.25$. After further treatment at 1373 K, single crystals of the composition $Na_{2.1}Ru_4O_9$ were obtained [29]. Shaplygin and Lazarev [113] prepared a pellet with stoichiometric amounts of Na_2O_2 and RuO_2 and applied, in a stream of oxygen, a two-step heating program with 10 h at 500 K-873 K and 20-24 h at 850 K-1173 K. The resulting polycrystalline sample had the composition $Na_2Ru_4O_9$. Cao et al. [22] grew single crystals of $Na_2Ru_4O_9$ by conducting growth experiments from a Na-rich flux of Na_2CO_3 and RuO_2 in a Na:Ru ratio of 4:1. The maximum temperature of 1673 K was held for 2 h with a subsequent cooling rate of 5 K/h. Subsequently, deoxygenated single crystals $Na_2Ru_4O_{9-\delta}$ were obtained by heating the sample for 100 h at 673-823 K in sealed quartz tubes [22]. Regan et al. [103] prepared polycrystalline samples of $Na_{2.73}Ru_4O_9$ by heating pellets of Na_2CO_3 and preheated RuO_2 with a Na:Ru starting ratio of 3:4 in an alumina boat in Ar flow with the subsequent temperature

program: 24 h at 973 K, 18 h at 1223 K and 24 h at 1173 K. Comparably, Yogi et al. [137] synthesised polycrystalline samples of $Na_{2.7}Ru_4O_9$ by performing a solid-state reaction between Na_2CO_3 and preheated RuO_2 at 1173 K for 72 h. In contrast, this synthesis process was performed in an Ar-gas environment and was accompanied by intermediate grindings and pelletisations [137].

1.1.4.2 $Na_{27}Ru_{14}O_{48}$

The crystal structure of $Na_{27}Ru_{14}O_{48}$ ($P\bar{1}$) is mainly characterised by two isolated Ru_7O_{24} clusters A and B (figure 1.9a) [3]. Each cluster consists of seven edge-sharing RuO_6 octahedra. The central RuO_6 octahedron with site symmetry $\bar{1}$ of its Ru cation is surrounded by further six RuO_6 octahedra (figure 1.9a). Therefore, four crystallographically inequivalent Ru positions are given in each of the pseudo-hexagonal clusters.
According to Allred et al. [3], bond-valence calculations indicate that in one cluster per formula unit the central Ru cation occupies the oxidation state Ru^{3+} and in the second cluster Ru is tetravalent, Ru^{4+}. The outer Ru cations of each cluster are of pentavalent oxidation state, Ru^{5+}. In cluster A and B the Ru-Ru distances show a maximal deviation of about 1.9 % and 1.7 %, respectively, which results in an average Ru-Ru distance of 3.15(1) Å for both clusters. The closest Ru-Ru distance between the A and B cluster is 5.7421(9) Å. Both clusters are nearly planar and canted by 16.6° with respect to each other. In between these clusters, Na ions are situated [3] and break the pseudo-hexagonal symmetry of each cluster. The clusters are stacked perpendicular to their pseudo-hexagonal faces along the *a*-axis. Due to their tilting, the formation of two distinct columns occurs (figure 1.9b). However, in the *bc*-plane rows of either A or B clusters are visible in direction of the *b*-axis (figure 1.9c).
In direction of the *c*-axis, adjacent rows are stacked in an AB arrangement and are slightly shifted with respect to each other to realise the close packing of atoms [3]. In total, the structure of $Na_{27}Ru_{14}O_{48}$ is described as a hexagonally close-packed arrangement of clusters with small Na ions filling the intermediate voids [3]. As a result of the slight distortion from the hexagonally close-packed arrangement of clusters, Allred et al. [3] reported the formation of stacking faults. In their study, they discussed the generation of residual Q peaks in difference electron density maps during the structure refinement process. This residual electron density in the B row suggests a likelihood of 5 % of an ABAAAB stacking sequence instead of an AB stacking sequence [3].
Single crystalline samples were obtained by heating pellets of preheated and mixed Na_2CO_3 and RuO_2 at 973 K in an alumina crucible in air for three days [3]. Crystallisation took place over a wide range of starting compositions, whereas highest phase purity and crystal quality was obtained by adding an excess of 10 % of Na_2CO_3 in order to compensate for Na volatility during the heating process. With this method, black and columnar crystals of 400 µm x 50 µm x 50 µm were grown. According to Allred et al. [3], exposing $Na_{27}Ru_{14}O_{48}$ to moisture yielded the decomposition of the sample.

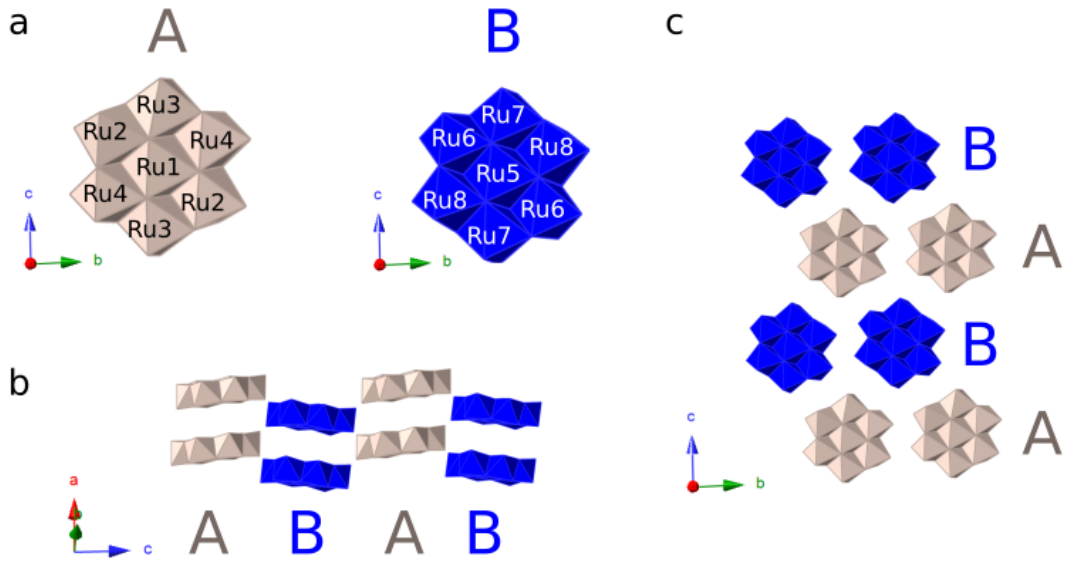

Figure 1.9: Main structural features of the $Na_{27}Ru_{14}O_{48}$ structure, after Allred et al. [3]. The simplified visualisation neglects the depiction of the atomic Li and O positions. (a) The cluster A and B (grey and blue, respectively) consist of edge-sharing RuO_6 octahedra of Ru1-Ru4 and Ru5-Ru8, respectively. (b) Tilted A and B columns in direction of the *a*-axis and corresponding perpendicular AB stacking sequence of A and B cluster. (c) Arrangement of A and B clusters in *bc*-plane with pristine cluster rows along the *b*-axis [3].

1.2 Magnetic properties

Recently, APGMO compounds attracted considerable attention due to their unconventional magnetic properties. With the proposition [25] and realisation of solid-state Kitaev physics [57] in A_2IrO_3 compounds (A = Li , Na) [11, 12, 118], the investigation of APGMO compounds became one of the most rapidly evolving fields of condensed-matter physics. To investigate the control of magnetic properties in A_2MO_3 compounds, substitutional effects were introduced, giving rise to $Li_2Ir_{1-x}Ru_xO_3$ [67], $Na_2Ir_{1-x}Ru_xO_3$ [72], $(Li_{1-x}Na_x)_2RuO_3$ [73], $Li_2Ir_{1-x}Rh_xO_3$ [64], and $(Li_{1-x}H_x)IrO_3$ [10]. Further structural and magnetic investigations of introduced APGMO compounds led to the detection of magnetolattice coupling in Li_2RuO_3 [47, 76], antiferromagnetic ordering in Li_3RuO_4 [70] and $Na_{27}Ru_{14}O_{48}$ [3], but also of a charge ordering phenomenon in $Na_{3-x}Ru_4O_9$ [103, 137].

1.2.1 Alkali iridates

First theoretical attempts to explore the field of Kitaev materials were implemented by Jackeli and Khaliullin [41]. They proposed alkali iridates with A_2IrO_3 honeycomb structure (A = Li; Na) to be successful candidates for the realisation of the Kitaev model [25, 41]. In the following, a short introduction into Kitaev physics is given. For further details and theoretical background, see *e.g.* the review article on Kitaev materials by Trebst [127].

The main prerequisite for a material realising Kitaev physics is the incorporation of a transition-metal with partially filled 4d or 5d shells [127]. In such compounds, the interplay of electronic correlations, spin-orbit entanglement, and crystal-field effects can lead to a variety of novel forms of quantum matter [100]. If in a material the incorporated 4d or 5d element, *e.g.* Ir^{4+} ($5d^5$) or Ru^{3+} ($4d^5$), is coordinated octahedrally, octahedral crystal-field splitting leads to the formation of two e_g and three t_{2g} levels. As in the case of Ir^{4+} ($5d^5$), the five d-electrons are located in the t_{2g} orbitals with a total magnetic moment $s = 1/2$ and an orbital moment $l = 1$. The evolution of magnetic states follows $|l-s| \leq j \leq l+s$ and, hence, yields the splitting into two magnetic spin states, $j = 3/2$ and $j = 1/2$. Due to strong spin-orbit coupling, which rises with Z^4, the $j = 3/2$ band is completely filled whilst the $j = 1/2$ band is half-filled [127], which results in a reduced bandwidth. These materials are characterised as spin-orbit assisted $j = 1/2$ Mott insulators [127]. A further basis for the realisation of Kitaev physics are bond-directional interactions which occur along the charge transfer paths in a compound, whereas the path orientation depends on the geometric orientation of neighbouring MO_6 octahedra [127]. If they share edges and local moments are aligned in hexagonal layers, bond-directional Kitaev-type exchanges are suggested to occur along the two *M*-O-*M* exchange paths with 90° [41, 51].

First theoretical proposals suggested Na_2IrO_3 to exhibit Kitaev physics [57]. This assumption paved the way for thorough investigations on this compound. According to Singh and Gegenwart [118], Na_2IrO_3 orders magnetically around T_N = 15 K. Further, they concluded that the system is highly magnetic frustrated, which is explained by next-nearest neighbour couplings within the 2D honeycomb network. Although Na_2IrO_3 was predicted to exhibit Kitaev physics [57], results from resonant X-ray magnetic scattering and inelastic neutron-scattering experiments explained the nature of the magnetic ordering to be of a zig-zag type [26, 68, 136]. The observation of 3D long-range antiferromagnetic ordering sharply contrasted the expectations and led to the breakdown of the Kitaev model in Na_2IrO_3 [68].
Like the isostructural Na_2IrO_3, α-Li_2IrO_3 undergoes magnetic ordering at T_N =15 K and is characterised as a Mott insulator [46]. Further investigations on single crystalline α-Li_2IrO_3 confirmed the realisation of Kitaev physics [39, 56, 133]. In the course of a pressure-induced structural phase transition of α-Li_2IrO_3 from $C2/m$ to $P\bar{1}$ symmetry, Ir dimerisation takes place [39]. With this, a change in magnetic properties from magnetic Kitaev to a breakdown of the magnetic order and a formation of a non-magnetic dimerised state was reported while maintaining the oxidation state of Ir^{4+}. Next to α-Li_2IrO_3 with a 2D honeycomb structure, two 3D honeycomb structures of Li_2IrO_3 are known: the hyper-honeycomb β-Li_2IrO_3 and the stripy-honeycomb γ-Li_2IrO_3 [77, 124]. Both were also characterised as Mott insulators with a magnetic ordering temperature of ∼38 K [11]. Additionally, they were suggested to exhibit dominant Kitaev-type bond-directional couplings [11, 12], which was confirmed by *ab initio* calculations [50, 53]. Further details on the realisation of Kitaev physics in honeycomb-related structures of alkali iridates are summarised in a review article of Winter et al. [135].

1.2.2 Lithium ruthenates

In Li_2RuO_3, the structural phase transition and formation of Ru-Ru dimers at 540 K is accompanied by a strong decrease in magnetisation [76]. Several proposals were made to understand the origin of this transition. On the one hand, it was described as a change from a highly correlated metal to a molecular-orbital insulator accompanied by the formation of a bond-dimer [75, 76]. On the other hand, the formation of spinless dimers due to a magnetoelastic mechanism was suggested [42]. Pair-distribution function analysis based on high-energy X-ray diffraction pointed out that dimers even exist in the HT phase but change their positions dynamically [55]. Jimenez-Segura et al. [47] described the transition at 540 K as a "melting" transition between the dimer-liquid and dimer-solid phases.
Detailed investigations revealed that the lattice parameters and the magnetic behaviour of Li_2RuO_3 strongly depend on the synthesis process and, hence, are sample-dependent. Further, a dependence of the transition temperature on the lattice parameters was reported [47]. It was shown that samples with larger a lattice parameter exhibit a broader magnetic transition than those with smaller a. Additionally, Jimenez-Segura et al. [47] showed that disorder in the structure causes a rounding of the curvature of the temperature-dependent magnetic susceptibility and this disorder is suggested to be retained even in the HT phase [47].
They further observed a strong decrease of magnetisation during the phase transition at 540 K. This was explained by the number of Ru ions being part of the dimerization [47]. Therefore, the origin of the magnetolattice coupling in Li_2RuO_3 was suggested to lay in the coherent formation of Ru dimers. According to Kimber et al. [55], the formation of two different dimers is observed. One dimer evolves in direction of the a-axis, whereas the other evolves in direction of the b-axis. It was suggested that the formation of both dimers requires the same amount of energy [55]. Simultaneously and in accordance with the Li_2MnO_3 structure type, stacking faults were observed and caused a broadening of the (h00) peaks in P-XRD [16]. In total, the magnetolattice coupling in Li_2RuO_3 is described as an interplay between lattice defects and the dimerisation process [47].

Magnetic susceptibility measurements of Li_3RuO_4 showed antiferromagnetic ordering, whereas the ordering temperature was discussed thoroughly. Whilst Soma and Sato [120] and Son et al. [121] determined a temperature of 66 K with experimental techniques and based on density-functional theory (DFT) calculations, Manuel et al. [70] and Alexander et al. [2] reported a temperature of 40 K and 50 K, respectively. These deviations might be explained by differences in synthesis methods and the composition of the investigated polycrystalline samples. At lower temperatures of 10 K or 32 K, Alexander et al. [2], Soma and Sato [120], and Son et al. [121] found a second magnetic transition. However, the magnetic behaviour of Li_3RuO_4 below this transition temperature T_2 was not discussed in the literature [2, 120, 121]. In total, the antiferromagnetic behaviour of Li_3RuO_4 can be described by three different types of antiferromagnetic interactions, either intrachain, interchain or between layers of chains (appendix table B.20). In Li_3RuO_4, strongest antiferromagnetic interactions take

place in the chains with shortest Ru-Ru distances (2.990(5) Å) [2]. This observation was confirmed by Manuel et al. [70] who then described the magnetism in Li_3RuO_4 of a quasi one-dimensional nature along the zig-zag chains. However, Son et al. [121] performed DFT calculations and supported the description of strongest intrachain interactions, but described the formation of a 3D antiferromagnetic lattice due to lower but existing interchain-exchanges. They proposed that, due to an interplay of strong intrachain exchanges (Ru-Ru: 2.990(5) Å and 5.10570(11) Å) and an interchain exchange within the *ab* plane (Ru-Ru: 4.999(9) Å), a spin-frustrated 2D antiferromagnetic lattice is formed first. Subsequently, due to another weak antiferromagnetic exchange path (Ru-Ru: 5.10620(11) Å) between the layers of zig-zag chains, the evolution of a 3D antiferromagnetic lattice was reported [121].

1.2.3 Lithium iridate-ruthenates

In $Li_2Ir_{1-x}Ru_xO_3$, Ru substitution gives rise to a change in magnetic properties [67]. Whilst in α-Li_2IrO_3 the antiferromagnetic transition occurs at 15 K, the increasing Ru content suppresses this transition and leads to the change of the sign of the Weiss temperature from negative to positive at $x = 0.4$ [67].
The influence of substitutional effects on the magnetic properties is observed in other compounds as well. In $(Li_{0.95}Na_{0.05})_2RuO_3$, the structural change caused by Na substitution is accompanied by a reversal of the magnetic anisotropy to a stronger character perpendicular to the honeycomb plane than parallel to it [73]. In contrast to Li_2RuO_3, the magnetostructural transition of $(Li_{0.95}Na_{0.05})_2RuO_3$ takes place in a single broad step instead of two, which is explained by the small structural disorder caused by Na substitution [73]. In $Li_2Ir_{1-x}Rh_xO_3$, the substitution of Rh suppresses the antiferromagnetic transition [64], whereas in $Na_2Ir_{1-x}Ru_xO_3$ a small substitutional amount of 5 % Ru yields the replacement of a long-range antiferromagnetic order by a spin glass-like state at $T_N = 15$ K [72].

1.2.4 Sodium ruthenates

In $Na_{3-x}Ru_4O_9$, during a first-order phase transition unconventional charge ordering was observed by Yogi et al. [137] (section 1.1.4.1). This was further proven by electrical resistivity, specific heat, and magnetic susceptibility measurements. From RT to 150 K a Pauli-paramagnetic behaviour was observed, which was followed by a Curie-like increase at LT [103, 137]. In contrast to this behaviour, magnetic susceptibility dropped above the first-order transition temperature. This drastic change might be explained by a loss of the conduction electrons [137] and was also reported by Onoda et al. [91].

Magnetic-susceptibility measurements of $Na_{27}Ru_{14}O_{48}$ show antiferromagnetic ordering at $T_N = 40$ K and a Curie-Weiss behaviour above T_N [3]. In accordance with the magnetic susceptibility data, heat-capacity measurements show a broad feature significantly below the magnetic transition. However, the type of magnetic transition is not yet understood, since no typical sign of a λ-transition for antiferromagnetic ordering was observed. Since the clusters were described to consist of Ru^{3+} ($4d^5$),

Ru^{4+} ($4d^4$), and Ru^{5+} ($4d^3$) cations (section 1.1.4.2), the magnetic behaviour of $Na_{27}Ru_{14}O_{48}$ was explained by different ordering phenomena above and below the transition temperature [3]. According to Allred et al. [3], at HT intra-cluster interactions lead to a short-range ordering which is mainly dominated by superexchange. At LT, strong inter-cluster interactions occur, where clusters are weakly coupled together as chains along the [100] direction. Since in each cluster the Ru-Ru distances are almost similar with a maximal deviation of about 1.9 %, Ru cations are arranged in six edge-sharing triangles. This geometry can be described as highly frustrated [3].

1.3 Electronic properties

Lithium iridates with 2D (Na_2IrO_3 and α-Li_2IrO_3) and 3D honeycomb structure (β- and γ-Li_2IrO_3) are characterised as insulators [77, 118, 119, 124]. In contrast, the 2D honeycomb compound Li_2RuO_3 undergoes a metal-to-insulator transition at 540 K and, hence, only shows insulating behaviour in its LT phase ($P2_1/m$) [76, 75]. The electrical resistivity behaviour of substitutional compounds is comparable to the ones of their end members. Samples of $Li_2Ir_{1-x}Ru_xO_3$ and $Na_2Ir_{1-x}Ru_xO_3$ remain insulating [67, 72], whereas samples of $Li_2Ir_{1-x}Rh_xO_3$ stay semiconducting throughout the whole series [64]. By extrapolating the behaviour to alkali ruthenates, an insulating behaviour for Li_3RuO_4 [70] and $(Li_{0.95}Na_{0.05})_2RuO_3$ is assumed [130]. In contrast, the sodium ruthenate compounds $Na_{3-x}Ru_4O_9$ and $Na_{27}Ru_{14}O_{48}$ do not behave like insulators. In $Na_{3-x}Ru_4O_9$, metallic conductivity is observed throughout the entire temperature range [137], whereas in $Na_{27}Ru_{14}O_{48}$ resistance measurements show semiconductiong behaviour [3].

1.4 Motivation

In recent times, alkali iridates and ruthenates of lithium and sodium as part of the APGMO family attracted considerable attention due to their magnetic properties. The current state of research on the crystal growth and structural aspects of lithium iridates and ruthenates reveals some gaps. This thesis aims the complementation of knowledge on this part of APGMO compounds.
In the present work, the focus of crystal-growth investigations is set on the CVTR method. Due to the successful growth of the honeycomb compounds α-, β-Li_2IrO_3 and Li_2RuO_3 with a CVTR setup, which was introduced by Freund et al. [35], its application on the growth investigations of the present work is yielded. Since no detailed information on the growth were given by Freund et al. [35], in the present work the understanding of growth processes of alkali iridates and ruthenates by the CVTR method is focussed. Prior to the conduction of CVTR experiments, the suitable educts are chosen. On the basis of assumed chemical reactions, thermodynamic considerations should be introduced to determine the optimum growth temperature, which is compared with the temperature range resting on the partial pressure behaviour of gaseous components. The thorough growth investigations also include the optimisation of the setup arrangement and examination of its influence on the growth results. Equally, time-dependent growth processes are studied.

During the detailed growth investigations of α-, β-Li_2IrO_3 and Li_2RuO_3, a comparative examination of growth processes in systems with similar and different partial pressures of gaseous components is of great interest (iridates and ruthenates, respectively). Further, the growth investigation of $Li_2Ir_{1-x}Ru_xO_3$ is approached to investigate the applicability of the experimental setup to a growth system with two platinum-group metals and to examine the influence of Ir on the crystal structure of Li_2RuO_3, which is characterised by its Ru-Ru dimers at RT [76]. Next to the focus on Li-based compounds, the application of the setup to sodium ruthenates is of particular interest. This extends the experimental setup to a growth system that has not been investigated in this regard.
For the structural investigations of grown crystals, SC-XRD measurements are aimed. To evaluate the structural solutions of the present work and compare these with already reported structural models, bond-valence calculations are performed. Whilst for some compounds different structural solutions were reported (α-Li_2IrO_3 [35, 90]; Li_2RuO_3 [76, 101]; $Na_{3-x}Ru_4O_9$ [29, 103, 137]), other structural models were only reported once (γ-Li_2IrO_3 [77]; $Na_{27}Ru_{14}O_{48}$ [3]) or are based on polycrystalline samples (Li_3RuO_4 [2]; $Li_2Ir_{1-x}Ru_xO_3$ [67]). Moreover, for $Li_2Ir_{1-x}Ru_xO_3$, RT and LT P-XRD measurements are approached to examine the influence of the Ir substitution and the temperature on the crystal structure. For all compounds, the investigation of structural aspects further includes the comparison between different growth methods and conditions and its influence on the crystal structures. The examinations on growth processes and structural aspects is complemented by elemental and thermal analysis. The homogeneity of grown crystals is studied by Energy-dispersive X-ray spectroscopy (EDX) to obtain information on elemental clustering or gradients. Moreover, the search for temperature-dependent phase transitions is aimed.

The present work is structured as follows: In the next two chapters, the principles and techniques of crystal growth and the methods of characterisation are introduced. In the following chapters, the results of this thesis are presented and discussed. The results chapters are divided into four growth systems regarding their chemical composition: the *Li-Ir-O system*, the *Li-Ru-O system*, the *Li-Ir-Ru-O system*, and the *Na-Ru-O system*. The thesis is completed with an overall conclusion.

Chapter 2

Principles and techniques of single-crystal growth

2.1 Introduction to single-crystal growth

With the beginnings of the 17th century, when Kepler observed snow flakes and discovered the correlation between crystal morphology and internal framework and Nicolous Steno proposed the law of constancy of interfacial angles by investigating quartz and haematite crystals, the principles of the modern crystallography and crystal growth were shaped. With time, the knowledge on principles and techniques of crystal growth was extended. From World War II on, better understanding of formation processes led to large bulk crystals of high quality. The physical and chemical properties of single crystals became even more essential [31]. During the last decades not only inorganic, but also organic and biological crystals gained importance. Until now, the variety of grown crystals for applications like *e.g.* electronics, optics, magnetic devices, sensors, non-linear devices, and lasers seems to be unlimited.

The principle of crystal formation is descibed as an array of atoms, ions or molecules, which form a 3D periodic arrangement. Though in reality, a crystal structure always shows disorder phenomena like defects or dislocations. To overcome such defects and reach the topmost aim of growing a perfect single crystal of a certain size, great efforts of crystal growers led to a variety of crystal-growth techniques, which fulfill different requirements depending on the desired single crystal and its application [132]. A crystal-growth process can always be described as a phase transition between a solid, liquid or vapour phase into a solid phase. The most important transformations are between two phases, liquid-solid and vapour-solid. To successfully grow a single crystal, three basic steps need to be taken [31]: The achievement of solution supersaturation or melt supercooling, the formation of the crystal nuclei, and the growth of the nuclei. Here, supersaturation or supercooling of the liquid or gaseous phase mostly drives the crystallisation process. The second step of nucleation can be either induced from outside or takes place spontaneously and is described by the Gibbs-Thomson equation [36]. The most important theoretical foundations about the crystal-growth process are the

surface-energy theory, the diffusion theory, the absorption-layer theory, and the screw-dislocation theory. Detailed discussions on these theories are not part of the present work but are found in *e.g.* Dhanaraj et al. [31].
Depending on the chemical process involved in the crystal growth, various crystal growth techniques have been developed. In this thesis, crystal growth was mainly performed by the Chemical Vapour Transport Reaction method (CVTR), but also by the solid-state reaction method. Both growth techniques are introduced in the following.

2.2 Chemical Vapour Transport Reaction

The Chemical Vapour Transport Reaction (CVTR) method is part of vapour-solid processes. A detailed overview on CVTR is given *e.g.* in Binnewies et al. [13]. The principle of CVTR is mainly based on a vapour reaction in which a condensed phase cannot volatile on its own due to an insufficient partial pressure, $p(i)$ [109]. By introducing a gaseous reactant, namely the transport agent, the condensed phase is volatilised and deposited somewhere else to form crystals. The deposition can only take place if a chemical equilibrium is maintained. Thereby, the equilibrium of the vapour reaction can be shifted with temperature in both directions of the reaction.
CVTR was first discovered by Bunsen [20] in 1852 by investigating natural processes. He observed the activity of volcanoes and noticed that hematite, Fe_2O_3, is dissolved into a gaseous phase in a stream of gaseous HCl, and precipitated at another place. Starting from this observation, a transport equation, including a dissolution and a deposition process, evolved. Later on in 1890, based on this knowledge the chemist Mond and his colleagues established the idea of the extraction and purification of Ni [80]. Here, solid Ni with both, Fe and Co as impurities, was observed to react with CO and form gaseous nickel carbonyl, $Ni(CO)_4$. Consequently, the impurities were left behind as solids. During a subsequent heating step, the gaseous $Ni(CO)_4$ decomposed again and formed pure solid Ni and gaseous CO. Further inventions like the halogen lamp or the Van Arkel de Boer process for the production of pure metals are based on the method of CVTR as well [129]. The application of CVTR as a crystal-growth technique was implemented by Nitsche and Schäfer [89, 109]. Simultaneously, the research on CVTR emerged in the GDR and was focused *e.g.* on the contribution of convection to the transport process on earth and in space [92].

The general principle of the CVTR method is based on the following equation [13, p. 2]:

$$\mathbf{A}(s) + \mathbf{B}(g) \rightleftarrows \mathbf{AB}(g) \tag{2.1}$$

A solid substance **A** reacts with a gaseous transport agent **B** to form the gaseous reaction product **AB**. The reaction product undergoes a reverse reaction to form crystalline **A** and the gaseous transport agent **B**. The place of volatilisation is called source, whereas the place of deposition is called sink. CVTR can be described as a reversible heterogeneous reaction. Due to a gradient in chemical potential,

which is here generated by a temperature difference ΔT, the gas motion takes place via diffusion. The different temperatures are set as T_1 and T_2, with $T_1 < T_2$. Depending on the reaction enthalpy $\Delta_R H$ of the above mentioned reaction, the reversible heterogeneous reaction is either endothermic ($\Delta_R H > 0$) or exothermic ($\Delta_R H < 0$).
In general, the equilibrium position of reaction 2.1 can be shifted with temperature. Therefore, the reaction temperature not only determines the equilibrium position but also the chemical potential. For yielding a reaction process, the equilibrium has to be maintained. During the growth process, ΔT needs to be adjusted that the divergence from chemical equilibrium is large enough to prefer the growth of the already present crystal seeds but small enough to avoid further nucleation. With this, supersaturation is maintained.

Crystal-growth setups for Chemical Vapour Transport reactions [13, pp. 555-557]
Two different setups for performing CVTR experiments are commonly used in laboratories and are either characterised by a closed (figure 2.1) or an open system. Experiments in a closed system are commonly in sealed ampoules. Due to high growth temperatures, ampoules are made of fused silica. During the experiment, the transport agent remains inside the reaction chamber and, therefore, can re-enter the reaction process. With this, the growth conditions and the reaction atmosphere are kept constant during growth. In contrast, an open system consists of an open glass or ceramic tube which is flooded with the transport agent. To ensure a continuous presence of the transport agent at the source, the gas flow is kept constant. Ergo, in an open system the consumption of the transport agent is larger than in a closed system. However, both systems have advantages making them useful for different growth applications. Independent of the type of system, experiments are performed inside a two-zone furnace with a temperature gradient ΔT. This temperature gradient between source and sink equals a gradient in chemical potential and depends on the reaction enthalpy and, hence, the type of transport, *i.e.* endothermic or exothermic. For realising a growth experiment, an initial solid is placed on the source site of the ampoule or open tube. Depending on the system, the transport agent is either placed on the source site (closed system) or added to the system by using a constant gas flow (open system). Due to the temperature gradient, the transport takes place and crystal growth occurs on the sink side. To free the sink side from possible pre-experimental deposits, the temperature gradient is reversed right before starting the growth attempt.
As an example for an endothermic transport experiment inside a closed ampoule, a scheme is given in figure 2.1a. Here, the solid substance **A** is placed at the source site with a higher temperature T_2 and transported to the sink side with a lower temperature T_1, where the crystalline phase **A** forms. If the temperature gradient is realised along the vertical axis of the ampoule, transport can also take place along the short distance (figure 2.1b). The use of a long or short-distance transport experiment depends on the level of transportability of the substances.

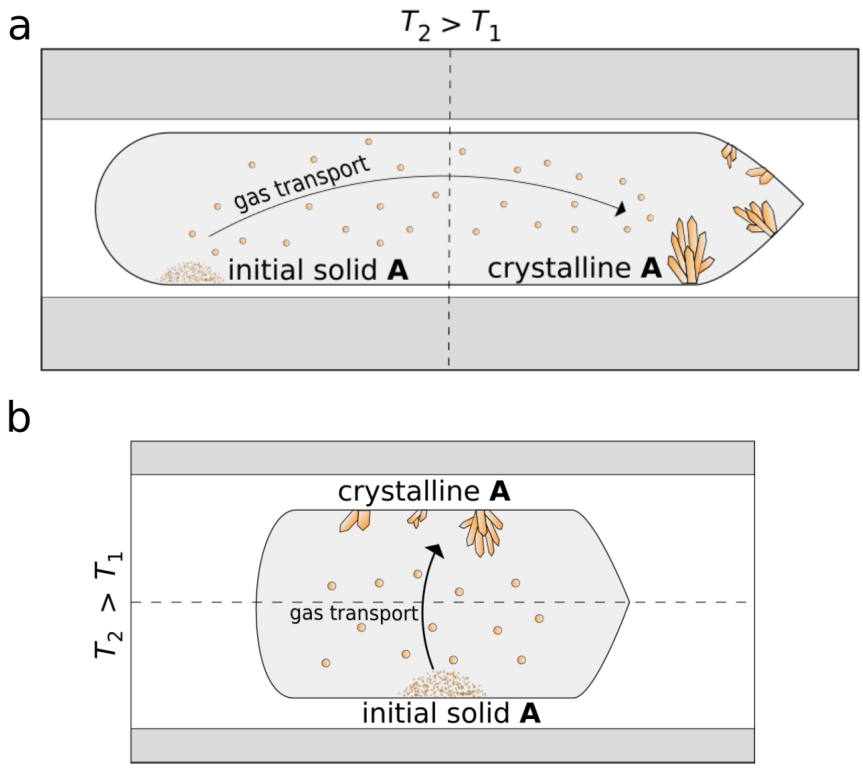

Figure 2.1: Chemical Vapour Transport Reaction in a closed system. Examples of an endothermic transport of a solid **A** from higher (T_2) to lower temperature (T_1), where crystallisation of **A** takes place. (a) Long-distance transport: The temperature gradient is realised along the horizontal axis of the ampoule. (b) Short-distance transport: The temperature gradient is realised along the vertical axis of the ampoule.

2.2.1 Thermodynamic fundamentals

Prior to the execution of CVTR experiments, several thermodynamic considerations have to be made. For a successful CVTR experiment, a transport agent, reaction temperature, transport direction, and rate of mass transport have to be chosen [13, p. 2]. Furthermore, a suitable model of the CVTR experiment must be established by taking the thermodynamic data of the reaction process into account. In the following sections, these considerations are outlined.

Estimation of thermodynamic data

To describe a chemical transport reaction, model calculations of the transport reactions have to be carried out [13, pp. 527-531]. Therefore, the thermodynamic data of the substances that are part of the chemical transport reaction must be known. These are values of the standard enthalpy of formation ΔH^0, the standard entropy ΔS^0, and the heat capacity as a function of temperature C_T^0. Thermodynamic data can be determined by several methods, *e.g.* calorimetric methods such as Differential Thermal Analysis (DTA) and Differential Scanning Calorimetry (DSC), or electrochemical methods. Due to

individual uncertainties of these methods, Binnewies et al. [13] proposed to consider listed values of ΔH^0 with a fixed uncertainty of $\pm$ 10 to 20 kJ mol^{-1}. In the present work, the thermodynamic data are mostly taken from thermochemical tables [58, 59]. If the required thermodynamic data are not known, they have to be estimated.

In contrast to ΔS^0 and temperature-dependent values of C_T^0, there is no uniform method for the estimation of ΔH^0 of a solid phase. Therefore, estimated data of ΔH^0 are often not as reliable as the values of ΔS^0 and C_T^0. The estimation of ΔH^0 is based on known data of homologous series or chemically similar substances. However, if this data is not given, one need to find another approach for estimation. In this case, the estimation of ΔH^0 of a ternary solid compound is based on the assumption that a ternary solid compound $MM'O_{x+y}$(s) is formed out of the binary base materials MO_x(s) and $M'O_y$(s) [13, p. 529]:

$$MO_x(s) + M'O_y(s) \rightarrow MM'O_{x+y}(s) \tag{2.2}$$

Such a reaction is exothermic in principle and a typical value for its reaction enthalpy is roughly -20 kJ per metal atom in the yielded solid compound [110]. With respect to the Hess Law (equation 2.3), which describes the linkage between the reaction enthalpy $\Delta_R H$ and the enthalpy of formation of its reaction educts and products ΔH^0_{educts} and $\Delta H^0_{products}$, the ΔH^0 of the ternary solid compound $MM'O_{x+y}$(s) is estimated (equation 2.4) [110, p. 105]:

$$\Delta_R H = \sum \Delta H^0_{products} - \sum \Delta H^0_{educts} \tag{2.3}$$

$$\sum \Delta H^0_{products} = \sum \Delta H^0_{educts} + \Delta_R H \tag{2.4}$$

The estimation of the temperature-dependent heat capacity follows two concepts, the Dulong-Petit law and the Neumann-Kopp law. According to the first, the heat capacity of solid elements at 298 K is approximately 25 to 30 J K^{-1} per mole per atom they contain [13, p. 530]. Neumann extended the Dulong-Petit law to compound substances. For this approach, a typical solid-state reaction as given in equation 2.2 is considered. Since the Neumann-Kopp law states that the reaction entropy $\Delta_R S$ and the change of C_T^0 are close to zero, ΔS^0 and C_T^0 of a ternary solid compound can be estimated as the sum of values of their binary starting components [13, pp. 530-531]. Typically, these values have an error range of $\pm$ 8 J mol^{-1} K^{-1} compared to experimentally determined ones [13, pp. 531]. By following this strategy, the values for C_T^0 are more exact than calculated by the standardised approach following the Dulong-Petit law. In addition to the Dulong-Petit law, which just gives a single value for the heat capacity, the estimation after the Neumann-Kopp law also allows a temperature-dependent description of the heat capacity by following the polynomial of equation 2.5 with the numerical values a, b, c, and d [13, p. 530]:

$$C^0_{p,T} = a + b \cdot T + c \cdot T^{-2} + d \cdot T^2 \tag{2.5}$$

By combining the heat capacity polynomial and the measured or estimated values of ΔS^0_{298} and ΔH^0_{298}, one can calculate their temperature-dependent numerical values ΔH^0_T and ΔS^0_T [13, p. 530]:

$$\Delta H_T^0 = \Delta H_{298}^0 + \int_{298}^{T} C_p^0 dT \tag{2.6}$$

$$\Delta S_T^0 = \Delta S_{298}^0 + \int_{298}^{T} C_p^0 \frac{dT}{T} \tag{2.7}$$

Suitable transport agent

Next to the required knowledge on thermodynamic data of the involved phases, the choice of a suitable transport agent needs to be considered. A suitable transport agent is selected to transfer all solid components into the gas phase [111]. On the basis of this, an appropriate transport equation has to be determined. Since a CVTR experiment requires a balanced equilibrium state, the calculation of the equilibrium constant K is substantial. K gives hints on the plausibility of the respective transport equation [15].

In most cases, the transport agents are either halogens or halogen compounds since they exhibit a certain volatility and, hence, prefer to go into the gaseous phase at moderate temperatures. This is valid for all halogens except fluorines, which are almost non-volatile [15]. In specific cases, the solid $\mathbf{AB}_x$(s) does not generate a transport effective partial pressure ($p(i) > 10^{-5}$ atm) of the gas species $\mathbf{AB}_x$(g) with the help of an additional transport agent [93]. In such cases, the solid $\mathbf{AB}_x$(s) is dissolved at elevated temperatures to $\mathbf{AB}_{x-n}$(s) and $n\mathbf{B}$(g) and forms its own transport agent by the incongruent thermal decomposition of the solid, which is then transferred into the gaseous phase. During this process, which is called auto transport, no additional external transport agent is needed [13, p. 14]:

$$\mathbf{AB}_x(s) \rightleftarrows \mathbf{AB}_{x-n}(s) + n\mathbf{B}(g) \tag{2.8}$$

Optimum transport temperature T_{opt}

Based on the thermodynamic data of the reaction, the optimum transport temperature T_{opt} can be calculated [111, p. 241]. By restricting the Gibbs free energy to $\Delta_R G_0^T \approx 0$, the Van't Hoff's equation describes a link between the equilibrium constant K_p and the entropy and enthalpy of reaction, $\Delta_R S_T^0$ and $\Delta_R H_T^0$, with respect to the ideal gas constant R [111, p. 241]:

$$lnK_p = -\frac{\Delta_R H_T^0}{R \cdot T} + \frac{\Delta_R S_T^0}{R} \tag{2.9}$$

By restricting K_p to ≈ 1, the optimum transport temperature T_{opt} at a balanced equilibrium position is calculated with an uncertainty of $\pm$ 100 K [111, p. 242]:

$$T_{opt} = \frac{\Delta_R H_T^0}{\Delta_R S_T^0} \tag{2.10}$$

Both approaches lead to the same result for T_{opt}. By following the Van't Hoff's equation 2.9, the temperature dependency of K_p is calculated. This approach is useful if the behaviour of different transport agents needs to be compared.

Another approach to determine T_{opt} is derived from the calculation of the partial pressures, $p(i)$, of the gaseous phases on the basis of their thermochemical data. To determine the temperature range in which the gaseous phase reaches a transport-effective $p(i)$ larger 10^{-5} atm, the thermochemical data of the substances involved in the transport reaction needs to be taken into account. In various comprehensive works [6, 14], temperature-dependent thermochemical data of substances are listed. In some cases, the temperature dependency of the decomposition pressures $p(O_2)$ are given as well [14]. If the equilibrium constant K(A(s)) and the partial pressure p(B(g)) are known, the temperature-dependent partial pressures of the transporting phase **AB**(g), p(AB(g)), of a reaction of type $\mathbf{A}(s) + n\mathbf{B}(g) \rightleftarrows m\mathbf{AB}(g)$ can be calculated on the basis of the following equations [14, p. 45]:

$$K(A(s)) = \frac{p(AB(g))^m}{p(B(g))^n} \tag{2.11}$$

$$p(AB(g))^m = K(A(s)) \cdot p(B(g))^n \tag{2.12}$$

With this approach, the temperature-dependent progression of the partial pressure of the transporting phase **AB**(g) is calculated and allows the determination of the temperature range, in which transport-effective values are reached.

Balanced equilibrium position

A balanced equilibrium position is the basic precondition for a successful CVTR experiment and is obtained when K_p is in the range from 10^{-4} up to 10^4 and $\Delta_R G_0$ is between approximately –100 to +100 kJ mol^{-1} [111, pp. 238-239]. The driving force for the transport of substances between dissolution and deposition is achieved by a gradient in chemical potential, *e.g.* a temperature or concentration gradient. If the equilibrium position is balanced, dissolution into the gas phase and subsequent re-sublimation into the solid are possible. A non-balanced and, therefore, extreme equilibrium position is maintained if the reaction is either highly exergonic or endergonic [111, p. 239]. In the first case, $\Delta_R G_0 < -100\,\mathrm{kJ\,mol^{-1}}$ ($K_p > 10^4$), a high dissolution of the solid into the gas phase is maintained. However, the back reaction/re-sublimation to the solid phase is not favoured. Here, the transporting compound is in gaseous state and situated almost completely on the source site. As a consequence, no deposition takes place on the sink side. In the second case, $\Delta_R G_0 > 100\,\mathrm{kJ\,mol^{-1}}$ ($K_p < 10^{-4}$), the dissolution of the solid into the gaseous phase is not favoured and the transport reaction cannot take place [111, p. 239]. To avoid an extreme equilibrium position, one can calculate the values of $\Delta_R G_0$ and K_p from the given or estimated thermodynamic data of the substances involved in the reaction [111, p. 239].

Transport direction

Based on the Van't Hoff equation (equation 2.9), the transport direction in a balanced heterogeneous equilibrium, can be described by the Clausius-Clapeyron relation if the transport reaction is triggered by a temperature gradient between source and sink [111, p. 243]:

$$\frac{dlnK_p}{d\frac{1}{T}} = -\frac{\Delta_R H_T^0}{R} \tag{2.13}$$

The transport direction is derived from the sign of $\Delta_R H_T^0$ based on Le Chatelier's principle [111]. If $\Delta_R H_T^0$ is negative, K_p increases with decreasing temperature. Therefore, dissolution takes place at lower temperatures and deposition at higher ones. The transport takes place from the colder to the hotter zone ($T_1 \rightarrow T_2$) [111, p. 243]:

$$\Delta_R H_T^0 < 0 \quad ; \quad dlnK_p \sim d1/T \tag{2.14}$$

If $\Delta_R H_T^0$ is positive, K_p increases with increasing temperature. Therefore, the dissolution takes place at higher and the deposition at lower temperatures. The transport takes place from the hotter to the colder zone ($T_2 \rightarrow T_1$) [111, p. 243]:

$$\Delta_R H_T^0 > 0 \quad ; \quad dlnK_p \sim dT \tag{2.15}$$

Rate of mass transport

The CVTR method is divided into three processes: the forward reaction of the solid educt **A** and the gaseous educt **B** at the source, the gas motion and the back reaction, where a solid product **A** is formed. The gas motion is the slowest and, therefore, the rate-determining step [111, p. 243].

If the total pressure is below 3 atm, the gas motion is mainly dominated by diffusion [109]. In processes with pressures above 3 atm, convection is dominant [111]. In CVTR experiments, diffusion should be the mainly dominating transport process. Based on this prerequisite, Schäfer [109] proposed a transport equation (*Schäfer's transport equation*), that can be used to calculate the rate of mass transport of the respective gaseous phases during the transport experiment. Here, the amount of deposited substance per time in the sink is calculated by including the stoichiometric coefficients of the transport equation, the $p(i)$ difference of the transport effective species, the total pressure, the average temperature along the diffusion path, the duration of the transport experiment, and the length and cross-section of the diffusion path [109]. However, this calculation is only valid for CVTR experiments in closed systems, where the pressure is adjusted to a specific value and kept constant [109]. In the present work, crystal-growth experiments are not conducted in a closed system so that a calculation of the rate of mass transport of the gaseous phases is not possible.

2.2.2 Experimental setup

The experimental setup for conducting CVTR experiments was preliminilarly invented by Freund et al. [35] and modified for the present work. The most characteristic feature of this setup is the separation of educts by rings with spikes, which act as crystallisation sites (figure 2.2).
Inside an Al_2O_3 crucible, rings with spikes are placed on top of each other forming a "spiral staircase". Above this "spiral staircase" a plate with a hole is placed. Prior to a growth attempt, one educt is positioned at the bottom of the crucible whereas the other educt is placed on top of the plate with hole (figure 2.2a). Due to their exposed position within the setup, highest rates of material transport occur at the spikes between the educts. Hence, these are referred as places of greatest supersaturation where crystallisation takes place (figure 2.2b). Due to the different heights of the spikes within the "spiral staircase", the crystals can grow at various crystallisation sites. During growth, the crucible is covered by a lid to prevent the volatilisation of the gaseous phases into the surrounding atmosphere. For ensuring pressure balance during the growth attempt, the crucible is only covered with a lid but not closed with ceramic glue. Experiments with open lid did not yield the chemical reaction, which coincides with the previous assumption on increased volatility.
Overall, the experimental setup is differentiated from the previously described crystal-growth setups for CVTR experiments (figure 2.1). In contrast to a closed system, the experimental setup realises the gradient in chemical potential by a concentration gradient of educts. Further, no external transport agent is added and adjusts the pressure and keeps it constant. Since the crucible is not completely closed, which ensures pressure balance, a small exchange of gaseous phases cannot be prevented but might also be necessary depending on the choice of transported solids. In the present work, the Li_2O educts is transported via H_2O(g) [13, p. 166], which might be derived from air-bounded water and underlines the required small exchange of gaseous phases for the successful conduction of growth experiments.
The experimental setup can be defined as a short-distance setup, in which the gradient of chemical potential is realised by a concentration gradient of separated educts and gas transport can take place along the short vertical axis of the setup. The assumed principle of the experimental setup is depicted in figure 2.2c. For realising the growth of the solid substance **AB**, two CVTR cycles need to intertwine. These CVTR cycles are formed by the two solid starting reactants, **A** and **B**. In the first step, **A** and **B** are supposed to react with a gaseous transport agent, **C** or **D**, to form the transport-effective species, **AC** or **BD**. Thereby, the formation of only one specific gaseous phase of type **AC** or **BD** is assumed, presumably the thermodynamically most favoured one. Subsequently, **AC** and **BD**, are supposed to undergo a joint reaction to form the yielded solid substance **AB** and the gaseous substances **C** and **D**, which can re-enter the reaction cycle. More details on assumed transport reactions are following in the results parts.

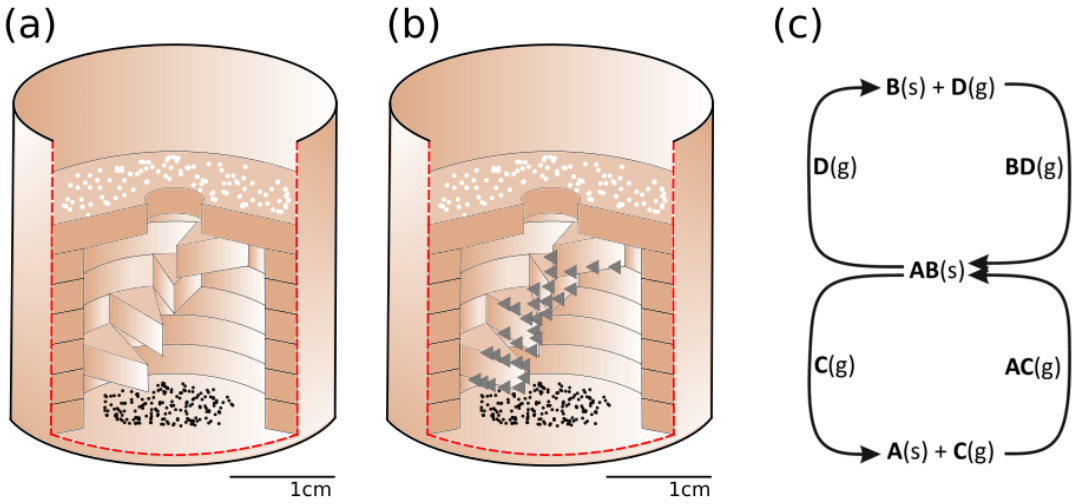

Figure 2.2: Experimental setup for CVTR experiments. (a) Two solid educts **A** (black) and **B** (white) are placed into the crucible and separated by rings with spikes forming a "spiral staircase". (b) Crystallisation (grey) takes place on the rings with spikes. (c) The assumed reaction cycle of the setup describes that, first, **A** and **B** react with gaseous phases **C** or **D** to form the transport-effective species **AC** and **BD**. These undergo a joint reaction and form the solid compound **AB** and the gaseous substances **C** and **D**, which can re-enter the reaction cycle. Figure parts (a) and (b) are modified after Freund et al. [35]. The dashed red lines in parts (a) and (b) mark the interruption of the crucible wall, which is chosen for a clearer and simplified visualisation but was not realised in experiments.

2.2.3 Preparation methods

The individual parts of the setup were reconstructed after Freund et al. [35]. The setup is made of Al_2O_3 parts. The different AL23 products were supplied from KYOCERA Fineceramics Solutions, formerly FRIATEC GmbH (figure 2.3). Whilst the crucible and plate with hole are produced by the company, further parts of the setup were constructed in-house from different ceramic parts. For the construction of spikes, a circular plate was cut with a diamond saw into eight circle segments of the same size. In the next step, a ceramic tube was cut into rings of 4 mm thickness. In the crystal-growth setup, these rings were used for holding the spikes at distinct heights, separating these spikes from the plate with hole and the bottomside of the crucible, where the educts were placed. For constructing rings with spikes, a small circle segment of the same size as the spike was cut out and removed from the rings. Finally, the spikes were glued into the open segment with ceramic glue, *Ceramabond503* by Kager GmbH. Glued parts were dried in a muffle furnace, type *Heraeus Instruments thermiconP(R)*, with applying the following temperature program: 373 K for 2 h, 533 K for 2 h, and 633 K for 2 h. The sizes of different parts of the setup are given in table 2.1.

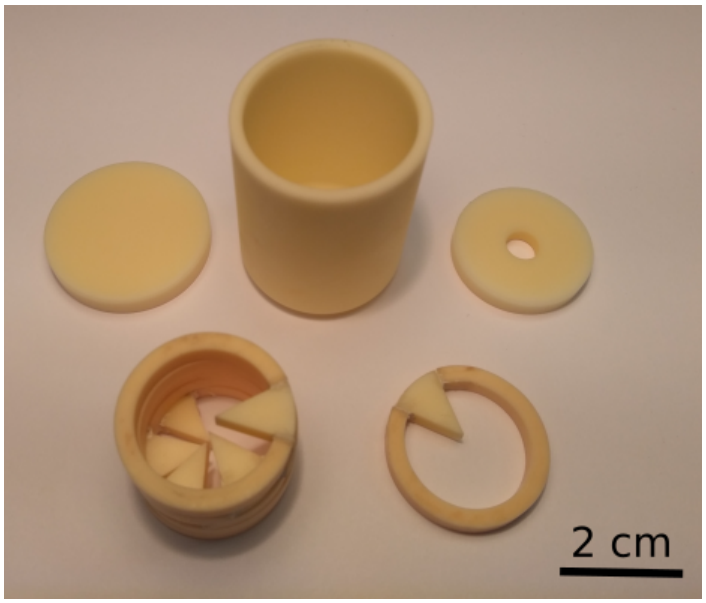

Figure 2.3: Constituent parts for the CVTR setup after Freund et al. [35] made out of Al_2O_3 parts (AL23, KYOCERA). Top row: lid, crucible and plate with hole are produced by the company. Bottom row: intermediate rings and rings with spikes are constructed from different Al23 products.

Table 2.1: Height and outer/inner diameter in mm of the constituent parts for the CVTR setup.

Part	Height / mm	Outer diameter / mm	Inner diameter / mm
Crucible	38	30	26
Lid	5	30	-
Plate with hole	4	25	6
Ring	4	25	20
Ring with Spike	4	25	20

Growth attempts in the *Na-Ru-O system* required the insertion of N_2 (chapter 7). Therefore, four vertical slits of $\sim$ 10 mm length were cut into the crucible wall, two of each at the lower and upper part of the crucible, respectively (figure 2.4). Those pairs of slits were cut at opposite sites of the crucible, whereas the position of pairs was shifted by 90° to each other to yield homogeneous gas exchange. At the beginning of the growth experiment, the crucible was placed in front of the fas inlet of the muffle furnace with one of the low slits of the crucible. During the growth experiment, gas exchange could take place via the slits. The continuity of the N_2 stream was controlled by rising bubbles in two washing bottles, which were partially filled with de-ionised water and situated in the gas-line between the gas port and the inlet of the muffle furnace.

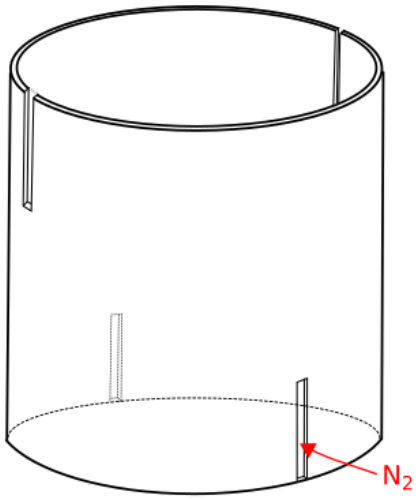

Figure 2.4: Prepared crucible with four slits for N_2 insertion and gas exchange during the growth experiment.

Depending on the growth experiment, the necessary parts were chosen and placed into a drying cabinet, type *Heraeus kelvitron(R)*, at 373 K for a minimum time of 12 h. To prevent a pre-reaction of the required chemicals, the subsequent preparation of the experiment was carried out in a glove box, type *MBraun UNIlab* equipped with a *Siemens simatic op7* operator panel. To maintain the clean and dry conditions ($H_2O < 0.1$ ppm and $O_2 < 0.1$ ppm) of the glove box, only dried parts and instruments were transferred into the glove box. Inside the glove box, the solid educts were weighed. For growth investigations in the Li-Ir-Ru-O system (section 6.1.2), the weighed Ir and RuO_2 amounts were homogenised to obtain a mixed bottom body. For each growth attempts, the first educt was placed on the bottom of the crucible with a funnel. After placing the plate with hole on top, the hole was closed with a small rubber plug to prevent the trickling of the second educt through the hole while placing it onto the plate. Both educts were spreaded equally over the respective area to ensure an even reaction surface. The prepared setup was then placed into an airtight Teflon box to prevent a pre-reaction of the educts with air during the transport between glove box and muffle furnace. For the same reason, the muffle furnace was pre-heated to 473 K in advance. Before placing the setup inside the muffle furnace, the rubber plug was removed from the hole and the crucible was closed with the lid.

2.2.4 External factors influencing the growth process

Growth attempts were performed inside a *Nabertherm P330* furnace. As already discussed in the previous sections, balanced conditions are a prerequisite for conducting crystal-growth experiments by the CVTR method and some external factors might have an influence on these. In a muffle furnace, a difference between set-point temperature and real temperature can occur and mostly depends on

the capacity of the heating elements. Therefore, the temperature profile of the muffle furnace was investigated at a certain set-point. Here, an equal temperature distribution was yielded throughout the whole setup to ensure homogeneous growth conditions. In the present work, only crucibles with a height of 38 mm were used (table 2.1). Thus, the temperature profile of the muffle furnace was investigated throughout the whole horizontal cross-section but also in three different vertical positions up to 40 mm from the bottom of the furnace, which corresponds with the crucible height. The set-point of the muffle furnace was chosen to be equal to T_{opt}. In accordance with growth experiments, a set-point of 1273 K was chosen. The temperature in the furnace was measured with a Pt thermocouple and read hourly.

In figure 2.5a, the position of the vertical and horizontal profile is shown schematically. In the vertical temperature profile in the center of the furnace (figure 2.5b), the temperature is homogeneous with a small temperature difference of $\Delta T = 2$ K. In the horizontal temperature profile close to the bottom of the furnace (figure 2.5c), the temperature in the center of the furnace is homogeneous. Lower temperatures at the front right corner of the furnace are explained by air movements due to an untight closing furnace door. To overcome these temperature variations, crucibles were placed in the center of the furnace. In total, the temperature conditions during a crystal-growth experiment were assumed to be nearly homogeneous.

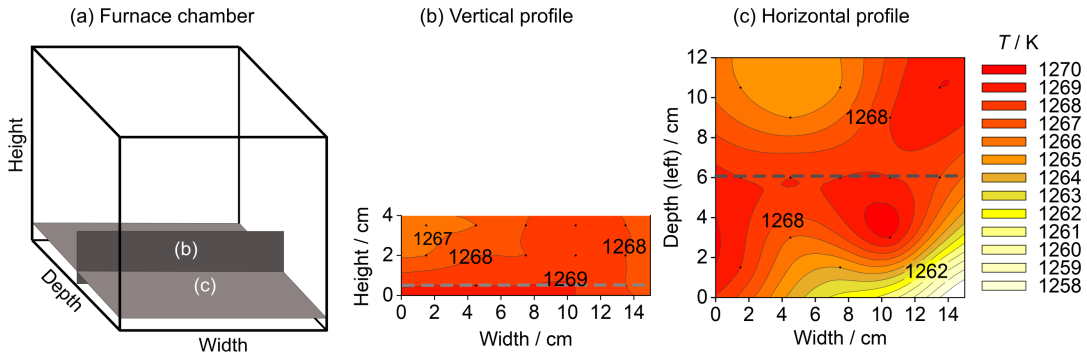

Figure 2.5: Temperature distribution of the muffle furnace at a set-point of 1273 K. (a) Simplified illustration of the furnace chamber with marked positions of the cross-sections, which show (b) a vertical and (c) a horizontal temperature profile of the muffle furnace. The position of the horizontal profile in the vertical profile is marked with a dashed line and vice versa.

The temperature profile was recorded just after the installation of new heating elements and right before the conduction of growth attempt V7 of the Li-Ir-O system (section 4.1). A second muffle furnace of the same type was only used for a few growth attempts, which are marked in the upcoming results chapters and tables on growth attempts (tables 4.1, 5.1, and 7.1). The second muffle furnace exhibits nearly homogeneous temperature conditions in the center of the furnace as well. However, at the same set-point of 1273 K, the measured average temperature in the center was only 1259 K and the temperature conditions at the furnace walls and corners were significantly lower than in the

center, which suggested a higher level of air movement in the second furnace compared to the first furnace. Hence, for growth attempts, which were conducted in the second furnace, the set-point temperature was chosen 10 K higher than intended. Further, the conduction of crystal-growth attempts was favoured in the first muffle furnace with the temperature profile in figure 2.5 and less air movement. The heating elements of both muffle furnaces were changed several times due to their loss of capacity and the following furnace failure. For further comparison of growth results, growth attempts with new heating elements are marked in the respective tables.
The investigation of the temperature profile shows nearly homogeneous temperature conditions in the middle of the furnace. However, it is suggested that an exchange of air through some gaps of the front door is possible. Therefore, the temperature and humidity conditions in the laboratory might have an influence on the growth process and were monitored. For this, during a period of 21 days, which corresponds to the maximum duration of a growth experiment, temperature and humidity data were recorded with a data logger of type *FreeTec NC-7004-675*, which was placed right next to the furnace door. In figure 2.6, the time-dependent progression of the temperature and relative humidity is presented.

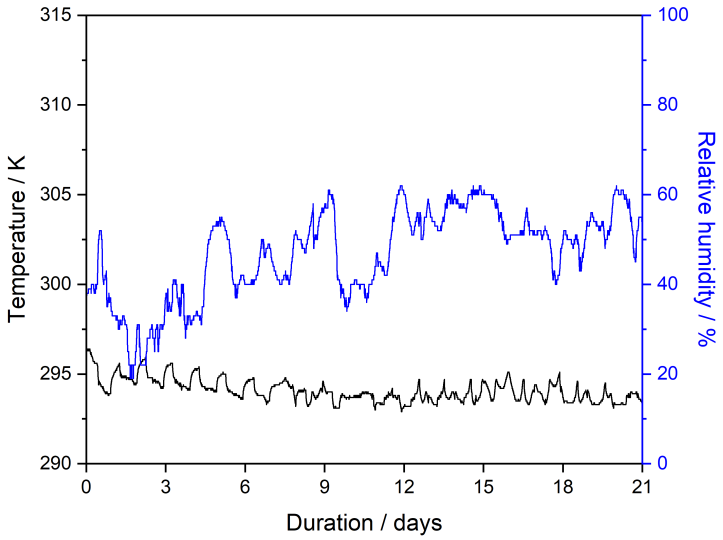

Figure 2.6: Progression of temperature and relative humidity conditions in the laboratory over a period of 21 days. The average temperature is 294.1(6) K (black). The larger fluctuations in the relative humidity curve (blue) result in an average value of 47(10) %.

The temperature curve mostly shows a day-night cycle with an average temperature of 294.1(6) K. In contrast to the almost constant temperature conditions, the relative humidity curve shows large fluctuations between 19.8 % and 62 % with an average relative humidity of 47(10) %. These fluctuations are not connected to the day-night cyclic variations in temperature. No conformance with outside weather data was found. Therefore, variations in relative humidity conditions are explained

by the in-house ventilation system. Hence, the fluctuations in relative humidity are assumed to be an uncontrollable external factor which might influence the crystal-growth experiments of the present work.

2.3 Solid-state reaction method

In addition to CVTR experiments, the solid-state reaction method was carried out in the course of growth investigations in the Na-Ru-O system (chapter 7). Here, the starting educts were Na_2CO_3 and RuO_2. This method was used to increase the reactivity between educts by isolating/keeping the volatiles inside the reaction chamber.
For the conduction of solid-state reaction experiments, an additional setup was used, which consists of a closed conic Al_2O_3 crucible. Prior to experiments, the educts were weighed depending on a specific ratio and homogenised for 15 min in a mortar. Subsequently, the mixture was placed into the predried crucible. Further, a lid was glued on top of the crucible with *Ceramabond 503*, Kager GmbH. To keep the volatile educts inside the reaction chamber but maintain the pressure balance during the growth experiment, a 0.1 µm capillary was placed into the glue before closing the lid (figure 2.7). Prior to the growth experiment, the ceramic glue was dried in a muffle furnace by applying the same temperature program as already described in the previous section 2.2.3. Subsequent growth attempts were performed inside a *Linn HighTerm G800P* furnace.
During the growth attempt, the setup was heated to a distinct maximum temperature within 24 h. The maximum temperature was chosen above the melting but below the boiling point of Na_2CO_3. After holding the maximum temperature for 36 h, the crucible was cooled down to 600 K at a rate of 3 $K\,h^{-1}$ and then cooled to 293 K in 48 h. Results on solid-state reaction experiments are described in section 7.1.

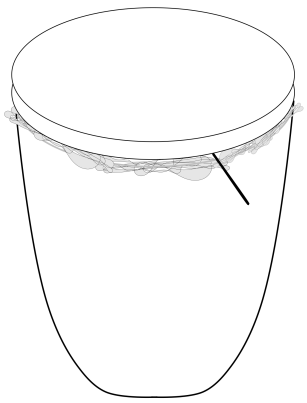

Figure 2.7: Closed conic crucible for the conduction of solid-state reaction experiments. The lid is glued with ceramic glue on top of the crucible. A small 0.1 µm capillary is placed into the glue.

2.4 Laboratory chemicals

The laboratory chemicals used for the crystal-growth experiments in the present work are listed in table 2.2. The two different batches of Ir(s) originated from the same producer but different sources. The first batch (16121401) was described as a product of recycling of metal, whereas the second batch (18081701) was sourced by the mining company *Impala*. For RuO_2, the different batches used in the present work were from the same producer and source. Different producers of Li_2CO_3 chemicals are explained by the restricted in-house availability.

Table 2.2: Laboratory chemicals used in the present work with further information on the producer, including specifications and batch number. Application describes the use of respective chemicals depending on the growth experiments, which are listed in the upcoming results chapters. Chemicals, which were used throughout the whole series of growth experiments are marked with "full-time", whereas the beginning or end of use are marked with "-" and the respective growth attempt.

Chemical	Application	Producer	Specifications	Batch number
Ir	- V12 LiIrO	Evochem GmbH	99,9 %, <10 µm	16121401
	V13 LiIrO -	Evochem GmbH	99,9 %, <10 µm	18081701
IrO_2	full-time	chemPUR	99,9%	030112
RuO_2	- S3 NaRuO	Alfa Aesar	Premion® 99.95%, <1 µm	Z07C042
	S3 NaRuO -	Alfa Aesar	Premion® 99.95%, <1 µm	T20D079
Li_2O	full-time	Sigma-Aldrich	97%	MKCD8632
Li_2CO_3	- S2 LiRuO	Merck KGaA	>99 %	K18699480
	S3 LiRuO -	Fluka Chemika	>98 %	361913/1, 44497
Na_2CO_3	full-time	chemPUR	99.9%	101209

Chapter 3

Methods of characterisation

3.1 Structural analysis

To study the structural aspects of grown crystals, P-XRD and SC-XRD experiments were conducted. P-XRD was used particularly for phase analysis. The structural refinement, based on P-XRD, was carried out with the software suite TOPAS, which was written by Alan Coelho [27]. SC-XRD was particularly used for structural solution and refinement of the crystal structures. For this, the software suite SHELX [115], written by George M. Sheldrick, was used. Crystal structures were visualised by the CrystalMaker version 9.2.9f1 [94] and morphologies were visualised by the VESTA version 3.4.0 [79]. In the following, the procedure of structural solution and refinement in the present work is outlined.

Pre-processing of single-crystal X-ray diffraction data
Structural solution was carried out on the basis of SC-XRD data. The measurement process was controlled by the Bruker APEX3 suite [19]. To determine an optimum data collection strategy for the SC-XRD measurement, a set of initial diffraction frames was collected. Subsequently, the detected reflections were harvested from the collected frames, indexed, and yielded the determination of the Bravais lattice type and the lattice parameters of the sample. On the basis of this unit cell, the APEX3 suite [19] defined the most efficient data-collection strategy to reach a high completeness and average multiplicity of measured reflections. Prior to the structural solution and refinement, the reflection intensities of the collected data were integrated and scaled. The integration of data was controlled by the SAINT Software package as part of the APEX3 suite [19]. During the scaling process, the measured data was put on the same scale by absorption correction. The absorption correction was carried out by a numerical method, which is based on the indexing of crystal faces [19]. Therefore, the crystal's shape was determined from the images of the microscope camera.

Structure solution

After the pre-processing of collected data, the solution of the crystal structure was aimed. In the present work, the structural solution was carried out based on the algorithm of the direct methods by Karle and Hauptman [49]. This requires, that the electron density is always positive and concentrated at the atomic positions. On this basis, the Sayre equation was derived [108], which describes a relationship between the structure factors F_{obs} of reflections. F_{obs} can be calculated from the sum of the product of the structure factors of all reflection pairs, whose indices sum up to the yielded *hkl* values. Since this sum is mainly dominated by strong values, all weak values can be neglected. Therefore, the sum of the products can be simplified to a triplet relationship between three particularly strong structure factors. The further elaboration of the tangent formula is based on normalised F_{obs} to eliminate their strong Θ-angular dependence. With this, the atoms are described to be point-like without exhibiting thermal movement and, therefore, fulfil the basic requirement for the implementation of direct methods. A detailed overview on the direct methods is given by *e.g.* Massa [71, pp. 138-148].

In SHELX [115], prior to the structural refinement, the initial R value R_{int} is calculated, which evaluates the choice of correct Laue/point group. R_{int} is described as the factor of agreement between the intensities ${F^2}_{obs}$ of the observed independent reflections and the mean intensities of symmetry-independent reflections, ${F^2}_{obs}(mean)$, based on the chosen Laue/point group. For an ideal experiment and a correct Laue/point group, the R_{int} value is close to zero [114]:

$$R_{int} = \frac{\sum |{F^2}_{obs} - {F^2}_{obs}(mean)|}{\sum {F^2}_{obs}} \tag{3.1}$$

Structure refinement

During structural solution, a first structural model is obtained, which substantially describes the crystal structure. In the subsequent structure refinement procedure, the least-squares method is used to continuously optimise the structural model and obtain its best fit. A detailed overview on the least-squares method is given by *e.g.* Massa [71, pp. 149-155]. The least-squares method is carried out in both software suites, TOPAS [27] and SHELX [115]. During this optimisation procedure, fit parameters like atomic positions and atomic displacement parameters are varied. For this, a minimisation function Δ is used, which is described as a weighted sum of deviation squares between the observed and the calculated data. Different minimisation functions can be chosen depending on the quantity of the observed data: The absolute value of F_{obs} or the intensities ${F^2}_{obs}$. The latter approach has a distinct advantage since all ${F^2}_{obs}$ values can be used independently of their sign, which might be negative due to measurement errors. In the present work using SHELX, the refinement of crystal structures was carried out against ${F^2}_{obs}$. The minimisation function is described as follows [71, 115]:

$$\Delta = \sum_{hkl} w({F^2}_{obs} - {F^2}_{cal})^2 \tag{3.2}$$

The weighting factor w equals $w = 1/\sigma^2({F^2}_{obs}) + (aP)^2 + bP$ with $P = ({F^2}_{obs} + 2{F^2}_{cal}{}^2)/3$ and includes the error of the observed structure factor, $\sigma^2({F^2}_{obs})$. During the automatic optimisation of

the weighting factor w, the fitting parameters a and b are adjusted so that an equal distribution over the different ranges of diffraction angle and intensity is reached. By combining ${F^2}_{obs}$ and ${F^2}_{cal}$ the statistical bias is reduced [71, 115, 134]. The iterative algorithm is finished when the minimisation function reaches convergence.
After the structural refinement, further quality indicators are calculated. In SHELX [115], the comparison of the structural model with the measured data, *i.e.* the ${F^2}_{cal}$ with the ${F^2}_{obs}$, yields the determination of the quality indicator R_1. This value can be calculated either with respect to all data or to an individually determined specific threshold regarding the minimum intensity of included reflections. In the present work using SHELX, this threshold is determined to $I > 2\sigma(I)$ [115]:

$$R_1 = \frac{\sum ||F_{obs}| - |F_{cal}||}{\sum |F_{obs}|} \tag{3.3}$$

In SHELX [115], the quality indicator w_{R2} includes the weighting factor w. In accordance with R_1, the weighted agreement factor w_{R2} can be calculated either with respect to all data or a specific threshold, which is determined to $I > 2\sigma(I)$ in the present work [115]:

$$w_{R2} = \sqrt{\frac{\sum w({F^2}_{obs} - {F^2}_{cal})^2}{\sum w({F^2}_{obs})^2}} \tag{3.4}$$

The Goodness of Fit (GOF) is an additional quality indicator based on F^2 [71]. This agreement factor is calculated in both software suites, SHELX [115] and TOPAS [27]. In the latter, the GOF is defined as χ^2.

$$GOF = \chi^2 = \sqrt{\frac{\sum_{hkl} w({F^2}_{obs} - {F^2}_{cal})^2}{(m-n)}} \tag{3.5}$$

Here, the difference between observed and calculated intensities is weighted based on the weighting parameter w and normalised to the difference between the number of reflections m and the total number of refined parameters n, which represents the statistical degrees of freedom. Moreover, the GOF includes the rate of redundancy. If a crystal structure and the weighting scheme are correct, the GOF parameter should be close to 1 [71, p. 158].

Evaluation of data: Bond-valence theory

After obtaining a structural model, the stability of the crystal structure is evaluated on the basis of bond-valence calculations. The bond-valence theory (BVT) is based on Pauling's concept of bond strength from 1929 [98]. For its applicability, the following main assumptions need to be fulfilled [17]:

1. A chemical structure can be described as a network of atoms and bonds building its nodes and edges.

2. Any atom is distinguished by its atomic number Z , valence V, and electronegativity χ. Atoms with negative V are named anions, those with a positive V are named cation. The sum of V in a chemical structure must be zero.

3. Chemical bonds exist between neighbouring atoms with opposite valences.

4. Every bond is described by its bond valence s and its bond length R. s is the bond strength or bond number and calculated from the number of electron pairs being part of the bond. R is the distance between the atomic nuclei of the bonded atoms.

5. In an atomic network, the sum of j bond valences s of an atom i is equal to the atomic valence V_i. This assumption defines the *valence-sum rule*:

$$\sum_j s_{ij} = V_i \tag{3.6}$$

   Related to this, the *equal-valence rule* describes a symmetric distribution of atomic valences among the bonds:

$$\sum_{loop} s_{ij} = 0 \tag{3.7}$$

R and s are connected via the following relationship, which contains the empirically determined parameters R_0 and B and the bond length R [17]:

$$s_{ij} = exp(\frac{R_0 - R}{B}) \tag{3.8}$$

Mostly, the adjustment parameter B is set to 0.37 Å. The bond-valence parameters R_0 and B for various pairs of bonded atoms are summarised in a database provided by Brown [18]. On the basis of the bond-valence model of an investigated crystal structure, its structural stability can be evaluated by calculating the global instability index (GII) [107]:

$$GII = \sqrt{\sum_{i=1}^{N} (\sum_j s_{ij} - V_i)^2 / N} \tag{3.9}$$

with the atomic valences V_i, the bond valences s, and the total number N of inequivalent atomic positions in the given crystal structure. Minimum sum deviations indicate high structural stability, whereas a GII > 0.2 may predict a structure not being stable due to intrinsic strains [107].

3.1.1 Instruments

XRD data were collected using both, P-XRD and SC-XRD. P-XRD data was mainly used to identify grown single crystals and synthesised powder samples. SC-XRD data was used to identify and refine the crystal structure of grown single crystals. For these purposes, different diffraction instruments were used.

3.1.1.1 Powder X-ray diffraction

For P-XRD experiments, reflection and transmission geometry were used. P-XRD experiments in transmission geometry were carried out with a *STOE StadiMP* diffractometer with Cu Kα_1 radiation (λ = 1.5406 Å), equipped with a curved image plate detector (IP-PSD) and Germanium (111) monochromator. Diffraction measurements were conducted with 40 kV and 30 mA over a 140° 2Θ range with an exposure time of 3000 sec of one range and a step size of 0.03° 2Θ. A transmission sample holder for flat specimens was used. For this purpose, powder samples were homogenised and evenly distributed between two Kapton foils with a thin layer of silicon grease and placed into the sample holders. Collected P-XRD data were processed with the WinXPow 3.11 software package [122]. To identify the phases, the observed 2Θ positions of experimentally collected powder patterns were compared with 2Θ positions of *hkl* reflections of calculated P-XRD patterns of already published crystal structures. Calculated powder patterns were generated with the *THEO* package as part of the WinXPow software [122].
Acquisition of P-XRD data in Bragg-Brentano Θ-Θ reflection geometry was carried out with a *Bruker D8 DISCOVER* diffractometer with Cu Kα_1/Kα_2 radiation, equipped with a one-dimensional energy-dispersive strip detector (LynxEye XE, Bruker), 2.5° Soller slits, and a fixed divergence slit at 0.3°. Temperature-dependent experiments between 12 K and RT were carried out with a closed cycle helium cryostat Oxford *PheniX* under high vacuum, which is mounted on the Bruker diffractometer. In this temperature range, 30 measurements with a ΔT of 10 K were conducted. P-XRD measurements were carried out using 40 kV and 40 mA in a 2Θ range from 14° to 120° with a counting time of 1 s and a step size of 0.01° 2Θ. Powder samples were distributed homogeneously onto a silicon zero-background sample holder, which was slightly greased with silicon grease preliminarly. To obtain a flat and height-adjusted sample surface, the sample was gently pressed with a glass slide. Phase analysis and refinements were conducted after the Rietveld method using the Bruker DIFFRAC.TOPAS 4.2 software package [27].

3.1.1.2 Single-crystal X-ray diffraction

SC-XRD experiments were carried out on a four-circle *Bruker D8 VENTURE Kappa Duo PHOTON 100* diffractometer, equipped with a IμS micro-focus sealed tube and a graphite monochromator. The instrument is situated in the working group of Prof. Ivan Neměc at the Departement of Inorganic Chemistry, Charles University in Prague, Czech Republic, and was used during a research visit. In

the single-crystal X-ray diffractometer, an X-ray tube with a Mo-Anode generates Mo Kα radiation (λ = 0.71373 Å). During data collection, the sample temperature is controlled by a stream of N_2 using a Oxford CryostreamCooler 800. The measurement was controlled by the APEX3 program suite [19]. Afterwards, the collected data was integrated with the Bruker SAINT software package using a narrow-frame algorithm. Absorption corrections were carried out using a numerical method based on the crystal shape determined from the images of a microscope camera. By using this algorithm, the values for atomic displacement parameters are more reliable compared to the Multiscan Absorption correction algorithm, which only constructs a model for the sample shape based on redundant reflections. The structure was solved by direct methods and refined by the full-matrix least-squares method based on F^2 using the Bruker SHELXTL Software Package [114, 115].

3.2 Thermal analysis

To investigate the temperature-dependent behaviour of grown compounds, two thermal-analysis methods were used: Differential Thermal Analysis (DTA) and Differential Scanning Calorimetry (DSC). Both methods were used to characterise and analyse thermal events with either endothermic (*e.g.* melting) or exothermic behaviour (*e.g.* crystallisation). Whilst DTA measures the temperature difference between a reference sample and a sample of interest, DSC measures the heat flow of a sample and an inert reference sample during a controlled temperature-time program, using a constant heating rate dT/dt.

DTA experiments were carried out using a *PerkinElmer DTA7*. The sample and reference material were placed into 100 mm^3 Pt liners, which are situated in a uniform homogeneous environment. To ensure an inert environment, Ar is used as purge gas. The temperature is controlled by a matched pair of Pt/PtRh10 thermocouples, which are placed underneath the Pt liners. The temperature program is composed of isothermal and dynamical steps, *e.g.* cooling or heating sequences with specific rates. Details on the temperature programs are described in the respective sections in the results chapters 4, 5, and 7. The chosen reference material is Al_2O_3 due to its thermally inert behaviour in the investigated temperature range. After the final step of measurement, the cooling process to RT is supported by an air-cooling system using compressed air. Control and evaluation of each measurement is realised by the *Pyris^{TM} Software suite*. By detecting a phase reaction, a peak in the DTA curve evolves. After the substraction of the baseline, the area under the peak equals the change in enthalpy ΔH of the thermal event. For an exothermic phase reaction ΔH is negative and for an endothermic phase reaction ΔH is positive.

Simultaneous thermal analysis with DSC and thermogravimetry (TG) were carried out with a *NETZSCH STA 449 F3*, using a DSC-TG sensor and Al_2O_3 pans with lid. Here, the heat flow difference between a sample in a sample pan and an empty sample pan is detected over a specific temperature range to measure the heat flow towards or from the sample while removing the thermal behaviour of the sample pan. A DSC signal occurs during *e.g.* melting or a structural phase transition of the sample. Simultaneously, the change of the sample mass is detected by the TG sensor. Experiments

were carried out with a controlled temperature program, which will be described in the respective sections in the results chapter 7. To prevent sample oxidation even at elevated temperatures, the chosen purge gas should be inert as in the case of Ar. N_2 is set as the protective gas. After substracting the baseline, the area under a peak is proportional to ΔH_R which is negative for exothermic and positive for endothermic phase reactions. To compensate for a drift of the TG balance, for each measurement program a correction curve was recorded and subtracted from the measured TG curve. In the following sections on DSC/TG measurements, only the corrected TG curves are shown.

3.3 Spectroscopic analysis

In the present work, Energy Dispersive X-Ray Spectroscopy (EDX) as well as Raman Spectroscopy experiments were carried out to analyse the sample composition.

3.3.1 Energy Dispersive X-Ray Spectroscopy

Energy Dispersive X-Ray Spectroscopy (EDX) is an analytical technique, which is used for measuring the elemental composition on a sample surface and is performed in conjunction with Scanning Electron Microscopy (SEM). The principle of EDX rests on the interaction between the sample and an excitation source [37, pp.524]. If the EDX setup is connected to a SEM, electron-beam excitation is used. In its ground state, an atom consists of unexcited electrons, which are located in electron shells bound to the nucleus. By focussing the electron beam on the sample surface, an electron in the inner shell is excited and ejected from this shell, which leads to the creation of an electron hole. This hole is filled by an electron from a higher energy shell. The resulting energy difference between the higher-energy and lower-energy shell is released in form of X-ray photons. The amount and energy of X-rays, which are emitted from a specimen, is measured with an energy-dispersive spectrometer. The resulting energy-dispersive X-ray spectrum outlines a set of the characteristic energy differences of measured elements. With this, the elemental distribution on a sample surface is measured. Further, based on the counting intensities in a spectrum, the relative abundance of measured elements is estimated. EDX is limited to elements with atomic number 4 (Be) or higher [37, pp.524]. Whilst H and He do not have characteristic X-rays, the Li X-rays of the K shell are underneath the energy limit of EDX and cannot be detected. Therefore, in the present work, only the compositional information regarding the Na, Ir, Ru, and O content of grown crystals were investigated by EDX. Hence, for lithium iridates and ruthenates only the O/Ir or O/Ru ratio was obtained. For sodium ruthenates, the overall elemental composition could be determined.

A prerequisite for reliable measurements is a perfectly smooth sample surface. Therefore, the samples were embedded in resin and polished thoroughly. First, each sample was placed on double-sided tape adhering on a glass slide. The area of embedding was limited by a plastic ring, which was sealed with petroleum jelly to the glass slide. The epoxy resin *EpoThin2* (*Buehler*) was mixed

with a hardening agent in the ratio 2:1 and filled inside the plastic ring where the sample was placed. The hardening process took place for 12 h on a heating plate at 343 K. During the hardening, the viscosity of the resin increased. After removing the holder with the embedded sample from the glass slide, it was slightly lapped with SiC grinding papers with 1200- and 4000-grit. Most samples were polished on a *Depiereux* device with a synthetic silk polish cloth, 1 µm diamond spray, and ethylene glycol acting as lubricant. However, if the sample was very sensitive to mechanical processing, like in the case of needle-shaped crystals, a less harmful polishing device was used. For that purpose, a vibrating polishing device *VibroMet* (*Buehler*) with *OP-U NonDry* (*Struers*) as polishing agent was used. Here, each sample was placed onto the polish cloth of type *MicroFloc* (*Buehler*) and polished by the vibration of the device without applying an external pressure.
The final preparational step was the sputtering of the sample surface to ensure its conductivity. A thoroughly conducting surface prevents the sample from charging under the electron beam. The preferred sputtering material is C since it influences the intensity of the X-rays only at a minimum. For sample sputtering, a *Quorum Q150T ES* device was used. Here, the pulsed rod evaporation profile was applied, where sharpened carbon rods are set under high-voltage in vacuum ($1x10^{-5}$ Pa). As a result, heat is generated leading to the vaporisation and the equal distribution of the carbon on the sample surface. A successful sputtering process is evaluated by a homogeneous brownish discolorisation of the sample surface.
Prior to EDX measurements, samples are loaded onto a specific sample holder, which can carry a maximum of three samples. Each sample is placed onto three pieces of conductive carbon tape to ensure a planar orientation and conductivity. To improve the conductivity, two pieces of copper tape are placed onto each sample connecting it to the conducting sample holder. To prevent a reaction of the sample surface with the surroundings, samples were stored in a desiccator in between the preparational steps until their transfer into the vacuum chamber of the instrument.

SEM and EDX measurements were carried out using a *Zeiss GeminiSEM Sigma 300VP*, equipped with a *Oxford X-Man^{N}80* detector and a 120 µm aperture at an acceleration voltage of 20 kV. The samples were adjusted without a tilting and with a distance to the detector of ∼10 mm to obtain an optimum counting rate, which sets the statistical error at a minimum. The points of measurements were set manually at regular intervals along a line. Each point of measurement was enlarged to a circular area to obtain better measurement statistics. The detection limit of EDX is 0.1 w%. The precision of results is mostly influenced by surface flatness, polishing, and conductivity of the sample. To compensate for these, EDX data with a minimum uncertainty of 1 rel% are considered as reliable and discussed in the results chapters.

3.3.2 Raman Spectroscopy

Raman Spectroscopy is an analytical technique, which investigates the chemical structure of a sample based on the observation of polarisable vibrational modes of its molecules [8, chap. 8]. In detail, it can

give information on the bonding conditions or the symmetry of structural units within a compound. On this basis, phase identification can be yielded.

The principle of Raman Spectroscopy rests on a light-scattering phenomenon and is thoroughly discussed *e.g.* in Bernath [8, chap. 8]. By illuminating a sample surface with a monochromatic light source, such as a laser light, an interaction between the laser and the molecular vibrations of the sample occurs. The wavelength of the inelastically scattered light depends on the characteristics of the molecular vibrations. If the frequency of the scattered light is at the original frequency, this is referred to as Rayleigh scattering. At shifted frequency, the scattering is referred to as Raman scattering. If the shift is to lower frequencies, it is called Stokes scattering, whereas a shift to higher frequencies is named Anti-Stokes scattering. Due to its high intensity signal, the Rayleigh scattering is removed. Since the Anti-Stokes scattering is even more scarce than the Stokes scattering, only the latter is processed to acquire a Raman spectrum. The energy difference is called Raman shift and is expressed in wavenumbers.

Raman spectroscopic measurements were carried out with a *Renishaw inVia Qontor* microscope, equipped with a *Renishaw Centrus 05TJ52* detector and a 532 nm laser source with a laser beam size of 1 µm in a range of Raman shift of 100 to 3600 cm^{-1}. To achieve good results and mitigate the scattering of the laser beam, the sample surface was flat and thoroughly polished.

Chapter 4

Li-Ir-O system

At present, the three modifications of Li_2IrO_3 [11, 77, 90] and the trigonal Li_8IrO_6 [63] are known within the Li-Ir-O system of APGMOs (appendix table A.1). As discussed in the introductory chapter 1.1.1, in the present work the focus is set on α-, β-, and γ-Li_2IrO_3.

4.1 Crystal-growth investigations

In the present work, the growth of α-, β- and γ-Li_2IrO_3 by the CVTR method is yielded. To determine the optimum conditions, growth parameters are controlled. Further, the time-dependent crystallisation process is investigated in detail. Prior to growth experiments, thermodynamic considerations are introduced to understand the reaction mechanism behind the crystal growth process and to define first suitable growth parameters.

4.1.1 Thermodynamic considerations

Prior to the execution of crystal-growth experiments by the CVTR method yielding Li_2IrO_3, suitable educts were chosen: Li_2O(s) and Ir(s)/IrO_2(s). According to [13, p. 166;217], Li_2O(s) is transported by H_2O(g) forming the transport-effective species LiOH(g) and IrO_2(s) is transported by O_2(g) forming the transport-effective species IrO_3(g):

$$Li_2O\ (s) + H_2O\ (g) \Leftrightarrow 2\ LiOH\ (g)$$
$$IrO_2\ (s) + 0.5\ O_2(g) \Leftrightarrow IrO_3\ (g)$$

The volatility of Li_2O in the presence of water vapour was thoroughly investigated by Arkel et al. [5] and Berkowitz-Mattuck and Büchler [7]. Therefore, Li_2O(s) is a suitable educt for crystal-growth attempts in the introduced experimental setup (section 2.2.2). Similarly, the transport of Ir(s)/IrO_2(s) is feasible with the setup, since the transport of Ir(s)/IrO_2(s) is described as an auto transport reaction in the presence of O_2(g) [93]. Such a reaction takes place if the transported solid (IrO_2) can form its own transport agent (O_2) by incongruent thermal decomposition. Hence, Ir/IrO_2 is transported under its own decompositional pressure by its transport effective species [93]. In the present work, the use

of both, Ir(s) and IrO_2(s), as educt was investigated to determine the most effective choice of Ir-based educt for the growth of Li_2IrO_3.
Based on the transport reactions, the following chemical reaction is assumed coinciding with considerations by Freund et al. [35]:

$$2\ \mathrm{LiOH\ (g)} + \mathrm{IrO_3(g)} \Leftrightarrow \mathrm{Li_2IrO_3(s)} + \mathrm{H_2O} + 0.5\ \mathrm{O_2(g)}$$

Suitable growth conditions for Li_2IrO_3

On the basis of the transport reactions, the suitable temperature range for growth experiments has to be chosen. For reaching transport effective behaviour, IrO_3(g) and LiOH(g) need to exhibit a partial pressure, $p(i)$, larger than 10^{-5} atm [93]. Based on equations 2.11 and 2.12, the temperature-dependent values of $p(i)$ of the transport-effective species can be calculated from thermochemical standard data. For IrO_2(g) and IrO_3(g), thermochemical standard data were taken from Barin [6]. On the basis of temperature-dependent data of p(LiOH) [52], a logarithmic regression curve is fitted. In figure 4.1, the temperature-dependent behaviour of $p(i)$ of IrO_3(g) and LiOH(g) is depicted and can be described as similar. Both gaseous phases reach transport-effective behaviour at $T \geq 1205$ K. In contrast, the $p(i)$ of IrO_2(g) does not reach a transport-effective value within this temperature range. Hence, the transport of Ir/IrO_2 only takes place via IrO_3(g).

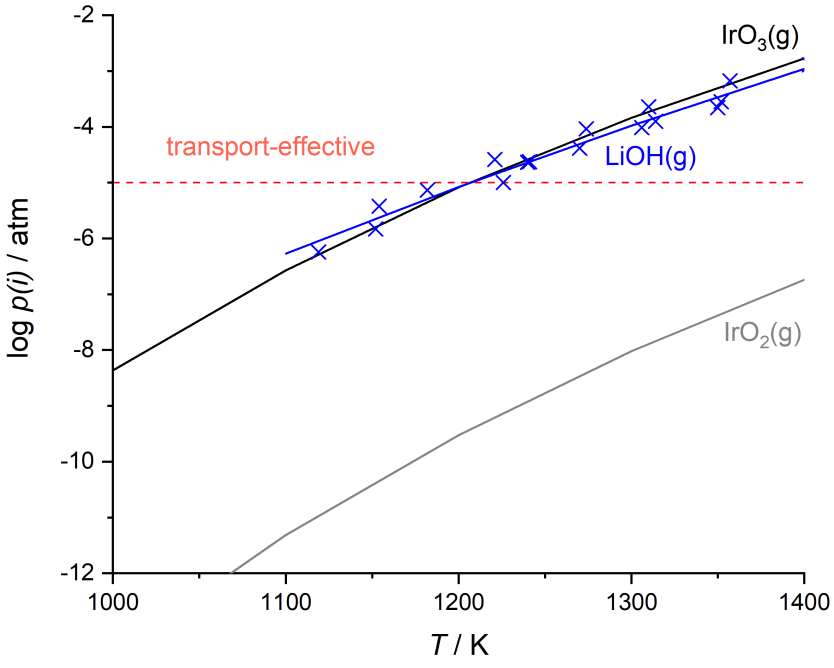

Figure 4.1: Temperature-dependent progress of $p(i)$ of IrO_2(g) and IrO_3(g) on the basis of Barin [6] (grey and black, respectively) and LiOH(g) after Kikuchi [52] (blue, crosses) including a calculated logarithmic regression curve (blue, line). The limitation of $p(i)$ for reaching transport-effective values is marked with a red dashed line.

As previously discussed in section 2.2.1, T_{opt} is also calculated from the quotient of ΔH_R and ΔS_R of the overall chemical reaction (equation 2.10) [111]. For this, the temperature-dependent thermodynamical data of the involved phases are required. Temperature-dependent values of ΔH_T^0 and ΔS_T^0 are listed in Barin [6]. For Li_2IrO_3(s) these values were calculated from the sum of the respective values of its decomposition products Li_2O(s) and IrO_2(s). At RT, the calculated values for Li_2IrO_3, $\Delta H_{298}^0 = -888(20)$ kJmol^{-1} and ΔS_{298}^0 = 89(15) Jmol^{-1}K^{-1}, coincide within the error range with the reported values for α-Li_2IrO_3 from Freund et al. [35]. Further temperature-dependent values in the temperature range up to 1368 K are listed in the appendix table A.2.
For calculating the temperature-dependent ΔH_R and ΔS_R of the assumed transport reaction, the listed and estimated temperature-dependent values for ΔH_T^0 and ΔS_T^0 were combined following the equations 2.7 and 2.6. The resulting values in the range from 298 K to 1368 K are listed in the appendix table A.3. At 1273 K, the reaction has a ΔH_R = -754(30) kJmol^{-1} and a ΔS_R = -580(25) Jmol^{-1}K^{-1}. Therefore, the reaction is defined as an exothermic reaction ($\Delta H_R < 0$). The subsequent calculation of T_{opt} rests on equation 2.10 and resulted in T_{opt} = 1301 K. According to [111, p. 242], this approach includes an uncertainty of $\pm$ 100 K of T_{opt}. Hence, both values, which were derived from either the $p(i)$ behaviour of the transport-effective species IrO_3 and LiOH ($T_{opt} \geq 1205$ K) and from thermodynamical values of the overall chemical reaction (T_{opt} = 1301(100) K) coincide with each other. Moreover, at 1300 K the overall reaction can be defined as balanced ($\Delta_R G_0 \sim 0$ kJmol^{-1}). Further considerations on the rate of mass transport or the transport direction of the growth process could not be made, since the chosen setup does not fulfil the requirements for these calculations [109].

Proposed reaction cycle for the growth of Li_2IrO_3 single crystals

In the introduced experimental setup, the educts Li_2O(s) and Ir/IrO_2(s) are separated from each other. The proposed reaction cycle is depicted in figure 4.2. By following the principle of the experimental setup (section 2.2.2), it is assumed that two reaction cycles intertwine with each other and form a solid compound. In a first step, the solid starting educts (Li_2O and Ir/IrO_2) react with their respective transport agent (H_2O and O_2) to form gaseous reaction products, which act as the transport effective species (LiOH and IrO_3). Subsequently, a joint reaction of both gaseous components is assumed, which yields the solid substance Li_2IrO_3. The gaseous substances H_2O and O_2 can re-enter the reaction cycle.

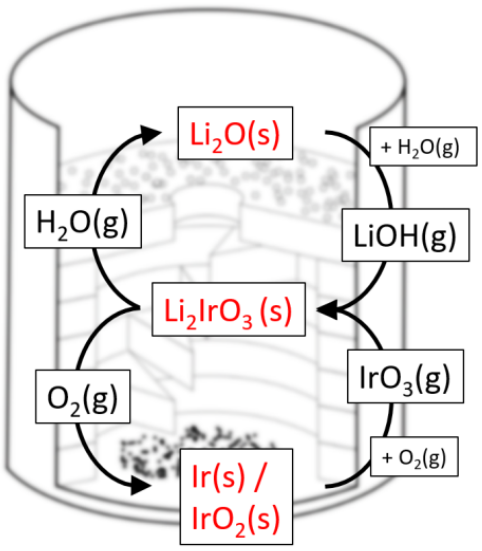

Figure 4.2: Reaction cycle for the growth of Li_2IrO_3 single crystals. Two separate chemical reactions, Li_2O (s) + H_2O (g) $\Leftrightarrow$ 2 LiOH (g) and IrO_2 (s) + 0.5 O_2(g) $\Leftrightarrow$ IrO_3 (g) [13, pp. 166,217] are assumed to intertwine with each other to yield Li_2IrO_3. The gaseous substances H_2O and O_2 can re-enter the reaction cycle.

4.1.2 General observations

By combining the thermodynamic calculations of the present work and the growth conditions for first α- and β-Li_2IrO_3 crystals, which were obtained by the CVTR method by Freund et al. [35], the following temperature range for growth experiments was chosen: $T \geq 1273$ K. In the present work, single crystals of α- and β-Li_2IrO_3 were grown. The growth of γ-Li_2IrO_3 could not be obtained. In table 4.1, the growth experiments in the Li-Ir-O system are listed and include information on the growth conditions, the composition of the Ir bottom body and of grown single crystals. Detailed growth investigations of α- and β-Li_2IrO_3 are described in sections 4.1.3 and 4.1.4. Further results on the time-dependent crystal formation process (section 4.1.6) and the bottom-body formation process (section 4.1.7) are presented.

Due to the variety of growth attempts (table 4.1), some general observations on the growth of Li_2IrO_3 single crystals can be made. Growth attempts at higher temperatures did not yield a reaction and formation of Li_2IrO_3 (1373 K; V2 in table 4.1). This is explained by an increased volatility of LiOH and IrO_3 due to larger $p(i)$ values. The choice of the most suitable Ir-based educt was made by comparing growth results using Ir, IrO_2, or a mixture of both. Since the usage of Ir led to the best growth results, crystal-growth experiments were conducted using distinct Li_2O:Ir ratios.

Growth attempts show that single crystals of α- and β-Li_2IrO_3 preferred and started to grow on the rims of the stairs. Since the stairs have an exposed position within the reaction chamber of the setup, where the material transport should be highest, they are defined as place of greatest supersaturation (section 2.2.2). With time, crystallisation also took place on the surface of the stairs. Single crystals, which grew on the rim of the spikes, preferred to point in direction of the Ir body. Further, most and largest crystals grew on the second stair close to the Ir body. In the following, the lowest stair is assigned with stair 1 and the topmost stair is assigned with stair 4 (table 4.1). Single-crystal growth not only occurred on the stairs of the spiral staircase but also on the inner surface of the surrounding Al_2O_3 rings. Here, the more crystal growth took place on the stair, the more single crystals were observed on the respective surrounding ring. Further growth of Li_2IrO_3 phases occurred at the bottom of the crucible, where the Ir educt was placed prior to the experiment. Overall, a reaction of Li_2O with the Al_2O_3 parts of the setup often led to the formation of lithium aluminates, $LiAl_2O_4$ or $LiAlO_2$. If this reaction took place at the connection between lid and crucible and resulted in an attachment of both parts and, hence, a closure of the setup, the growth of Li_2IrO_3 was significantly increased.
In the study of Freund et al. [35] no information on the setup arrangement were given. Solely, the crucible diameter of 16 mm was noted. In the present work, a crucible with diameter of 30 mm was used to enlargen the reaction chamber and the surface of possible crystallisation sites (section 2.2.2). To further optimise the crystal-growth setup and to determine the most suitable distance between the separated educts, several growth attempts were made. In total, the optimum setup arrangement for the growth of Li_2IrO_3 single crystals was determined and consisted of four spikes with two rings each separating the stairs from the bottom of the crucible and the plate with hole on top, respectively. This arrangement resulted in a distance of 2.8 cm between the educts. In general, the Ir body was placed at the bottom of the crucible whereas Li_2O was placed on the plate with hole. Several changes of the setup arrangement like a reversed position of the educts (V15T1), the shortening of the distance (V16), or the change of the orientation of the setup from vertical to horizontal (V15T2) did not lead to a significant and optimised growth of Li_2IrO_3 single crystals.

Table 4.1: Growth experiments in the Li-Ir-O system including growth conditions with set-point temperature T_{SP}, composition of the bottom body derived from P-XRD data (amount of IrO_2, α-, and β-Li_2IrO_3 in %), and resulting crystals (α-/β-Li_2IrO_3) on distinct stairs 1-4. The distance between the educts is 2.8 cm (four stairs). Growth experiment V3, V6, V21 are not listed due to furnace failure. * marks growth attempts in a second furnace, ^{x} marks new heating elements.

Name	T_{SP} / K	Duration / d	Mass / g	Educts	Crucible	Ratio	IrO_2 / %	α / β / %	Stair		Note
V1	1293	3	1.5	Li_2O:Ir	T1	1:1	-	-	1-3	α	
V2	1373	14	1	Li_2O:Ir	T1	1:1	100	-	-	-	T too high
				Li_2O:IrO_2	T2	1:1	100	-	-	-	
				Li_2O:(Ir+IrO_2)	T3	1:1	100	-	-	-	
V4	1273	14	0.8	Li_2O:Ir	T1	3:1	30	<5/>65	1-3	α	
					T2	2:1	100	-	3	α	
					T3	1:1	100	-	-	-	
					T4	1:2	100	-	-	-	
V5	1273	14	0.6	Li_2O:Ir	T1	3:1	100	-	1-3	α	
					T2	4:1	30	10/50	1-3	α	
					T3	4:1	85	0/15	1-3	α	stairs with half height
					T4	5:1	-	60/40	1-3	α	
					T5	6:1	-	40/60	1-3	α	
V7^x	1273	21	1	Li_2O:Ir	T3	3:1	35	0/65	3	β	
									2	α/β	
									1	β	
					T5	4:1	-	30/70	1-3	α	
V1y	1273	14	0.6	Li_2O:Ir	T4	5:1	40	10/50	1-3	α	
					T6	6:1	<5	30/65	1-3	α	
					T7	7:1	-	30/70	1-3	α	
V8	1273	21	1	Li_2O:Ir	T3	3:1	20	<5/>75	4	α/β	
									3	β	
									1-2	α/β	
					T5	4:1	-	10/90	3	α/β	
V8					T5				2	α	

Continued on next page...

Table 4.1 – continued from previous page

Name	T_{SP} / K	Duration / d	Mass / g	Educts	Crucible	Ratio	IrO_2 / %	α / β / %	Stair		Note
									1	α/β	
V9	1283	14	0.8	Li_2O:Ir	T4	1:1	100	-	-	-	
					T5	2:1	70	0/30	1-3	α	
					T8	3:1	50	<5/>45	1-3	α	
V10	1283	21	1	Li_2O:Ir	T3	2:1	100	-	4	α/β	
									1-3	α	
					T4	3:1	30	<5/>65	4	α/β	
									1-3	α	
					T5	4:1	-	15/85	1-4	α	
V11*, x	1303	21	1	Li_2O:Ir	T6	2:1	65	0/35	4	α/β	
									3	β	
									1-2	α/β	
					T7	3:1	20	<5/>75	4	α/β	
									1-3	α	
					T8	4:1	-	15/85	3-4	α	
									2	α/β	
									1	α	
V12*	1293	21	1	Li_2O:Ir	T3	2.5:1	100	-	1-4	α	
					T4	3:1	50	10/40	1-4	α	
					T5	3.5:1	20	10/70	1-4	α	
V13	1273	21	1	Li_2O:Ir	T6	3:1	65	15/20	1-4	α	
					T7	3.5:1	-	80/20	1-4	α	
					T8	4:1	45	35/20	1-4	α	
V14	1293	5.25	1	Li_2O:Ir	T1	4:1	100	-	1-4	α	time-dependent
		10.5			T2	4:1	20	45/35	1-4	α	crystallisation
		15.75			T3	4:1	10	55/35	1-4	α	process
		21			T4	4:1	-	65/35	1-4	α	

Continued on next page...

Table 4.1 – continued from previous page

Name	T_{SP} / K	Duration / d	Mass / g	Educts	Crucible	Ratio	IrO_2 / %	α / β / %	Stair		Note
V15	1273	21	1	Li_2O:Ir	T1	3:1	-	-	hole	α/β	reversed educts
					T2	3:1	100	-	4	$LiAlO_2$	horizontal setup
									1-2	α	
V16	1273	14	0.6	Li_2O:Ir	T1	6:1	-	100/0	hole	α	short distance
									1	α	one stair
V17	1273	21	1	Li_2O:Ir	T1	2.5:1	25	75/0	1-4	α	educt distribution on stairs
V18	1273	14	0.6	Li_2O:IrO_2	T4	3:1	100	-	-	-	recycled IrO_2
V19	1293	21	1	Li_2O:Ir	T3	4:1	-	100/0	1	α/β	quenched (air)
									2-3	α	
					T4	4:1	-	90/10	1-2	α	quenched (Cu, 5min)
V20	1293	21	1	Li_2O:Ir	T3	4:1	-	80/20	1-4	α	quenched (air)
					T5	4:1	-	70/30	1-3	α	quenched (Cu, 30s)
$V22^x$	1293	21	1	Li_2O:Ir	T3	4:1	-	80/20	1-2	α	quenched (Cu, 15s)
V23	1293	14	0.6	Li_2O:Ir	T4	2:1	100	-	-	-	slightly opened lid

4.1.3 α-Li_2IrO_3

First single crystals of α-Li_2IrO_3 were grown by Freund et al. [35] by the CVTR method using separated educts. Since the growth conditions and process were not described in detail, a thorough investigation is a main goal of the present work to obtain large single crystals of α-Li_2IrO_3. Therefore, a variety of growth experiments were performed which are listed in table 4.1.
α-Li_2IrO_3 was successfully grown in a temperature range of 1273 K-1293 K, a duration of 21 days, a starting Li_2O:Ir ratio of 4:1, and a distance between Ir at the bottom of the crucible and Li_2O at the top of 2.8 cm (*e.g.* growth attempt V10T5/V13T8, respectively). As emphasised in section 2.2.4, the time-dependent reduction of the heat capacity of the muffle furnace is assumed to lead to a decrease in real temperature compared to the set-point temperature. Therefore, the optimum growth temperature is determined to $\sim$ 1273 K, which coincides with T_{opt} for Li_2IrO_3.
At a low educt ratio of 1:1, no growth of α-Li_2IrO_3 was observed (V1T1). Only at higher ratios, the growth occurred on the stairs (*e.g.* 2:1; V4T2, figure 4.3a). This proves the required excess of Li_2O to compensate for the volatility of Li with increasing temperatures. The higher volatility of Li compared to Ir was shown by reversing the positions of the educts (V15T1). In this case, crystal growth of Li_2IrO_3 only occurred on top of the plate with hole, *i.e.* at the place of the former Ir body. If the ratio of educts was too high (>5:1, V5T5) or the distance between the educts was too short (V16T1), which means that the concentration of Li was high and the equilibrium position was unbalanced, dendritic α-Li_2IrO_3 crystals grew (figure 4.3b).

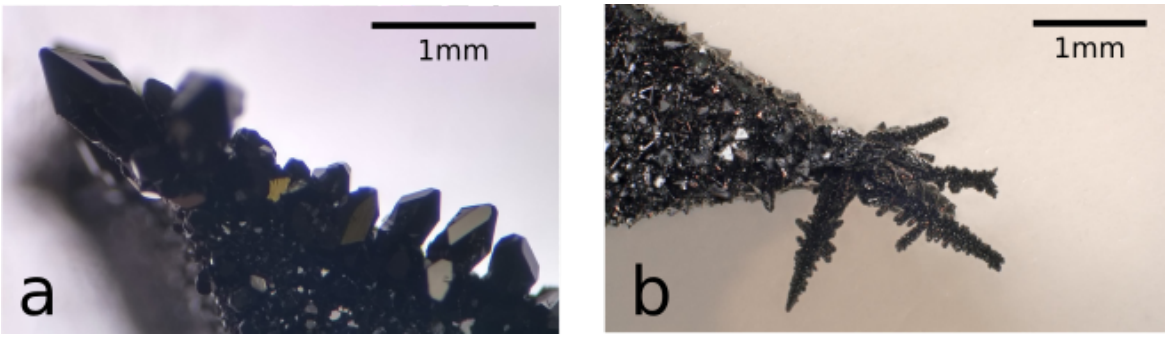

Figure 4.3: (a) Single crystals of α-Li_2IrO_3 of the present work preferred to grow at the rim of the stairs. (b) At high Li concentrations, the equilibrium was unbalanced and dendritic growth occurred.

Single crystals of α-Li_2IrO_3 grew in different morphologies (figure 4.4). Platy single crystals exhibit a large (001) crystal face, which corresponds to the 2D honeycomb plane of the crystal structure (figure 4.4a). Their almost hexagonal shape results from crystal faces of types {110} and {010}. The size of platy crystals varies between 300 µm and 500 µm. The large (001) crystal face is identified as the slowest growing one, whereas crystal faces of type {110} and {010} are faster growing. Due to their same size, their growth velocity is assumed to be similar. Most single crystals of α-Li_2IrO_3 grew in isometric habitus (figure 4.4b,c). The largest size of these crystals were found on the second lowest stair. The morphology of isometric crystals is described by crystal faces of types {110} and {011} of

similar size and, hence, with a similar growth velocity. Isometric crystals are found in different sizes of 30 µm and 1 mm (figure 4.4b and c, respectively). An connection between the morphologies of platy and isometric crystals is not found.

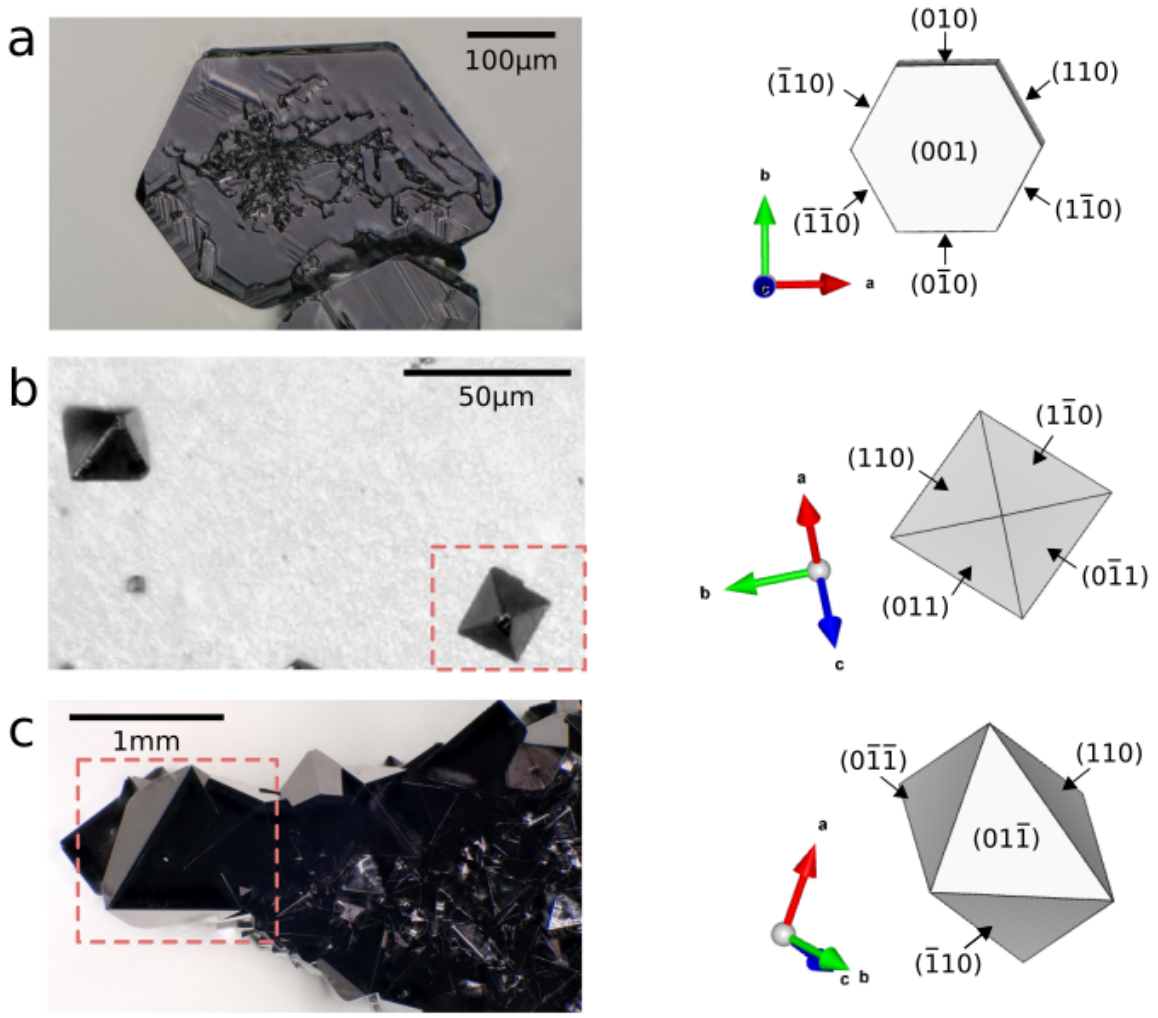

Figure 4.4: Comparison of single crystals of α-Li_2IrO_3 (left) and crystal morphology calculated from the crystal metric (right). (a) Platy single crystals are characterised by their large (001) crystal face. The almost hexagonal shape results from crystal faces of types {110} and {010}. (b,c) Isometric crystals were found in (b) small size of 30 µm and (c) larger size of 1 mm. Their morphology is determined by crystal faces of types {110} and {011}. Red dashed boxes on the left side mark the crystals, whose morphology is shown schematically on the right side.

4.1.4 β-Li_2IrO_3

Previous investigations on the growth of α- and β-Li_2IrO_3 reported that β-Li_2IrO_3 is obtained by a simulated annealing of α-Li_2IrO_3 [11, 106, 124]. Hence, β-Li_2IrO_3 was suggested as HT modification. In addition, similar to α-Li_2IrO_3, the growth of β-Li_2IrO_3 by the CVTR method was reported [35]. In the present work, the conditions of the growth by the CVTR method were investigated.
Crystal growth of β-Li_2IrO_3 was observed after 21 days at 1273 K with a starting Li_2O:Ir ratio of 3:1 and a distance between Ir at the bottom of the crucible and Li_2O at the top of 2.8 cm (growth attempt V7T3, figure 4.5 (a,b), table 4.1). Again, the excess of Li_2O was chosen to compensate for the volatility of Li with increasing temperatures. On the basis of two further growth attempts with the same parameters (V8T3 and V13T6), the reproducibility of the growth results was tested. However, both experiments led to differing results. In V8T3, not only β- but also α-Li_2IrO_3 crystals were observed. In the second comparable growth attempt (V13T6), only single crystals of α-Li_2IrO_3 occurred. This strong difference is explained by an assumed decrease of the real temperature of the muffle furnace due to a time-dependent reduction of the heat capacity of the muffle furnace. Right before starting growth attempt V7, new heating elements were installed and a temperature profile was recorded (figure 2.5). The nearly homogeneous temperature distribution with an average temperature close to the set point underlines the strong capacity of new heating elements during V7. With time, the capacity of a heating element decreases, which yields a decrease of real temperature within the furnace while applying the same set-point temperature. This explains why in V7 β-Li_2IrO_3 grew, which is formed at HT, but in the following growth attempts the growth of β-Li_2IrO_3 was more unfavoured (V8 *et seq.*). The same effect was observed in V11 which was conducted in a second muffle furnace right after changing the respective heating elements. Again, the pristine growth of β-Li_2IrO_3 was observed, whereas the following growth attempt only led to the growth of α-Li_2IrO_3. These growth investigations imply that β-Li_2IrO_3 is formed at HT and its growth is highly sensitive to the temperature conditions, which depend on the capacity of heating elements of the furnace. The simultaneous growth of both, α- and β-Li_2IrO_3, within a variety of attempts emphasises that the chosen temperature range is close to their phase boundary.
Single crystals of β-Li_2IrO_3 grew in a maximum size of 300 µm and with (001) as their largest crystal face (figure 4.5). Therefore, it is identified as slowest growing. In the crystal structure of β-Li_2IrO_3, the (001) layer mainly characterises the 3D honeycomb network including zig-zag chains of edge-sharing IrO_6 octahedra (section 1.1.1.2). The crystal morphology of β-Li_2IrO_3 is further characterised by crystal faces of type $\{111\}$, which resulted in a rhombus-shaped (001) face (figure 4.5a). Those crystals were observed on the flat surface of the stairs. However, if the growth of β-Li_2IrO_3 was observed at the rim of the stairs, the (001) crystal face is pseudo-hexagonal and defined by crystal faces of types $\{01l\}$ and $\{11l\}$ with $l = 1; 2$ (figure 4.5b). Further, these crystals exhibit a greater thickness. The differences in morphology and thickness might be explained by the larger space for expansion and a higher material transport at the rim of stairs.

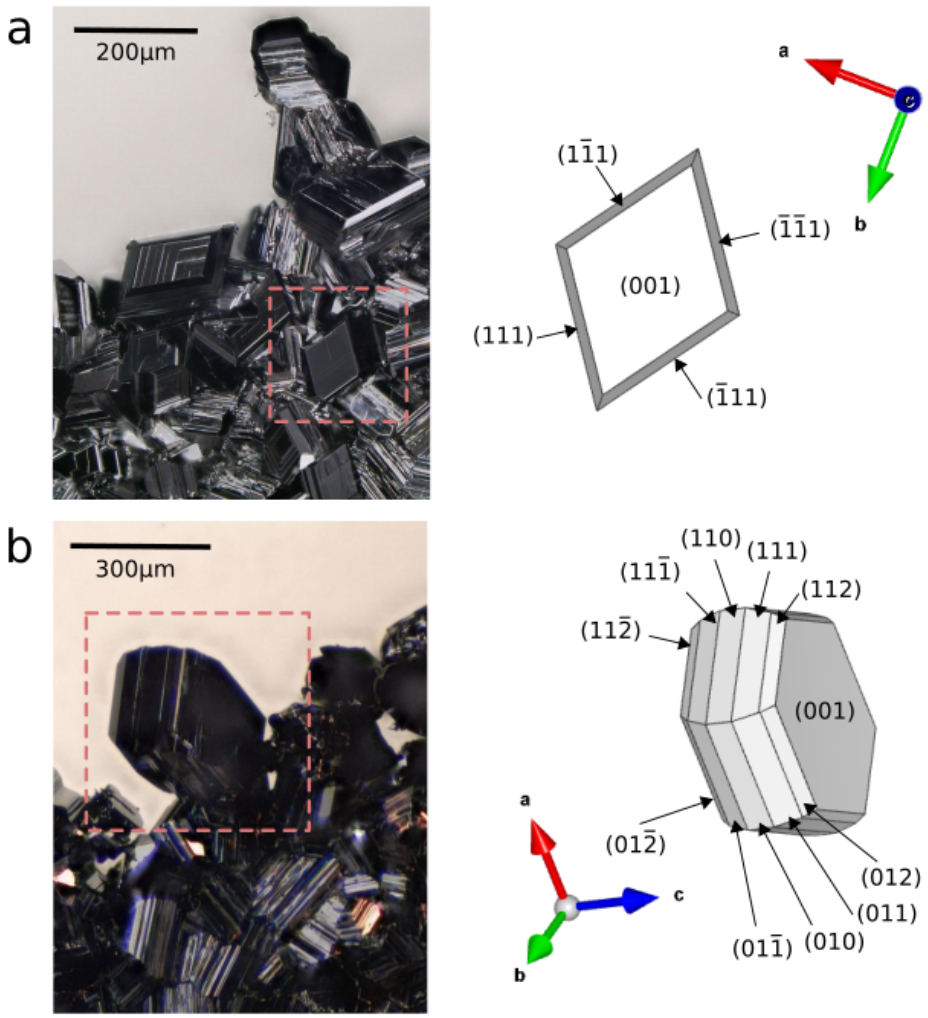

Figure 4.5: Comparison of single crystals of β-Li_2IrO_3 (left) and morphology calculated from the crystal metric (right). The morphology of single crystals is characterised by a large (001) crystal face. Crystals which grew (a) on the surface of stairs, exhibited a rhombus shape of the (001) face, whereas those crystals (b) at the rim of stairs grew with a pseudo- hexagonal (001) crystal face. Red dashed boxes on the left side mark the crystals whose morphology is shown schematically on the right side.

4.1.5 γ-Li_2IrO_3

Since α- and β-Li_2IrO_3 crystals were successfully grown by the CVTR method in the present work, there was a major effort to grow γ-Li_2IrO_3 as well. For this purpose, different growth parameters were used and combined. However, neither variations in the temperature or the duration of the experiment nor in the starting ratio or in the setup arrangement yielded γ-Li_2IrO_3 but always another modification (table 4.1). Further, the cooling process was varied. Neither by cooling the crucible outside the furnace from growth temperature to RT nor by rapidly quenching the crucible onto a Cu block to RT, the formation of the γ-Li_2IrO_3 phase was achieved (*e.g.* V19).

Modic et al. [77] discussed the growth of γ-Li_2IrO_3 by reacting a polycrystalline pellet in molten

LiOH. No information was given on the composition of this pellet. Since both, Kobayashi et al. [61] and O'Malley et al. [90], obtained polycrystalline samples of α-Li_2IrO_3 by performing the same classical solid-state reaction method as in the work of Modic et al. [77], it might be assumed that the obtained pellet in Modic et al. [77] also was of this composition. In the studies of Biffin et al. [11], Ruiz et al. [106], and the present work (section 4.2.4) β-Li_2IrO_3 was obtained from a sample of α-Li_2IrO_3. Further, Takayama et al. [124] obtained β-Li_2IrO_3 by a reaction of α-li_2IrO_3 with LiCl. The interpretation of these growth processes might assume that in Modic et al. [77] the resulting sample was β-Li_2IrO_3. No further observations on the growth of γ-Li_2IrO_3 were reported in literature.

4.1.6 Time-dependent crystallisation process

To understand the crystallisation process of Li_2IrO_3, time-dependent experiments were performed (figure 4.6). Therefore, five identical setups with the same starting ratio of educts were prepared and placed simultaneously into the muffle furnace. The experiment was performed at 1293 K with a starting ratio Li_2O:Ir of 4:1. Crucibles were removed after 5, 10, 15, and 21 days.
At the beginning of the crystallisation process, only Ir(s) and Li_2O(s) were present on the crucible bottom and plate with hole, respectively. By reaching the experiment temperature, first reactions took place in the Ir bottom body. After five days, Ir(s) was almost completely oxidised to IrO_2(s). P-XRD data showed a fraction of IrO_2(s) of 90 %. First single crystals of α-Li_2IrO_3 grew (figure 4.6). Crystallisation mainly took place at the rim of the stairs, which are characterised as preferred crystallisation sites (see section 4.1.2). Different morphologies of α-Li_2IrO_3 grew on different heights inside the crucible. At the very beginning, platy single crystals grew. Those grew at the rim of the topmost stair of the crucible and did not increase in size with time. Simultaneously, only a small amount of isometric crystals was observed. Those grew on the lower stairs of the crucible and their size increased with time and the closer the crystals grew to Ir. With time, the crystallisation of isometric α-Li_2IrO_3 expanded onto the planes of the stairs. After 21 days, a maximum size of 1 mm was reached. Since isometric crystals increased in size over the observed time scale whilst the growth of platy crystals stagnated, the growth of isometric crystals can be described as more favoured.
Next to the progress of crystal growth on the spiral staircase, the composition of the Ir body changed with time as well. After ten days, the Ir body consisted of 20 % IrO_2, 45 % α-, and 35 % β-Li_2IrO_3. After 15 days, a further P-XRD analysis on the Ir body showed that the amount of α-Li_2IrO_3 increased to 55 %, whilst the amount of β-Li_2IrO_3 stayed constant, and the amount of IrO_2(s) decreased to 10 %. After 21 days, the bottom body only consisted of a pristine mixture of the α- and β-Li_2IrO_3 phases with 65 % and 35 %, respectively. Li_2O(s) was depleted. The preferred formation of α-Li_2IrO_3 within the bottom body and on the spiral staircase revealed that the real temperature of the muffle furnace was not high enough to lead to the formation of β-Li_2IrO_3.

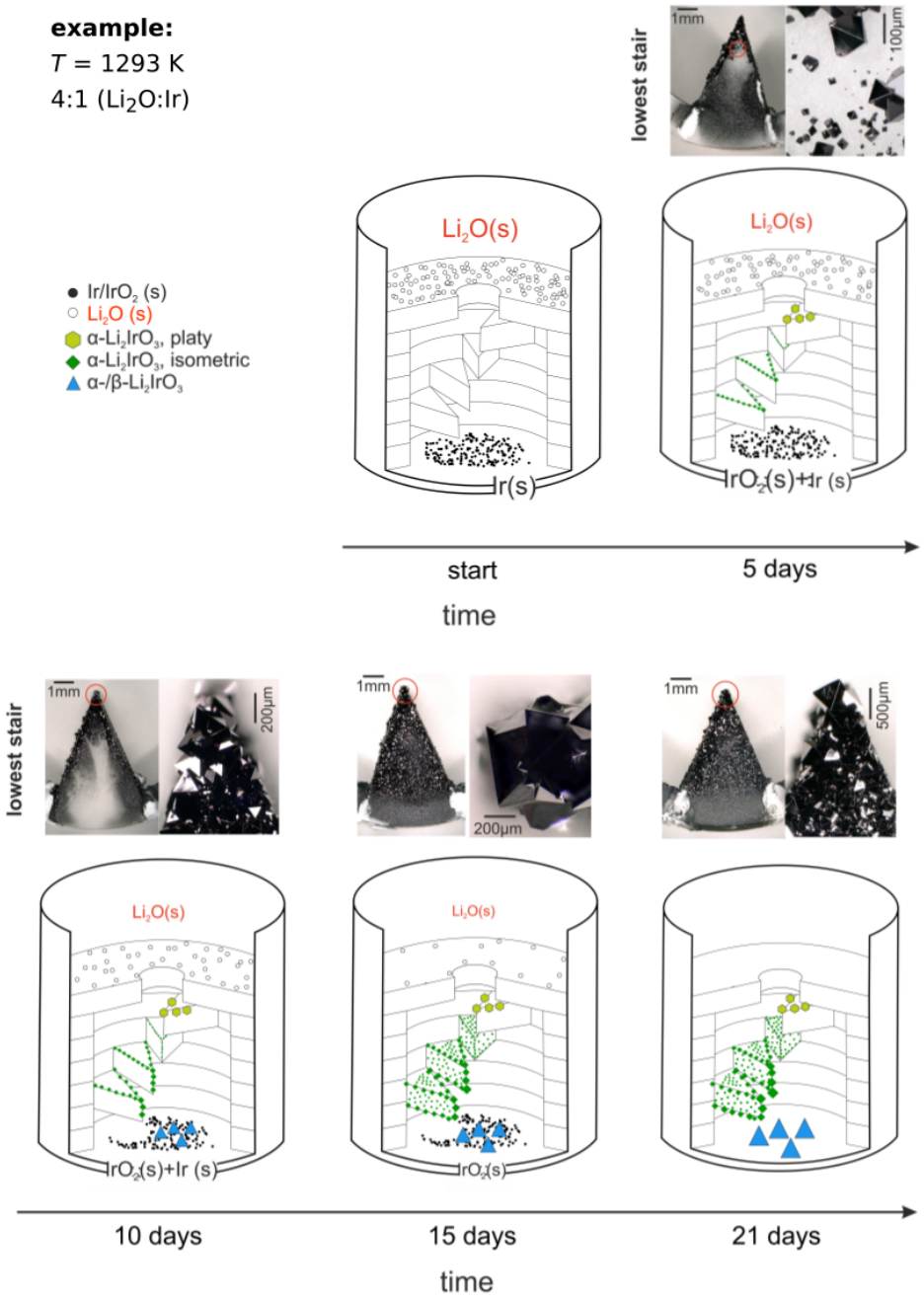

Figure 4.6: Time-dependent crystallisation process of Li_2IrO_3 at 1293 K with a starting ratio Li_2O:Ir of 4:1. Time steps after 5, 10, 15, and 21 days show the change of the educts and the growth of different Li_2IrO_3 phases inside the setup. Pictures of the lowest stair of the setup show the time-dependent growth of α-Li_2IrO_3 crystals. Left pictures give the whole stair and right pictures are the zoomed region of the stair (red circle). Increasing sizes of symbols show an increase in size/amount of phases on the stairs and in the Ir body, respectively.

4.1.7 Bottom-body formation process

The variety of growth attempts in the Li-Ir-O system show that the Ir bottom body tended to oxidise and form IrO_2 in an early stage of the growth (table 4.1). The oxidation and formation of IrO_2 is independent of the starting ratio and temperature. However, with an increasing Li_2O:Ir ratio, the formation of Li_2IrO_3 phases is favoured in the bottom body. By setting the ratio to 3:1 or higher, one or more modifications of Li_2IrO_3 are formed in the bottom body independent of the duration of experiment (table 4.1, *e.g.* V5). Mostly, mixed bottom bodies, which consist of IrO_2 and one or more Li_2IrO_3 phases, are formed. In the following, the ratio of 3:1 is investigated in more detail. Quantitative analysis were performed based on P-XRD data. At a ratio of 3:1, the bottom body consists of IrO_2 and modifications of Li_2IrO_3. If the bottom body only consists of IrO_2 and β-Li_2IrO_3, the relative amount of IrO_2 is $\sim 30\,\%$ and independent of the temperature or duration of the experiment (V4T1; V10T4). If the bottom body consists of α-, β-Li_2IrO_3, and IrO_2, while maintaining the 3:1 ratio, the IrO_2 content is slightly higher (V12T4; V13T6). Here, the content of α- compared to β-Li_2IrO_3 decreases with increasing temperature. By increasing the ratio Li_2O:Ir to 4:1, the bottom body solely consists of Li_2IrO_3 without the presence of IrO_2 (*e.g.* V7T5). Here, the amount of β-Li_2IrO_3 is significantly higher than of α-Li_2IrO_3 and increases with increasing temperature and duration of the experiment to $\sim 85\,\%$ (V11T8). These growth systematics are also found in bottom bodies, which were formed during growth experiments with even higher ratios of up to 7:1. Overall, this implies that the content of the bottom body is significantly temperature-dependent and the amount of β-Li_2IrO_3 increases with increasing temperature, which underlines that β-Li_2IrO_3 is formed at HT.

Further investigations on the bottom bodies of the growth experiments show that the bottom body mostly consists of two parts, a loose and a compact part (figure 4.7). Whilst the compact part is found directly at the bottom of the crucible being partially solidified to it, the loose part is found on the top of the bottom body. P-XRD data confirm α- and β-Li_2IrO_3 in the compact part. The largest crystals exhibit a rhombus-shaped (001) crystal face and are identified as β-Li_2IrO_3. Hence, the surrounding matrix is α-Li_2IrO_3. In contrast to the compact part, the loose part solely consists of α-Li_2IrO_3. Since the compact part is situated right at the bottom of the crucible, where the heating up of the Al_2O_3 crucible yields higher temperatures, this difference in content further underlines the favoured formation of β-Li_2IrO_3 at HT compared to α-Li_2IrO_3.

Figure 4.7: Solidified part of the bottom body consisting of rhombus-shaped β-Li_2IrO_3 crystals in a matrix of α-Li_2IrO_3.

4.2 Material characterisation

4.2.1 Structural aspects

First structural classification of grown single crystals was carried out by P-XRD. In appendix table A.1, the lattice parameters of the three modifications α-, β-, and γ-Li_2IrO_3 are compared. The comparison of calculated P-XRD patterns of α-, β-, and γ-Li_2IrO_3 based on structural models by O'Malley et al. [90], Biffin et al. [11], and Modic et al. [77], respectively, is given in figure 4.8.

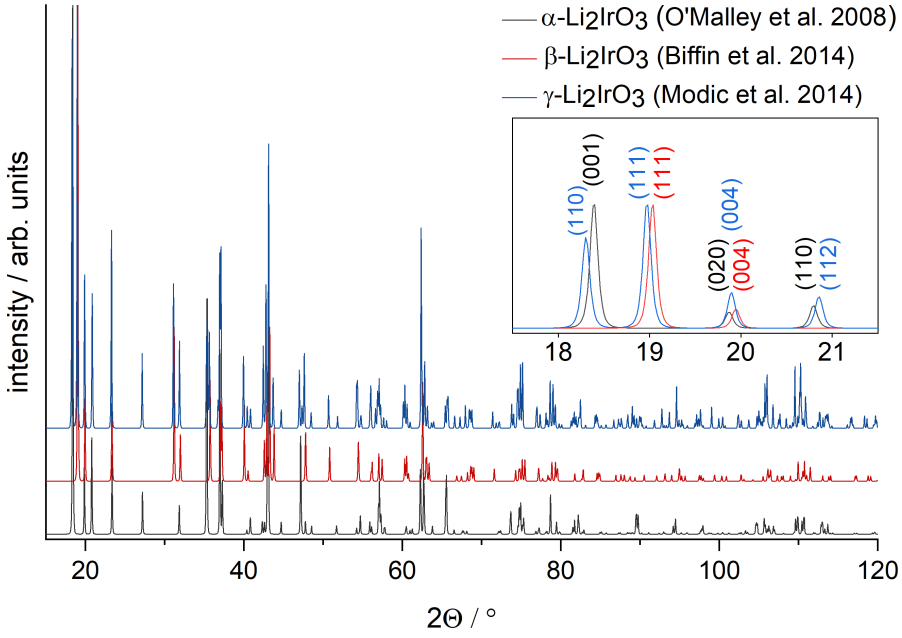

Figure 4.8: Calculated P-XRD pattern of α-, β-, and γ-Li_2IrO_3 based on structural models by O'Malley et al. [90], Biffin et al. [11], and Modic et al. [77]. For better visualisation, the low 2Θ range is enlarged and *hkl* reflections are indexed.

The theoretical powder pattern of α-Li_2IrO_3 can be differentiated from the ones of orthorhombic β- and γ-modifications on the basis of its distinct 2Θ positions, *e.g.* of the three reflections (001), (020) and (110) at a low diffraction angle of 17° to 22° 2Θ (figure 4.8). First, the (001) reflection does not fulfil the (00l) reflection conditions for the space groups *Fddd* (β-Li_2IrO_3, $l = 4n$) and *Cccm* (γ-Li_2IrO_3, $l = 2n$). Furthermore, for 0k0 reflections, the reflection condition for β- and γ-Li_2IrO_3 is $k = 4n$. Hence, the (020) reflection only occurs in α-Li_2IrO_3 with space group $C2/m$ ($0k0 : k = 2n$). If we compare the theroetical powder diffraction patterns of the two orthorhombic modifications β- and γ-Li_2IrO_3 with space groups *Fddd* and *Cccm* in the range between 17° and 22° 2Θ (figure 4.8), two common allowed reflections (111) and (004) are observed. Due to the minimal differences in

lattice parameters of β- and γ-Li_2IrO_3 (appendix table A.1), both reflections are situated at almost the same 2Θ value with only a small shift towards higher 2Θ for β-Li_2IrO_3 having slightly smaller lattice parameters. In contrast to this, the (110) and (112) reflections are present for γ-Li_2IrO_3 (*Cccm*) but forbidden for β-Li_2IrO_3 (*Fddd*; *hk*0: $h+k, h+l, k+l = 2n$; *hkl*: $h,k = 2n$). After first classifications of grown crystals, the structural solution was carried out using SC-XRD data.

4.2.1.1 α-Li_2IrO_3

In the present work, the crystal structure of α-Li_2IrO_3 was determined by SC-XRD. Instrumental details were given in chapter 3.1.1.2. Experimental details are listed with refinement results in the upcoming table 4.2. All atomic displacement parameters were refined anisotropically (appendix table A.4). Further information on bond angles, bond distances, and bond valence sums (BVS) are listed in the appendix tables A.5 and A.6, respectively.
In monoclinic α-Li_2IrO_3 ($C2/m$), the structure is mainly characterised by edge-sharing IrO_6 octahedra, which build up a 2D honeycomb network (section 1.1.1.1). The center of each honeycomb is filled up by one Li atom, Li2 (figure 1.1a). This results in a mixed metal layer which is alternatingly stacked along the c-axis with layers consisting of pristine Li atoms, Li3/Li4 (figure 1.1b). The structural solution and refinement of α-Li_2IrO_3 crystals grown by the CVTR method confirmed the crystal structure with its almost equal Ir-Ir distances of a_1 = 2.9755(8) Å and a_2 = 2.9768(5) Å, which results in a nearly hexagonal 2D honeycomb network (figure 4.9).

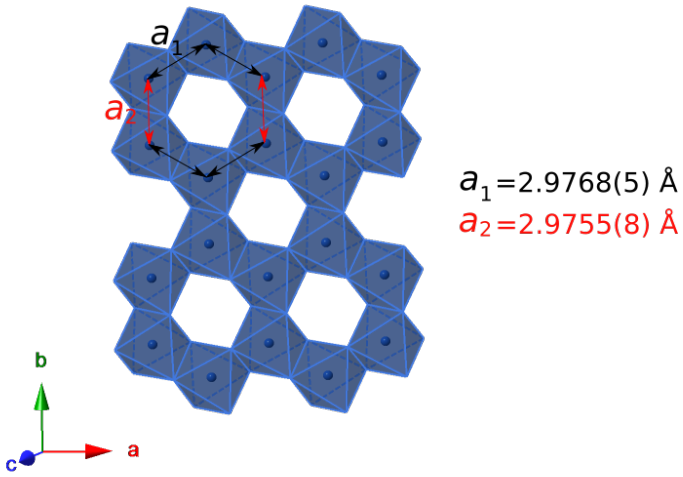

Figure 4.9: In α-Li_2IrO_3, the Ir-Ir distances a_1 and a_2 between edge-sharing IrO_6 octahedra are almost similar. The simplified structure neglects the depiction of the atomic O and Li positions.

Table 4.2: Structural model of α-Li_2IrO_3 from the present work including measurement details, lattice parameters (a, b, c, β), cell volume V, atomic positions with Wyckoff site symmetry, and fractional coordinates (x, y, z). Further information like anisotropic atomic displacement parameters for all atom sites, bond valence sums, bond distances, and bond angles are found in the appendix.

α-Li_2IrO_3	
Space group	$C2/m$
Z	4
a, b, c, β	5.1589(5) Å, 8.9227(8) Å, 5.1021(7) Å, 109.730(2)°
V	221.07(4) Å^3
ρ_{calc}	7.634 g cm^{-3}
T	120(2) K
Radiation wavelength	0.71073 Å
Crystal information	
Colour/shape	black, platy
Size	0.025 mm x 0.057 mm x 0.081 mm
Growth conditions	CTR, 1273 K, 21 days, Li_2O:Ir ratio 2.5:1, grown on staircase
Data collection	
Θ range	4.24° to 35.04°
Independent reflections	590
R_{int}	0.0485
Data reduction	
Absorption correction	numerical
μ	60.076 mm^{-1}
F(000)	428
Refined parameters	35
Final R-values with I > 2σ(I)	
R_1	0.0346
w_{R2}	0.0943
GOF on F^2	1.065

Structure solution and refinement: SHELXT-2014/5 [114] , SHELXL-2018/3 [115]

Atom	Site	x	y	z
Ir1	4g	0.0000	0.33326(4)	0.0000
Li2	2a	0.0000	0.0000	0.0000
Li3	4h	0.0000	0.841(3)	0.5000
Li4	2d	0.0000	0.5000	0.5000
O5	8j	0.249(3)	0.3268(8)	0.768(2)
O6	4i	0.269(3)	0.0000	0.764(3)

In table 4.3, the lattice parameters of the three structural models of α-Li_2IrO_3 of the present work, of Freund et al. [35], and of O'Malley et al. [90] are compared. The latter structural models are listed in the appendix tables A.7 and A.8, respectively. Between the three structures, variations of lattice parameters are noted on the second decimal place. Slightly smaller lattice parameter in the structural model of the present work are explained by the lower measurement temperature of 120(2) K compared to RT measurements in the literature [35, 90]. However, different synthesis and diffraction methods might also influence the lattice parameters. Further comparison between the three structural models show strong differences in bond-valence calculations (table 4.3, detailed register in appendix tables A.6, A.9, and A.10). Calculated GIIs of the structural models of α-Li_2IrO_3 show strong deviations between the structure solved from P-XRD [90] and the ones from SC-XRD data from Freund et al. [35] and the present work (table 4.3).

Table 4.3: Lattice parameters (a, b, c, and β) and global instability indices (GII) of α-Li_2IrO_3, $C2/m$ ($Z = 4$), from the present work (SC-XRD), by Freund et al. [35] (SC-XRD), and by O'Malley et al. [90] (P-XRD).

Author	a / Å	b / Å	c / Å	β / °	GII
present work	5.1589(5)	8.9227(8)	5.1021(7)	109.730(2)	0.0318
Freund et al. [35]	5.1749(2)	8.9359(2)	5.1194(2)	109.827(2)	0.0950
O'Malley et al. [90]	5.1633(2)	8.9294(3)	5.1219(2)	109.759(3)	0.1584

The high GII calculated from the structural model of O'Malley et al. [90] (0.1584) is explained by a deviating y-coordinate of the Li3 position and shared site occupancies of the Ir1 and Li2 positions. The different y-coordinate of the Li3 position (y = 0.809(6) [90]) compared to the one from the present work (y = 0.841(3)) results in a bond-valence sum (BVS) of 1.168(46) for the Li3-O bond instead of 0.959(20). Hence, in the structural model of O'Malley et al. [90] the BVS deviates from the ideal value of +1 by 16.8 % instead of 4.4 % for the structural model of the present work.
Further difference between crystal structures is found on the Ir1 and Li2 sites, for which O'Malley et al. [90] proposed shared occupancies of Ir and Li [90]. They reported that one position is mainly occupied by Ir (90.2(2) %), whereas the other one is mainly occupied by Li (80.4(3) %). This sharing of atomic positions should be considered with caution. Not only the different oxidation states of Li^+ and Ir^{4+}, which result in different ionic radii for octahedral coordination (0.76 Å and 0.625 Å [1], respectively), but also the varying bond lengths of a Ir – O and a Li – O bond ($\approx$ 2.020 Å and $\approx$ 2.129 Å [105], respectively) question the validity of the cryystal structure if Ir and Li share an atomic position. Moreover, the calculation of BVS shows a strong deviation from ideal values and, therefore, an increased GII. Besides, O'Malley et al. [90] solved and refined the structure on the basis of P-XRD data. Structural solution from P-XRD data is never as precise as data obtained from SC-XRD. In SC-XRD, fractional coordinates can be determined more precisely since the complete 3D space is considered and each reflection is measured individually. Due to its better counting statistics, a higher peak-to-background ratio is reached which yields a better structural solution. O'Malley et al. [90]

discussed difficulties in curve fitting due to structural disorder in powder samples of α-Li_2IrO_3, which further questions the significance of refined site occupancies from the P-XRD data (section 1.1.1.1). Apart from stacking faults in alkali iridates of the Li_2MnO_3 structure type [26, 90], crystallographic twins were observed by Freund et al. [35]. In the present work, no evidence of stacking faults or crystallographic twinning was observed in single crystalline α-Li_2IrO_3.
By opposing the structural model of Freund et al. [35] (appendix table A.7) with the one from the present work, one compares structural models of single crystals grown by the similar method (CVTR) but with differing growth conditions. Both structural models exhibit only small differences in lattice parameters and fractional coordinates of atomic positions. The comparison of BVS of both structural models (appendix tables A.6 and A.9) shows lower deviations from the ideal BVS in the structural model of the present work. The most significant improvement is observed for the O6 position, where the deviation is 0.327 % for the structural model of the present work and 8.719 % for the one of Freund et al. [35]. By combining these results with fractional coordinates with a decimal place more, the GII of the structural model of the present work is lower than the one of the structural model of Freund et al. [35].

Temperature-dependent behaviour of α-Li_2IrO_3
Since for the 2D honeycomb structure Li_2RuO_3 a temperature-dependent dimerisation phenomenon was reported in the literature [76] (section 1.1.2.1), the thermal behaviour of the iridate counterpart α-Li_2IrO_3 was investigated by LT P-XRD measurements between RT and 12 K. No temperature-induced phase transition was detected, which confirms structural stability in the studied temperature regime.

4.2.1.2 β-Li_2IrO_3

The crystal structure of β-Li_2IrO_3 was determined by SC-XRD. Instrumental details are given in the methods chapter 3.1.1.2. Experimental details are listed with refinement results in the upcoming table 4.5. The atomic displacement parameters of Ir and O were refined anisotropically (appendix table A.11). Further information on bond angles, bond distances, and bond valence sums are listed in the appendix tables A.12 and A.13, respectively.
In the "hyperhoneycomb" β-Li_2IrO_3, open honeycomb rings of edge-sharing IrO_6 octahedra build up the main structural feature (section 1.1.1.2, figure 1.3a). These are situated in two distinct layers along the $a \pm b$ diagonals. In between this IrO_6 network, Li atoms, Li2/Li3, are situated on the octahedral sites (figure 1.3a). In accordance with the previous structural investigations on α-Li_2IrO_3, the Ir-Ir distances in β-Li_2IrO_3 are almost equal with a_1 = 2.9674(4) Å and a_2 = 2.9684(8) Å (figure 4.10b).

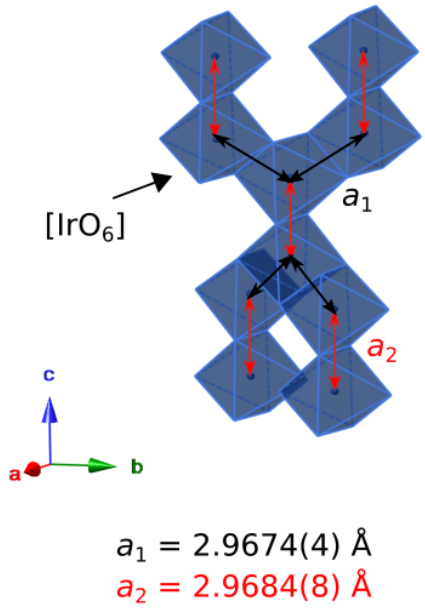

Figure 4.10: In β-Li_2IrO_3, the Ir-Ir distances a_1 and a_2 between edge-sharing IrO_6 octahedra are almost similar. The simplified structure neglects the depiction of the atomic O and Li positions.

In table 4.4 the lattice parameters and GII of structural models of the present work and of Biffin et al. [11] (appendix table A.14) are compared. Both datasets were obtained by SC-XRD at LT (150 K and 100 K, respectively), whereas samples were grown by different methods. Deviations in lattice parameters are observed on the third decimal place. The fractional coordinates of atomic positions differ by a maximum of the second decimal place. The calculated BVS show smaller deviations from their ideal values and, therefore, result in a smaller GII for the structural model of the present work than of Biffin et al. [11] (0.0585 and 0.0917, respectively). An overview on BVS is shown in appendix tables A.13 and A.15.

Table 4.4: Lattice parameters and global instability indices (GII) of structural models of β-Li_2IrO_3 crystallising in *Fddd* ($Z = 16$) from the present work and by Biffin et al. [11]. Crystals were grown by Chemical Vapour Transport Reaction (CVTR) and by repetitive annealing of pellets.

	Growth method	a / Å	b / Å	c / Å	GII
present work	CVTR	5.8959(4)	8.4288(5)	17.7962(14)	0.0585
Biffin et al. [11]	repetitive annealing	5.8903(2)	8.4261(3)	17.79240(70)	0.0917

Table 4.5: Structural model of β-Li_2IrO_3 from the present work including measurement details, lattice parameters (a, b, c, β), cell volume V, atomic positions with Wyckoff site symmetry, and fractional coordinates (x, y, z). Further information like anisotropic atomic displacement parameters, bond valence sums, bond distances, and bond angles are found in the appendix.

β-Li_2IrO_3	
Space group	*Fddd*, origin 2
Z	16
a, b, c	5.8959(4) Å; 8.4288(5) Å; 17.7962(14) Å
V	884.39(11) Å^3
ρ_{calc}	7.633 g cm^{-3}
T	150(2) K
Radiation wavelength	0.71073 Å
Crystal information	
Colour/shape	black, prism-like
Size	0.030 mm x 0.034 mm x 0.041 mm
Growth conditions	CTR, 1293 K, 21 days, Li_2O:Ir ratio 4:1
	quenched in air, growth in bottom body
Data collection	
Θ range	4.37° to 29.88°
Independent reflections	317
R_{int}	0.0241
Data reduction	
Absorption correction	numerical
μ	60.068 mm^{-1}
F(000)	1712
Refined parameters	24
Final R-values with I > 2σ(I)	
R_1	0.0131
w_{R2}	0.0326
GOF on F^2	1.107

Structure solution and refinement: SHELXT-2014/5 [114] , SHELXL-2018/3 [115]

Atom	Site	x	y	z	U_{iso} / Å^2
Ir1	16g	0.125	0.125	0.70840(2)	-
Li2	16g	0.125	0.125	0.0412(10)	0.010(3)
Li3	16g	0.125	0.125	0.8819(11)	0.011(5)
O4	16e	0.8667(11)	0.125	0.125	-
O5	32h	0.6385(8)	0.3651(1)	0.03838(18)	-

4.2.1.3 γ-Li_2IrO_3

In the present work, growth attempts yielding γ-Li_2IrO_3 (figure 1.4) were not successful. Hence, in the following the structural models of Analytis [4] and Modic et al. [77] are evaluated. Due to differences in the magnetic ordering temperature of grown crystals, Modic et al. [77] suggested a deviating crystal structure and implemented further structural investigations. Three different structural models of γ-Li_2IrO_3 were distributed in the supplementary material, supplied as crystallographic information file, and via e-mail (appendix tables A.16, A.17 and A.18). The structural models show slight deviations in lattice parameters, but also different fractional coordinates of atomic positions and ADPs. According to Modic et al. [77], the Li positions were not refined but are only idealised atomic positions to obtain the fundamental building blocks of edge-sharing IrO_6 and LiO_6 octahedra as in the already known Li_2IrO_3 modifications. No information on the quality of data collection, absorption correction, or the refinement process were given.

To evaluate the stability of the proposed γ-Li_2IrO_3 structures, the interatomic distances and angles of each MO_6 octahedron (M = Li; Ir) need to be investigated. For comparison, the average interatomic distances of all three modifications of Li_2IrO_3 are listed in table 4.6. The structural models of α- and β-Li_2IrO_3 of the present work show almost ideal Ir-Ir, Li-Li, and Li-Ir interatomic distances, which emphasises their almost ideal honeycomb structures. The Li – O and Ir – O bond lengths are close to the expected values of 2.129 Å and 2.020 Å [105]. Moreover, the average deviations of the O-M-O angles (M = Li; Ir) from an ideal angle of 90° are small. Whilst the average deviation for the O-Li-O angle is slightly higher for β- (3.7(4)°) than for α-Li_2IrO_3 (3.3(5)°), for the O-Ir-O angle the average deviation is similiar in both structures (2.4(5)°). The interatomic bond angles in α- and β-Li_2IrO_3 are listed in the appendix tables A.5 and A.12. These considerations imply almost ideal IrO_6- and LiO_6-octahedra in α- and β-Li_2IrO_3 and give further evidence for stable crystal structures, which was already verified in low GIIs of 0.0318 and 0.0450, respectively. To evaluate the γ-Li_2IrO_3 structures, the BVS of the three models were calculated (appendix tables A.19, A.20, and A.21). For comparison, the structural model with the lowest GII of 0.15 and published ADPs was chosen (appendix tables A.18 and A.21) [4].

Table 4.6: Comparison of the average interatomic distances in α- and β-Li_2IrO_3 of the present work, and of γ-Li_2IrO_3 distributed by [4]. A complete listing of interatomic distances is found in the appendix tables A.6, A.13, and A.21.

		α-Li_2IrO_3 $C2/m$	β-Li_2IrO_3 $Fddd$	γ-Li_2IrO_3 [4] $Cccm$
Distances / Å	Ir-Ir	2.98(1)	2.97(1)	2.97(1)
	Li-Li	2.96(8)	2.95(8)	2.97(1)
	Li-Ir	2.97(2)	2.97(7)	2.97(1)
Bond lengths / Å	Li – O	2.134(8)	2.137(9)	2.134(100)
	Ir – O	2.022(5)	2.026(2)	2.040(50)

In accordance with α- and β-Li_2IrO_3, the Ir/Li network in γ-Li_2IrO_3 [4] is characterised by similar interatomic distances and small uncertainties (table 4.6, figure 4.11). The absolute values of the average Li – O and Ir – O bond lengths are close to the ones in α- and β-Li_2IrO_3. However, the uncertainties are significantly higher. In the structure of γ-Li_2IrO_3 [4], two IrO_6- and five LiO_6-octahedra are reported (appendix table A.18). The IrO_6 octahedra show similar and moderate distortions with small deviations in interatomic distances on the second decimal place and an average deviation from the ideal O-Ir-O angle of $2.4(3)^\circ$.

For the LiO_6 octahedra, the distortions are significantly higher and differ for each other. The LiO_6 octahedra, which surround Li1, Li2, and Li3, share edges with each other and are situated between the two interlacing layers of IrO_6 honeycomb rings (figure 4.11). These LiO_6 octahedra have Li – O bond lengths of 2.13(3) Å, 2.14(2) Å, and 2.16(2) Å, which roughly coincide within the uncertainty with the ideal value of 2.129 Å [105]. However, the average deviation from the ideal O-Li-O angle of 90° differs between the three types of LiO_6 octahedra and is significantly higher for Li3 (6°) than for Li1 (3.3°) and Li2 (2.7°). This shows a higher distortion for LiO_6 octahedra of Li3 than of Li1 and Li2. The LiO_6 octahedra surrounding Li4 and Li5 exhibit different bond lengths. For Li4, which is situated in the center of each honeycomb ring (figure 4.11), the Li – O bond length has an average value of 2.23(3) Å, which is significantly too high for a Li – O or a Ir – O bond. On the contrary, the bond lengths between Li5 and its surrounding O atoms is 2.04(3) Å, which is close to a typical Ir – O bond but not to a Li – O bond (2.02 Å and 2.129 Å, respectively [105]). This might indicate that the Li5 position was wrongly defined as a Li position instead of a Ir position and explains the high uncertainty of the average Li – O bond length in γ-Li_2IrO_3 (table 4.6). The LiO_6 octahedra surrounding Li5 are strongly distorted with an average deviation of 5.5° from the ideal angle. These observations are found in all three proposed structural models of γ-Li_2IrO_3 [4, 77]. Moreover, in all three structural models the x-fractional coordinate of the O3 atomic positon equals 0 within the uncertainties, which is close to a special position. However, a Wyckoff site with $0, y, 0$ is not allowed in space group *Cccm*. Therefore, this might be a further indication for a wrong structural solution.

Overall, the deviating interatomic distances and angles of the proposed structural model of γ-Li_2IrO_3 [4] result in a high GII of 0.15 compared to the lower GIIs for the structural models of α- (0.0388) and β-Li_2IrO_3 (0.0450) of the present work. The two other reported structural models of Modic et al. [77] show an equal or even higher GII (0.14 and 0.25, appendix table A.20 and A.19, respectively). Together with the assumption of a wrongly assigned Li5 atom and the questionable x fractional coordinate of O3, it might be suggested that the reported structureal models of γ-Li_2IrO_3 are not correct. The reason for a wrongly chosen symmetry might lay in the occurrence of stacking faults, which were reported by Modic et al. [77] and could cause imprecise diffraction peak positions. As a consequence, the peak position might not be selected correctly during the data collection strategy, which results in a wrongly chosen space group. This may cause that the electron density map does not show one precise Q-peak due to the movement of atoms. When choosing slightly wrong atomic positions for these atoms, distorted MO_6 octahedra (M = Li; Ir) are formed.

Ergo, the proposed γ-Li_2IrO_3 structure might be a wrong setup of one of the already known Li_2IrO_3

modifications. β-Li_2IrO_3 exhibits the same metric as the proposed γ-Li_2IrO_3 unit cell but with a different space group (appendix table A.1). Further, a possible transformation to the α-Li_2IrO_3 structure was already proposed by Modic et al. [77] since the angle between the interlacing honeycomb layers in γ-Li_2IrO_3 is equal to the monoclinic angle in α-Li_2IrO_3. All these remarks concerning the proposed structural models of γ-Li_2IrO_3 of Analytis [4] and Modic et al. [77] lead to a certain degree of doubt as to whether it may exist.

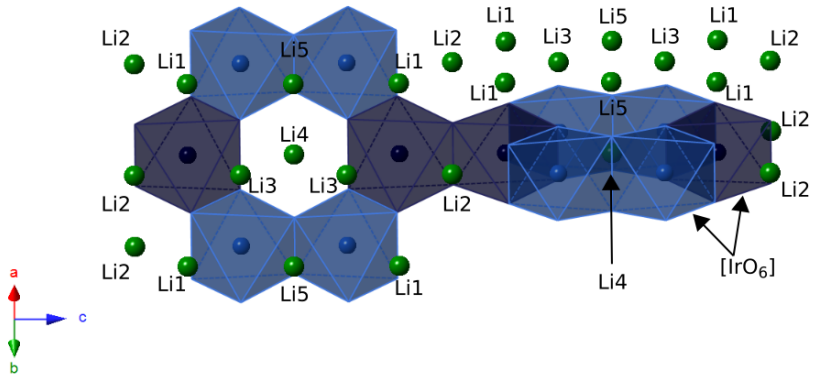

Figure 4.11: Position of Li atoms (green; Li1-Li5) in the crystal structure of γ-Li_2IrO_3 [4], which is mainly characterised by edge-sharing IrO_6 octahedra of Ir1 and Ir2 (dark and bright blue, respectively). The simplified structure neglects the depiction of the atomic O positions.

4.2.2 Chemical instability

During the sample preparation for EDX measurements, Li_2IrO_3 crystals showed a time-dependent chemical instability against ethanol and/or ethyleneglycol in air. Both chemicals were used during the polishing treatment. After several hours, the sample showed corrosion in the form of a thin fluid on their freshly polished surface. Whilst on the surface of β-Li_2IrO_3 crystals only a thin liquid layer was formed, the corrosive reaction on the surface of α-Li_2IrO_3 crystals was stronger and led to the growth of colourless elongated single crystals with time (figure 4.12). Since only the detection of O and Ir is possible by EDX, Raman spectroscopy was used for the subsequent characterisation.
In the Raman spectrum, different vibrational modes in their characteristic ranges of Raman shift (Li-O, C-H, C-O, and O-H) were detected (appendix figure A.1). These vibrational modes indicate an organometallic reaction product of Li and an organic compound. Since the surface of Li_2IrO_3 crystals was previously handled with both, ethanol and ethyleneglycol, single crystals of *e.g.* ethyllithium (LiC_2H_5) or lithium ethylene glycolate ($Li(C_2H_4O_2)$) might have formed. For both compounds colourless single crystals and an orthorhombic symmetry with space groups *Pcan* [32] and *Pbca* [69] were reported. Due to a lack of Raman spectroscopic data of these compounds, no clear determination of the grown single crystals was possible. Further, the small size of the colourless crystals of maximum 5 µm x 5 µm x 25 µm did not allow for P-XRD or SC-XRD measurements.

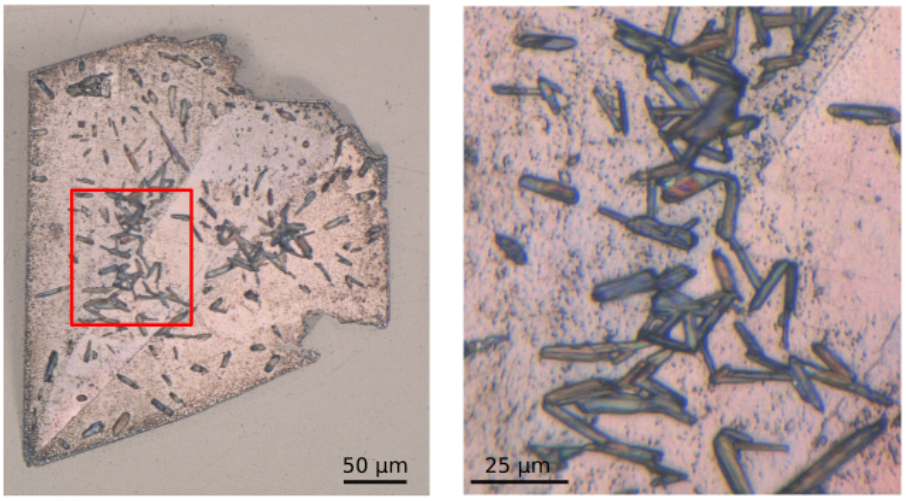

Figure 4.12: Colourless single crystals on top of the surface of freshly polished α-Li_2IrO_3 after exposure to ethanol and/or ethylenglycol in air. The red box inset in the left figure is zoomed on the right side.

These observations showed the chemical instability of α- and β-Li_2IrO_3 single crystals but with different reactivity. The significantly higher reactivity of the surface of α- compared to β-Li_2IrO_3 might be explained by the Li positions in the crystal structures. In 3D hyper-honeycomb β-Li_2IrO_3, which is build up by two interlacing layers of edge-sharing IrO_6 octahedra, Li ions are positioned in between those layers and, hence, are part of the 3D network. In contrast, the 2D honeycomb α-Li_2IrO_3 structure is build up by two layers, a mixed metal $LiIr_2$ and a Li layer. Thus, in the α-Li_2IrO_3 structure Li is less interconnected with the surrounding structural network and, therefore, might be more moveable and more reactive than in β-Li_2IrO_3.

4.2.3 Elemental analysis

To gain further information on the growth process of both modifications, elemental analysis of the crystals were conducted. For this, the surface of thoroughly polished crystals was investigated by EDX regarding their homogeneity. Since with EDX Li quantities cannot be measured, the homogeneity was investigated by measuring Ir and O quantities and investigating the O/Ir ratio. The presented and discussed data are in the area of reliability (section 3.3.1).

4.2.3.1 α-Li_2IrO_3

Single crystals of α-Li_2IrO_3 grew in different morphologies depending on their growth conditions and positions (section 4.1.3). α-Li_2IrO_3 crystals mostly grew isometric (section 4.1.3). In figure 4.13, a side face of type {110} or {011} and the top of the crystal, which pointed into the reaction chamber, is shown. During the polishing of the sample surface, a thin layer of the crystal was removed so that the delimitation of the shown crystal does not coincide with its sharp corners and edges. In figure 4.13, lines a,b, and c point to the top of the crystal, whereas line d crosses the crystal surface in perpendicular

direction. To the top corner of the crystal there seems to be an increase of relative values of the O/Ir ratio, indicating a slight decrease in Ir. Though in absolute values, these small changes are within the errors. Therefore, isometric α-Li_2IrO_3 crystals are defined as homogeneous. A detailed investigation on the composition of single crystals of α-Li_2IrO_3 from the same growth attempt but from different stairs (*i.e.* heights in the crucible) did not show a systematic change in composition. Further analyses of single crystals of α-Li_2IrO_3, which were grown in the time-dependent crystallisation process, did not show differences in composition as well.

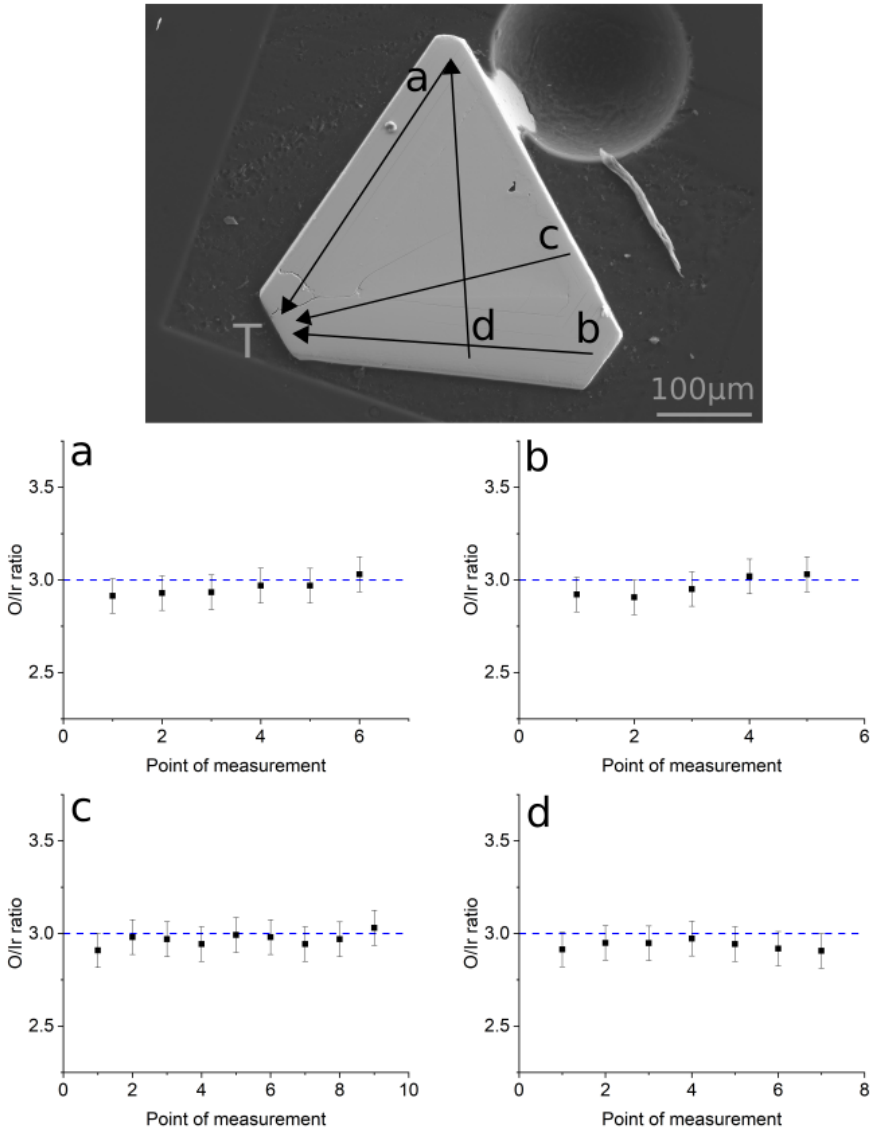

Figure 4.13: SEM image and element distribution of Ir and O of an isometric α-Li_2IrO_3 single crystal. T marks the top of the crystal pointing into the growth chamber. The blue-dashed line marks the expected O/Ir ratio.

Next to isometric crystals, which grew on all stairs of the crucible, crystal growth of platy crystals with (001) as largest crystal face only occurred on the topmost stair and at the beginning of growth attempts. Elemental analysis of platy crystals show a strong compositional difference between the point of attachment on the stair, *i.e.* the beginning of the crystal growth, and the remaining platy surface (figure 4.14a and b/c, respectively). During preparation it was observed that the first grown part of the crystal is far thinner than the remaining part. The progress of the O/Ir ratio shows that at the beginning of growth the Ir amount was lower than at the end of the growth. Together with the previous observation that platy crystals grew first, this indicates a required lower Ir concentration for the growth of platy crystals. The balanced O/Ir ratio to the top of crystal shows that during the growth process the ideal composition of Li_2IrO_3 is yielded.

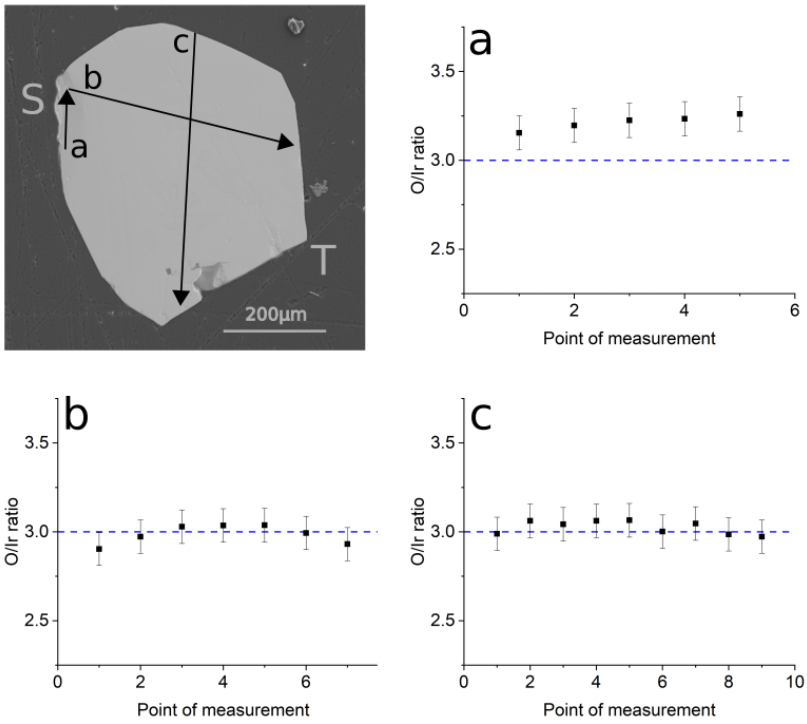

Figure 4.14: SEM image and element distribution of Ir and O of the large (001) face of a platy crystal of α-Li_2IrO_3. S marks the point of attachment to the Al_2O_3 setup/the start of growth and T marks the top of the crystal pointing into the growth chamber. The blue-dashed line marks the expected O/Ir ratio.

If the concentration of Li inside the reaction chamber was too high, dendritic crystals grew. EDX measurements on the polished surface of dendritic crystals show that the O/Ir ratio is below the expected ratio for Li_2IrO_3 compounds (figure 4.15). Since P-XRD confirmed the $C2/m$ structure of α-Li_2IrO_3 for dendritic crystals, a deviation from ideal composition does not give evidence on another structure type but shows the incorporation of either a higher Ir amount or a lower O amount. Since the O/Ir ratio increases to the top of the crystal, the amount of incorporated Ir decreased during growth and got closer to the expected ratio for Li_2IrO_3 compounds.

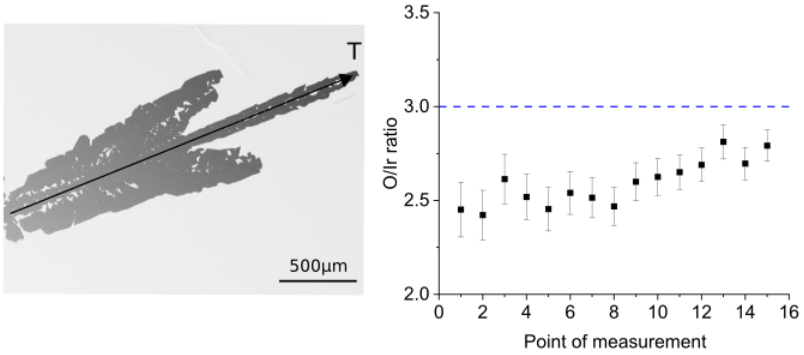

Figure 4.15: SEM image and element distribution of Ir and O of a dendritic crystal of α-Li_2IrO_3. T marks the top of the crystal pointing into the growth chamber. The blue-dashed line marks the expected O/Ir ratio.

4.2.3.2 β-Li_2IrO_3

To investigate the homogeneity of β-Li_2IrO_3 crystals during the growth process, the most elongated single crystal was prepared for EDX measurements. The polishing of the crystal face (001) was not successful due to a continuous chipping of the crystals at their outer rim and an overall rough and coarse surface. Therefore, the crystal was polished orthogonal to the (001) crystal face, hence with orientation (*hk*0). EDX measurements show a homogeneous elemental distribution in β-Li_2IrO_3 with neither a gradient from the point of attachment to the top of the crystal nor perpendicular to this direction (figure 4.16a,b).

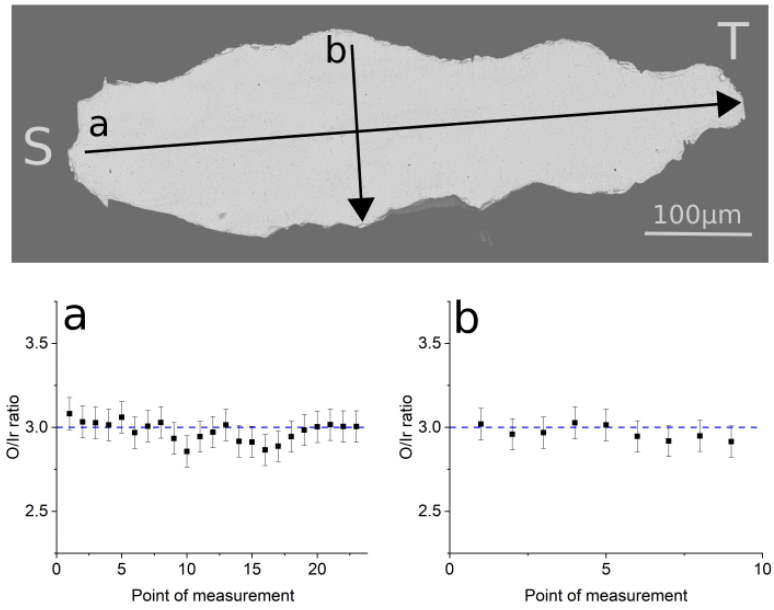

Figure 4.16: SEM image and element distribution of Ir and O of a polished surface with orientation (*hk*0) of β-Li_2IrO_3. S marks the point of attachment to the Al_2O_3 setup/the start of growth and T marks the top of the crystal pointing into the growth chamber. The blue-dashed line marks the expected O/Ir ratio.

4.2.4 Thermal analysis

Thermal analyses of the grown α- and β-Li_2IrO_3 single crystals were conducted. The results from DTA measurements show decomposition reactions of both modifications, whereas temperature-dependent long-time experiments confirm that α-Li_2IrO_3 is formed at LT and β-Li_2IrO_3 is formed at HT. In the following, these reactions will be discussed.

4.2.4.1 Decomposition reactions of α- and β-Li_2IrO_3

Thermal stability measurements of both, α- and β-Li_2IrO_3, show endothermic decomposition reactions during the heating sequence and an exothermic reaction during the cooling sequence (figure 4.17). Whilst the onset temperatures of endothermic reactions coincide within the error, the enthalpy of the decomposition reaction of β-Li_2IrO_3 is slightly higher than of α-Li_2IrO_3 (table 4.7). These differences were confirmed by measuring a sample composed of both Li_2IrO_3 modifications. Here, two distinct endothermic reactions were observed in the heating sequence.

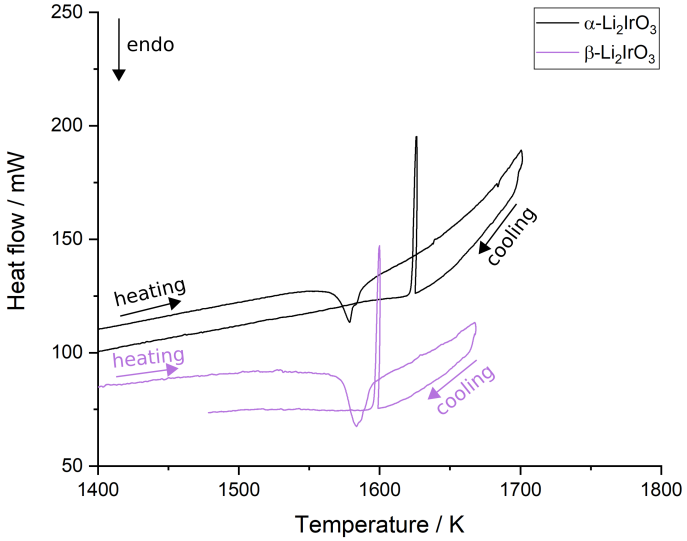

Figure 4.17: Temperature-dependent progress of the heatflow of α- (black) and β-Li_2IrO_3 (purple) measured by Differential Thermal Analysis with a heating and cooling rate of 10 K/ min.

Table 4.7: Results from thermal analysis of α- and β-Li_2IrO_3 with reaction temperature (T_{onset}) and enthalpy of reaction (ΔH_R) of endothermic and exothermic reactions.

	endothermic		exothermic	
Modification	T_{onset} / K	ΔH_R / Jg^{-1}	T_{onset} / K	ΔH_R / Jg^{-1}
α-Li_2IrO_3	1570(5)	102(6)	1626(2)	-61(4)
β-Li_2IrO_3	1575(5)	137(7)	1600(2)	-50(2)

After the DTA measurements, P-XRD analyses revealed a mixture of Li_2O and Ir. Hence, the observed endothermic reactions are described as complete decomposition reactions of α-Li_2IrO_3 and β-Li_2IrO_3 following the assumed reaction:

$$Li_2IrO_3\ (s) \rightarrow Li_2O\ (s) + Ir\ (s) + O_2\ (g)$$

The observed exothermic reaction during the cooling sequence might be explained the following: By extracting sample material for P-XRD subsequent to the DTA measurements, a large part of reaction product was bound to the inner surface of the crucible and could not be removed. Therefore, the exothermic reaction is assigned to a reaction between the crucible and a reaction product. Evidence was given by measuring a cut and flattened part of the inner surface of the crucible by P-XRD in reflection mode, which showed the P-XRD pattern of a PtIr alloy. Furthermore, the results of a semi-quantitative P-XRD analysis of the decomposition products support a reaction of Ir with the crucible: After a complete decomposition of Li_2IrO_3 one would expect a ratio of 1:1 of the solid products Li_2O and Ir. However, the semi-quantitative analysis of reaction products revealed a deviating ratio with Ir deficiency. This gives evidence for a partial reaction of Ir with the Pt crucible after the decomposition reaction.
DTA measurments of α-Li_2IrO_3 were already reported by O'Malley et al. [90]. In this, a two-step decomposition reaction with a first weight loss of $\approx$ 6 w% at 475 K in forming gas H_2:N_2 (5:95) is shown. In non-reducing atmospheres (O_2, air, and N_2), α-Li_2IrO_3 is stable until 1475 K. In the present work, DTA measurements were performed in N_2 purge gas. In comparison to the results from O'Malley et al. [90], the onset temperature differs about $\approx$ 100 K. This deviation might be a result of various factors. Whilst in both studies a platinum crucible and a heating rate of 10 K/min was used, the gas flow rate in O'Malley et al. [90] was set to 40 ml/min which is twice as much as applied in the present work. Moreover, the samples were grown by different synthesis methods and might differ in their temperature-dependent behaviour: In O'Malley et al. [90], a solid-state reaction led to the synthesis of polycrystalline material, whereas in the present work, single crystals of α-Li_2IrO_3 were obtained by the CVTR method.

4.2.4.2 Phase transition between α- and β-Li_2IrO_3

In the previous section, no phase transition between the two modifications α- and β-Li_2IrO_3 was observed. However, crystal-growth investigations of the present work reveal that α-Li_2IrO_3 is preferably formed at LT, whereas β-Li_2IrO_3 is formed at HT. These investigations coincide with observations in the literature [11, 106, 124]. To further investigate the temperature- and time-dependent phase transition between α- and β-Li_2IrO_3, long-term experiments at different temperatures were conducted.
In a first long-term experiment, a sample composed of $\sim$ 50 % of both, α-Li_2IrO_3 and β-Li_2IrO_3, was heated to 1303 K for seven days. Subsequent P-XRD analysis proved the sample to solely consist of β-Li_2IrO_3. To investigate a back-transformation from β-Li_2IrO_3 to α-Li_2IrO_3, long-term experiments were conducted at lower temperatures on a sample composed of $\sim$ 10 % α-Li_2IrO_3 and $\sim$ 90 %

β-Li_2IrO_3. The first experiment at 873 K lasted four weeks. P-XRD analysis did not show a change of composition of the sample. Therefore, the following experiment on the same sample was conducted at 973 K for four weeks. P-XRD analysis showed an increase of α-Li_2IrO_3 to $\sim$ 20% and, hence, a decrease of β-Li_2IrO_3 to $\sim$ 80%. Another experiment with the same parameters confirmed this, by showing an increase of α-Li_2IrO_3 to $\sim$ 24 % (β-Li_2IrO_3: $\sim$ 76 %).
These investigations underline that α-Li_2IrO_3 is formed at LT, whereas β-Li_2IrO_3 is preferably formed at HT. These observations are in accordance with crystal-growth investigations, which determined the phase boundary between both modifications at $\sim$ 1273 K. The transformation from α- to β-Li_2IrO_3 at HT is significantly faster than the back-transformation at LT. This emphasises that the transformation from β- to α-Li_2IrO_3 is a slowly proceeding reaction, which is kinetically inhibited. Further, it explains the presence of both modifications after a growth attempt, in which the crucible was cooled down rapidly from growth temperature and, hence, the slowly proceeding back-transformation could not take place.

Chapter 5

Li-Ru-O system

In the Li-Ru-O system of APGMOs, a variety of compounds with the common structural feature of edge-sharing RuO_6 octahedra are known in the literature (appendix table B.1). As pointed out in the introductory chapter 1.1.2, in the present work the focus is set on the investigation of growth processes and structural aspects of Li_2RuO_3 and Li_3RuO_4.

5.1 Crystal-growth investigations

In the following, the growth of Li_2RuO_3 and Li_3RuO_4 by the CVTR method is investigated. As for the Li-Ir-O system, the control of growth parameters is crucial for determining the optimum growth conditions. Further, the time-dependent crystallisation process of Li_2RuO_3 is investigated in detail. Prior to growth experiments, thermodynamic considerations are introduced to understand the reaction mechanism behind the crystal growth process and to define first suitable growth parameters.

5.1.1 Thermodynamic considerations

In close similarity to the Li-Ir-O system, Li_2O(s) and RuO_2(s) were chosen as suitable educts. According to [13, pp. 166,214], the transport reactions are:

$$Li_2O\ (s) + H_2O\ (g) \Leftrightarrow 2\ LiOH\ (g)$$
$$RuO_2\ (s) + 0.5\ O_2\ (g) \Leftrightarrow RuO_3\ (g)$$

The volatility of Li_2O in the presence of water vapour was thoroughly investigated by Arkel et al. [5] and Berkowitz-Mattuck and Büchler [7]. As for Ir, Ru is transported via auto transport [93]. Hence, the assumed chemical reactions yielding Li_2RuO_3 and Li_3RuO_4 are:

$$2\ LiOH\ (g) + RuO_3\ (g) \Leftrightarrow Li_2RuO_3(s) + H_2O\ (g) + 0.5\ O_2(g)$$
$$3\ LiOH\ (g) + RuO_3\ (g) \Leftrightarrow Li_3RuO_4(s) + 1.5\ H_2O\ (g) + 0.25\ O_2(g)$$

Suitable growth conditions for Li_2RuO_3 and Li_3RuO_4

For reaching transport-effective behaviour, RuO_3(g) and LiOH(g) need to exhibit a $p(i) \geq 10^{-5}$ atm [93]. The temperature-dependent progression of $p(i)$ is shown in figure 5.1. As discussed for the Li-Ir-O system, LiOH(g) reaches transport-effective behaviour at $T \geq 1205$ K [52]. Due to the low $p(i)$ of RuO_4(g) in the respective temperature range, the transport of RuO_2(s) takes place via RuO_3(g). The $p(i)$ of RuO_3(g) reaches transport-effective behaviour at $T \geq 1300$ K. Hence, the $p(i)$ behaviour of both gaseous reactants differs and results in different $p(i)$ at a specific temperature. To fulfil the requirement of transportability of the gaseous reactants ($p(i) \geq 10^{-5}$ atm), growth attempts in the Li-Ru-O system were carried out at temperatures of $\sim$ 1300 K. At this temperature, p(LiOH) is of a magnitude larger than $p(RuO_3)$. The following calculations on temperature-dependent thermodynamical data are performed as for Li_2IrO_3.

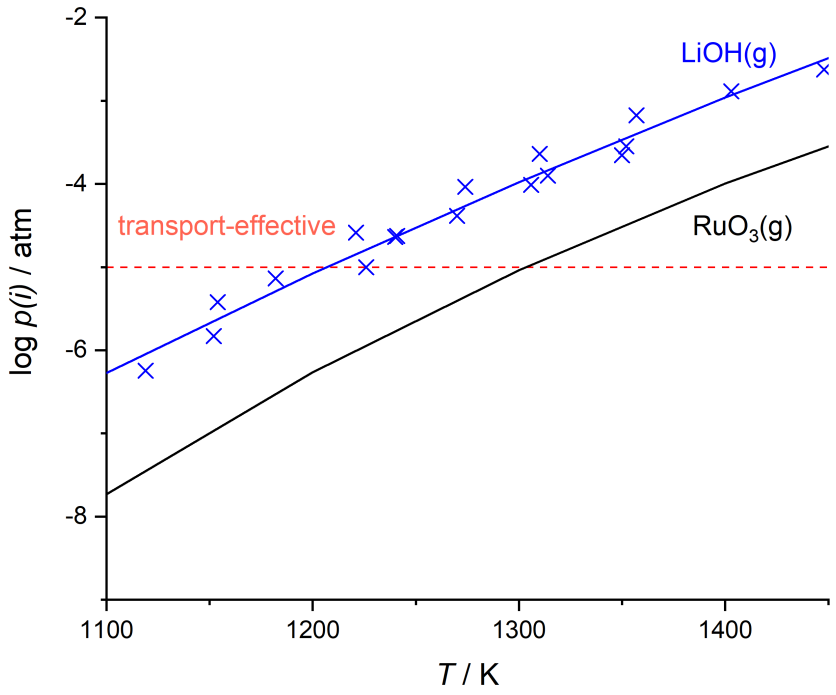

Figure 5.1: Temperature-dependent progress of the partial pressures, $p(i)$ of RuO_3(g) on the basis of standard data from Barin [6] in black and LiOH(g) after Kikuchi [52] (blue, crosses) including a calculated logarithmic regression curve (blue, line). The limitation of $p(i)$ for reaching transport-effective values is marked with a red dashed line.

Li_2RuO_3

At RT, the values for Li_2RuO_3, ΔH^0_{298} = -944(20) kJmol^{-1} and ΔS^0_{298} = 96(15) Jmol^{-1}K^{-1}, are close to the respective values for Li_2IrO_3. Further temperature-dependent values up to 1400 K are listed in the appendix table B.2. At 1300 K, the reaction has a ΔH_R = -708(30) kJmol^{-1} and a

$\Delta S_R = -544(25)$ Jmol^{-1}K^{-1}, which results in T_{opt} = 1300 K and $\Delta_R G_0 \sim 0$ kJmol^{-1} (appendix table B.3). Hence, at 1300 K the chemical reaction is strongly exothermic and in equilibrium. Further, T_{opt} coincides with previous considerations based on $p(i)$.

Li_3RuO_4

At RT, the values for Li_3RuO_4 are ΔH^0_{298} = -1253(20) kJmol^{-1} and ΔS^0_{298} = 115(15) Jmol^{-1}K^{-1}. Further temperature-dependent values up to 1400 K are listed in the appendix table B.4. At 1300 K, the reaction has a ΔH_R = -922(30) kJmol^{-1} and a ΔS_R = -676(25) Jmol^{-1}K^{-1}, which results in a T_{opt} = 1365 K and $\Delta_R G_0 < 0$ kJmol^{-1} (appendix table B.5). These calculations indicate that for an optimum growth of Li_3RuO_4 higher temperatures are needed than for Li_2RuO_3.

Proposed reaction cycle for the growth of Li_2RuO_3 and Li_3RuO_4

Similar to Li_2IrO_3, crystal-growth experiments yielding Li_2RuO_3 and Li_3RuO_4 were conducted with the introduced experimental setup, in which the educts Li_2O(s) and RuO_2(s) are separated from each other. The assumed reaction cycle for the growth of Li_2RuO_3 and Li_3RuO_4 follows the same principle as for Li_2IrO_3 and is depicted in figure 5.2.

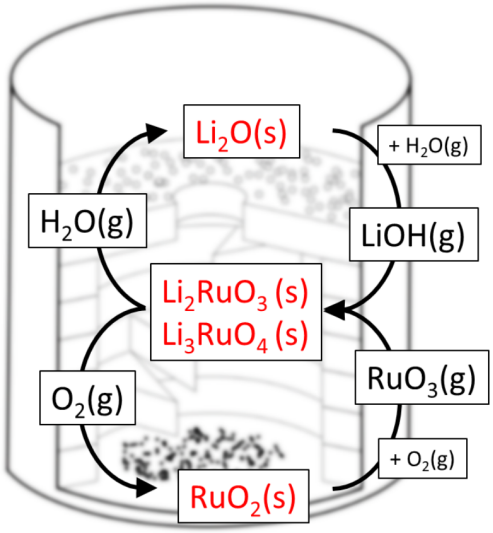

Figure 5.2: Reaction cycle for the growth of Li_2RuO_3 and Li_3RuO_4. Two separate chemical reactions, Li_2O (s) + H_2O (g) $\Leftrightarrow$ 2 LiOH (g) and RuO_2 (s) + 0.5 O_2(g) $\Leftrightarrow$ RuO_3 (g) [13, pp. 166,214] intertwine with each other to yield Li_2RuO_3 and Li_3RuO_4. The gaseous substances H_2O and O_2 can re-enter the reaction cycle.

On the basis of the previous thermodynamic considerations, growth attempts yielding Li_2RuO_3 and Li_3RuO_4 were performed and are listed in table 5.1.

Table 5.1: Growth experiments in the Li-Ru-O system including growth conditions, composition of the bottom body and grown crystals. Abbreviations: 213 (Li_2RuO_3); 314 (Li_3RuO_3); LP (plate with hole); mod: (modified). Growth attempt V7 is not listed due to furnace failure. * marks growth attempts in a second furnace.

name	T / K	Duration / d	Mass / g	Educts	Crucible	Ratio	RuO_2 / %	213 / 314 / %	Stair	Crystals	Note
V1	1273	14	0.6	Li_2O:RuO_2	T1x	1:1	100	-	LP	213	4 stairs
									2-4	213	
					T2x	3.4:1	86	14/0	LP	314	4 stairs
									4	314/213	
									1-3	213	
V2	1273	14	0.6	Li_2O:RuO_2	T1x	1:1	100	-	-	-	5 stairs
					T2x	2:1	94	6/0	2-5	213	5 stairs
					T3x	4:1	-	50/50	LP	314	2 stairs
									1-2	314/213	
					Tox	5:1	-	40/60	LP	314	1 stair
									1	314/213	
V3	1273	21	1	Li_2O:RuO_2	T1x	3:1	28	72/0	LP; 1-4	213	4 stairs
					T2x	2:1	100	-	LP	213	
									3-4	213	4 stairs
					T3x	4:1	-	40/60	LP	314/213	0 stairs, 1 ring, mod. LP
									ring	314/213	
					T4x	4:1	-	30/70	LP	314	0 stairs, 2 rings, mod. LP
									rings	314/213	
					T5x	4:1	-	50/50	LP	314	1 stair
									1	314/213	
V4	1273	21	0.8	Li_2O:RuO_2	T1x	5:1	90	10/0	LP	213	6 stairs with intermediate LP
					T3x	3:1	-	35/65	LP	213/314	reversed
					T4x	4:1	-	50/50	LP	314	1 stair, mod. LP
									1	213	
					T5x	5:1	-	80/20	4	314	6 stairs, crystal seeds

Continued on next page...

Table 5.1 – continued from previous page

name	T / K	Duration / d	Mass / g	Educts	Crucible	Ratio	RuO_2 / %	213 / 314 / %	Stair	Crystals	Note
									1-3	213	
V5	1273	14	0.6	Li_2O:RuO_2	T3x	4:1	-	35/65	LP	314	1 stair, mod. LP
									1	213	
					T4x	4:1	100	-	2-5	213	5 stairs, mod. LP
					T5x	3:1	78	22/0	1-2	213	5 stairs
					Tox	2:1	80	20/0	1-3	213	3 stairs
V6	1273	14	0.6	Li_2O:RuO_2	T3x	3:1	-	60/40	LP	314/213	1 stair, seeds
									1	213/314	
					T4x	2:1	15	85/0	LP, 2-3	213	3 stairs, half-height
					T5x	3:1	-	90/10	1;3	213/314	3 stairs, half-height
									2	213	
					Tox	4:1	-	30/70	LP	314	1 stair, mod. LP
									1	213/314	
V8*	1283	14	0.6	Li_2O:RuO_2	T4x	4:1	-	100/0	LP	213	1 stair, mod. LP
									1	213	
V9	1273	14	0.6	Li_2O:RuO_2	T3x	4:1	-	35/65	LP	213	1 stair, mod. LP
									1	213	
					T4x	4:1	-	30/70	LP	314	1 stair, mod. LP
									1	213	
					T5x	4:1	-	20/80	LP	314/213	1 stair, mod. LP
									1	213	
					Tox	4:1	-	20/80	LP	314	1 stair, mod. LP
									1	213	
V10*	1283	5	0.6	Li_2O:RuO_2	T1	4:1	85	15/0	1-4	213	time dependent
		8			T2	4:1	30	70/0	1-4	213	crystal formation
		11			T3	4:1	10	90/0	1-4	213	4 stairs
		14			T4	4:1	10	90/0	1-4	213	

5.1.2 Li_2RuO_3

Single crystals of Li_2RuO_3 were grown at 1273 K with a duration of 14 days, a starting Li_2O:RuO_2 ratio of 4:1, and a distance of 2.8 cm between RuO_2 at the bottom and Li_2O at the top (figure 5.3). Various growth attempts showed that lower educt ratios also led to the growth of Li_2RuO_3 crystals but of smaller amount and size (table 5.1, V3T1x 3:1 and T2x 2:1). Changes in the setup, *e.g.* in the distance between the educts or their position (V4), did not lead to an optimised growth of Li_2RuO_3 crystals. Further, the implementation of seed crystals did not yield larger size but preferred growth of new crystal seeds on the top of the crystal surface.

Single crystals of Li_2RuO_3 either grew isometric or as plates. Isometric crystals grew on all stairs of the setup with a maximum size of 500 µm (figure 5.3a,b). The morphology of isometric crystals is determined by crystal faces of types $\{110\}$ and $\{011\}$. However, slight differences between grown crystals are noted. Most crystals exhibit crystal faces of similar size, which indicates a similar growth velocity. These crystals are identified by its sharp corner at the tip of the crystal reaching into the reaction chamber (figure 5.3a). In some cases, an edge is observed at the tip of the crystal (figure 5.3b), which results from different sizes of crystal faces and points towards a different growth velocity of one of the types of crystal faces.

Platy crystals grew on the lowest stair and their respective surrounding ring with a maximum size of 300 µm (figure 5.3c,d). As for platy crystals of α-Li_2IrO_3, their largest crystal face is (001), which corresponds to the 2D honeycomb plane in the crystal structure. Further, it presents the crystal face with slowest growth velocity. The morphology of platy crystals further depends on the growth velocity of the crystal faces of types $\{110\}$ and $\{010\}$. If the growth velocity was equal, an almost hexagonal shape of the platy crystal resulted (figure 5.3c). If the growth velocity of one of these types of crystal faces, *e.g.* $\{010\}$, was faster than of the other type, an almost rhombus-shaped crystal was formed (figure 5.3d).

In contrast to the Li-Ir-O system, in which two modifications with honeycomb-related structures, α- and β-Li_2IrO_3, were grown by the CVTR method, only one type of Li_2RuO_3 crystals was observed. By applying high Li concentrations in the Li-Ru-O system, dendritic crystals grew and were characterised as Li_3RuO_4 by P-XRD. This in further contrast to the Li-Ir-O system, where dendritic α-Li_2IrO_3 grew at high Li concentrations. Crystal growth investigations on Li_3RuO_4 are discussed in the upcoming section 5.1.3.

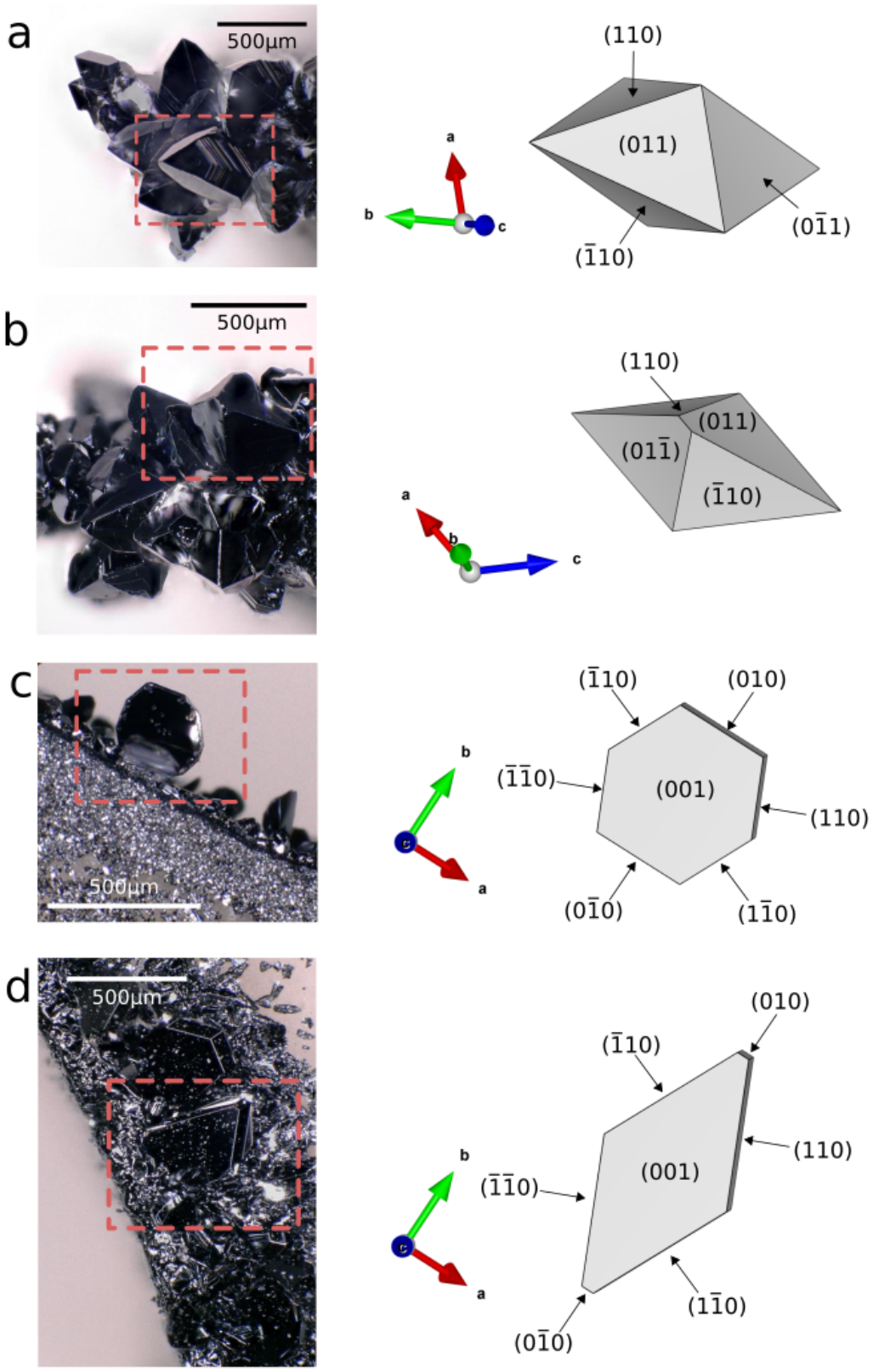

Figure 5.3: Comparison of crystals of Li_2RuO_3 (left) and morphology calculated from the crystal metric (right). (a, b) Isometric crystals are defined by crystal faces of types {110} and {011}. (c,d) Platy single crystals are mostly characterised by their large (001) crystal face. Red dashed boxes on the left side mark the crystals whose morphology is shown schematically on the right side.

Time-dependent crystallisation process of Li_2RuO_3

To understand the crystallisation process of Li_2RuO_3, time-dependent experiments were performed following the same procedure as described for α-Li_2IrO_3. The experiments were conducted with a starting Li_2O:RuO_2 ratio of 4:1. Crucibles were removed after 5, 8, 11, and 14 days (figure 5.4). Due to the failure of the first muffle furnace, time-dependent experiments were performed in the second furnace and, hence, at a set-point temperature of 1283 K (section 2.2.4). In comparison to previous experiments, the amount of grown crystals was smaller, which is explained by the usage of the second furnace, which exhibits an higher air movement.

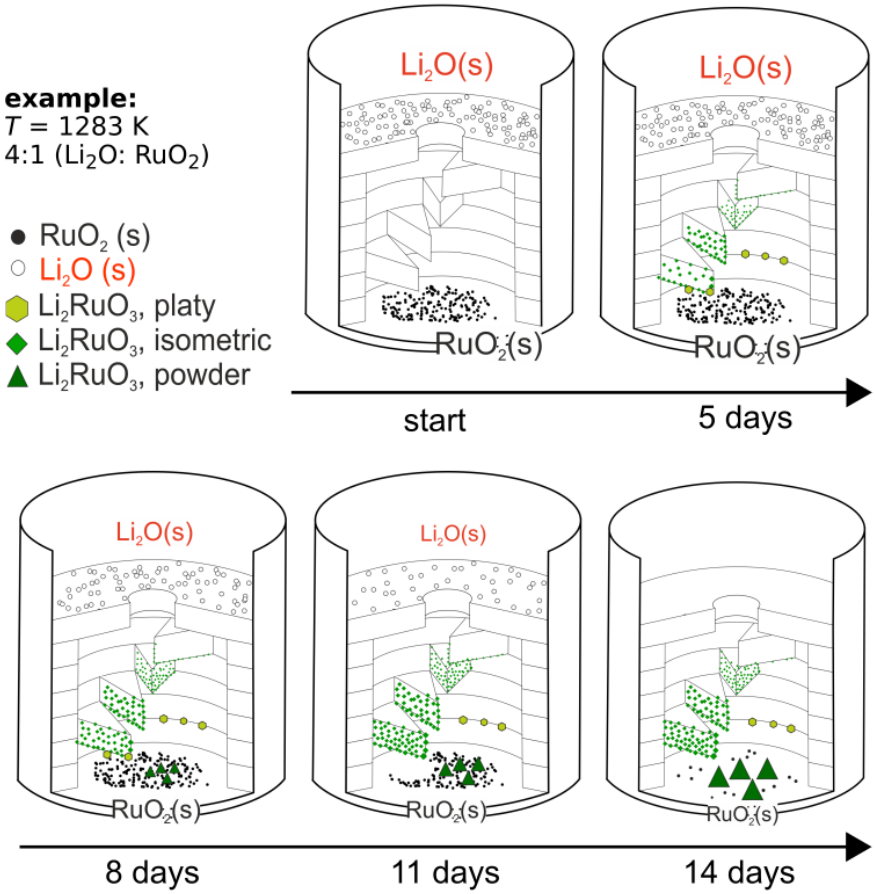

Figure 5.4: Time-dependent crystallisation process of a crystal-growth experiment yielding Li_2RuO_3 at 1283 K with a starting Li_2O:RuO_2 ratio of 4:1. Time steps after 5, 8, 11 and 14 days show the change of educts and the growth of different morphologies of Li_2RuO_3. Increasing sizes of symbols show an increase in size/amount of phase on the stairs and in the Ru body, respectively.

At the beginning of the crystallisation process, only RuO_2(s) and Li_2O(s) were present. After five days, the growth of Li_2RuO_3 was observed (figure 5.4). Crystallisation mainly took place at the rim of the stairs. Isometric crystals grew on all stairs of the crucible but mostly on the second-lowest stair.

In contrast, platy single crystals only grew on the lowest stair and on the respective surrounding rings. This is in difference to previous observations on the growth of platy crystals of α-Li_2IrO_3, which only grew on the topmost stair of the crucible. With time, platy crystals of Li_2RuO_3 increased in their size or grew on other positions within the crucible. The amount and size of isometric crystals increased with decreasing distance to the Ru body. On the topmost stair, almost no single crystal growth occurred.
Results from P-XRD analysis revealed a time-dependent change in composition of the Ru bottom body. After 8 days, the Ru bottom body consisted of 30 % RuO_2 and 70 % Li_2RuO_3. With time, the Li_2RuO_3 fraction increased with a simultaneous decrease of the RuO_2 fraction. After 14 days, the Ru body consisted of 90 % Li_2RuO_3 and 10 % RuO_2, and Li_2O was depleted (figure 5.4).

5.1.3 Li_3RuO_4

In the literature, different synthesis approaches did not lead to the successful growth of single crystals but only of polycrystalline material of Li_3RuO_4 [2, 21, 43, 120]. In the present work, first Li_3RuO_4 crystals were observed. Crystallisation took place underneath the plate with hole during a growth attempt at 1273 K with a Li_2O:RuO_2 ratio of 3.4:1 (table 5.1, figure 5.5a,b). Simultaneously, the growth of Li_2RuO_3 was observed on the stairs. By combining a higher ratio and a shorter distance, *i.e.* increasing the Li concentration in the growth setup, a higher amount of Li_3RuO_4 crystals grew underneath the plate with hole (figure 5.5a,b). Thus, a modified plate with hole was built from Al_2O_3 parts. Three additional slim spikes were glued to the bottom side of the plate with hole pointing into the middle of the hole (figure 5.5c). This created additional preferred crystallisation sites and resulted in an increased amount of Li_3RuO_4 crystals.
The largest amount of Li_3RuO_4 crystals occurred in a experiment at 1273 K with a Li_2O:RuO_2 ratio of 4:1 and a distance of 1.6 cm between RuO_2 and Li_2O (V5T3x). The distance results from one stair, which was placed in between two rings. To optimise the crystal growth, different arrangements of Al_2O_3 parts were tried. As an example, the distance between the educts was varied by using different amounts of spacers (rings/stairs). The variety of growth attempts showed that crystals of Li_3RuO_4 are of small size and always grow in the presence of larger Li_2RuO_3. This observation can be explained by non-optimised growth conditions for the growth of Li_3RuO_4 due to the low growth temperature of 1273 K compared to the calculated T_{opt} = 1365 K. In contrast, for Li_2RuO_3 the calculated T_{opt} is 1300 K, which explains the favoured growth of Li_2RuO_3. In growth attempt V5T3x, a separated growth of both compounds was yielded. Whilst Li_3RuO_4 grew at the modified plate with hole, crystal growth of Li_2RuO_3 was observed on the separating stair between both educts. By respecting the stoichiometric fractions of Li and Ru of both compounds, Li_3RuO_4 requires a lower fraction of Ru compared to Li_2RuO_3. This might explain the preferred growth of Li_2RuO_3 at the separating stair due to its increased requirement for Ru compared to Li_3RuO_4. Reversely, the growth of Li_3RuO_4 close to the Li educt might be explained by its higher requirement of Li compared to Li_2RuO_3. By combining these considerations with observations on the growth, the separating stair seems to play a

crucial role for the separated growth of Li_3RuO_4 at the modified plate and Li_2RuO_3 at the lower stair. By applying lower concentrations, (almost) no growth of Li_3RuO_4 but of Li_2RuO_3 was observed, which again indicates the requirement of a higher Li concentration for the growth of Li_3RuO_4 than for Li_2RuO_3. Longer experiments did not yield an increased size or amount of Li_3RuO_4 crystals. Higher Li concentrations did not lead to an increased size but amount of crystals. Another approach implied the slowdown of the growth process by increasing the distance between the educts to six stairs and increasing the ratio of educts to 5:1 (V4T1x). Here, only the growth of Li_2RuO_3 was yielded.

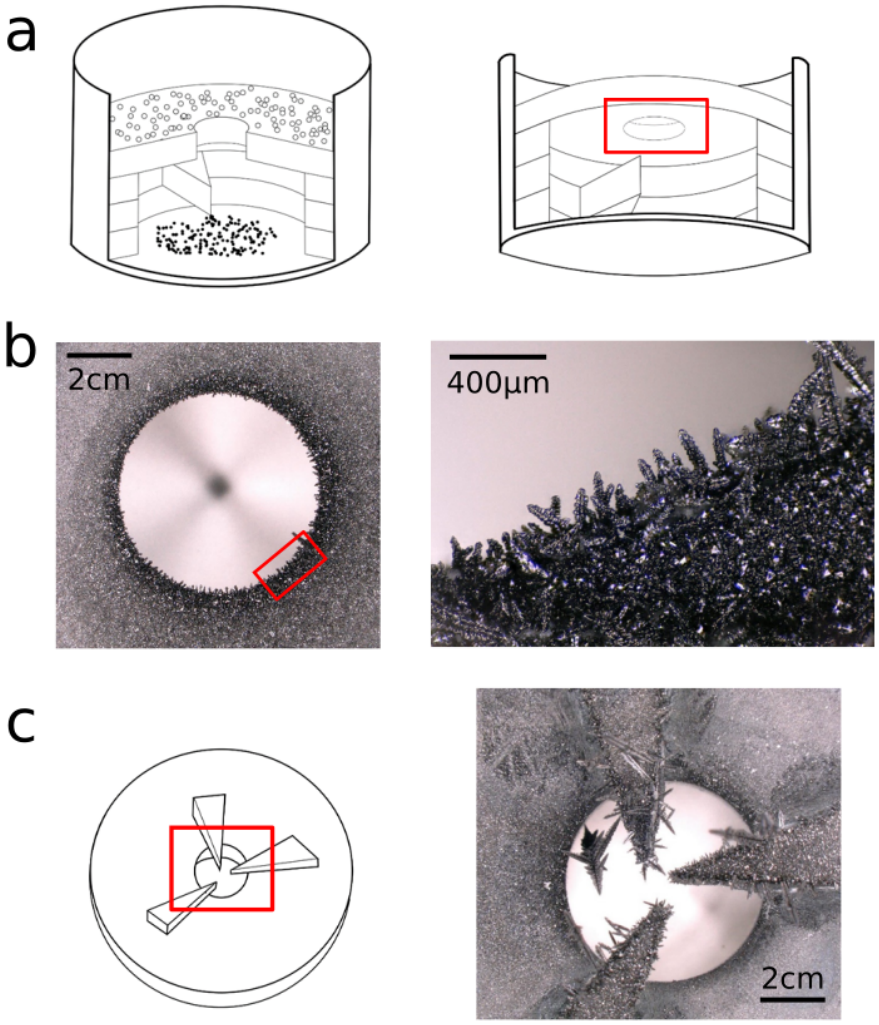

Figure 5.5: Crystal growth of Li_3RuO_4. (a) The general construction of the setup consists of two rings and one stair with a distance between RuO_2 and Li_2O of 1.6 cm. (b) First Li_3RuO_4 grew underneath the plate with hole, see red boxes in (a) and (b). (c) Modified plate with hole with three spikes, enhancing crystallisation of Li_3RuO_4 (right).

5.1.4 Bottom-body formation process

Investigations of the Ru bottom body showed that its composition mostly depends on the ratio and the composition of grown crystals. If the ratio of the educts was too low, *e.g.* 1:1 or 2:1, or the distance between the educts was too high (table 5.1; V2/V4T1x), almost no reaction between the educts took place, which resulted in a RuO_2 bottom body. In experiments yielding Li_2RuO_3, the bottom body consisted of RuO_2 and Li_2RuO_3, whereas the amount of RuO_2 decreased with the duration of the experiment but never reached zero (table 5.1; V10). In contrast, in experiments yielding Li_3RuO_4, the bottom body consisted of 30 % Li_2RuO_3 and 70 % Li_3RuO_4 with no trace of RuO_2 (V9).

5.2 Material characterisation

5.2.1 Structural aspects

As for Li_2IrO_3 compounds, the first structural classification of lithium ruthenates was carried out by P-XRD. Detailed discussions on the reported structural models of Li_2RuO_3 and the distinction of their P-XRD pattern based on systematic absences were given in the introductory section 1.1.2.1. Further, the requirement for high-quality SC-XRD data to obtain the crystal structure of Li_2RuO_3 was emphasised. The crystal structure of Li_3RuO_4 was confirmed by P-XRD.

5.2.1.1 Li_2RuO_3

The crystal structure of Li_2RuO_3 was solved and refined in space group $P2_1/m$. Instrumental details were given in section 3.1.1.2. The refinement results and measurement details are listed in table 5.2. All atomic displacement parameters were refined anisotropically and are listed in appendix table B.12. Further information on bond distances and BVS are listed in the appendix table B.13.
In figure 5.6, the crystal structure of $P2_1/m$, which was obtained in the present work, is depicted. Edge-sharing RuO_6 octahedra build up the 2D honeycomb structure. In each honeycomb center a Li1 atom is situated (figure 5.6a). In between the mixed metal $LiRu_2$ layers, Li2/Li3 atoms build up a Li atomic layer (figure 5.6b). The honeycomb ring, which consists of edge-sharing RuO_6 octahedra, is characterised by its unequal Ru-Ru distances a_1, a_2 and a_3 leading to Ru dimerisation (figure 5.6c, table 5.3).

Table 5.2: Structural model of Li_2RuO_3 ($P2_1/m$) of the present work including measurement details, lattice parameters (a, b, c, β), cell volume V, atomic positions with Wyckoff site symmetry, and fractional coordinates (x, y, z). Further information like anisotropic atomic displacement parameters for all atom sites, bond valence sums, bond distances and bond angles are found in the appendix.

Li_2RuO_3	
Space group	$P2_1/m$
Z	4
a, b, c, β	4.9132(3) Å, 8.7686(6) Å, 5.8790(7) Å, 124.360(2)°
V	209.08(2) Å^3
ρ_{calc}	5.177 g cm^{-3}
T	120(2) K
Radiation wavelength	0.71073 Å
Crystal information	
Colour/shape	metallic black, prism
Size	0.126 mm x 0.160 mm x 0.162 mm
Growth conditions	CTR, 1273 K, 21 days, Li_2O:Ir ratio 5:1, growth on staircase
Data collection	
Θ range	4.37° to 30.04°
Independent reflections	327
R_{int}	0.0314
Data reduction	
Absorption correction	numerical
μ	7.159 mm^{-1}
F(000)	296
Refined parameters	62
Final R-values with I > 2σ(I)	
R_1	0.0163
w_{R2}	0.0494
GOF on F^2	1.353

Structure solution and refinement: SHELXT-2014/5 [114] , SHELXL-2018/3 [115]

Atom	Site	x	y	z
Ru1	4f	0.27515(5)	0.07683(2)	-0.00402(3)
Li1	2e	0.7668(15)	0.25	-0.0084(11)
Li2	4f	0.2620(11)	0.0931(8)	0.4920(8)
Li3	2e	0.7652(17)	0.25	0.5131(12)
O1	4f	0.7582(6)	0.0830(2)	0.2555(5)
O2	4f	0.7772(6)	0.0781(2)	0.7721(5)
O3	2e	0.2617(7)	0.25	0.2192(6)
O4	2e	0.2750(7)	0.25	0.7656(6)

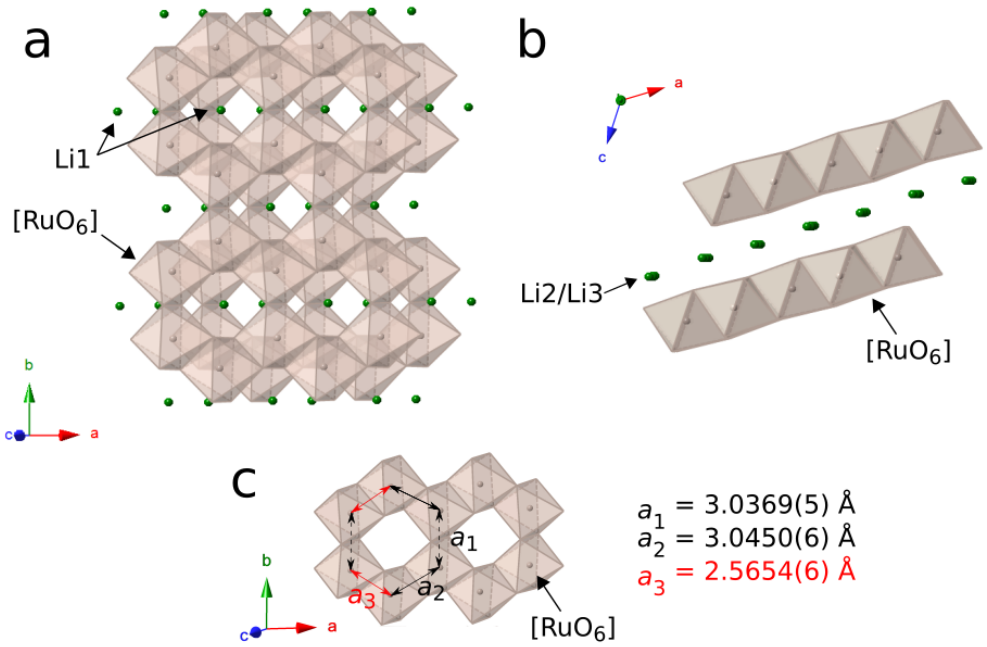

Figure 5.6: Crystal structure of Li_2RuO_3 ($P2_1/m$). (a) Edge-sharing RuO_6 octahedra (grey) build up the 2D honeycomb structure of Li_2RuO_3. In each honeycomb center Li1 atoms (green) are situated and build up edge-sharing LiO_6 octahedra. (b) In between the mixed metal layers, Li2/3 atoms (green) form a Li atomic layer. (c) In the honeycomb ring, the Ru-Ru distances a_1, a_2, and a_3 are unequal. The simplified structural visualisations neglect the depiction of the atomic O positions and LiO_6 octahedra.

In table 5.3, the Li_2RuO_3 structures ($P2_1/m$) of the present work and of Miura et al. [76] are compared. The small deviation of lattice parameters on the second decimal place is explained by different measurement temperatures. The comparison of fractional coordinates of atomic positions shows deviations on the second decimal place for Li and O and on the third decimal place for Ru. Due to the high similarity, the Ru-Ru distances in the honeycomb rings coincide for both structures with a maximum deviation between the longest and shortest distance (a_2-a_3)/a_3 of 18.7 % (table 5.3, figure 5.6c). This shows Ru dimerisation in Li_2RuO_3 single crystals grown by the CVTR method. Ergo, the dimerised phase of Li_2RuO_3, which was reported by Miura et al. [76], is confirmed. Structural investigations did not find the non-dimerised $C2/m$ phase, which coincides with its suggested stability at $T > 540$ K [76] and low measurement temperatures of 120 K.

The largest difference between fractional coordinates of atomic positions of both structural models is found for Li1, which is situated in the honeycomb center and builds up a mixed-metal layer with Ru1 (figure 5.6). Here, the z-coordinate differs between z = -0.068(2) in [76] and z = -0.0084(11) in the present work. Since the latter coordinate is close to the z-coordinate of Ru1 atoms (z = -0.00402(3), table 5.2), it is considered as more reasonable. This difference leads to a lower GII for the structural model of the present work (GII: 0.146, appendix table B.13) than for the one reported by Miura et al. [76] (GII: 0.206, appendix table B.11).

Table 5.3: Comparison of lattice parameters a, b, c, β, global instability indices (GII) and Ru-Ru distances of the structural model of Li_2RuO_3 ($P2_1/m$) of the present work and of Miura et al. [76].

	Li_2RuO_3	
	present work	Miura et al. [76]
Space group	$P2_1/m$	$P2_1/m$
a / Å	4.9132(3)	4.9210(2)
b / Å	8.7686(6)	8.7829(2)
c / Å	5.8790(7)	5.8941(2)
β / °	124.360(2)°	124.342(2)
GII	0.146	0.206
T / K	120(2)	298
Method	SC-XRD	P-ND
GOF	1.35	1.36
Ru-Ru distances		
a_1 / Å	3.0369(5)	3.045
a_2 / Å	3.0450(6)	3.049
a_3 / Å	2.5654(6)	2.568
$(a_2$-$a_3)/a_3$ / %	18.7	18.7

5.2.1.2 Li_3RuO_4

The crystal structure of Li_3RuO_4 ($P2/a$) was previously described in the introductory part in section 1.1.2.2 and is depicted in figure 1.7. In the literature, two structural models of Li_3RuO_4 with space group $P2/a$ were reported (table 5.4) [2, 43].

Both structural models are listed in appendix tables B.14 and B.15. The calculation of BVS revealed a strong difference in GII for both structures (table 5.4). Whilst the GII of the structural model by Jacquet et al. [43] is rather low (0.08), the GII of the structure by Alexander et al. [2] is 0.13 (appendix tables B.16 and B.17). Mostly, this can be explained by slight deviations in fractional coordinates of O1 and O2 in the structural model of Jacquet et al. [43], which leads to more reasonable Li – O and Ru – O bond lengths and, hence, to less distorted LiO_6 and RuO_6 octahedra. Further, due to Li/Ru mixing in the structure of Alexander et al. [2], *e.g.* Li3/Ru3, the deviation from the ideal BVS sum is larger, which yields a larger GII.

Table 5.4: Lattice parameters a, b, c, β, unit cell volume V, global instability indices (GII), diffraction method (P-XRD: powder X-ray diffraction; P-ND: powder neutron diffraction), and Goodness of Fit of refinement (GOF) of Li_3RuO_4 ($P2/a$) derived from the present work and from Alexander et al. [2] and Jacquet et al. [43].

Composition	Li_3RuO_4 present work	Li_3RuO_4 Jacquet et al. [43]	$Li_{2.81(2)}Ru_{1.04(2)}O_4$ Alexander et al. [2]
Space group	$P2/a$	$P2/a$	$P2/a$
a / Å	5.0828(2)	5.08487(3)	5.1057(1)
b / Å	5.8665(2)	5.87207(3)	5.8545(1)
c / Å	5.1243(2)	5.12450(2)	5.1062(1)
β / °	110.190(3)	110.2130(4)	110.039(1)
V / Å^3	143.410(11)	143.5878	143.689(6)
GOF	1.84	2.20	1.672
GII	0.22	0.08	0.13
Diffraction method	P-XRD	P-ND	P-ND
ICSD Coll Code	-	243927	99333

As described in section 5.1.3, Li_3RuO_4 was grown by the CVTR method. However, due to their dendritic growth and small size, no suitable single crystal for SC-XRD could be selected. Therefore, the structural refinement was carried out based on P-XRD data collected in reflection geometry (figure 5.7). Measurement parameters were given in section 3.1.1.1. Next to the Li_3RuO_4 phase, a small amount of phase impurity was found. Since the 2Θ values of the reflections of the phase impurity do not overlap with those of Li_3RuO_4, the impurity phase did not have an influence on the structural refinement of Li_3RuO_4. The phase impurity is assumed to be a lithium aluminate compound, which was collected next to Li_3RuO_4 crystals during sample preparation from the glued parts of the modified plate. However, its precise assignment was not possible.

The first refinement step of P-XRD data was carried out with a *hkl* phase to assign the peak positions to the Li_3RuO_4 phase. An additional peaks phase with three peak positions was added to the refinement range to prevent the influence of the impurity phase on the subsequent data refinement (figure 5.7). The lattice parameters of the refined *hkl* phase are in closer similarity to those of Jacquet et al. [43] than of Alexander et al. [2]. The refinement of the *hkl* phase resulted in a GOF of 1.67. Further refinement was carried out on the basis of the structural model by Jacquet et al. [43]. The refined structure and calculated BVS of Li_3RuO_4 are listed in appendix tables B.18 and B.19.

In comparison to the fractional coordinates of atomic positions of Jacquet et al. [43], in the present work the calculated errors are one order of magnitude larger. Further, the Li and O atomic positions differ at the second decimal place from the ones by Jacquet et al. [43]. These differences are explained by the applied diffraction methods. In contrast to the refinement based on P-XRD data, Jacquet et al. [43] and Alexander et al. [2] collected P-ND data, which gives more plausible results. Since Alexander et al. [2] reported the shared occupancies of some atomic positions, their refinement was also attempted in the present work. Since this led to negative SOFs and ADPs, the refinement of site occupancies could not be obtained from P-XRD in the present work.

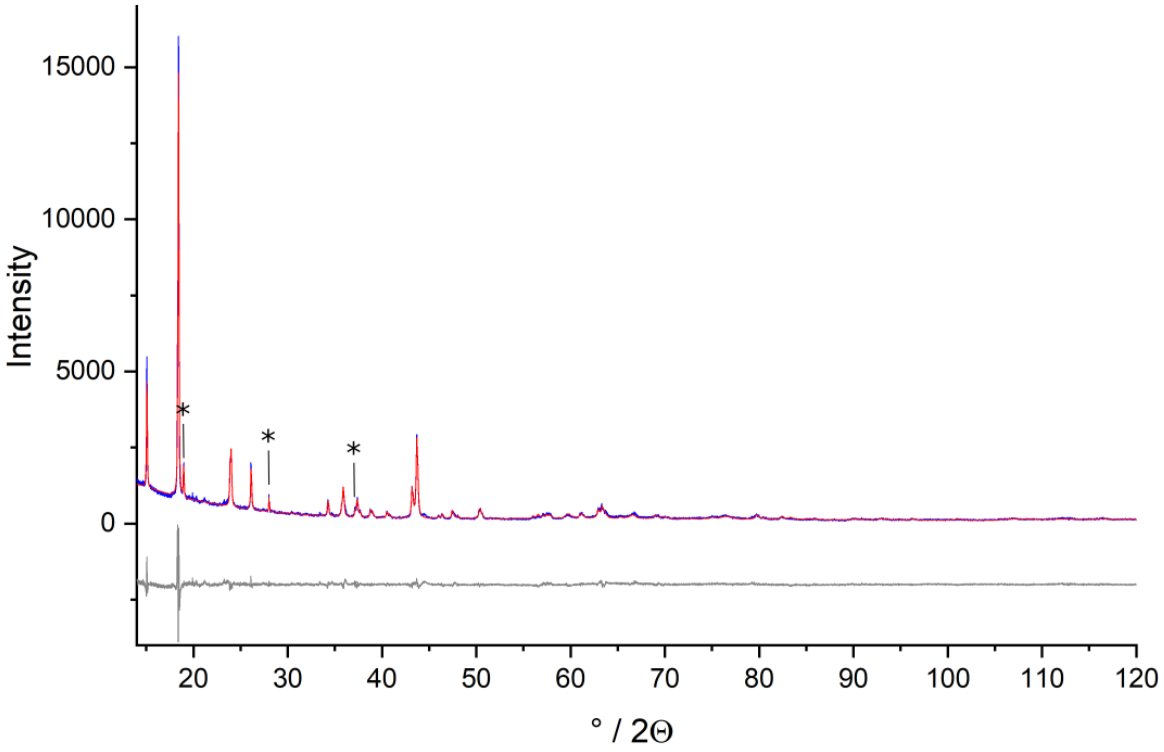

Figure 5.7: Powder X-ray diffraction pattern of Li_3RuO_4 crystals grown by the CVTR method in the 2Θ range between 14° and 120 °. The blue line represents the measured data, the red line the calculated intensities based on the structural model and the grey line the difference curve. The three peak positions marked with an asterix are assigned to an impurity phase.

In section 1.2.2, the antiferromagnetic ordering of Li_3RuO_4 was described [2, 121], which is characterised by inter- and intrachain interactions of Ru atoms. The interactions are strongest for shortest Ru-Ru distances [121]. Due to only small deviations in Ru fractional coordinates and similar Ru-Ru distances (appendix table B.20), the structural requirement for the proposed antiferromagnetic behaviour is given in Li_3RuO_4 crystals of the present work.

5.2.2 Chemical instability

Comparable to Li_2IrO_3 crystals, single crystals of Li_2RuO_3 and Li_3RuO_4 reacted with ethanol, C_2H_5OH, and/or ethyleneglycol, $C_2H_4(OH)_2$. The reactivity of Li_3RuO_4 was significantly higher than the reactivity of Li_2RuO_3. This might be explained by the less interconnected Li atoms in the structure of Li_3RuO_4 and, hence, an assumed higher mobility of Li. These considerations coincide with the ones for Li_2IrO_3.

5.2.3 Elemental analysis

Thoroughly polished crystals of Li_2RuO_3 and Li_3RuO_4 were investigated by EDX regarding their crystal homogeneity by measuring Ru and O quantities. For a Li_2RuO_3 compound the ideal O/Ru ratio is 3.0, whereas for Li_3RuO_4 the ideal value is 4.0. The presented and discussed data are in the area of reliability (section 3.3.1).

5.2.3.1 Li_2RuO_3

Single crystals of Li_2RuO_3 grew in different morphologies (section 5.1.2). In figure 5.8, a crystal face of type {110} or {011} of an isometric crystal is shown. During polishing, a thin layer of the crystal was removed and the break off of crystal margins was observed. Therefore, the delimitation of the shown crystal does not coincide with its sharp corners and edges. In isometric Li_2RuO_3, a homogeneous distribution of O and Ru is observed with a slightly lower incorporated Ru amount than expected for a composition of Li_2RuO_3.

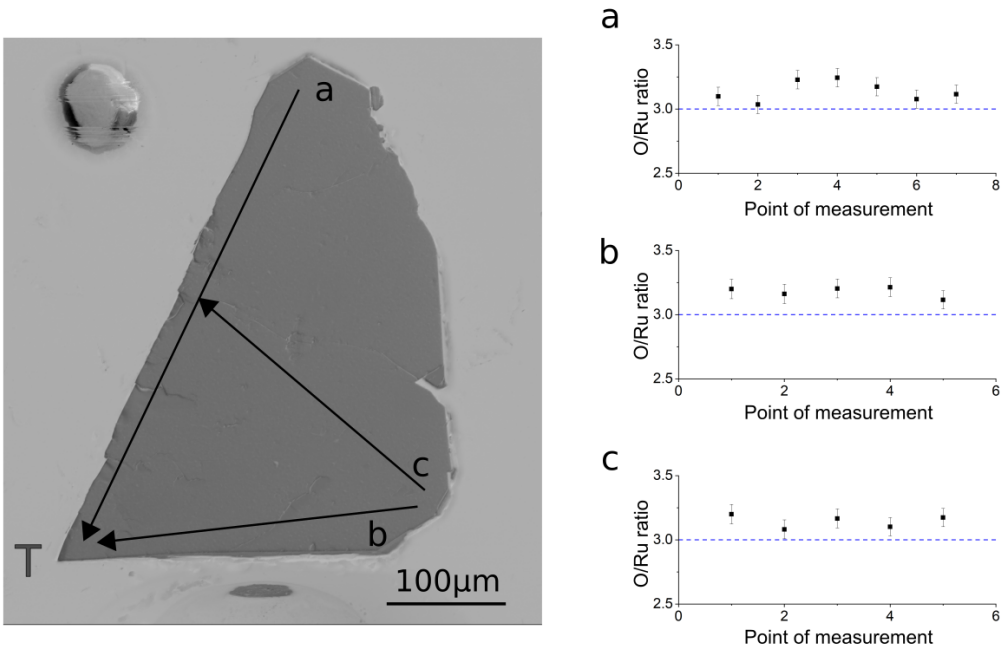

Figure 5.8: SEM image and element distribution of Ru and O of (a-c) isometric and (d) platy Li_2RuO_3 with a side face of type {110} or {011}. T marks the top of crystal pointing into the growth chamber and S marks the point of attachment to the Al_2O_3 setup. The blue-dashed lines mark the expected O/Ru ratio.

The polishing of platy single crystals was challenging, since the crystals preferred to break off at the rims and, subsequently, scratched themselves. Due to the uneven surface, between the points of measurement the relative values of the O/Ru ratio differ from each other. However, in absolute terms the O/Ru ratios coincide with each other and are within the errors (figure 5.9). Hence, EDX analysis of the (001) face of platy single crystals shows homogeneity. No difference in composition

was detected between the point of attachment on the Al_2O_3 setup and the remaining crystal surface. This observation is in contrast to platy α-Li_2IrO_3 and indicates homogeneous conditions during the growth of platy Li_2RuO_3 crystals.

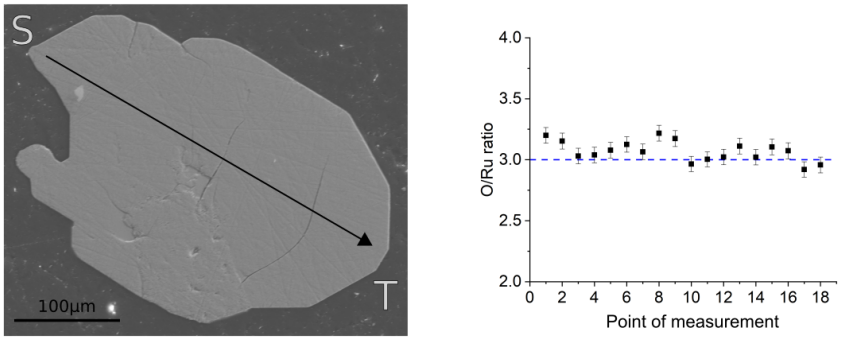

Figure 5.9: SEM image and element distribution of Ru and O of platy Li_2RuO_3 with large (001) crystal face. T marks the top of crystal pointing into the growth chamber and S marks the point of attachment to the Al_2O_3 setup. The blue-dashed line marks the expected O/Ru ratio.

5.2.3.2 Li_3RuO_4

The polishing of Li_3RuO_4 crystals was significantly more challenging than of Li_2RuO_3 crystals so that no perfectly polished surface was obtained. This is reflected in variations in the O/Ru ratio (figure 5.10). As for platy Li_2RuO_3, the absolute values of the O/Ru ratio are within the errors. Hence, crystals of Li_3RuO_4 are defined as homogeneous. A deviation from the ideal composition Li_3RuO_4 to $Li_{2.81}Ru_{1.04}O_4$ [2] could neither be confirmed nor refuted by EDX due to its poor precision.

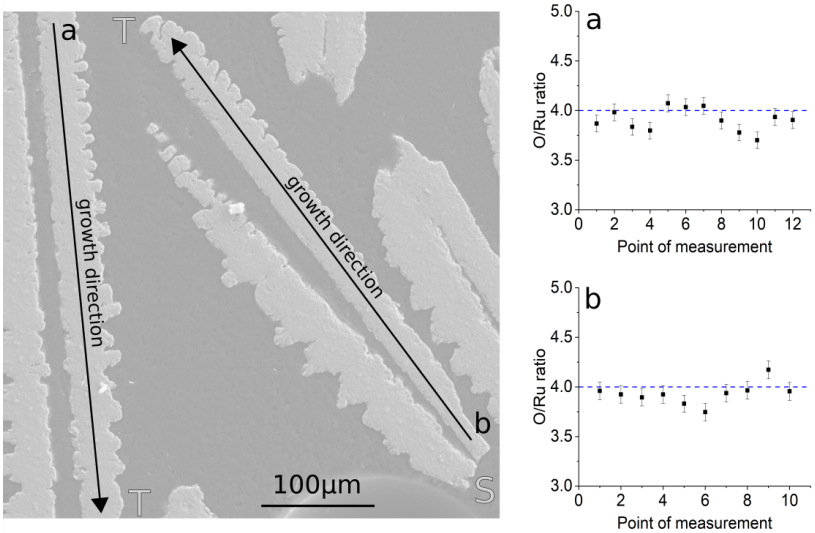

Figure 5.10: SEM image and element distribution of Ru and O in Li_3RuO_4. T marks the top of crystal pointing into the growth chamber and S marks the point of attachment to the Al_2O_3 setup. The blue-dashed line marks the expected O/Ru ratio.

5.2.4 Thermal analysis

5.2.4.1 Decomposition reaction of Li_3RuO_4

DTA measurements on Li_3RuO_4 show a strong endothermic reaction during the heating sequence ($T_{onset} \approx 1533$ K) and an exothermic reaction during the cooling sequence ($T_{onset} \approx 1433$ K, figure 5.11). Subsequent P-XRD analysis revealed a Li_2RuO_3/Li_2O mixture. Hence, during the heating sequence the following decomposition reaction is assumed:

$$Li_3RuO_4(s) \Leftrightarrow Li_2RuO_3(s) + 0.5\ Li_2O(s) + 0.25\ O_2(g)$$

The observed exothermic reaction during cooling might be explained by a partial reaction of Ru with the Pt crucible, which was already observed in the Li-Ir-O system (section 4.2.4).

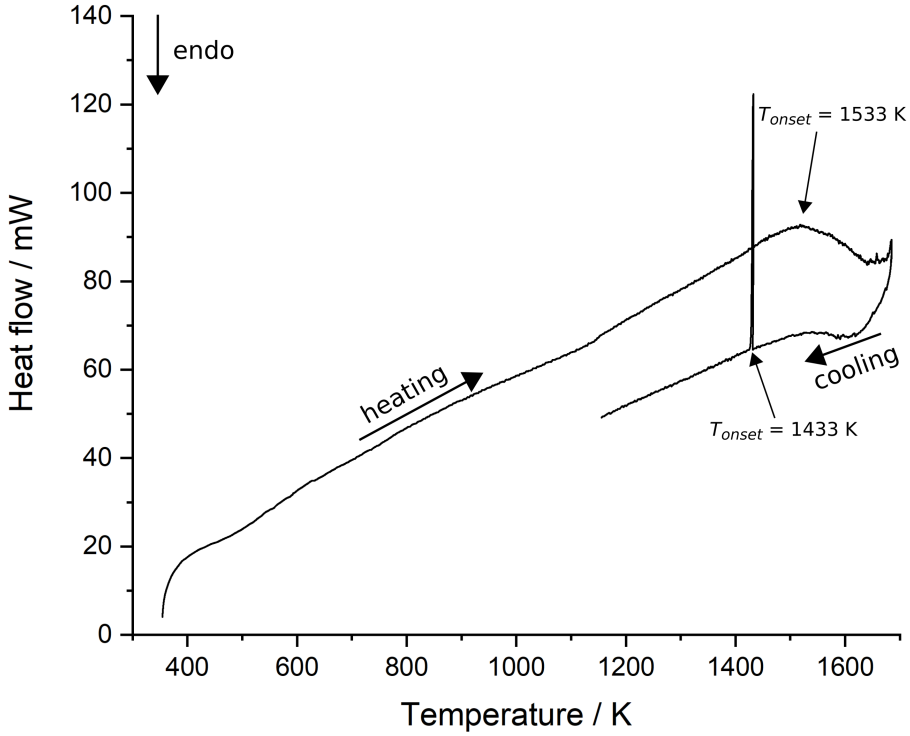

Figure 5.11: DTA measurement of Li_3RuO_4 with an endothermic reaction during the heating cycle at $T_{onset} \approx 1533$ K and an exothermic reaction during the cooling cycle at $T_{onset} \approx 1433$ K.

5.2.4.2 Thermal behaviour of Li_2RuO_3

In two recent studies of Miura et al. [76, 75], for polycrystalline Li_2RuO_3 a structural phase transition was reported at 540 K between the $C2/m$ (HT) and the $P2_1/m$ (LT) phase (section 1.1.2.1). In contrast, Wang et al. [130] reported the absence of a phase transition in single crystals, which were grown from Na_2CO_3 and RuO_2 but at higher temperatures than applied for the synthesis of polycrystalline Li_2RuO_3 in Miura et al. [76]. Hence, Wang et al. [130] assumed a dependency of the phase transition

on the synthesis conditions. Since in the present work single crystals of Li_2RuO_3 were grown by the CVTR method and this adds another synthesis method, their thermal behaviour was investigated by DTA and DSC measurements. DTA analysis in a temperature range up to 1720 K did not show a thermal event. P-XRD data of the sample confirmed the preservation of space group $P2_1/m$. Therefore, an irreversible phase transition could be excluded. In a subsequent DSC measurement, neither in the DSC curve nor in its first derivative a thermal event was observed. Therefore, in accordance with the results of Wang et al. [130], in the present work the occurrence of a structural phase transition in single crystals of Li_2RuO_3 could not be observed.

Chapter 6

Li-Ir-Ru-O system

In the Li-Ir-Ru-O system of APGMOs, polycrystalline $Li_2Ir_{1-x}Ru_xO_3$ is reported in the literature [67]. In the introductory section 1.1.3 the temperature-dependent structural complexity of the end members of $Li_2Ir_{1-x}Ru_xO_3$ was discussed and turns its crystal growth and structural investigation into a field of interest. In the present work, the crystal growth of $Li_2Ir_{1-x}Ru_xO_3$ by the CVTR method is examined and followed by structural and elemental analysis of obtained crystals.

6.1 Crystal-growth investigations

In the Li-Ir-Ru-O system of APGMOs, growth investigations of $Li_2Ir_{1-x}Ru_xO_3$ by the CVTR method are aimed. As for previous growth systems, prior to the conduction of experiments thermodynamic considerations were made to determine optimum growth conditions.

6.1.1 Thermodynamic considerations

Since single crystals of both, α-Li_2IrO_3 and Li_2RuO_3, were grown by the CVTR method, crystal growth of $Li_2Ir_{1-x}Ru_xO_3$ was attempted using the similar setup. Based on the assumed transport reactions of Li_2O, Ir, and RuO_2, the reaction cycle for CVTR experiments in the Li-Ir-Ru-O system is suggested as for α-Li_2IrO_3 and Li_2RuO_3. The three transport-effective species (LiOH, IrO_3, and RuO_3) are assumed to undergo a joint reaction to yield $Li_2Ir_{1-x}Ru_xO_3$ (figure 6.1). The following chemical reaction is expected:

$$2\ \mathrm{LiOH\ (g)} + 1\text{-}x\ \mathrm{IrO_3(g)} + x\ \mathrm{RuO_3(g)} \Leftrightarrow \mathrm{Li_2Ir_{1-x}Ru_xO_3\ (s)} + \mathrm{H_2O(g)} + 0.5\ \mathrm{O_2(g)}$$

Previous considerations showed different temperature-dependent transport behaviour of LiOH, IrO_3, and RuO_3 (sections 4.1.1 and 5.1.1). For reaching transportability ($p(i) \geq 10^{-5}$ atm) the required minimum temperatures of the gaseous phases differ. Whilst LiOH(g) and IrO_3(g) achieve this value at $T \geq 1205$ K, RuO_3(g) requires $T \geq 1300$ K. Hence, the Li-Ir-Ru-O system represents a complex growth system with different $p(i)$ behaviour of its gaseous phases.

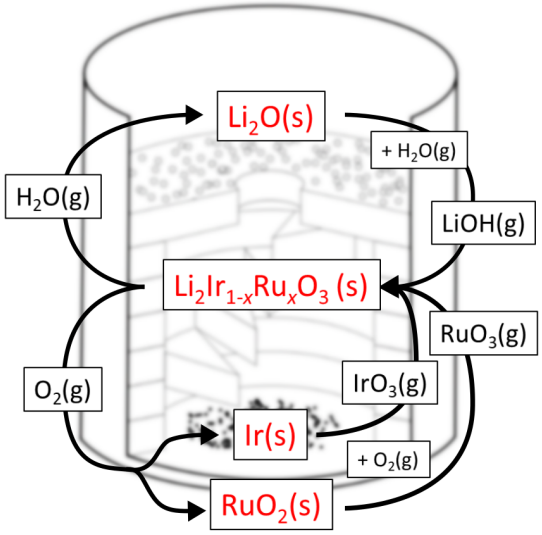

Figure 6.1: Reaction cycle for the growth of $Li_2Ir_{1-x}Ru_xO_3$. Three separate chemical reactions, Li_2O (s) + H_2O (g) $\Leftrightarrow$ 2 LiOH (g), Ir (s) + 1.5 O_2(g) $\Leftrightarrow$ IrO_3 (g), and RuO_2 (s) + 0.5 O_2(g) $\Leftrightarrow$ RuO_3 (g) [13, pp. 166, 214, 217] intertwine with each other to yield $Li_2Ir_{1-x}Ru_xO_3$. The gaseous substances H_2O and O_2 can re-enter the reaction cycle.

CVTR experiments with differences in $p(i)$ were already discussed in the literature, *e.g.* for the ZnS - CdS system [104]. Here, growth attempts were conducted in a setup with separated chambers for the educts. To realise optimum transport temperatures at different times and the evaporation of compounds at distinct times the setup was movable. According to Reimers [104], the $p(i)$ for the transport of CdS is larger than the one for the transport of Zns. Hence, at lower temperatures the sublimation was limited to CdS, whereas with elevated temperatures ZnS was sublimated [104]. With this method, graded crystals of $Zn_{1-x}Cd_xS$ were grown, which is explained by the different $p(i)$ of the transport-effective species. This growth investigations emphasised the influence of different $p(i)$ of gaseous phases on the growth by the CVTR method.

In difference to the study by Reimers [104], the experimental setup in the present work is neither suitable for the separation of educts into different temperature regimes nor for its movement within a two-zone furnace. During a growth attempt, the temperature is held constant. According to the $p(i)$ behaviour, in the Li-Ir-Ru-O system, the sublimation is limited to IrO_3(g) and LiOH(g) at $T \sim 1205$ K. In contrast, at higher temperatures of $T \geq 1300$ K, the transport of RuO_3(g) is favoured as well. Therefore, higher growth temperatures of 1300 K are necessary for reaching transportability of all gaseous phases. This optimum growth temperature coincides with the ones yielding the growth of the end members α-Li_2IrO_3 and Li_2RuO_3 (sections 4.1.3 and 5.1.2). Due to a higher $p(i)$ of LiOH(g) and IrO_3(g) at growth temperature than of RuO_3(g), the composition of the gas phase is unknown and does not coincide with the predefined ratios of educts. In total, the differences in $p(i)$ point towards a complex growth process of $Li_2Ir_{1-x}Ru_xO_3$.

As for the Li-Ir-O and the Li-Ru-O system, thermodynamic calculations on the assumed chemical

reaction yielding $Li_2Ir_{1-x}Ru_xO_3$ were carried out. In accordance with discussions on the growth of α-Li_2IrO_3 and Li_2RuO_3 and independent of the relative amount of Ru in $Li_2Ir_{1-x}Ru_xO_3$, T_{opt} is 1300 K. This temperature coincides with the previous considerations on the minimum temperature, which is required for reaching transportability of the gaseous phases. The complete listing of ΔH_T^0, ΔS_T^0, C_p, ΔH_R, and ΔS_R is found in the appendix table C.1.

6.1.2 $Li_2Ir_{1-x}Ru_xO_3$

Crystal growth was obtained at 1300 K with a Li_2O:(1-x Ir + x RuO_2) ratio of 4:1 and a experiment duration of 14 days. Nine crystal-growth attempts were carried out with varying relative amounts of Ru in the bottom body: $0.1 \leq x \leq 0.9$ with an x-increment of 0.1. For the first growth attempt (V1) even x-values and for the second growth attempt (V2) odd x-values were chosen.
Crystal growth was observed along the whole series of x values, hence for all relative amounts of Ru, and mostly occurred on all four stairs of the crucible. In accordance with α-Li_2IrO_3 and Li_2RuO_3, the most and largest crystals with a size up to 500 µm grew on the second lowest stair and pointed to the Ir/RuO_2 bottom body (figure 6.2). By comparing the growth attempts V1 and V2, a higher amount of crystals was obtained in V1 than in V2. This is explained by a change of the muffle furnace due to the failure of the first one. Because of a lower real temperature of the second furnace, the growth temperature was set 10 K higher than in the first growth attempt (methods section 2.2.4). Due to a gradient in temperature from the center with homogeneous temperature conditions to the walls of the furnace, a higher air movement in the second furnace than in the first furnace was expected. The higher air movement is assumed to have an influence on the growth and, therefore, explains the lower amount of $Li_2Ir_{1-x}Ru_xO_3$ crystals of the growth attempt in the second furnace. A similar observation was made on the time-dependent crystallisation process of Li_2RuO_3 (section 5.1.2). No other differences between both growth attempts are known.
The crystal morphology of the $P2_1/m$ phase with dimerised honeycombs and the $C2/m$ phase with non-dimerised honeycombs is similar and defined by crystal faces of types {110} and {011} (section 4.1.3 and 5.1.2). Hence, a distinction of grown phases in dependency of the crystal morphology was not possible.

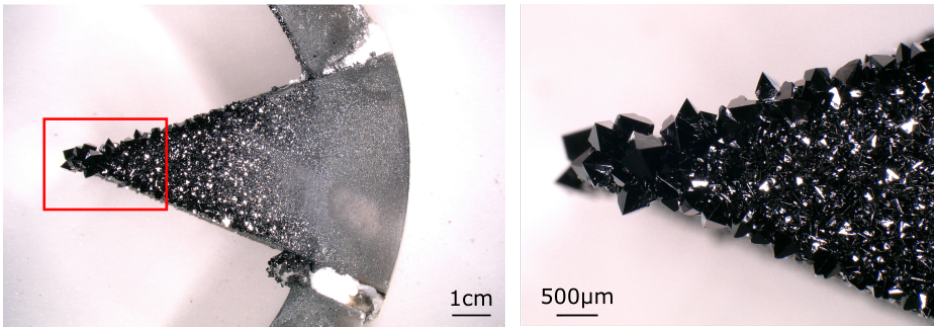

Figure 6.2: Single crystals of $Li_2Ir_{1-x}Ru_xO_3$ grown by the CVTR method. The tip of the stair is enlarged on the right side (red box).

6.2 Material characterisation

6.2.1 Elemental analysis

To investigate the elemental composition of grown crystals, EDX analysis were conducted on thoroughly polished surfaces. The focus was set on the ratio of Ru and Ir. Since Li cannot be detected via EDX, the Li:(Ir+Ru) ratio cannot be determined. The presented and discussed data are in the area of reliability (section 3.3.1). As discussed for previous EDX results, the delimitation of the measured crystal does not coincide with its sharp corners and edges due to loss of material during polishing. Based on elemental analysis, in growth systems with known composition of the parent phase, *e.g.* of the melt, a distribution coefficient can be calculated. However, for CVTR experiments, this composition is unknown and, hence, does not enable such a calculation. Growth experiments and results from elemental analysis are shown in table 6.1. For every growth experiment, the weighed relative amount of Ru (x_{in}) and for every sample the measured relative amount of Ru via EDX (x_m) is listed. Further, for every growth attempt $x_{d,max}$ represents the maximum relative difference of x_m between the highest and lowest stair. Results are visualised in figure 6.3, where results are assigned to V1 and V2 (a and b, respectively).

EDX analysis confirm the incorporation of Ru and Ir in grown crystals of the Li-Ir-Ru-O system throughout the whole x_{in}-range. With this, the growth of $Li_2Ir_{1-x}Ru_xO_3$ crystals by the CVTR method was confirmed. Figure 6.3 shows that within the uncertainty of data the x_m of two samples from one stair coincide with each other. In all growth attempts, the x_m of samples from different stairs varies and yields x_d. With exception of $x_{in} = 0.1$, crystals of $Li_2Ir_{1-x}Ru_xO_3$ incorporate the highest relative Ru amount (x_m) the closer they are to the bottom body during growth, where the transport path for Ir/Ru is shortest. Ergo, the larger the distance, the higher is the amount of incorporated Ir. This might be explained by the higher $p(i)$ of IrO_3 at growth temperature than of RuO_3. This effect might be increased with increasing transport path. Due to the varying incorporation of Ir and Ru on different stairs of the setup, the availability of the gaseous components in the growth system might be balanced. For $x_{in} = 0.1$, the calculated x_d is only small. Independent of the growth position, the x_m values are equal and small differences disappear in the uncertainty of data. This homogeneous growth of crystals might be explained by a low x_{in}, *i.e.* a high relative Ir amount. Due to the higher $p(i)$ of IrO_3(g) than of RuO_3(g), a higher availabilty of IrO_3(g) and, thus, a favoured transport and incorporation of Ir might be assumed. Though, these considerations cannot be supported by measured data, since no data on the availability of gaseous components in the growth system have been reported so far.

Table 6.1: Growth experiments with starting ratio Li_2O:(1-x Ir+ x RuO_2), of 4:1 to yield $Li_2Ir_{1-x}Ru_xO_3$ crystals with compositional information on crystals from different stairs (S1-S4). x_{in}: weighed relative amount of Ru; x_m: measured relative amount of Ru via EDX; $x_{d,max}$: maximum relative difference of x_m between the highest and lowest stair.

Experiment	x_{in}	Stair	x_m(sample 1)	x_m(sample 2)	$x_{d,max}$ in %
V2T1	0.1	S3	0.12(2)	0.13(2)	
		S2	0.13(2)	0.13(2)	
		S1	0.12(2)		+2.4
V1T1	0.2	S3	0.23(1)	0.26(2)	
		S2	0.25(1)	0.23(1)	
		S1	0.28(1)	0.28(2)	-17.8
V2T2	0.3	S4	0.28(3)	0.30(2)	
		S3	0.31(4)		
		S2	0.31(3)	0.31(3)	
		S1	0.31(3)	0.31(3)	-9.7
V1T2	0.4	S3	0.40(2)	0.40(1)	
		S2	0.45(2)	0.37(2)	
		S1	0.45(2)	0.44(2)	-11.1
V2T3x	0.5	S4	0.45(3)	0.45(4)	
		S3	0.47(2)	0.49(4)	
		S2	0.49(4)	0.51(4)	-11.8
V1T3x	0.6	S4	0.60(3)		
		S3	0.61(3)	0.67(6)	
		S1/S2	0.67(3)	0.71(3)	-15.5
V2T4x	0.7	S4	0.68(1)	0.71(4)	
		S3	0.71(2)		
		S2	0.70(2)	0.71(3)	-4.2
V1T4x	0.8	S4	0.79(2)	0.76(3)	
		S3	0.81(1)	0.80(1)	
		S2	0.87(1)	0.86(1)	-12.6
V2Tox	0.9	S3	0.88(1)		
		S2	0.91(1)	0.91(1)	
		S1	0.92(1)	0.93(1)	-5.4

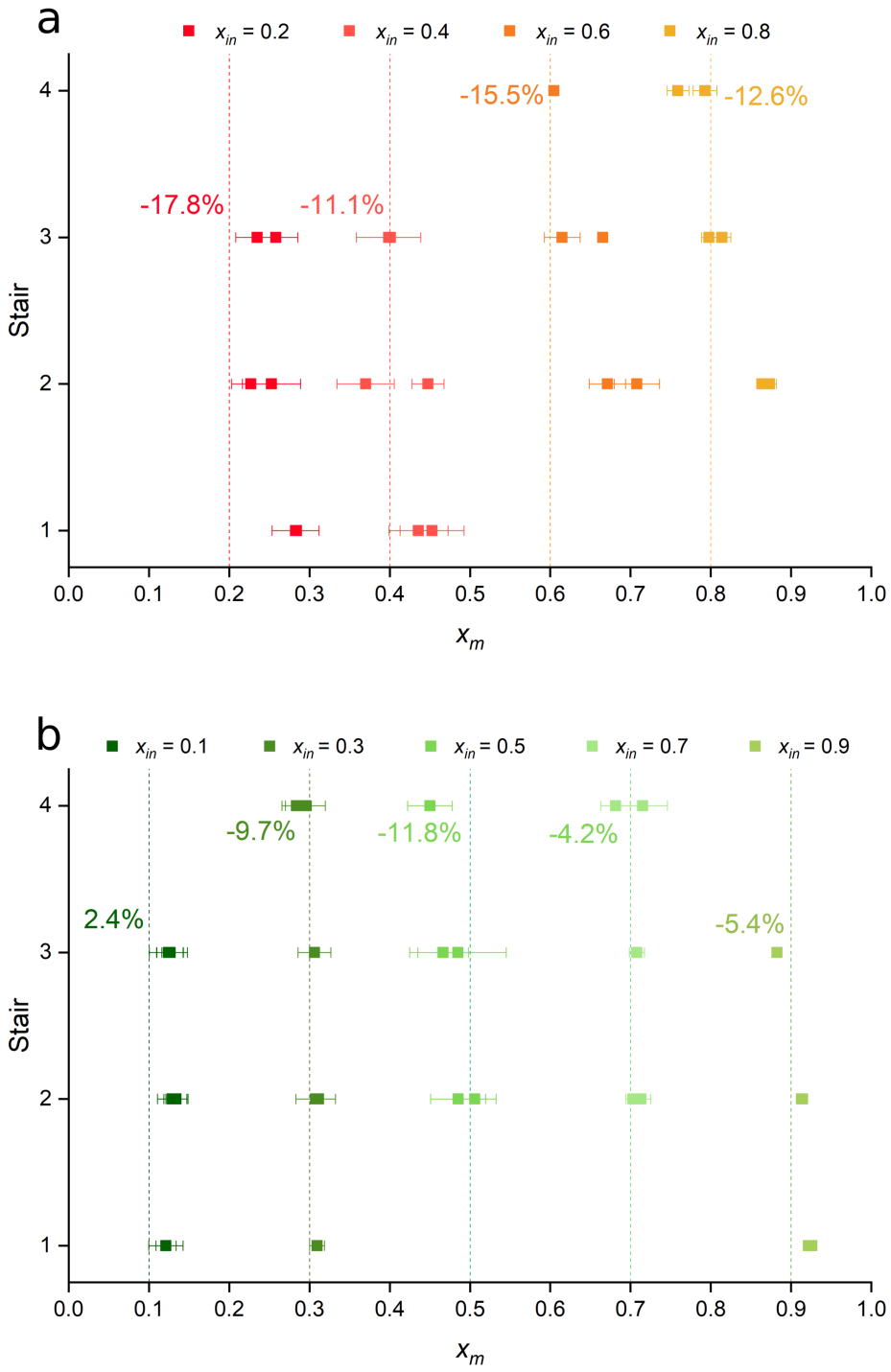

Figure 6.3: Measured relative amount of Ru x_m via EDX of crystals of $Li_2Ir_{1-x}Ru_xO_3$ grown at different stairs in the crucible in (a) V1 and (b) V2 with respect to the weighed relative amount of Ru x_{in}, which is marked with a dashed vertical line for each experiment. The values in percent are $x_{d,max}$, which is the maximum relative difference of x_m between the highest and lowest stair.

Single crystals of $Li_2Ir_{1-x}Ru_xO_3$ mostly show a homogeneous distribution of x_m. However, in some crystals a compositional difference is noticed (figure 6.4). Whilst in the exterior part of the crystal differences in x_m values are within the uncertainty of data (figure 6.4a, b), line profiles between the exterior and the interior part of the crystal show compositional differences (figure 6.4c, d, e). Here, x_m is larger in the exterior than in the interior part. Most significant differences are found in line profile e, which reaches to the top of the crystal pointing into the reaction chamber. This shows that at the end of crystal growth the incorporated relative Ru amount was increased. This observation is in accordance with the previously discussed study by Reimers [104], who obtained graded crystals due to different $p(i)$ of the gaseous components.

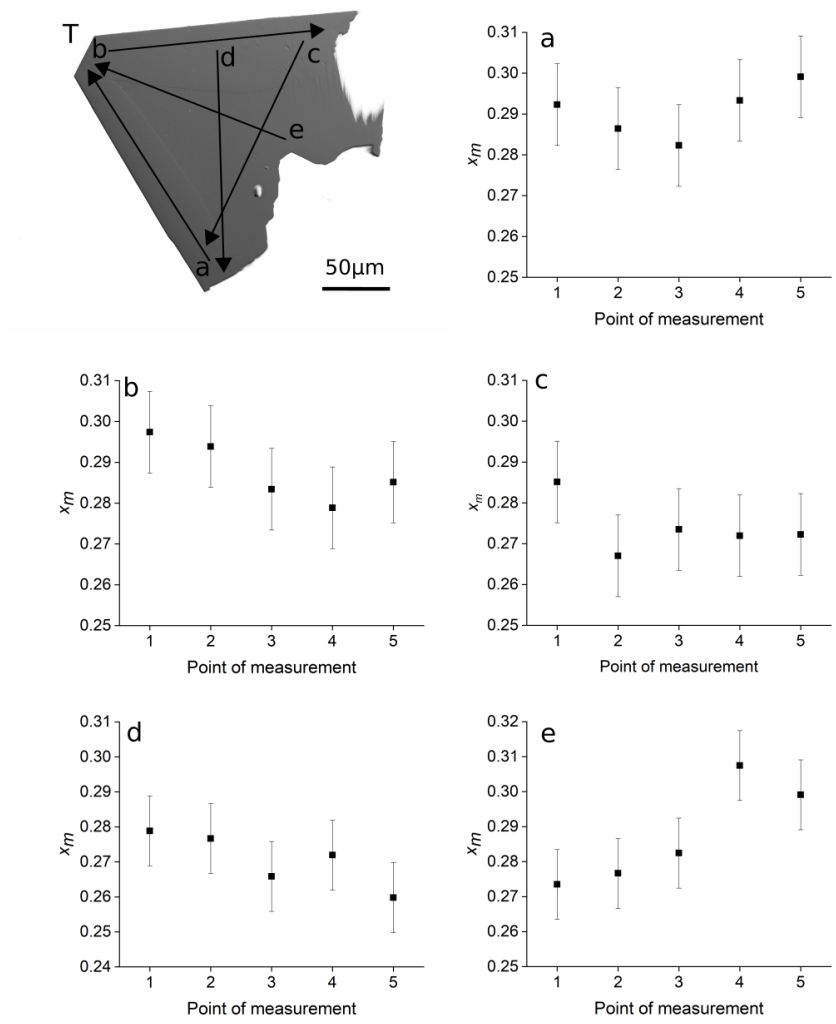

Figure 6.4: SEM image and distribution of the measured relative Ru amount, x_m along different line profiles of a $Li_2Ir_{1-x}Ru_xO_3$ crystal (sample V1T1S1-1). T marks the top of the crystal pointing into the reaction chamber.

6.2.2 Structural aspects

The influence of both, the substitution of relative Ir amounts and the temperature, on the crystal structure of Li_2RuO_3 is investigated. In the introductory section 1.1.3, it was shown that a unit cell transformation of the non-dimerised $C2/m$ and the dimerised $P2_1/m$ phase of Li_2RuO_3 yield the unit cell choice of α-Li_2IrO_3 ($C2/m$, [90]) and Li_2RuO_3 ($P2_1/m$, [67]), respectively. Hence, these structures are considered as isostructural. The comparison of lattice parameters was presented in table 1.2.

6.2.2.1 Room-temperature measurements

For analysing the phase content at RT, RT P-XRD measurements were performed. The obtained data was refined starting from structural models of α-Li_2IrO_3 ($C2/m$) and Li_2RuO_3 ($P2_1/m$). For comparison of the lattice parameters, for the latter the transformed unit cell was chosen. In the following, the results of nine RT measurements of $Li_2Ir_{1-x}Ru_xO_3$ are discussed. The samples differ in their averaged relative amount of Ru ($\bar{x}_m$).

Depending on $\bar{x}_m$, the powder pattern could be refined with either the $C2/m$ or the $P2_1/m$ phase. At a low relative Ru amount, the refinement yielded a non-dimerised $C2/m$ phase ($0 \leq \bar{x}_m \leq 0.41(3)$). At a high relative Ru amount, the refinement resulted in a dimerised $P2_1/m$ phase ($0.81(1) \leq x_m \leq 1$). Both observations coincide with the crystal structures of the end members at RT. In figures 6.5 and 6.6, sections of the P-XRD patterns of $Li_2Ir_{1-x}Ru_xO_3$ with x_m = 0.28(2) and 0.93(1) between 15° and 85° 2Θ are compared with the calculated P-XRD patterns of the respective $C2/m$ and $P2_1/m$ phase. For the calculated P-XRD patterns, the strongest reflections are indexed. For comparison, the intensity scales of the measured P-XRD patterns are enlarged. Accordingly to a strong preferred orientation (001), the (00l) reflections at higher 2Θ angles show increased intensities as well. Hence, reflections with low intensities in the calculated pattern, *e.g.* (221), get lost in the background noise of measured P-XRD patterns. Despite this, the comparison of P-XRD and calculated patterns confirms the non-dimerised $C2/m$ phase at a high relative amount of Ir and the dimerised $P2_1/m$ phase at a high relative amount of Ru.

At medium $\bar{x}_m$, the refinement of P-XRD patterns was possible with either the $C2/m$ or the $P2_1/m$ phase and yielded similar lattice parameters. In figure 6.7, the P-XRD pattern of a sample with $\bar{x}_m$ = 0.71(3) is shown and compared with calculated patterns of $C2/m$ and $P2_1/m$. In the case of $Li_2Ir_{1-x}Ru_xO_3$, only a few reflections with low relative intensities distinguish the dimerised $P2_1/m$ from the non-dimerised $C2/m$ phase (figure 6.7). This is explained by systematic absences, which are derived from the reflection conditions of each space group. For $P2_1/m$, the only present reflection condition is for 0k0 reflections with $k = 2n$ due to the screw axis 2_1. In contrast, in $C2/m$, the reflection conditions are: hkl: $h+k = 2n$, $h0l$: $l = 2n; h = 2n$, $0kl$: $k = 2n$, $hk0$: $h+k = 2n$, $0k0$: $k = 2n$, and $h00$: $h = 2n$. Hence, in $P2_1/m$ more reflections are allowed which are absent in $C2/m$. As an example, the $(\bar{1}01)$ reflection occurs in $P2_1/m$, but is not allowed in $C2/m$ due to the reflection condition for $h0l$ ($l = 2n; h = 2n$).

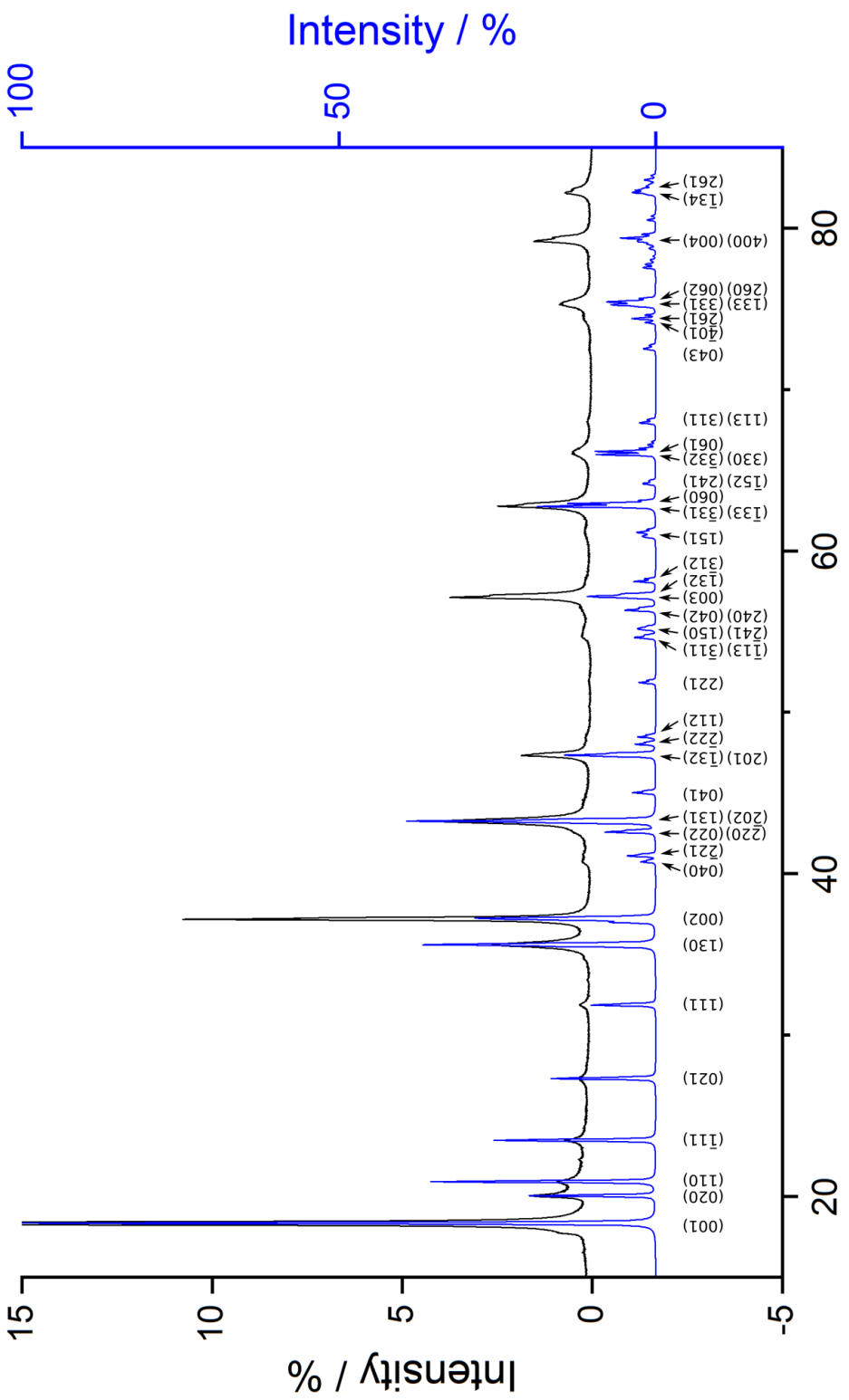

Figure 6.5: Comparison of room-temperature powder X-ray diffraction pattern of $Li_2Ir_{1-x}Ru_xO_3$ with $\bar{x}_m$ =0.28(2) (black) and calculated powder pattern of the $C2/m$ phase (blue) with indexed reflections of the strongest peaks.

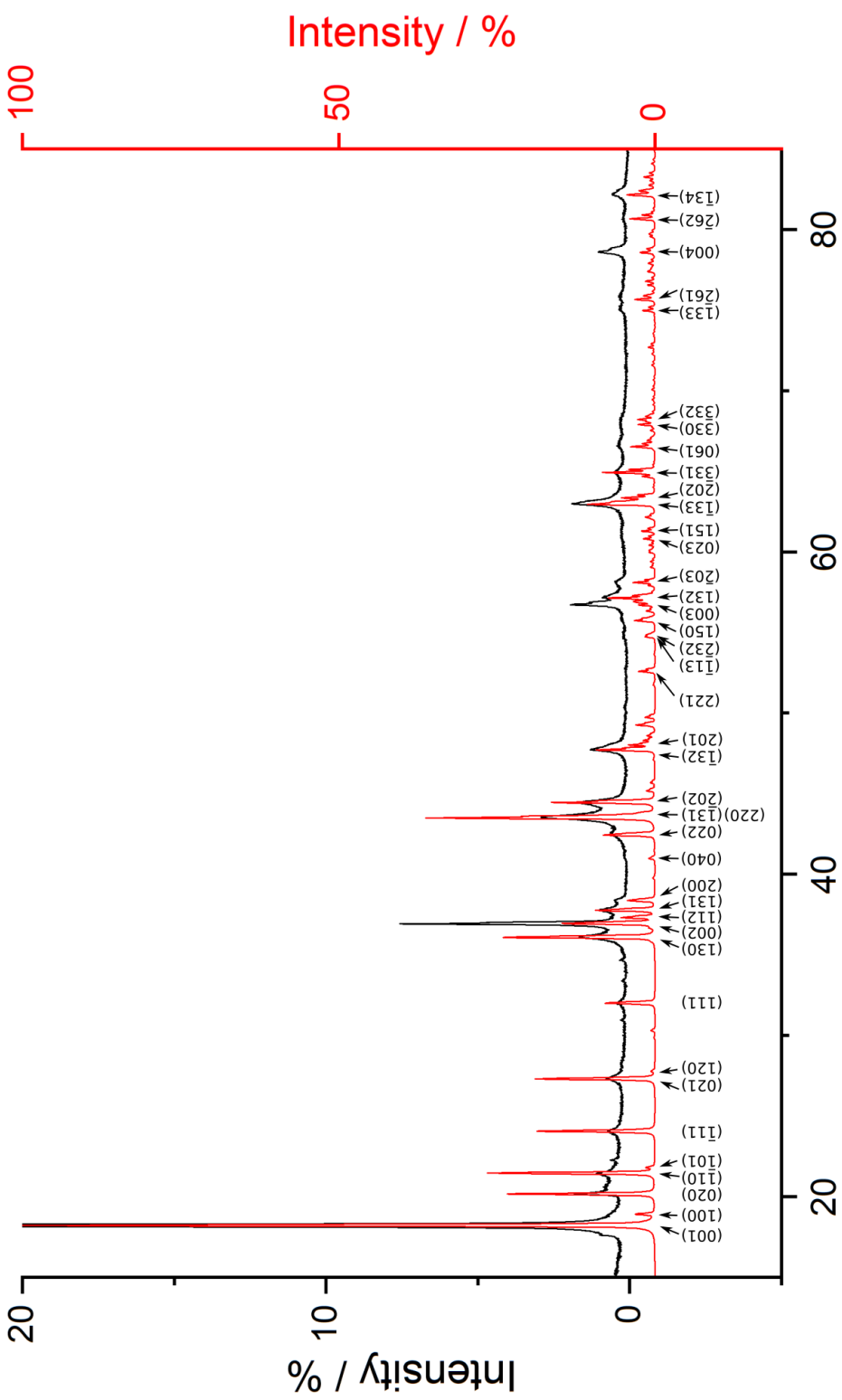

Figure 6.6: Comparison of room-temperature powder X-ray diffraction pattern of $Li_2Ir_{1-x}Ru_xO_3$ with $\bar{x}_m$ =0.93(1) (black) and calculated powder pattern of the $P2_1/m$ phase (red) with indexed reflections of the strongest peaks.

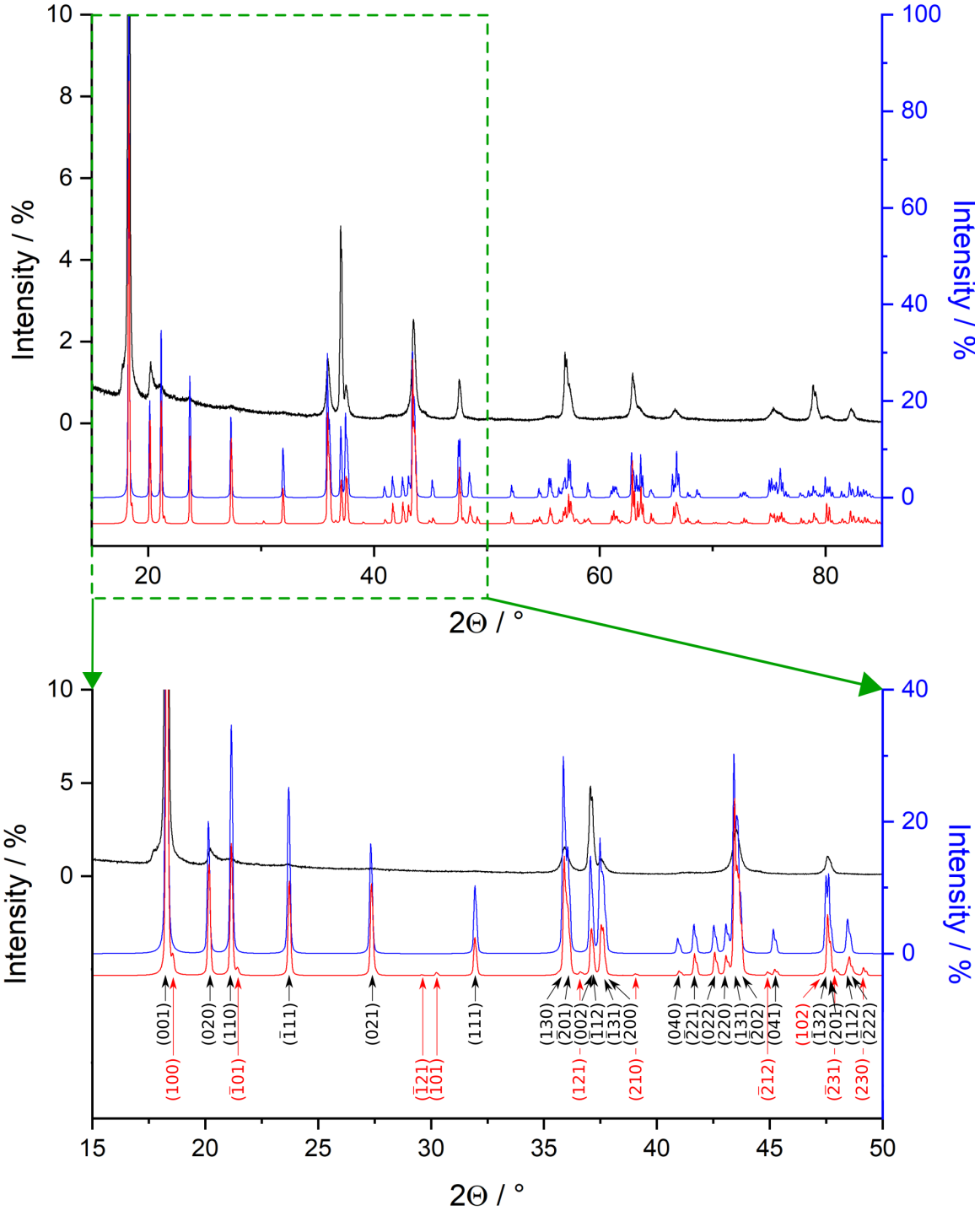

Figure 6.7: Comparison of room-temperature powder X-ray diffraction pattern of $Li_2Ir_{1-x}Ru_xO_3$ with $\bar{x}_m = 0.71(3)$ (black) and calculated powder pattern of the $P2_1/m$ and $C2/m$ phases (red and blue, respectively). The green dashed box in the upper part marks the enlarged area in the lower part. Black indexed reflections are observed in both patterns, red ones are only present in $P2_1/m$.

Further, *hkl* reflections with $h+k = 2n+1$, *e.g.* (121), are only allowed in $P2_1/m$ but absent in $C2/m$ ($h+k = 2n$). The same applies to the (100) and (210) reflections due to the respective reflection conditions of $C2/m$. Since the reflections, which are only allowed in $P2_1/m$, show low relatives intensities, *e.g.* 1.3 rel% of the $(\bar{1}01)$ reflection, these minor differences cannot be identified from the measured P-XRD data. Because this is the best result of P-XRD patterns that could be obtained after different sample preparation attempts, for $0.50(5) \leq \bar{x}_m \leq 0.71(3)$ an assignment of the crystal symmetry based on P-XRD data is not definite.

In the following, the RT P-XRD patterns of $Li_2Ir_{1-x}Ru_xO_3$ in the 2Θ range of 15 - 120° are presented (figure 6.8). Due to the high concordance of P-XRD patterns of the $C2/m$ and the $P2_1/m$ phase at medium $\bar{x}_m$ (figure 6.7), the indexing of reflections coincides for both symmetries and no separate discussion is necessary. For better visualisation, the reflection positions in two 2Θ ranges are compared: 30 - 45° and 50 - 100° (figure 6.8 parts A and B, respectively). Here, only reflections with significantly high intensities are indexed and focussed. Differences in reflection intensities with changing $\bar{x}_m$ are explained by different magnitudes of preferred orientation (00*l*) in each sample and do not necessarily correspond for a change in phase content. As an example, the (103) reflection at $\bar{x}_m$ = 0.81(1) and 0.93(1) in figure 6.8B is assigned to the $P2_1/m$ phase, but forbidden in $C2/m$. However, the absence of the (103) reflection in P-XRD patterns at medium $\bar{x}_m$ does not imply the exclusion of the dimerised $P2_1/m$ phase due to its weak relative intensity below 1%. The reflections of highest intensity are of type (00*l*), hence the preferred orientation. Independent of $\bar{x}_m$, the positions of the (00*l*) reflections remain at a similar value, which indicates an almost consistent *c* lattice parameter. In contrast, the reflection position of (200) shifts to higher 2Θ with increasing $\bar{x}_m$, which points towards a decrease of the *a* lattice parameter. In accordance with the (200) reflection, a general peak shift of reflections to higher 2Θ with increasing $\bar{x}_m$ is noticed. The most significant peak shift is observed for (*hkl*) with high *h* and *k*, *e.g.* the $(\bar{3}31)$ reflection (figure 6.8B). This general peak shift indicates a decrease in cell volume with increasing $\bar{x}_m$ for both, the non-dimerised $C2/m$ and the dimerised $P2_1/m$ phase. Next to the $C2/m$ or the $P2_1/m$ phase, an impurity phase is observed at low 2Θ and determined as a lithium aluminate phase (figure 6.8A).

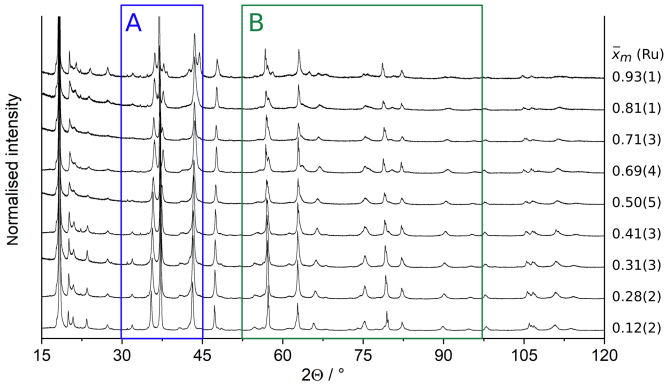

Figure 6.8: Room temperature powder X-ray diffraction patterns of $Li_2Ir_{1-x}Ru_xO_3$ in a $\bar{x}_m$ range from 0.12(2) to 0.93(1). Boxes A and B are enlarged in the following parts.

...continued from previous page

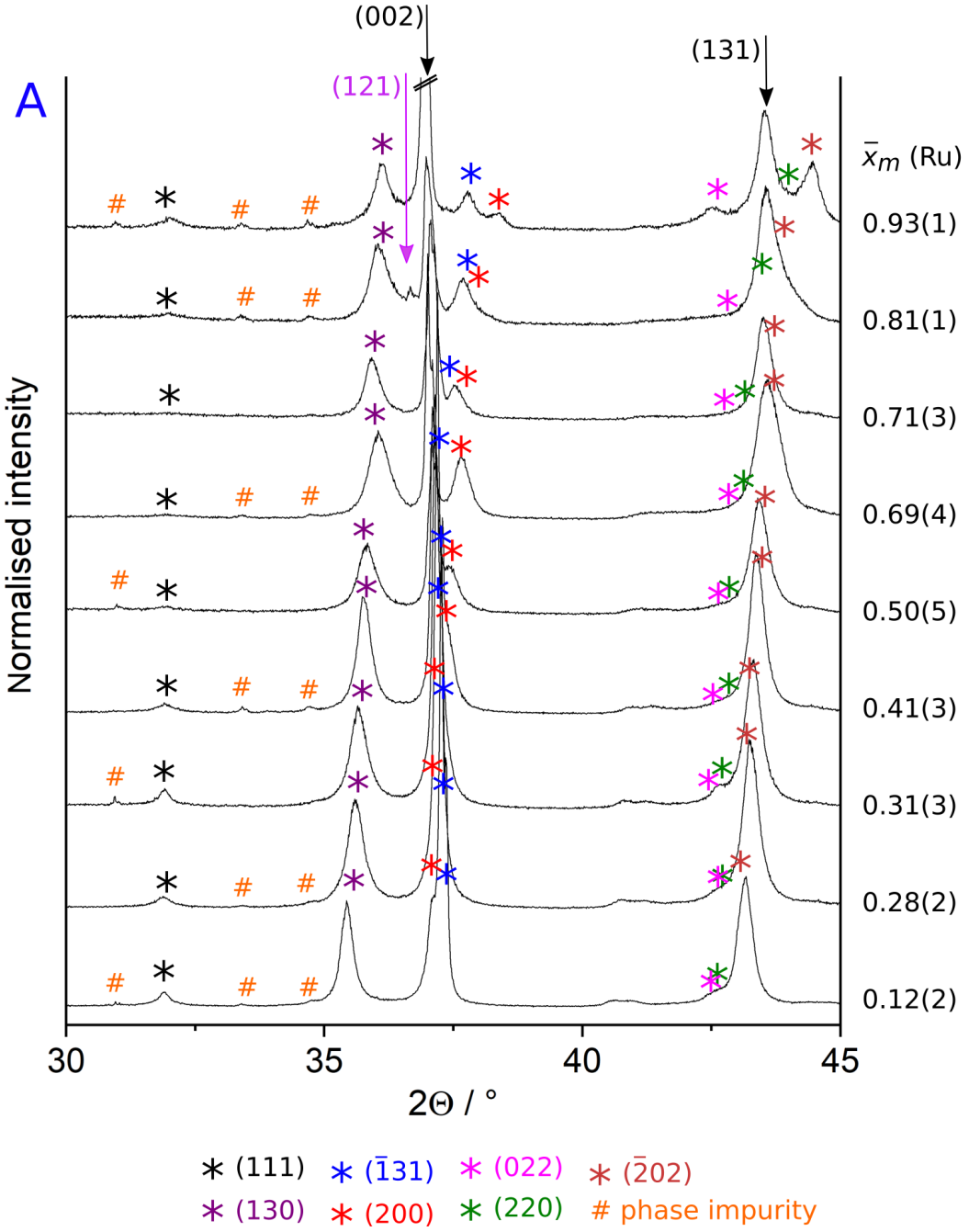

Box A: Shift of reflection positions of the $P2_1/m$ or $C2/m$ phase in P-XRD patterns between 30 and 45° 2Θ of $Li_2Ir_{1-x}Ru_xO_3$ in a $\bar{x}_m$ range from 0.12(2) to 0.93(1).

...continued from previous page

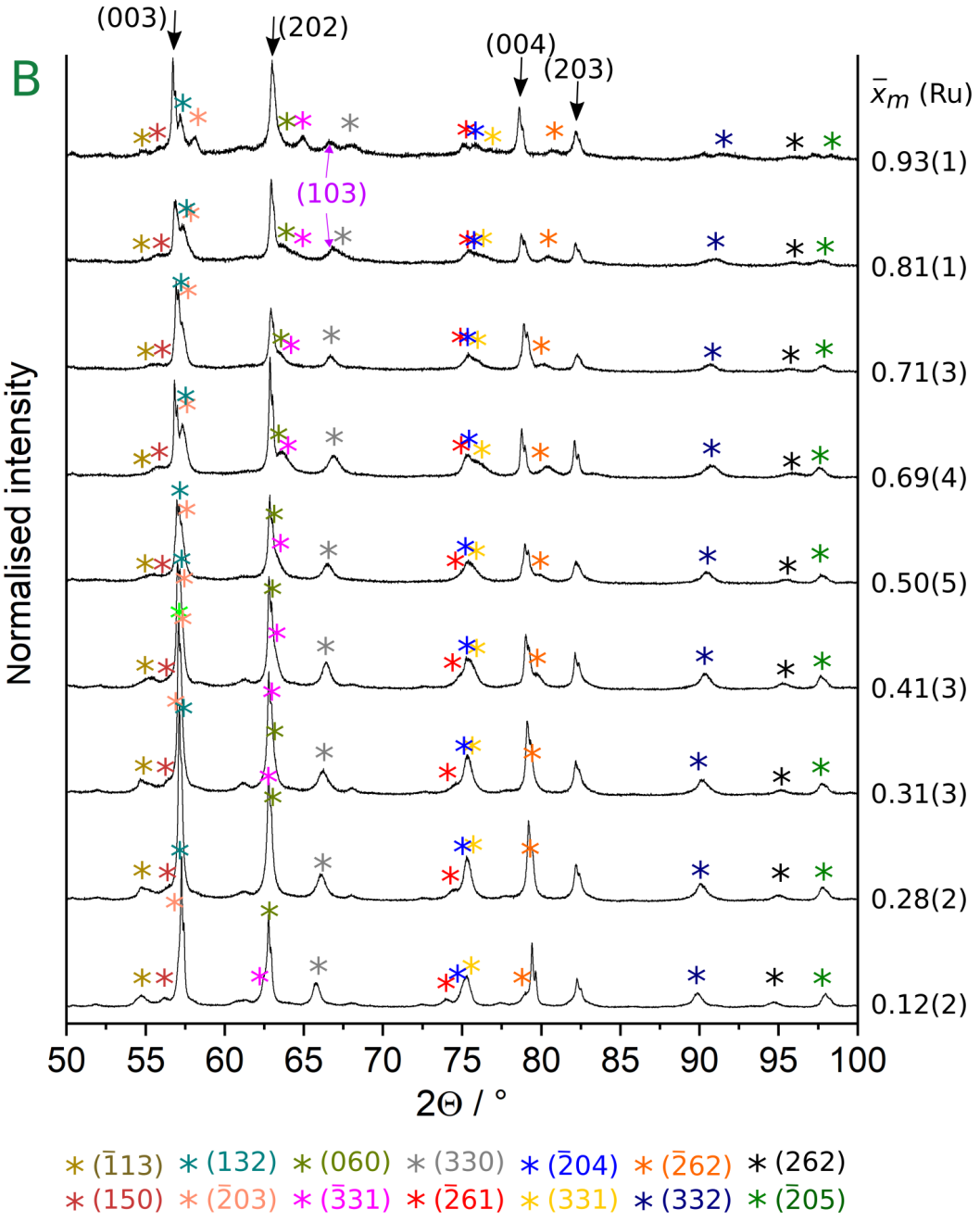

Box B: Shift of reflection positions of the $P2_1/m$ or $C2/m$ phase in P-XRD patterns between 50 and 100° 2Θ of $Li_2Ir_{1-x}Ru_xO_3$ in a $\bar{x}_m$ range from 0.12(2) to 0.93(1).

The refinement of P-XRD data at medium $\bar{x}_m$ with either the dimerised $P2_1/m$ or the non-dimerised $C2/m$ phase coincides with data from Lei et al. [67]. In this study, P-XRD patterns of $Li_2Ir_{1-x}Ru_xO_3$ could be fitted by using one of both structural models in the range of $0.3 \leq x \leq 0.6$. In figure 6.9, the progression of lattice parameters and cell volume with $\bar{x}_m$ is shown for refinement results from the present work and compared with data from Lei et al. [67]. The lattice parameters of the present work are listed in appendix table C.4. Both data sets show similar trends in a, b, c, β, and V. Whereas a, b, and β decrease with increasing $\bar{x}_m$, c barely changes throughout the $\bar{x}_m$ range, which coincides with observations on the shift of reflection positions. With increasing $\bar{x}_m$, the cell volume V decreases for both, the $C2/m$ and the $P2_1/m$ phase. This can be explained by a slightly smaller ionic radius of Ru^{4+} compared to Ir^{4+} [67]. Small differences in lattice parameters between both data sets are explained by different synthesis methods.

The refinement of atomic positions or SOF of structural models did not yield significant values since this only influences the fit of reflection intensities. However, the combination with EDX data confirmed the incorporation of both, Ir and Ru, in crystals of $Li_2Ir_{1-x}Ru_xO_3$. At HT, independent of the relative amount of Ru, the phase crystallises in the non-dimerised $C2/m$ structure. Results from RT P-XRD measurements show that the occurrence of a structural phase transition to the LT $P2_1/m$ phase with Ru-Ru dimers depends on $\bar{x}_m$. The phase transition to the $P2_1/m$ phase between growth temperature and RT is only favoured at a high $\bar{x}_m$, *i.e.* at a low relative amount of Ir of $\leq 19\%$. Hence, the $C2/m$ phase is maintained at high relative Ir amounts. This is explained by a smaller ionic radius of Ru^{4+} than of Ir^{4+}. Due to an ambiguous assignment of the structure at medium $\bar{x}_m$, the limit of the relative Ir amount between the stability areas of the non-dimerised $C2/m$ and the dimerised $P2_1/m$ phase at RT is not clearly determinable. However, taking together results from the present work and reported by Lei et al. [67], this limit might be close to a relative amount of Ru of 0.5 - 0.6.

Results of RT P-XRD measurements on grown crystals of $Li_2Ir_{1-x}Ru_xO_3$ showed that a clear space group determination between the dimerised $P2_1/m$ and the non-dimerised $C2/m$ is only possible for the outer limits of $\bar{x}_m$. To overcome the difficulties of strong preferred orientation in reflection mode and to determine the crystal structures for the whole $Li_2Ir_{1-x}Ru_xO_3$ series, SC-XRD measurements should be yielded. Further, temperature-dependent SC-XRD measurements should investigate the phase transition, whose temperature is expected to be shifted depending on the relative amount of Ir.

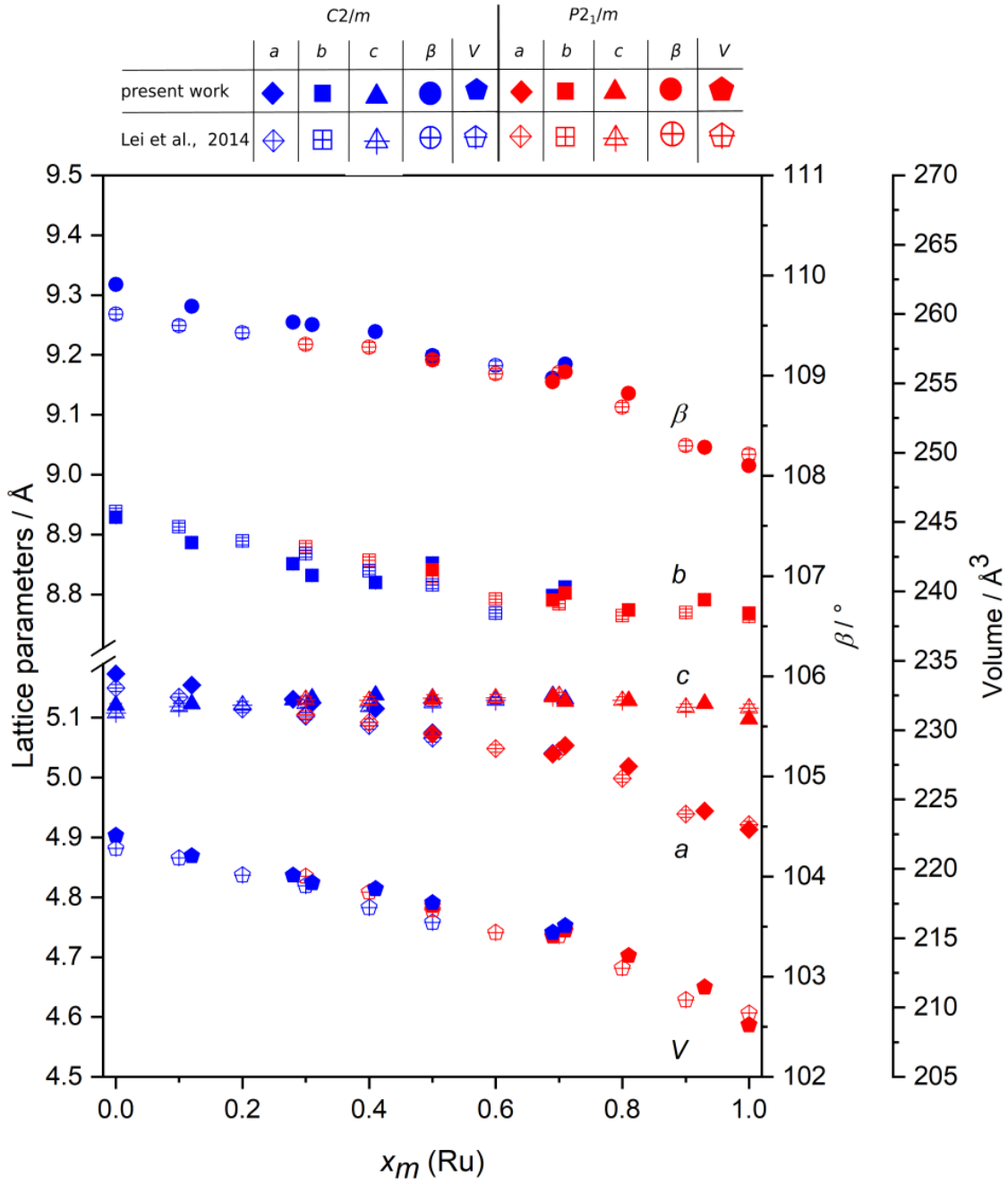

Figure 6.9: Progression of lattice parameters a, b, c, β, and cell volume V of $Li_2Ir_{1-x}Ru_xO_3$ depending on $\bar{x}_m$ with space group $C2/m$ and $P2_1/m$ (blue and red, respectively). Data is taken from the present work and from Lei et al. [67] (filled and blank symbols, respectively). Error bars are smaller than symbols used.

6.2.2.2 Low-temperature measurements

Next to RT investigations, LT measurements were performed to investigate the influence of low temperature on the RT phases of $Li_2Ir_{1-x}Ru_xO_3$. LT P-XRD measurements were conducted, since no SC-XRD diffractometer with a helium cryo-chamber was available in the project area. Details on measurement conditions are given in section 3.1.1.1. The focus was set on the investigation of a possible phase transition between the non-dimerised $C2/m$ (HT) and the dimerised $P2_1/m$ phase (LT).

Depending on their composition and space group at RT, the samples were divided into three ranges (section 6.2.2.1). In the following, for each range the temperature-dependent P-XRD patterns and progression of lattice parameters of one sample is presented and discussed. Further results with similar behaviour are shown in figures of appendix C.

At high $\bar{x}_m$ ($P2_1/m$), no change of the P-XRD pattern is observed (figure 6.10). The reflection positions show a relatively small shift with temperature, which results in similar lattice parameters and a decrease of V by 0.6 % at 12 K compared to V at RT. This is explained by a small negative thermal expansion of the dimerised $P2_1/m$ phase with decreasing temperature. In similarity, in the low $\bar{x}_m$ range ($C2/m$) no change in the P-XRD pattern is observed yielding similar lattice parameters and a decrease of V by 0.4% (figure 6.11). These observations in the outer $\bar{x}_m$ ranges coincide with the behaviour of the RT end members α-Li_2IrO_3 ($C2/m$) and Li_2RuO_3 ($P2_1/m$), where a small ΔV is observed throughout the investigated temperature range. In accordance, at medium $\bar{x}_m$, the P-XRD pattern does not change throughout the whole temperature range. However, as for RT measurements, no clear space group assignment based on P-XRD data was possible. For the whole temperature range, the refinement with either the $C2/m$ or the $P2_1/m$ structure yielded similar lattice parameters. Refinement results in figure 6.12 are based on the $C2/m$ phase. Hence, this measurement method is not suitable for the detection of a phase transition between both phases neither depending on the relative amount of Ir nor depending on the temperature.

In six out of eight measurements, a phase impurity with a broadened peak at 24.6° 2Θ is observed at T $\leq$ 190 K (figures 6.12, C.1, C.2, C.3, C.4, and C.5). This peak evolves independent of $\bar{x}_m$. Its position cannot be assigned to either the $C2/m$ or the $P2_1/m$ phase. The intensity of the impurity peak is low and only slightly higher than the background. Further, with decreasing temperature the peak shifts by about 1° 2Θ, which is considerably higher than the small temperature-dependent shift of reflections of the main phases. The smaller the maximum counts of the measurement, *i.e.* the smaller the amount of sample, the larger the intensity of the phase impurity peak (*e.g.* 22.000 maximum counts, 0.6 rel% intensity, figure 6.12). Accordingly, for measurements with high counts, *i.e.* a larger amount of sample, the phase impurity was not observed (*e.g.* 100.000 maximum counts, figure 6.11). Since each sample was homogeneously distributed on a thinly greased sample holder and the size of the empty sample holder surface is larger with decreasing sample amount, the phase impurity peak is assumed to be derived from the silicon grease. Moreover, the stability area of silicon grease is reported for $T \geq 210$ K, which roughly coincides with the evolution of the impurity peak at $T \leq 190$ K.

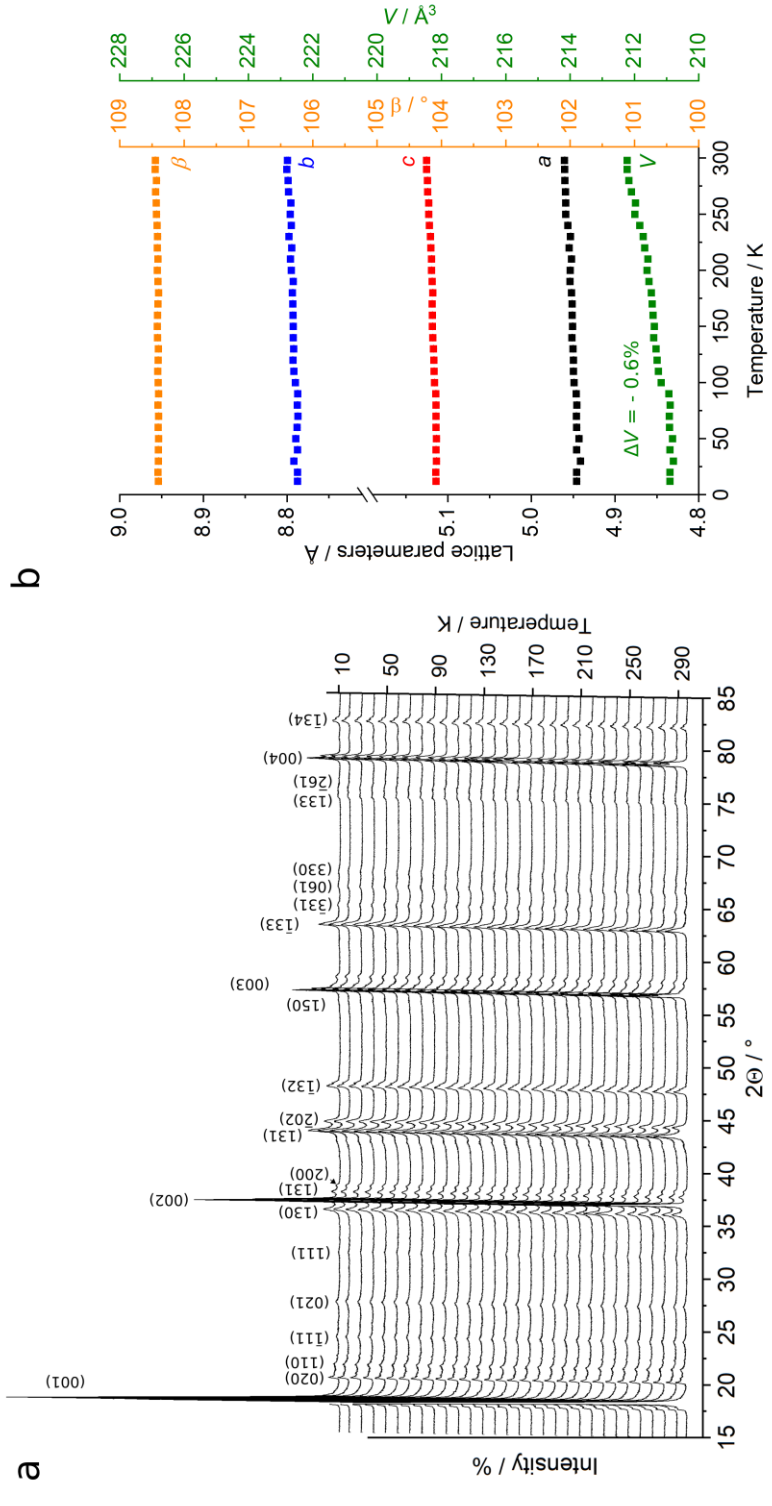

Figure 6.10: Low-temperature behaviour of $Li_2Ir_{1-x}Ru_xO_3$ with $\bar{x}_m = 0.87(3)$ with space group $P2_1/m$ (sample V1T4xS2). (a) Sequence of P-XRD measurements at temperatures between 298 K and 12 K. The strongest peaks of the $P2_1/m$ phase are indicated. (b) Progression of lattice parameters and cell volume with temperature. Error bars are smaller than symbols used.

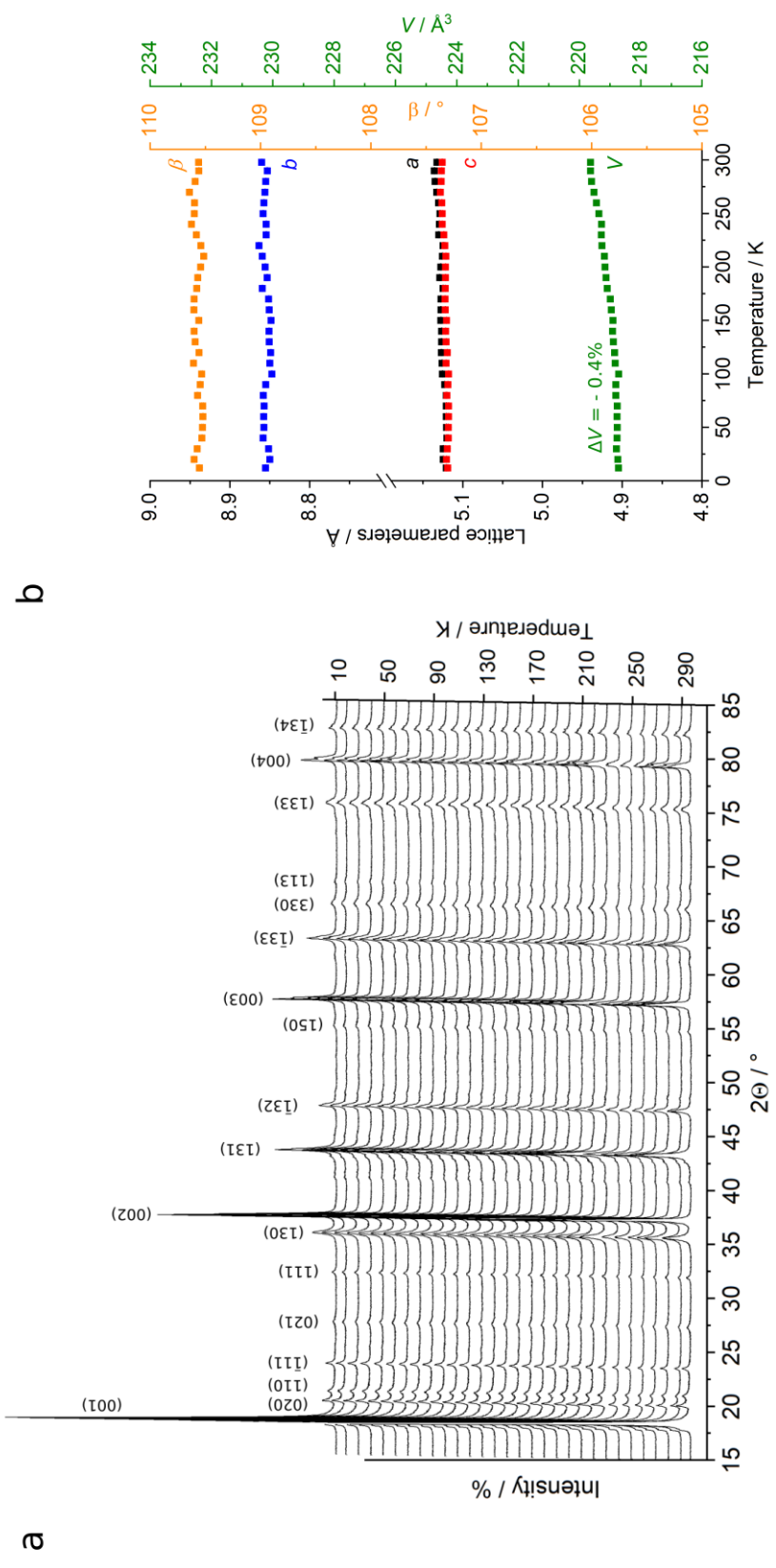

Figure 6.11: Low-temperature behaviour of $Li_2Ir_{1-x}Ru_xO_3$ with $\bar{x}_m = 0.24(2)$ with space group $C2/m$ (sample V1T1S2). (a) Sequence of P-XRD measurements at temperatures between 298 K and 12 K. The strongest peaks of the $C2/m$ phase are indicated. (b) Progression of lattice parameters and cell volume with temperature. Error bars are smaller than symbols used.

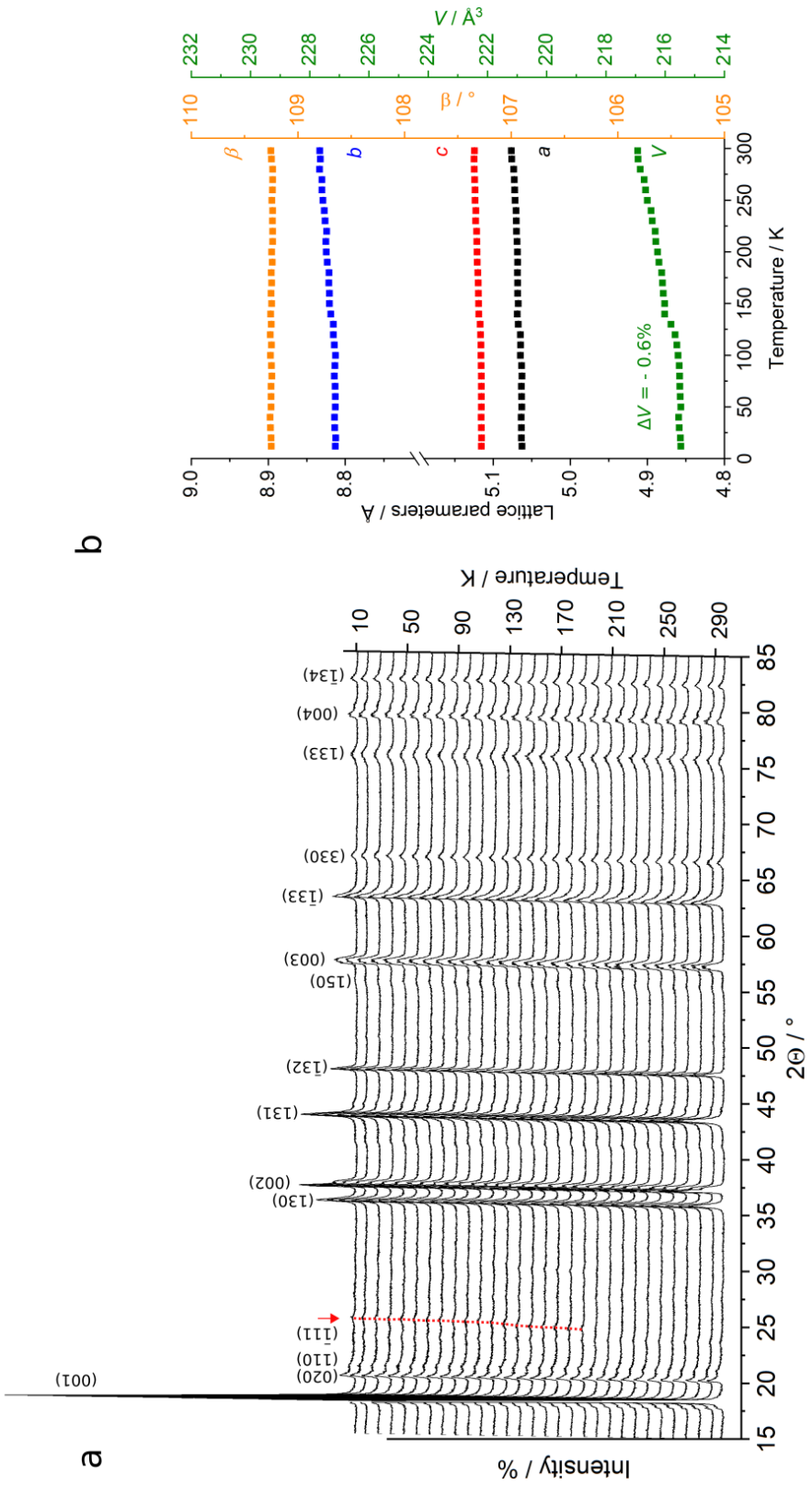

Figure 6.12: Low-temperature behaviour of $Li_2Ir_{1-x}Ru_xO_3$ with $\bar{x}_m$ = 0.60(3) (sample V1T3xS4). (a) Sequence of P-XRD measurements at temperatures between 298 K and 12 K. The strongest peaks of the $C2/m$ phase are indicated. The evolution of a phase impurity with 0.6 rel% intensity is marked in red. The dotted line gives a guide to the eye. (b) Progression of lattice parameters and cell volume with temperature. Error bars are smaller than symbols used.

On the basis of LT P-XRD measurements of $Li_2Ir_{1-x}Ru_xO_3$ no phase transition was observed independent of the relative amount of Ir. According to this, at a high relative amount of Ir, the stability area of the non-dimerised $C2/m$ phase was set to 12 K-1300 K. As already discussed for RT results, this shows a low tendency of the metal-metal dimerisation in 2D honeycomb phases at high relative amounts of Ir, which is explained by the larger ionic radius of Ir^{4+} compared to Ru^{4+}.
At high relative amounts of Ru ($\bar{x}_m$), the stability range of the dimerised $P2_1/m$ phase was confirmed between 12 K and RT. For the Ru-rich end member Li_2RuO_3, a phase transition was reported at 540 K [76]. To examine the phase transition temperature for $Li_2Ir_{1-x}Ru_xO_3$ with high relative Ru amounts, *i.e.* low relative amounts of Ir, temperature-dependent XRD measurements above RT should be yielded. Here, a shift of phase transition temperature with increasing relative Ir amount is expected. If available, HT SC-XRD measurements should be performed. Moreover, due to an ambiguous assignment of the crystal structure at medium $\bar{x}_m$ with P-XRD data, SC-XRD measurements should be aimed. If both, a HT and a LT SC-XRD diffractometer equipped with a He cryostat are available, the temperature-dependent behaviour between 12 K and 540 K should be investigated to determine the crystal structure and examine the temperature-dependent behaviour.

Chapter 7

Na-Ru-O system

In the Na-Ru-O system of APGMOs, a variety of compounds are known (appendix table D.1). As discussed in the introductory chapter 1.1.4, in the present work the growth of $Na_{3-x}Ru_4O_9$ and $Na_{27}Ru_{14}O_{48}$ is focussed. Following, the grown crystals are characterised regarding their structural aspects.

7.1 Crystal-growth investigations

In the present work, next to the focus on Li-based compounds the growth of sodium ruthenates by the CVTR method is aimed. This extends the experimental setup to a growth system that has not been investigated in this regard.

7.1.1 Thermodynamic considerations

Prior to the conduction of CVTR experiments yielding crystals of $Na_{3-x}Ru_4O_9$, the following thermodynamic considerations were made. Comparable to the Li-Ru-O system, RuO_2(s) was used as educt. The transport via RuO_3 is described in literature [93] and was already discussed in the previous chapters. Due to the high reactivity of Na_2O(s) [38, p. 168], Na_2CO_3(s) was chosen as second educt. According to Motzfeldt [81], the reaction of Na_2CO_3(s) takes place in different steps. Close to its melting point at 1123 K [6, p. 1117], Na_2CO_3 decomposes to Na_2O(s) and CO_2(g). For enabling the insertion of N_2(g) into the growth system and the escape of CO_2(g) from the area of reaction, the experimental setup was modified (section 2.2.3). Subsequently and in accordance with the transport reaction of Li_2O(s) [13, p. 166], Gmelin [38, pp.167, 168] reported the reaction of Na_2O(s) with H_2O(g) to form the transport-effective species NaOH(g). With this, the following transport reactions are assumed:

$$Na_2CO_3\ (s) + H_2O\ (g) \Leftrightarrow 2\ NaOH\ (g) + CO_2\ (g)$$
$$RuO_2\ (s) + 0.5\ O_2(g) \Leftrightarrow RuO_3\ (g)$$

Based on the transport reactions and by considering the stoichiometric coefficient of $Na_{3-x}Ru_4O_9$, the following chemical reaction might take place:

$$3\text{-}x\ \text{NaOH (g)} + 4\ \text{RuO}_3\ \text{(g)} \Leftrightarrow \text{Na}_{3-x}\text{Ru}_4\text{O}_9\ \text{(s)} + (3\text{-}x)/2\ \text{H}_2\text{O (g)} + (1.5 + (3\text{-}x)/4)\ \text{O}_2\ \text{(g)}$$

Suitable growth conditions

The suitable growth conditions for $Na_{3-x}Ru_4O_9$ were determined on the basis of thermodynamic calculations. The calulcations were carried out as for the previous systems and are based on the above transport reactions of the educts Na_2CO_3 and RuO_2 [13, p. 214]. For simplicity, the calculations were conducted on the composition $Na_3Ru_4O_9$. At RT, the values reach ΔH^0_{298} = -1953(20) kJmol^{-1} and ΔS^0_{298} = 347(15) Jmol^{-1}K^{-1}. Further temperature-dependent values are listed in the appendix table D.2. ΔH_R and ΔS_R of the above chemical reaction are calculated based on equations 2.7 and 2.6 and are listed in the appendix table D.3. At 1100 K, the transport reaction is close to equilibrium with ΔH_R = - 1630(30) kJmol^{-1}, ΔS_R = -1511(25) Jmol^{-1}K^{-1}, and T_{opt} = 1078 K. The calculation of T_{opt} includes an uncertainty of 100 K [111, p. 242].

As shown in the Li-Ru-O and Li-Ir-Ru-O system, the $p(i)$ of RuO_3(g) requires $T \geq 1300$ K to reach transport-effect values. Since this temperature contrasts T_{opt}, the temperature-dependent $p(i)$ behaviour of NaOH has to be taken into consideration. In this regard, no investigations are known in literature. The following considerations are based on standard data from Barin [6]. At 1100 K, $\Delta_R G$ of the assumed chemical reaction is 225.2 kJ mol^{-1}. Following $\Delta_R G = -RT\,lnK$ [6, p. 28], K is $\sim 2.0{\cdot}10^{-11}$. K can also be expressed by the ratio of $p(i)$ of educts and products with respecting the number of educts/products n (equation 2.11) [6, p. 45]:

$$K = (p^n_{products} \,/\, p^n_{educts}) = (p^3_{products} \,/\, p_{H_2O}) = 2.0 \cdot 10^{-11}$$

Since NaOH(g) equals two-thirds of the reaction product, 2NaOH(g) + CO_2(g), of the assumed transport reaction, the $p(i)$ of one mole of NaOH(g) or H_2O(g) is calculated:

$$p_{NaOH} = 2 \cdot (p(\text{H}_2\text{O}) \cdot K)^{1/3}$$
$$p_{H_2O} = (p(\text{NaOH})/2)^3 / K$$

Following the requirement for reaching transportability ($p_{NaOH} \geq 10^{-5}$ atm), $p(H_2O)_{min}$ equals $6.3{\cdot}10^{-6}$ atm at 1100 K. Since crystal growth experiments were conducted in air and the growth setup was modified to enable gas exchange, $p(H_2O)$ is considered to be connected to the relative humidity in the laboratory. Since $p(H_2O)$ reaches a value of $\sim$ 0.02 atm at standard conditions, the transport of NaOH is assumed to be feasible. Accordingly to the Li-Ru-O system, these investigations show a different $p(i)$ behavior of NaOH and RuO_3.

Proposed reaction cycle for the growth of $Na_{3-x}Ru_4O_9$

Accordingly to the previous growth systems, the reaction mechanism behind the growth process yielding $Na_{3-x}Ru_4O_9$ is assumed to consist of two intertwining transport reactions (figure 7.1). Here, $Na_2O(s)$ and $RuO_2(s)$ react with $H_2O(g)$ and $O_2(g)$ and form the transport-effective species NaOH(g) and $RuO_3(g)$ [13, p. 214] and [38, p. 168]. Subsequently, these gaseous reaction products are assumed to undergo a joint reaction forming $Na_{3-x}Ru_4O_9$. After the joint reaction, $H_2O(g)$ and $O_2(g)$ can re-enter the reaction cycle. During growth attempts, $N_2(g)$ was inserted into the system through slits in the crucible wall (figure 2.4). Further, $CO_2(g)$ did not participate in the reaction cycles since it was able to escape the system through the slits. The conducted growth experiments in the Na-Ru-O system are listed in table 7.1 and include information on the growth method and conditions, the setup, and the growth results.

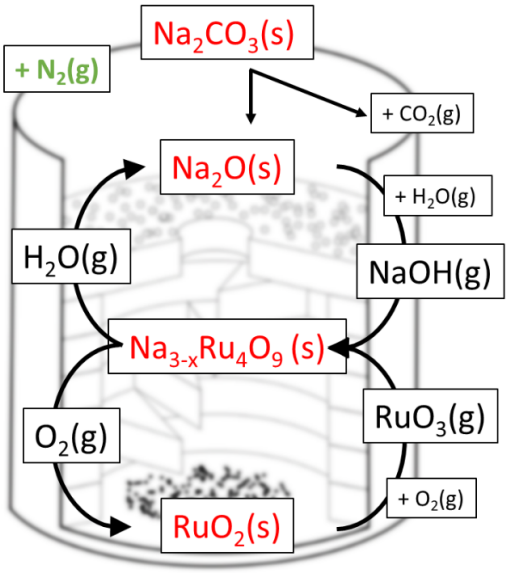

Figure 7.1: Reaction cycle for the growth of $Na_{3-x}Ru_4O_9$ by the CVTR method. After the decomposition of Na_2CO_3 into Na_2O and CO_2 [81], two separate chemical reactions, $Na_2O(s) + H_2O(g) \Leftrightarrow 2\ NaOH(g)$ [38, p. 168] and $RuO_2(s) + 0.5\ O_2(g) \Leftrightarrow RuO_3(g)$ [13, p. 217] are assumed to intertwine with each other to yield $Na_{3-x}Ru_4O_9$. The gaseous substances H_2O and O_2 can re-enter the reaction cycle. To prevent the back-reaction of CO_2 and the formation of a carbonatic compound, N_2 is inserted through slits into the system. Consequently, CO_2 can escape the system and does not contribute to the reaction cycle.

Table 7.1: Growth experiments in the Na-Ru-O system including temperature programs, growth conditions and growth results. Growth attempts with signature V were conducted using the CVTR method, growth attempts with S mark solid-state reaction experiments. Abbreviations for yielded compounds: Na_{3-x} = $Na_{3-x}Ru_4O_9$; Na_{27} = $Na_{27}Ru_{14}O_{48}$. *CVTR experiments were conducted in the second furnace.

Name	Program	Na_2CO_3:RuO_2	Crucible	Compound	Position	Note
S1	293 K to 1373 K in 24 h holding 1373 K for 36 h cooling to 873 K with 3 K/h cooling to 293 K in 48 h	0.86:1	T1	Na_{3-x} Na_{3-x}	bottom inner lid	
S2	20 K to 1223 K in 24 h holding 1223 K for 36 h cooling to 873 K with 3 K/h cooling to 293 K in 48 h	0.86:1 1.02:1	T2 T3	Na_{3-x} Na_{27}	bottom outer lid	
S3	293 K to 1173 K in 24 h holding 1173 K for 36 h cooling to 873 K with 3 K/h cooling to 293 K in 48 h	0.86:1	T2	Na_{27} Na_{27}	bottom outer lid	
S4	293 K to 1223 K in 24 h holding 1223 K for 36 h cooling to 873 K with 3 K/h cooling to 293 K in 48 h	1.02:1	T3	Na_{27}	outer lid	
V1*	14 days 1273 K, N_2	4:1	T1x	-	-	T too high
V2*	14 days 1173 K, N_2	3:1 4:1	T1x T2x	Na_{3-x} RuO_2	bottom body bottom body	centred position, slits, 2 stairs left position, slits, 2 stairs

7.1.2 $Na_{3-x}Ru_4O_9$

In the literature, a variety of synthesis methods led to the growth of poly- or single crystalline $Na_{3-x}Ru_4O_9$ compounds [22, 29, 102, 113, 137], but also of deoxygenated $Na_2Ru_4O_{9-\delta}$ [22]. In the present work, first growth investigations were conducted by the CVTR method.

Growth by Chemical Vapour Transport Reaction

For growth experiments yielding $Na_{3-x}Ru_4O_9$, Na_2CO_3 was placed on top of the plate with hole, whereas RuO_2 was placed at the bottom of the modified setup (figure 2.4). The crucible was placed in the middle of the muffle furnace with a slit in front of the N_2 gas inlet. Considering the $p(i)$ behaviour of RuO_3 and the growth temperature of lithium ruthenates, the first growth attempt was conducted at 1273 K. No crystallisation was observed, though the depletion of the Na_2CO_3 body. This is explained by the increased volatility of NaOH with increasing temperature and the escape of the volatiles through the evasive openings of the setup. Hence, at 1300 K the joint reaction of NaOH and RuO_3 was not feasible. To decrease the volatility of NaOH and fulfil T_{opt} = 1078 K $\pm$ 100 K, the experiment temperature was lowered to 1173 K. By applying a Na_2CO_3:RuO_2 ratio of 3:1 and a duration of 14 days, single crystals of $Na_{3-x}Ru_4O_9$ were grown (table 7.1, V2T1x, figure 7.2). Crystal growth was observed close to the slits at the bottom of the crucible. Next to $Na_{3-x}Ru_4O_9$, a small amount of RuO_2 crystals grew, which are recognisable by their triangular shape. In contrast to growth investigations in the Li-Ir-O, Li-Ru-O, and Li-Ir-Ru-O systems, no crystal growth occurred at the stairs of the spiral staircase, which is explained by the excape of volatiles through the openings of the setup and, hence, a decreased reaction between these. At the bottom of the crucible, black and needle-like crystals of $Na_{3-x}Ru_4O_9$ with metallic luster and a maximum size of 30 µm x 30 µm x 600 µm were obtained (figure 7.2). By maintaining the growth conditions but positioning the slit of the crucible not directly in front of the gas inlet, only RuO_2 crystals grew and no reaction with Na occurred (V2T2x). This observation emphasises the requirement of N_2 insertion into the growth system.

Figure 7.2: Black and needle-like crystals with metallic luster of $Na_{3-x}Ru_4O_9$ grown by the CVTR method using the modified experimental setup with vertical slits to ensure the exchange of gases during the growth attempt. Next to crystals of $Na_3 - xRu_4O_9$, a small amount of RuO_2 crystals grew (top left triangle).

The growth results show the application of the experimental setup for the growth of sodium ruthenates starting from Na_2CO_3 and RuO_2. However, the required evasive openings of the setup led to the favoured escape of volatile compounds from the growth chamber and, hence, resulted in crystals of small amount and size.

Solid-state reaction method

To offer a setup, which is more closed and prevents the escape of volatiles, solid-state reaction experiments were performed (section 2.3). Crystals of $Na_{3-x}Ru_4O_9$ were obtained at a Na_2CO_3:RuO_2 ratio of 0.86:1 and a maximum temperature of 1373 K. They preferably accumulated at the bottom of the crucible forming a fan-like cluster (figure 7.3a). Most elongated crystals were found at the inner walls and lid of the crucible, which is explained by the creep of the reaction product along the inner crucible walls (figure 7.3b). Solid-state reaction experiments led to the growth of black and needle-like $Na_{3-x}Ru_4O_9$ crystals with metallic luster and an increased maximum size of 50 µm x 100 µm x 5000 µm. The needle-like shape is presumably derived from a preferred growth direction along the longest *a*-axis and slower growing (010) and (001) crystal faces (figure 7.3).

Comparable investigations of both growth methods show a difference in required excess of Na_2CO_3. In $Na_{3-x}Ru_4O_9$ compounds, for $x = 0$ to $x = 1$ the stoichiometric Na:Ru ratio is 0.75-0.5 : 1. Whilst for solid-state reaction experiments a Na:Ru ratio of 1.72:1 was used, in CVTR experiments a Na:Ru ratio of 6:1 was applied. This underlines that, due to the isolation and limited escape of educts in solid-state reaction experiments, the required excess of Na_2CO_3 was significantly lower than in CVTR experiments.

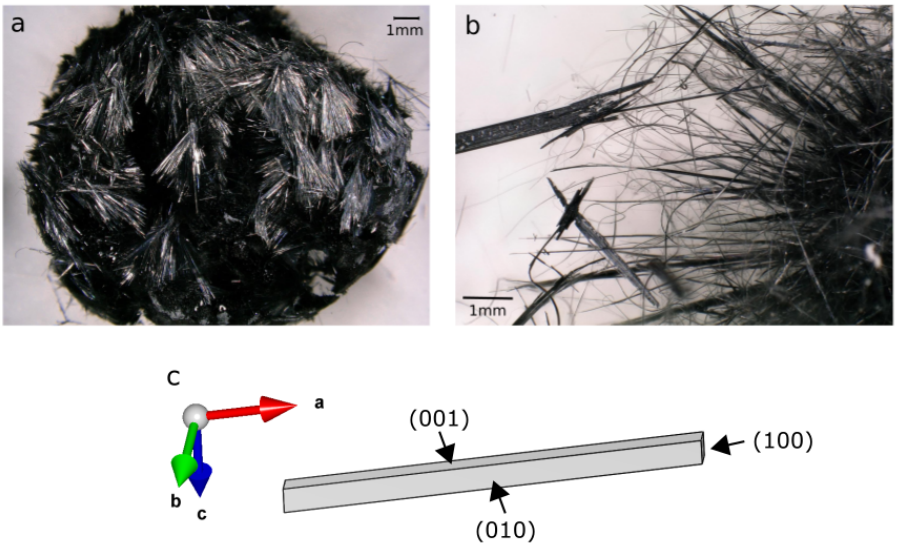

Figure 7.3: Black and needle-like crystals with metallic luster of $Na_{3-x}Ru_4O_9$ from solid-state reaction experiments. (a) Crystals preferably accumulate at the bottom of the crucible forming a cluster of fan-like crystals. (b) Elongated and large crystals are found at the inner walls of the crucibles. (c) Needle-like crystals of $Na_{3-x}Ru_4O_9$ result from the preferred growth direction along the *a*-axis.

To understand the reaction mechanism behind the solid-state reaction of Na_2CO_3 and RuO_2, the temperature program of a growth experiment was replicated by DSC/TG (figure 7.4). To compensate the drift of the TG balance, the TG curve was corrected (section 3.2). The first phase reaction is observed at a temperature below 373 K. Here, a strong endothermic reaction is accompanied by a significant mass loss of $\sim$ 6.5 %. Both observations in the DSC and TG curves can be explained by a dehydration process. Due to the high hygroscopicity of Na_2CO_3, the adsorption of H_2O during sample preparation is assumed. The mass loss of $\sim$ 6.5 % corresponds to a loss of $\sim$ 0.93 molecules H_2O per formula unit. During the heating segment, a second endothermic reaction between 1073 and 1123 K is detected in the DSC curve. It is accompanied by a continuous mass loss in the TG curve. Here, the mass loss is strongest during the endothermic reaction. This reaction is explained by the decomposition of Na_2CO_3 into Na_2O(s) and CO_2(g), which volatilises and leads to the mass loss in the TG curve. This observation is in accordance with the decomposition reaction of Na_2CO_3 described by Motzfeldt [81]. Since the mass loss is observed throughout the whole temperature range, the decomposition reaction is characterised as a slow proceeding reaction, which coincides with results of Kim and Lee [54]. The calculation of the expected residual mass after the decomposition reaction leads to a value of $\sim$ 76.4 %, which agrees with the observed residual mass of $\sim$ 76.3 % after the heating sequence. On the basis of these observations, the reaction mechanism yielding $Na_{3-x}Ru_4O_9$ crystals is described as a solid-state reaction with release of a gaseous phase.

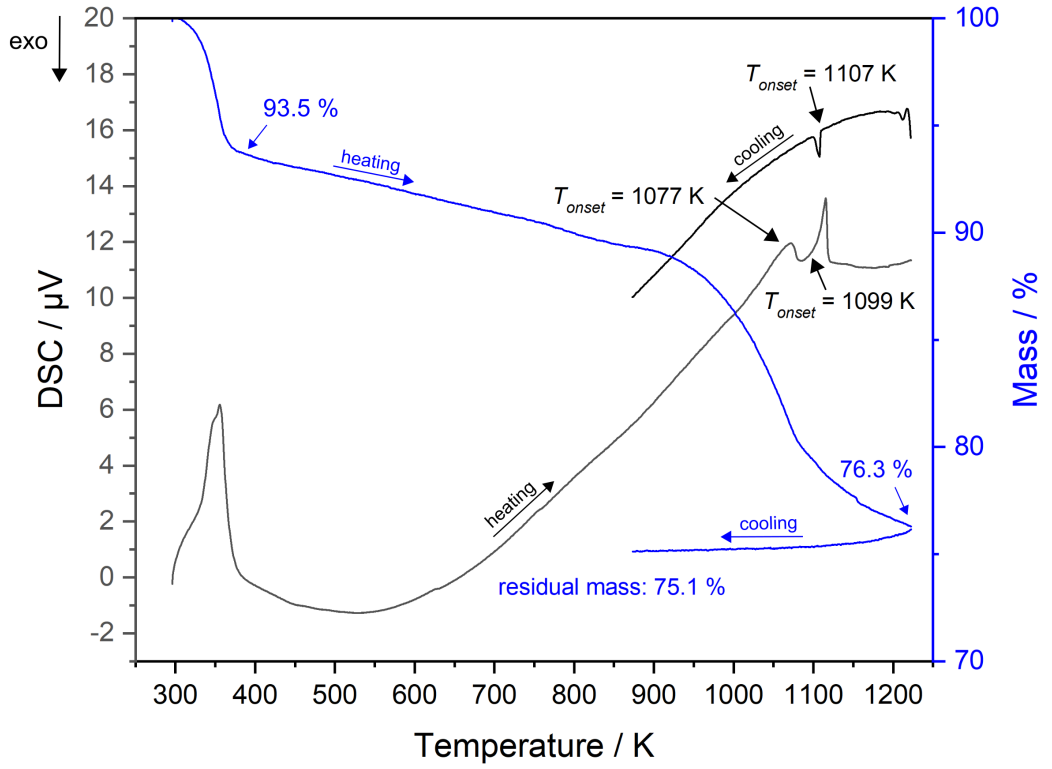

Figure 7.4: DSC/TG measurement of a homogeneous mixture of $Na_2CO_3 \cdot H_2O$ and RuO_2 in a ratio of 1.02:1. The heating rate up to 1223 K was set to 5 K/ min and the cooling rate down to 873 K was set to 3 K/ min.

During the cooling sequence, an exothermic reaction was observed at 1107 K. Since a P-XRD analysis after the DSC/TG measurement confirmed a sodium ruthenate compound, the exothermic signal might correspond to its crystallisation process. The small mass loss to a residual mass of $\sim$ 75.1 % might be explained by the partial escape of volatiles during the crystallisation process.

7.1.3 $Na_{27}Ru_{14}O_{48}$

The growth of $Na_{27}Ru_{14}O_{48}$ was observed as a secondary product of solid-state reaction experiments yielding $Na_{3-x}Ru_4O_9$. At a Na_2CO_3:RuO_2 ratio of 1.02:1 and a maximum temperature of 1223 K (table 7.1 S2, S4), crystal growth of $Na_{27}Ru_{14}O_{48}$ was observed at the outer rim of the lid next to the ceramic glue (figure 7.5). This growth position is explained by the creep of the reaction product up the crucible wall and the subsequent crystallisation at the ceramic glue. Due to the high alkalinity of Na_2CO_3 and NaOH, the ceramic glue shows corrosion. The weighing of the crucible prior and after the growth attempt revealed a small weight loss of $\sim$ 2 %. At a lower temperature and a lower educt ratio, crystal growth also occurred inside the crucible (table 7.1 S3). However, the largest amount of crystals was obtained in attempts S2 and S4 with a maximum temperature of 1223 K, a ratio of 1.02:1, and a growth at the outer rim of the crucible.
In comparison to the calculated Na:Ru ratio of 1.92:1 for $Na_{27}Ru_{14}O_{48}$ compounds and the applied Na_2CO_3 excess of 10 % in study of Allred et al. [3], in the present work crystal growth of $Na_{27}Ru_{14}O_{48}$ was obtained using a Na_2CO_3 excess of 6 % but also using a contrasting RuO_2 excess of 10 % (S3 and S4, respectively). These differences are explained by the experimental setup. Whilst in the study of Allred et al. [3] growth attempts were conducted in air, in the present work the application of closed crucibles, which prevented the escape of the volatile educts, led to a lower required Na_2CO_3 excess. Summarising, crystals of $Na_{27}Ru_{14}O_{48}$ are black and columnar, exhibit an uneven surface, and grew in a maximum size of 100 µm x 50 µm x 50 µm (figure 7.5).

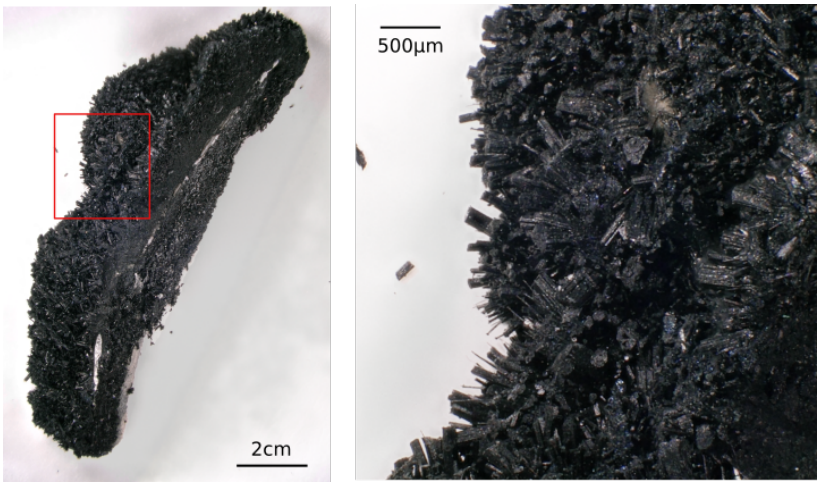

Figure 7.5: Growth of black and columnar crystals of $Na_{27}Ru_{14}O_{48}$ at the outer rim of the crucible close to the ceramic glue. The red box on the left is enlarged on the right.

7.2 Material characterisation

7.2.1 Structural aspects

In the present work, $Na_{3-x}Ru_4O_9$ and $Na_{27}Ru_{14}O_{48}$ are investigated by SC-XRD. For $Na_{3-x}Ru_4O_9$ compounds, a variety of structures was published [29, 103, 137]. In contrast, the structure of $Na_{27}Ru_{14}O_{48}$ was only reported once by Allred et al. [3] and described structural disorder.

7.2.1.1 $Na_{3-x}Ru_4O_9$

In the present work, single crystals of $Na_{3-x}Ru_4O_9$ were grown by the CVTR method and the solid-state reaction method. In the following, the obtained structural models of crystals grown by both methods are compared with each other and literature data. The structural models are listed in tables 7.3 and 7.4 and include the parameters of SC-XRD measurements and of the refinement strategies. Bond distances and BVS are listed in appendix tables D.4 and D.6. Atomic displacement parameters were refined anisotropically (appendix tables D.5 and D.7).
In the literature, a variety of structural models of $Na_{3-x}Ru_4O_9$ is reported by Darriet [29], Regan et al. [103], and Yogi et al. [137] (appendix table D.1, section 1.1.4.1). In the present work, the structures of $Na_{3-x}Ru_4O_9$ crystals were solved and refined in space group $C2/m$ comparable to the structural models of Darriet [29] and Regan et al. [103] (table 7.2). The latter structural models are listed in appendix tables D.8 and D.9. The comparison of lattice parameters of structural models of $Na_{3-x}Ru_4O_9$ ($C2/m$) of the present work and of Darriet [29] and Regan et al. [103] shows close similarity, whereas differences in the Na content are observed (table 7.2). The calculation of BVS leads to high GIIs for $Na_{2.1}Ru_4O_9$ (0.305) [29] and for $Na_{2.7}Ru_4O_9$ (0.233) [103] (appendix tables D.10 and D.11).

Table 7.2: Comparison of lattice parameters a, b, c, β, unit-cell volume V, global instability indices (GII) and quality indicators of refinement (R_1 and Goodness of fit (GOF)) of $Na_{3-x}Ru_4O_9$ structures of the present work and published in the literature [29, 103]. Detailed information on these structural models including results from bond-valence calculations are found in appendix D.

Chemical formula	$Na_{2.1}Ru_4O_9$	$Na_{2.73}Ru_4O_9$	$Na_{2.55(8)}Ru_4O_9$	$Na_{2.36(3)}Ru_4O_9$
Authors	Darriet [29]	Regan et al. [103]	present work	present work
Growth method	solid-state reaction	solid-state reaction	CVTR	solid-state reaction
	$C2/m$	$C2/m$	$C2/m$	$C2/m$
a / Å	23.180(6)	23.246(1)	23.20(2)	23.2474(12)
b / Å	2.831(2)	2.8411(1)	2.845(3)	2.81840(10)
c / Å	10.990(4)	11.0394(6)	10.954(10)	11.0186(6)
β / °	104.50(3)	104.766(5)	104.42(5)	104.469(2)
V / Å^3	698.22	705.01	700.2(11)	699.05(6)
T / K	298	298	120(2)	120(2)
GII	0.305	0.233	0.143	0.127
R_1	-	0.074	0.0292	0.0133
GOF	-	-	2.797	1.206

Table 7.3: Structural model of $Na_{2.55(8)}Ru_4O_9$ grown by the CVTR method including measurement details, lattice parameters (a, b, c, β), cell volume V, atomic positions with Wyckoff site symmetry, fractional coordinates (x, y, z), and site occupancy factors (SOF). Further information, such as anisotropic atomic displacement parameters for all atom sites, bond valence sums, bond distances and bond angles are given in the appendix.

$Na_{2.55(8)}Ru_4O_9$	
Space group	$C2/m$
Z	4
a, b, c, β	23.20(2) Å, 2.845(3) Å, 10.954(10) Å, 104.42(5)°
V	700.2(11) Å^3
ρ_{calc}	5.763 g cm^{-3}
T	120(2) K
Radiation wavelength	0.71073 Å
Crystal information	
Colour/shape	black with metallic luster, needle
Size	0.021 mm x 0.030 mm x 0.090 mm
Growth conditions	CTR, 1273 K, 14 days, Na_2CO_3:RuO_2 3:1, growth at the bottom
Data collection	
Θ range	1.92° to 27.52°
Independent reflections	959
R_{int}	0.0201
Data reduction	
Absorption correction	numerical
μ	8.653 mm^{-1}
F(000)	1106
Refined parameters	110
Final R-values with I > 2σ(I)	
R_1	0.0292
w_{R2}	0.1017
GOF on F^2	2.797

Structure solution and refinement: SHELXT-2014/5 [114] , SHELXL-2018/3 [115]

Atom	Site	x	y	z	SOF
Ru1	2a	0.0	0.0	0.0	1.0
Ru2	2c	0.0	0.0	0.5	1.0
Ru3	4i	0.05758(3)	0.5	0.31121(8)	1.0
Ru4	4i	0.21452(3)	0.5	0.37861(7)	1.0
Ru5	4i	0.27215(3)	0.0	0.12943(7)	1.0
O1	4i	-0.0586(3)	0.5	0.0122(6)	1.0
O2	4i	0.0293(3)	0.0	0.1849(6)	1.0
O3	4i	0.1352(3)	0.5	0.2786(6)	1.0
O4	4i	0.0770(3)	0.0	0.4442(6)	1.0
O5	4i	-0.0223(3)	0.5	0.3658(6)	1.0
O6	4i	0.2028(3)	0.0	0.5001(7)	1.0
O7	4i	0.2380(3)	0.0	0.2760(6)	1.0
O8	4i	0.2124(3)	0.5	0.0464(6)	1.0
O9	4i	0.3298(3)	0.5	0.1985(6)	1.0
Na1	4i	0.13545(17)	0.0	0.1053(4)	0.968(17)
Na2	4i	0.1423(2)	0.5	0.6024(6)	0.743(19)
Na3	4i	0.0738(4)	0.0	0.8108(8)	0.62(2)
Na4	4i	0.0871(8)	0.5	0.8007(19)	0.22(2)

Table 7.4: Structural model of $Na_{2.36(3)}Ru_4O_9$ grown by solid-state reaction including measurement details, lattice parameters (a, b, c, β), cell volume V, atomic positions with Wyckoff site symmetry, fractional coordinates (x, y, z), and site occupancy factors (SOF). Further information, such as anisotropic atomic displacement parameters for all atom sites, bond valence sums, bond distances and bond angles are given in the appendix.

$Na_{2.36(3)}Ru_4O_9$	
Space group	$C2/m$
Z	4
a,b,c,β	23.2474(12) Å, 2.81840(10) Å, 11.0186(6) Å, 104.469(2)°
V	699.05(6) Å^3
ρ_{calc}	5.746 g cm^{-3}
T	120(2) K
Radiation wavelength	0.71073 Å
Crystal information	
Colour/shape	black with metallic luster, needle
Size	0.028 mm x 0.030 mm x 0.220 mm
Growth conditions	solid-state reaction, maximum temperature 1373 K, Na_2CO_3:RuO_2 0.86:1
Data collection	
Θ range	2.28° to 27.48°
Independent reflections	967
R_{int}	0.0260
Data reduction	
Absorption correction	numerical
μ	4.349 mm^{-1}
F(000)	562
Refined parameters	116
Final R-values with I > 2σ(I)	
R_1	0.0133
w_{R2}	0.0318
GOF on F^2	1.206

Structure solution and refinement: SHELXT-2014/5 [114] , SHELXL-2018/3 [115]

Atom	Site	x	y	z	SOF
Ru1	2a	0.0	0.0	0.0	1.0
Ru2	2c	0.0	0.0	0.5	1.0
Ru3	4i	0.05825(2)	0.5	0.31011(2)	1.0
Ru4	4i	0.21460(2)	0.5	37850(3)	1.0
Ru5	4i	0.27197(2)	0.0	0.12925(2)	1.0
O1	4i	-0.05829(10)	0.5	0.0127(2)	1.0
O2	4i	0.02892(10)	0.0	0.1843(2)	1.0
O3	4i	0.13482(10)	0.5	0.2790(2)	1.0
O4	4i	0.07665(11)	0.0	0.4439(2)	1.0
O5	4i	-0.02178(11)	0.5	0.3663(2)	1.0
O6	4i	0.20269(10)	0.0	0.4993(2)	1.0
O7	4i	0.23817(10)	0.0	0.2751(2)	1.0
O8	4i	0.21235(10)	0.5	0.0455(2)	1.0
O9	4i	0.32997(11)	0.5	0.1987(2)	1.0
Na1	4i	0.13585(7)	0.0	0.10391(15)	0.892(7)
Na2	4i	0.14323(9)	0.5	0.6042(2)	0.752(8)
Na3	4i	0.07624(16)	0.0	0.8186(3)	0.515(9)
Na4	4i	0.0876(3)	0.5	0.7990(6)	0.232(7)

The crystal structure of $Na_{3-x}Ru_4O_9$ ($C2/m$) is characterised by a tunnel structure with single, double, and triple groups of edge-sharing RuO_6 octahedra, which are interconnected via common oxygen ligands (figure 1.8, section 1.1.4.1). In accordance with the structural models of Darriet [29] and Regan et al. [103], the Ru-Ru distances clearly differ between edge-sharing and corner-connected RuO_6 octahedra. In the double and triple groups, which consist of edge-sharing RuO_6 octahedra, the Ru-Ru distances are significantly shorter (*e.g.* double groups Ru5 - Ru5 = 3.109(3) Å) than between the different types of groups, which are connected via common O atoms (*e.g.* triple and single group: Ru1 - Ru3 = 3.628(4) Å). The large cavities in between the RuO_6 groups, that form a tunnel-like arrangement along the *b*-axis, are filled with chains of four crystallographic inequivalent Na atoms, which is in contrast to three Na atoms in the structures published by Darriet [29] and Regan et al. [103] (figure 7.6).

In comparison to the published structural models by Darriet [29] and Regan et al. [103], the two structural solutions of the present work show differences in the fractional coordiantes of Ru and O atomic sites on the second or third decimal place. The most significant difference is found for Na atomic sites. Whilst the Na1, Na2, and Na3 positions are similar to the reported ones, a further Na position, Na4, was determined based on the residual electron density (figure 7.6). For both structural solutions, a refinement without the Na4 position was not reasonable and resulted in a poor GOF. In comparison to Na3, the Na4 position is situated at similar *x* and *z* but shows a shift of 0.5 for *y* (figure 7.6). The refinement of ADPS of all atomic positions showed isotropic ellipsoids for Ru and O atomic sites, but more anisotropic behaviour for Na (appendix tables D.5 and D.7). For all Na atomic sites, the largest atomic displacement parameter is U_{22}, which results in elongated displacement ellipsoids in direction of the *b*-axis, *i.e.* along the tunnels (figure 7.6). The most elongated displacement ellipsoids are found for Na2 and Na3, whereas the lowest anisotropy is found for Na1. This might be explained by the highest coordination number of the Na1 atomic site. The elongation of displacement ellipsoids in direction of the tunnels points towards a mobility of Na atoms and, hence, suggests conducting behaviour along the tunnel structure of $Na_{3-x}Ru_4O_9$. This coincides with results of Cao et al. [22] who reported metallic conductivity along the *b*-axis.

Due to different SOF of Na, the Na content in the two structural models of the present work varies. Whilst the occupancies of the Na2 and Na4 positions are similar, the Na1 and Na3 positions are $\sim$ 10 % less occupied in the structural model of a crystal grown from solid-state reaction experiments in comparison to the structural model from CVTR experiments. This results in a lower Na stoichiometric coefficient of 2.36(2) (solid-state reaction) compared to 2.55(8) (CVTR). Next to a deficiency in Na, the refinement of Ru deficiency was attempted as well, but led to high correlations between the SOF and the overall scaling factor. Hence, Ru deficiency was considered as not reasonable.

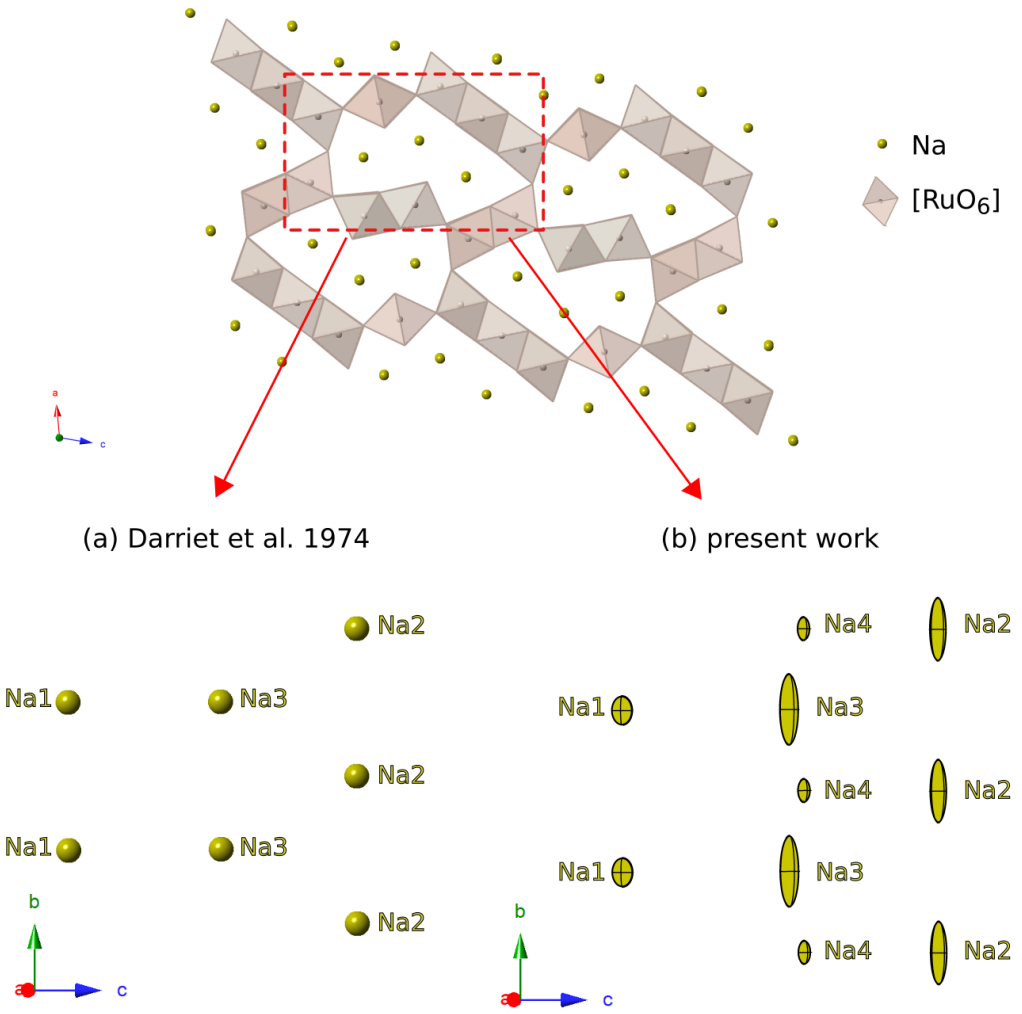

Figure 7.6: Na atomic positions in the $Na_{3-x}Ru_4O_9$ structure. In the upper section, a topview of the tunnel-like structure is shown. The red dashed box marks the large cavities, in which the Na1-Na4 atoms are situated and which are enlarged in the lower part in perpendicular view direction. For the crystal structure of (a) Darriet [29] no atomic displacement parameters of Na1-Na3 were refined, whereas (b) for the structure of the present work the atomic displacement parameters of Na1-Na4 were refined anisotropically.

Based on bond-valence calculations, a differing oxidation state for Ru was tested. In literature, the Ru^{3+}– O bond length is defined with 2.0265 Å and the Ru^{4+}– O bond length with 1.9840 Å [17]. Based on these values, the oxidation state of Ru2 can be determined as Ru^{3+}, whereas the Ru – O bond lenghts of Ru1, Ru3, Ru4, and Ru5 points towards a tetravalent oxidation state, Ru^{4+}. The RuO_6 octahedra, which surround Ru2, are situated in the centred position of the triple chain: Hence, they share edges with neighbouring RuO_6 octahedra with centred Ru^{4+} (figure 1.8). This is in contrast to the reported structural models of Darriet [29] and Regan et al. [103], where only a trivalent oxidation

state of Ru was described. By considering the Ru oxidations states, the GII of both structural models are 0.143 and 0.127 (solid-state reaction and CVTR, respectively). Details on the calculations are listed in appendix tables D.4 and D.6. The differences in GII are explained by small deviations in atomic positions of both structural models. In comparison to the structures by Darriet [29] and Regan et al. [103], the calculated GII are lower (table 7.2). By recalculating the BVS and considering the Ru oxidation states, lower GIIs of 0.167 and 0.177 for the structural models of Darriet [29] and Regan et al. [103] are yielded (appendix tables D.12 and D.13). However, these calculations do not result in lower GIIs than obtained for the structural models of the present work.

Concludingly, both structural models of the present work are in close comparison to the structural models of Darriet [29] and Regan et al. [102]. The non-stoichiometry of Na sites results from their partial vacancies, ergo vacancy defects within the structure, which allows for Na^+ migration within the tunnels [91]. Since the Na stoichiometric amount differs between structural models, it is considered as synthesis-dependent. The assignment of Ru oxidation states based on bond-valence calculations led to a lowered GIIs of structural models of the present work and the literature [29, 103]. Therefore, this assignment might give an improvement of the structural model of $Na_{3-x}Ru_4O_9$ with space group $C2/m$.

7.2.1.2 $Na_{27}Ru_{14}O_{48}$

In the present work, on the basis of SC-XRD data the crystal structure of $Na_{27}Ru_{14}O_{48}$ was solved and refined in $P\bar{1}$ symmetry. In table 7.5, the measurement and refinement parameters are listed. Since the refinement of ADPs led to negative values, these were refined isotropically. In the following, the structural solution of a crystal, which grew at the outer rim of the crucible, is discussed.

Table 7.5: Structural model of $Na_{25.7(1)}Ru_{14}O_{48}$ including measurement details, lattice parameters (a, b, c, β), cell volume V, atomic positions with Wyckoff site symmetry and oxidation state, fractional coordinates (x, y, z), isotropic atomic displacement parameters (U_{iso}), site occupancy factors (SOF) and bond valence sums (BVS). The resulting global instability index is 0.129. The U_{iso} of Ru1 had to be restrained to prevent negative atomic displacement parameters.

$Na_{25.7(1)}Ru_{14}O_{48}$	
Space group	$P\bar{1}$
Z	1
a, b, c	5.7549(6) Å, 10.9661(11) Å, 18.1427(18) Å
α, β, γ	88.509(3)°, 87.262(3)°, 75.190(3)°
V	1105.55(19) Å^3
ρ_{calc}	4.211 g cm^{-3}
T	120(2) K
Radiation wavelength	0.71073 Å
Crystal information	
Colour/shape	black with metallic luster, rectangular
Size	0.045 mm x 0.095 mm x 0.105 mm
Growth conditions	solid-state reaction, outer rim of crucible,
	T_{max} = 1223 K, Na_2CO_3:RuO_2 1.02:1
Data collection	
Θ range	1.92° to 27.54°
Independent reflections	5075
R_{int}	0.0332
Data reduction	
Absorption correction	numerical
μ	5.034 mm^{-1}
F(000)	1297
Refined parameters	265
Final R-values with I > 2σ(I)	
R_1	0.0702
GOF on F^2	1.133

Structure solution and refinement: SHELXT-2014/5 [114] , SHELXL-2018/3 [115]

– continued from previous page

Atom	Site	Ox. state	x	y	z	U_{iso} / Å^2	SOF	BVS
Ru1	1*a*	3+	0.0	0.0	0.0	0.002	1.0	3.031(25)
Ru2	2*i*	5+	-0.25498(15)	0.23650(8)	-0.09691(5)	0.00274(19)	1.0	4.874(47)
Ru3	2*i*	5+	0.02806(15)	0.02922(8)	0.17148(5)	0.00213(19)	1.0	4.936(45)
Ru4	2*i*	5+	-0.21629(15)	0.26229(8)	0.07437(5)	0.00205(19)	1.0	4.991(47)
Ru5	1*g*	4+	0.0	-0.5	0.5	0.0026(6)	0.857(10)	3.916(39)
Ru6	2*i*	5+	-0.14373(16)	-0.26915(9)	0.39322(5)	0.0047(3)	0.960(6)	4.958(33)
Ru7	2*i*	5+	0.10147(16)	0.46132(8)	0.32966(5)	0.0036(3)	0.964(6)	5.044(53)
Ru8	2*i*	5+	0.27548(17)	0.23077(9)	0.43810(5)	0.0061(3)	0.955(6)	4.958(54)
Na1	2*i*	1+	0.1296(9)	0.4060(4)	0.1533(3)	0.0088(9)	1.0	1.189(13)
Na2	2*i*	1+	0.1491(9)	0.3659(4)	-0.0457(3)	0.0096(9)	1.0	1.112(13)
Na3	2*i*	1+	0.2665(9)	-0.1992(5)	0.2760(3)	0.0102(9)	1.0	1.189(14)
Na4	2*i*	1+	0.3959(10)	0.2017(5)	0.2468(3)	0.0176(11)	1.0	1.052(12)
Na5	2*i*	1+	-0.4471(9)	0.5074(5)	0.1834(3)	0.0132(10)	1.0	1.121(14)
Na6	2*i*	1+	-0.3988(9)	-0.0733(5)	0.1582(3)	0.0121(10)	1.0	1.156(13)
Na7	2*i*	1+	0.1185(9)	0.3169(5)	-0.2199(3)	0.0125(10)	1.0	1.332(15)
Na8	2*i*	1+	-0.0295(9)	0.0869(5)	0.3397(3)	0.0067(16)	0.93(2)	1.235(14)
Na9	2*i*	1+	-0.6243(9)	0.1408(5)	0.0506(3)	0.0068(16)	0.93(2)	1.142(13)
Na10	2*i*	1+	0.1901(11)	-0.1170(6)	0.4937(3)	0.016(2)	0.91(3)	1.069(14)
Na11	2*i*	1+	0.5417(12)	-0.0213(6)	0.3541(4)	0.0297(14)	1.0	0.943(13)
Na12	2*i*	1+	0.4141(11)	-0.3745(6)	0.4249(3)	0.010(2)	0.80(3)	0.994(14)
Na13	2*i*	1+	0.6705(11)	0.3671(6)	0.3605(3)	0.009(2)	0.78(2)	1.157(15)
Na14	1*e*	1+	0.5	0.5	0.0	0.034(2)	1.0	1.179(11)
O1	2*i*	2-	-0.0154(14)	-0.1821(7)	0.0176(4)	0.0029(14)	1.0	1.915(19)
O2	2*i*	2-	-0.4536(14)	0.2890(7)	-0.0049(4)	0.0036(14)	1.0	2.286(24)
O3	2*i*	2-	0.1289(14)	-0.3611(7)	0.3291(4)	0.0057(15)	1.0	2.175(25)
O4	2*i*	2-	-0.2189(14)	0.0682(7)	0.0838(4)	0.0029(14)	1.0	2.008(20)
O5	2*i*	2-	0.0470(14)	0.2019(7)	0.1428(4)	0.0044(14)	1.0	1.961(25)
O6	2*i*	2-	0.5679(17)	0.1785(9)	0.3887(5)	0.0156(18)	1.0	2.030(32)
O7	2*i*	2-	0.0216(14)	-0.1515(7)	0.1744(4)	0.0059(15)	1.0	2.279(25)
O8	2*i*	2-	0.5849(17)	-0.2124(9)	0.4645(5)	0.0157(18)	1.0	2.135(31)
O9	2*i*	2-	-0.1496(15)	0.4192(8)	0.0628(4)	0.0074(15)	1.0	1.999(30)
O10	2*i*	2-	-0.2604(14)	0.0457(7)	-0.0770(4)	0.0035(14)	1.0	1.868(19)
O11	2*i*	2-	-0.5262(15)	0.2714(8)	-0.1528(5)	0.0079(15)	1.0	1.932(29)
O12	2*i*	2-	0.0788(15)	0.2864(8)	0.3511(5)	0.0080(15)	1.0	2.141(29)
O13	2*i*	2-	0.0384(16)	-0.3245(8)	0.4923(5)	0.0116(17)	1.0	1.937(24)
O14	2*i*	2-	0.2851(16)	-0.5746(8)	0.4315(5)	0.0122(17)	1.0	1.920(23)
O15	2*i*	2-	0.2694(14)	0.0106(7)	0.2384(4)	0.0052(14)	1.0	1.990(26)
O16	2*i*	2-	0.8248(16)	-0.4611(8)	0.4095(5)	0.0107(17)	1.0	2.135(26)
O17	2*i*	2-	-0.1854(15)	0.3906(8)	-0.1161(5)	0.0088(16)	1.0	1.918(30)
O18	2*i*	2-	0.1961(16)	0.0795(8)	0.4410(5)	0.0103(16)	1.0	2.022(34)
O19	2*i*	2-	-0.2259(14)	0.0661(7)	0.2365(4)	0.0062(15)	1.0	2.024(28)
O20	2*i*	2-	-0.1175(16)	0.4830(8)	0.2568(5)	0.0129(17)	1.0	1.994(32)
O21	2*i*	2-	0.6395(18)	-0.2353(9)	0.3195(5)	0.0177(19)	1.0	1.928(33)
O22	2*i*	2-	-0.4663(14)	0.3057(7)	0.1399(4)	0.0064(15)	1.0	2.000(28)
O23	2*i*	2-	0.3744(16)	0.4118(8)	0.2736(5)	0.0115(17)	1.0	2.140(33)
O24	2*i*	2-	-0.0446(15)	-0.1230(8)	0.3848(5)	0.0096(16)	1.0	1.806(32)

By comparing the crystal structure of $Na_{27}Ru_{14}O_{48}$ obtained in the present work with the structure of Allred et al. [3], slightly smaller lattice parameters result in a decreased V of about 1 % (table 7.6). This is due to the lower measurement temperature of 120(2) K compared to the RT measurement in Allred et al. [3]. In the present work, the quality indicators R_{int}, R_1, and GOF are higher. However, the GIIs of both structural models are almost similar.

Table 7.6: Comparison of lattice parameters a, b, c, α, β, γ, quality indicators of refinement (R_1, R_{int}, Goodness of fit (GOF)), and global instability indices (GII) of $Na_{27}Ru_{14}O_{48}$ of the present work and reported by Allred et al. [3].

Compound	$Na_{27}Ru_{14}O_{48}$	
Space group	$P\bar{1}$	
Authors	present work	Allred et al. [3]
a / Å	5.7549(6)	5.7763(4)
b / Å	10.9661(11)	10.9910(9)
c / Å	18.1427(18)	18.2042(13)
α / °	88.509(3)	88.517(4)
β / °	87.262(3)	87.194(3)
γ / °	75.190(3)	75.165(3)
V / Å^3	1105.55(19)	1115.77(14)
T / K	120(2)	296(2)
R_{int}	0.0332	0.0231
R_1	0.0702	0.0424
GOF	1.134	1.067
GII	0.129	0.126

The crystal structure of $Na_{27}Ru_{14}O_{48}$ is mainly characterised by two isolated Ru_7O_{24} clusters A and B with Na ions in between (section 1.1.4.2, figure 1.9, appendix table D.14). In accordance with Allred et al. [3], in both clusters the Ru cation of the central RuO_6 octahedron has site symmetry $\bar{1}$. The central Ru of cluster A is Ru1 and the one of cluster B is Ru5 (figure 7.7). Within each cluster, the Ru - Ru distances deviate at a maximum of about 1.7 % (Ru1) and 2.2 % (Ru5) from each other with an average Ru - Ru distance of 3.15(2) Å and 3.14(3) Å, respectively. Further, the average angle between the surrounding Ru with respect to the centered Ru is in both clusters 60.0(1)°. The tilting between the clusters is 16.12(3)°, which is slightly lower than reported by Allred et al. [3]. As a consequence, the closest Ru - Ru distance between both clusters (5.4776(9) Å) is about 5 % shorter than in Allred et al. [3].

On the basis of bond-valence calculations, the oxidation state was set to 3+ for Ru1 (cluster A) to 4+ for Ru5 (cluster B, table 7.5). In both clusters, all surrounding Ru ions are in oxidation state +5. As a result, the mean oxidation state of Ru is +4.71 in cluster A and +4.86 in cluster B. During data processing, the refinement of SOF of Ru positions was attempted. For the Ru5 - Ru8 positions (cluster B) partial occupancy was refined. Based on residual electron density, four additional atomic positions, Ru5A to Ru8A, were found (figure 7.7, appendix table D.15). These additional atomic positions are closely situated to the respective Ru5-Ru8 atoms with distances of only 0.5-1 Å, low SOF of only 5 %, and build up an almost hexagonal cluster B2 itself (figure 7.7a). This coincides with the study of Allred et al. [3] and explained by the occurrence of stacking faults inside the structure with a probability of 5 %. By cumulating the site occupancies, for every Ru position an overall occupancy of 1.0 is reached. In contrast to results of Allred et al. [3], residual electron density was only found close to cluster B. Cluster B2 is canted by $\sim 22°$ from cluster B, which leads to an almost similar orientation of the B2 and the A cluster with an angle of $\sim 174°$ in between (figure 7.7b).

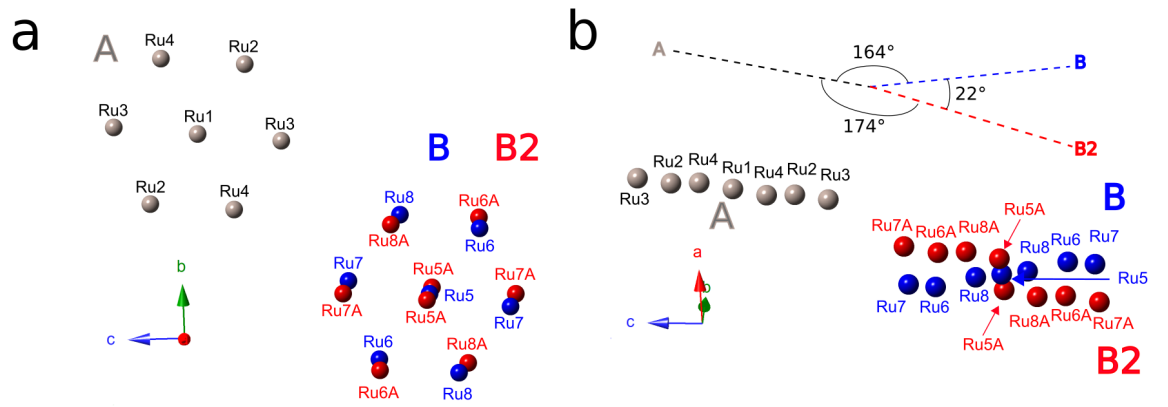

Figure 7.7: Arrangement of clusters in the $Na_{27}Ru_{14}O_{48}$ structure of the present work. Two different clusters with central Ru1 (A, light grey) and Ru5 (B, blue) were characterised. Close to the B cluster, the additional atomic positions Ru5A to Ru8A build up the B2 cluster (red). (a) Position of Ru atomic positions in the clusters. (b) Orientation of clusters to each other: The angle between A and B cluster is 164°. Due to the canting of the B2 cluster, a similar orientation of B2 and A is yielded (174°). The simplified visualisations neglect the depiction of atomic O positions and Na positions.

Next to the refinement of SOF of Ru atomic positions, the SOF of surrounding Na atomic positions were also refined. In contrast to Allred et al. [3], five Na site occupancies were refined. In the structural model of the present work, only one of these atomic positions (Na9) is situated above the A cluster, whereas the others (Na8, Na10, Na12, and Na13) are situated above the B cluster where the occurrence of stacking faults was observed (figure 7.8). These observations are in accordance with Allred et al. [3], who described a correlation between site occupancies and stacking faults.

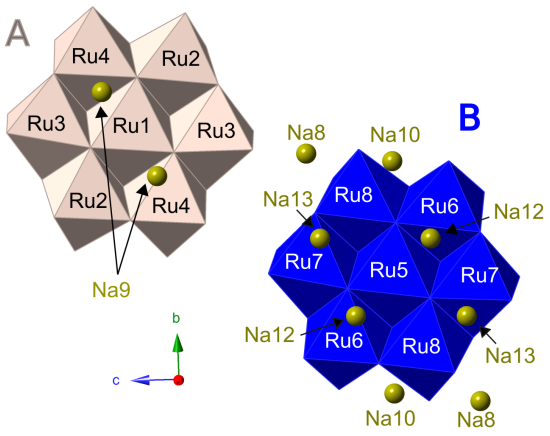

Figure 7.8: In the crystal structure of $Na_{27}Ru_{14}O_{48}$, partially occupied Na sites (yellow) are situated centrally above the Ru clusters of edge-sharing RuO_6 octahedra. Whilst Na9 is situated above the A cluster (grey), Na8, Na10, Na12, and Na13 are close to the B cluster (blue). The simplified visualisations neglects the depiction of atomic O positions.

SC-XRD measurements on further samples either confirmed the structural model or yielded a structural solution with different *c*-axis and α angle (c = 27.6569(16) Å; α = 99.859(2)°, appendix table D.16). The refinement of the crystal structure with the first structural model [3] led to worse refinement results with much diffractional intensity outside integration and a reasonable twin law was not possible to find. This structural solution cannot be derived from different growth conditions or measurement parameters.

In accordance with the first structural model of the present work and of Allred et al. [3], the structure, which is described the following, is characterised by two different Ru_7O_{24} clusters, which are differentiated by their central Ru. However, only the central Ru5 of cluster B has site symmetry $\bar{1}$, whereas the central Ru1 of cluster A has site symmetry 1 (figure 7.9a). Accordingly to the previous structural model, the Ru - Ru distances are almost equal with 3.15(2) Å (Ru1, cluster A) and 3.14(3) Å (Ru5, cluster B), and an average angle of 60.0(7)°. The shortest Ru - Ru distance between both clusters is 5.3242(14) Å, which is slightly shorter than in the first structural model. The shortest Ru - Ru distance between A clusters is larger (5.5105(13) Å). On the basis of bond-valence calculations, the oxidation states of Ru were determined and coincide with the ones of the first structural model.

In figure 7.9, a view along [100] compares the orientation of both unit cells. In part a, the red unit cell of the second structural model (c = 27.6569(16) Å and α = 99.859(2)°) is marked with a red box. In part b, the link between both unit cells is shown. For comparison, the atomic positions of the first structure are shifted by -0.5*b*, -0.5*c*, yielding the centring of the Ru5 position (cluster B) at the origin of the unit cell (black box). Starting from this unit cell, one would yield the red unit cell by changing the α-angle and, hence, increasing the length of the *c*-axis to the Ru1 position. However, this change of unit cell is not allowed due to the $\bar{1}$ site symmetry of the Ru1 and Ru5 atomic positions. Hence, it shows that the unit-cell choice is determined by the site symmetry of the central Ru1 (cluster A).

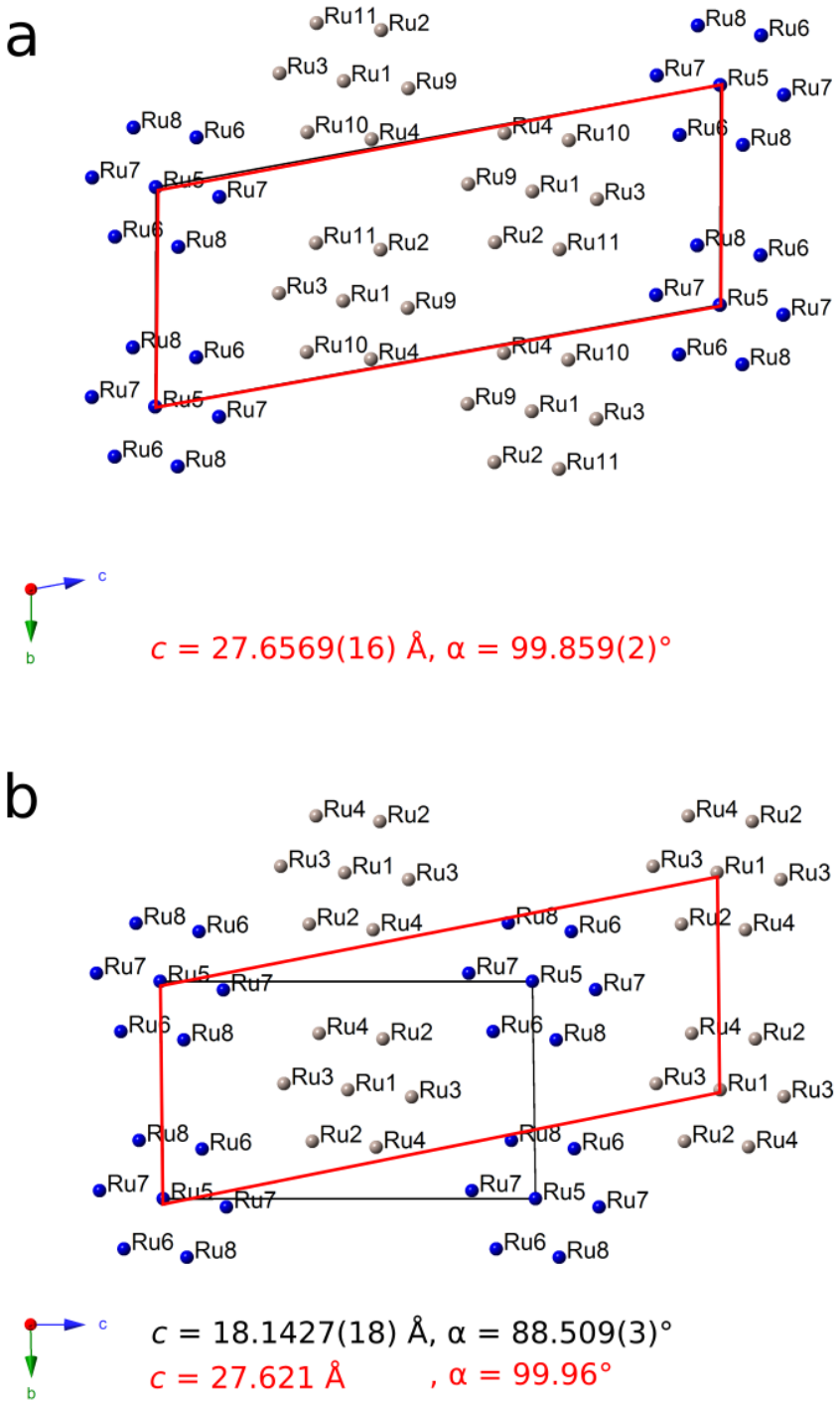

Figure 7.9: Comparison of unit cells of $Na_{27}Ru_{14}O_{48}$. (a) The red unit-cell choice with c = 27.6569(16) Å and α = 99.859(2)° would be yielded if in (b) the α-angle of the black unit cell would be changed, resulting in a different length of the c-axis. Ru cations of cluster A are coloured in light grey and those of cluster B in blue. The simplified visualisations neglects the depiction of Na and O positions.

Further structural investigations show that the orientation of clusters in both structural models differs, which determines the unit-cell choice as well. In the second structural model, the canting between both clusters is 155° (figure 7.10). In direction of the *c*-axis, instead of a BABA stacking order in the first structural model, the stacking order is BAABAA. As before, stacking faults only occur at the B cluster with a probability of 5%. In contrast, only three additional atomic positions were determined based on residual electron density and build up cluster B2 (Ru6A-Ru8A). The canting between cluster B and B2 is 23°. Therefore, the orientation of cluster A and B2 is more equal (178°) than in the first structural model (174°).

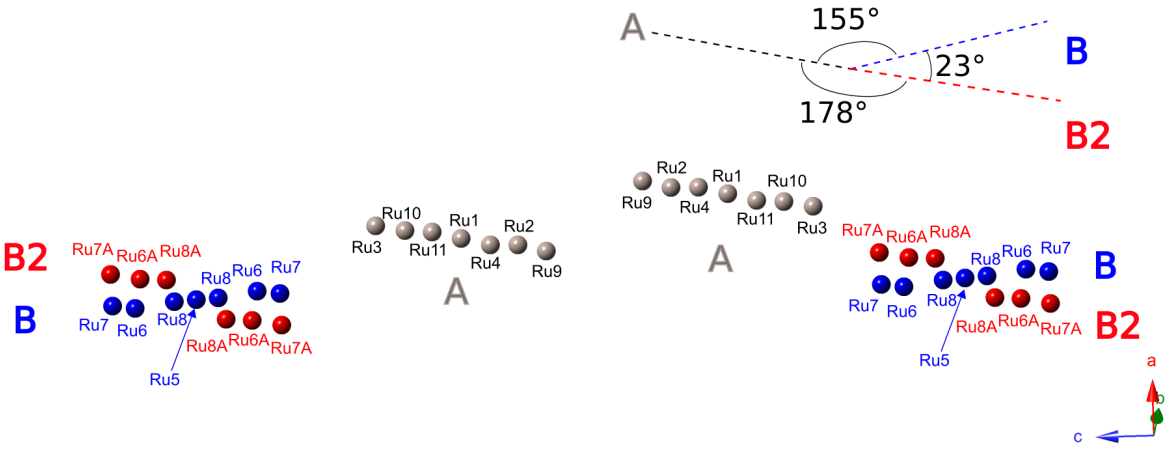

Figure 7.10: Orientation of Ru clusters within the second $Na_{27}Ru_{14}O_{48}$ structure. The angle between A and B cluster is 155°, whereas the canting of the B2 cluster yields a similar orientation of B2 and A with an angle of 178°. The simplified visualisations neglects the depiction of atomic O positions and Na positions.

In both structural models, in relation to the A and B cluster the Na positions are comparable (figure 7.11). However, due to the different stacking sequence, *i.e.* canting and position of clusters in the unit cell, the absolute Na positions in the crystal structure differ. In contrast to the first structural model, all Na atomic positions are partially occupied. This leads to the overall stoichiometry $Na_{37.1(4)}Ru_{21}O_{72}$. For comparison, the stoichiometric coefficients are calculated to 48 oxygen: $Na_{24.8(4)}Ru_{14}O_{48}$. This composition is close to the one of the first structural model ($Na_{25.7(1)}Ru_{14}O_{48}$). A distinct determination of the Na content on the basis of this refinement is not possible due to a correlation between stacking faults and partial occupancies [3]. However, the partial occupation of all Na atomic positions might give a hint for a higher level of disorder in the second structural model. Since partially occupied Na positions are above both clusters, stacking faults might also occur at the A cluster, which coincides with previous discussions of Allred et al. [3]. However, the refinement of the SOF of Na atomic positions was more favoured than of Ru atomic positions of cluster A and an anisotropic refinement of ADPs yielded in negative values.

Overall, the data quality of the second measurement was not sufficient enough to give results which afford the certainty that those are correct. However, these results indicate that a higher structural disorder led to a different atomic positions and, hence, a different unit-cell choice.

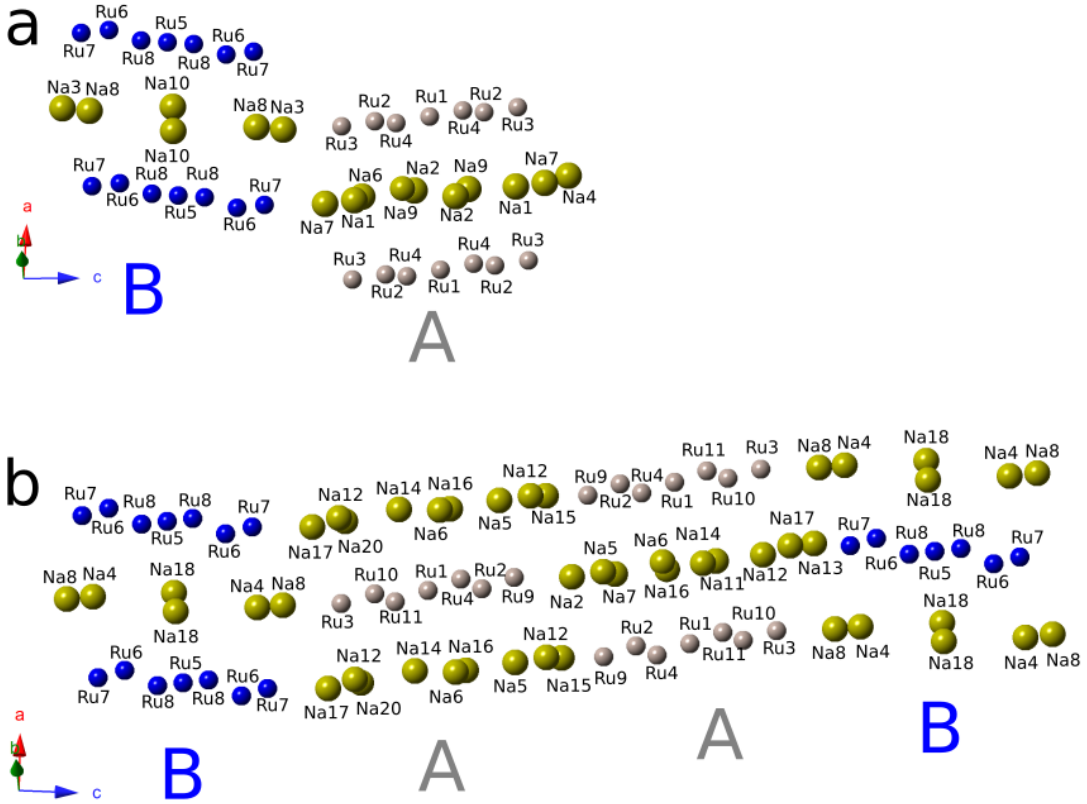

Figure 7.11: Comparison of Na positions (yellow) in the crystal structure of $Na_{27}Ru_{14}O_{48}$ with (a) the published unit cell by Allred et al. [3] and (b) the larger unit cell with deviating orientation and length of the *c*-axis. In both structures, in relation to the A and B clusters (light grey and blue, respectively) the position of Na^+ ions is comparable. The simplified visualisations neglects the depiction of atomic O positions.

7.2.2 Chemical instability

The chemical instability of $Na_{27}Ru_{14}O_{48}$ crystals was observed in air. By exposing the crystals to moisture, the formation of an orange solution was observed. This is in accordance with the investigations of Allred et al. [3] who reported the decomposition of $Na_{27}Ru_{14}O_{48}$ crystals in moisture and the dilution of mineral acids to produce an orange solution. The orange solution could not be characterised neither by Allred et al. [3] nor in the present work. A similar reaction could not be observed for $Na_{3-x}Ru_4O_9$ crystals.

7.2.3 Elemental analysis

Due to the strong reaction of $Na_{27}Ru_{14}O_{48}$ with moisture, attempts to prepare samples for EDX measurements led to the decomposition of the sample. Therefore, only samples of $Na_{3-x}Ru_4O_9$ were analysed by EDX. In contrast to prior EDX analyses, in the case of $Na_{3-x}Ru_4O_9$ the distribution of all three elements (Na, Ru, O) could be measured. The presented and discussed data are in the area of reliability (section 3.3.1).

For first polishing attempts, a fan-like accumulation of single crystals was horizontally embedded. However, in this position the polishing of crystals caused the breaking of single fibres. To overcome this, horizontally embedded and dried samples were cut perpendicular to the preferred growth direction [100]. With this, the top face (100) of the crystals was exposed. The following, the resin block with sample was embedded and could be polished.

After measuring the Na, Ru, and O content with EDX, the Na and Ru contents were converted to nine O to compare the data with the $Na_{3-x}Ru_4O_9$ composition, which was derived from SC-XRD data. In figure 7.12, the converted element distribution of Na and Ru is depicted for two samples, which were grown by the CVTR method and by the solid-state reaction method. In both samples, the distribution of elements is almost homogeneous. Slight variations are within the errors. Due to an uneven sample surface, the measurement errors are enlarged. In relative comparison to the measured values, the errors in both samples are of equal size. Both samples show a similar Ru content of ~ 4.0. In the sample grown by the CVTR method the relative Na content is slightly lower than in the sample grown by the solid-state reaction method ($Na_{2.17(17)}$ and $Na_{2.40(18)}$, respectively). However, due to the enlarged error, the absolute Na contents of both samples coincide. Hence, a difference in Na content between both samples could neither be refuted nor confirmed by EDX due to its poor precision. In comparison to results from SC-XRD, the Na content, which was determined by EDX, differs. Though, this is explained by the poor precision of the EDX method but might also be derived from a time-dependent change in sample composition.

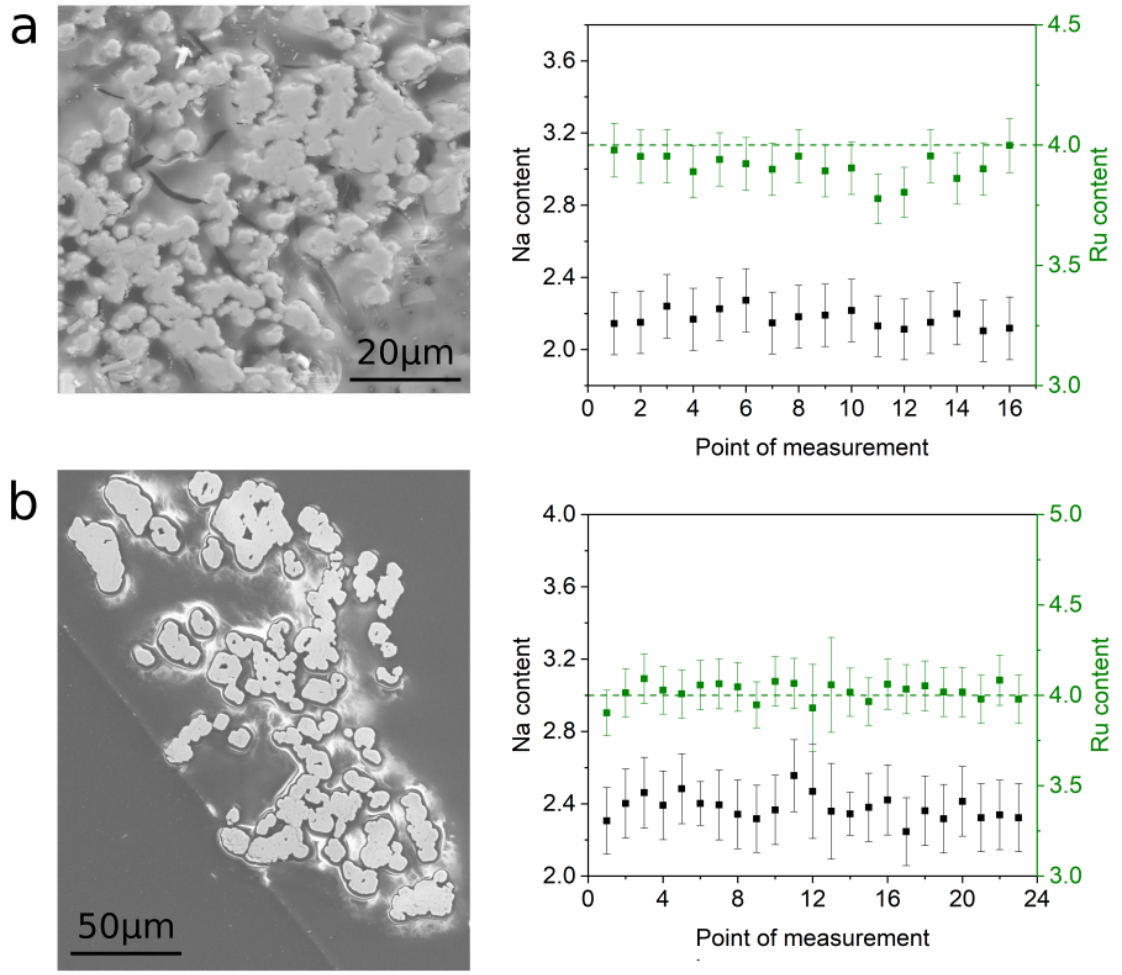

Figure 7.12: SEM image and element distribution of Na and Ru in (001) crystal faces of $Na_{3-x}Ru_4O_9$ grown by (a) the CVTR method and (b) the solid-state reaction method. The amount of O was fixed at the stoichiometric value of 9, so that the presented values of Na and Ru give the stoichiometry $Na_{3-x}Ru_4O_9$. The green-dashed line marks the expected Ru content.

7.2.4 Thermal analysis

DTA of $Na_{3-x}Ru_4O_9$ crystals in a temperature range up to $\sim$ 1700 K detected a weak endothermic reaction at 337 K and a very strong endothermic reaction at $\sim$ 1463 K (figure 7.13). During the cooling sequence, no reaction was observed. A subsequent P-XRD measurement revealed a pure Ru sample without traces of a Na compound. Therefore, the strong endothermic reaction at $\sim$ 1463 K is assumed as a decomposition reaction of $Na_{3-x}Ru_4O_9$ yielding metallic Ru.

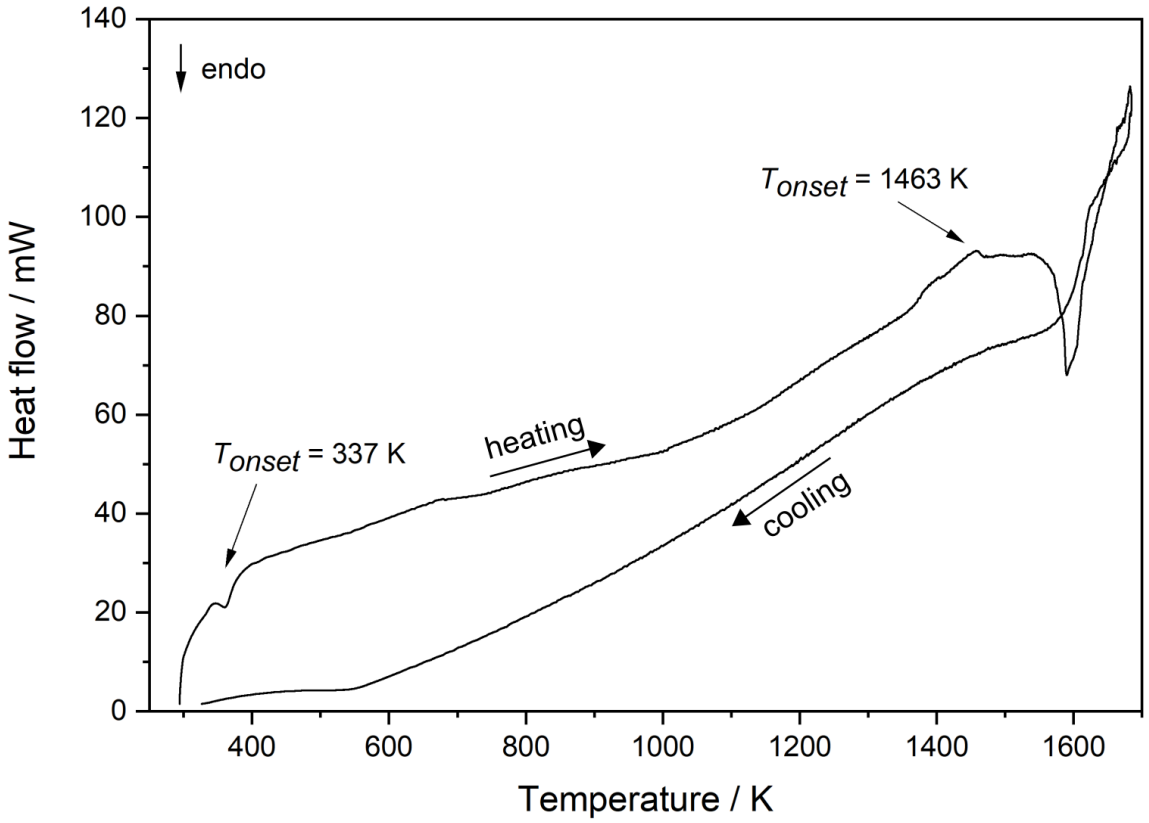

Figure 7.13: DTA measurement on a sample of $Na_{3-x}Ru_4O_9$ in the temperature range from room temperature up to $\sim$ 1700 K, using Ar as purge gas and a heating rate of 10 K/ min.

To investigate the weak endothermic reaction of $Na_{3-x}Ru_4O_9$ at 337 K, a DSC/TG measurement was carried out. Here, the endothermic reaction could be observed at a similar temperature with T_{onset} = 341 K (figure 7.14). To compensate for the drift of the TG balance, the TG curve was corrected (section 3.2). Simultaneously, between RT and 400 K a mass loss of $\sim$ 1.5% is noticed. The temperature and signal of this reaction coincide with the observed loss of adsorbed H_2O in a previous DSC/TG measurement on a mixture of Na_2CO_3 and RuO_2 (figure 7.4). Since a high hygroscopicity was already described for the sodium ruthenate compound $Na_{27}Ru_{14}O_{48}$, a similar behaviour against moisture might be expected for $Na_{3-x}Ru_4O_9$. Hence, the observed reaction is explained by a loss of adsorbed H_2O of the $Na_{3-x}Ru_4O_9$ sample. For the calculation on mass loss, the Na stoichiometric

content was set to 2.4 based on results from SC-XRD. The mass loss of $\sim 1.5\%$ corresponds to the loss of 0.5 H_2O molecules per formula unit.
In the DSC curve, no further reactions are observed during measurement. In the TG curve, a continuous mass loss is noticed with a residual mass of $\sim 94.5\%$ at the end of the measurement. Subsequent P-XRD analysis of the sample confirmed the $Na_{3-x}Ru_4O_9$ structure with space group $C2/m$. The reason for this mass loss might be a change in stoichiometry of the compound during the DSC/TG measurement and the simultaneous volatilisation of components. By assuming a stoichiometry of $Na_{2.4}Ru_4O_9$ after the loss of H_2O, the observed mass loss would coincide either with a loss of 1.08 Na yielding $Na_{1.32}Ru_4O_9$ or with a loss of 0.4 Na_2O yielding $Na_{1.6}Ru_4O_{8.6}$. Both considerations are in accordance with observations on the non-stoichiometry of $Na_{3-x}Ru_4O_9$ compounds based on SC-XRD data. The mass loss might also be assigned to a loss of O. However, since the sample might be altered between structural and thermal investigations leading to a change in composition, a distinct assignment of the observed mass loss is not possible.

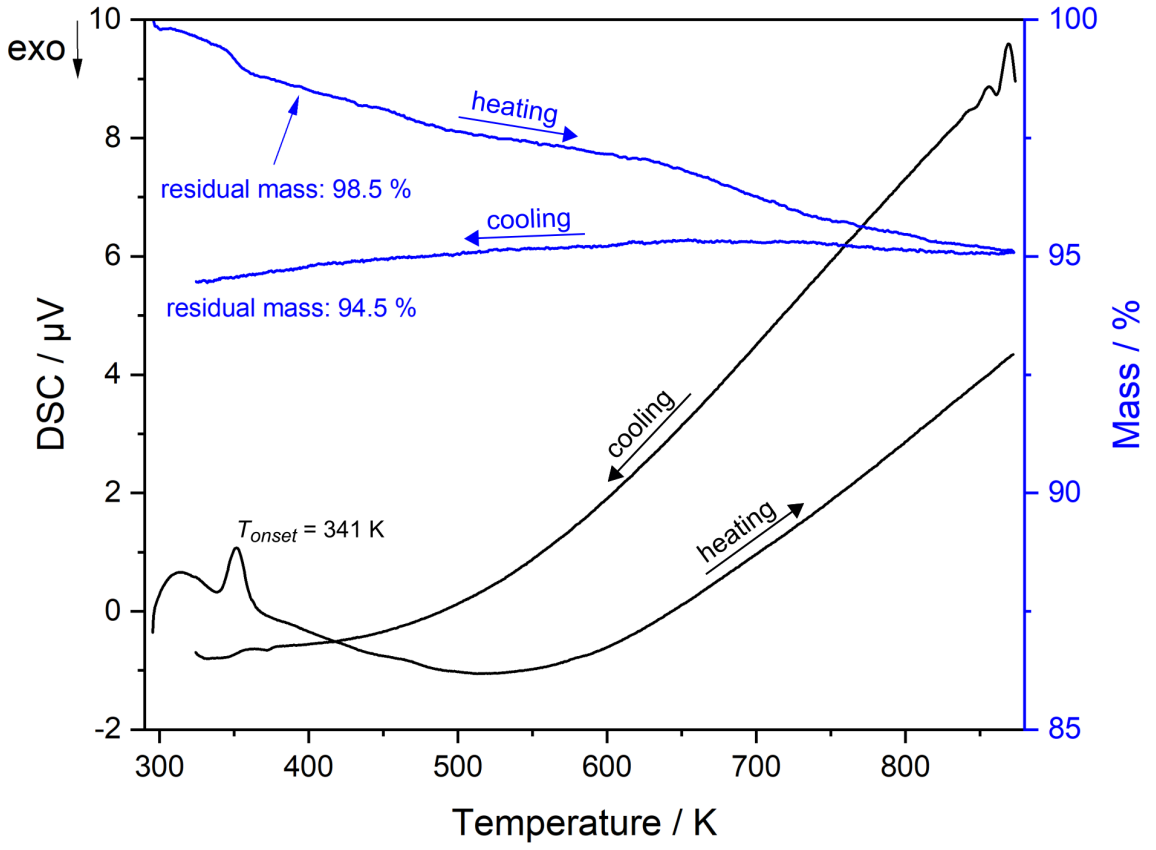

Figure 7.14: DSC/TG measurement of $Na_{3-x}Ru_4O_9$ in the temperature range from room temperature up to 873 K with a heating rate of 5 K/ min and a cooling rate of 3 K/ min.

Chapter 8

Conclusion and Outlook

The objective of the present work was the crystal-growth and structural investigation of alkali iridates and ruthenates of lithium and sodium as part of the Alkali-Platinum Group Metal Oxides (APGMO) family. Crystal growth was performed by the Chemical Vapour Transport Reaction (CVTR) and solid-state reaction method. The following conclusions are based on comparative observations, which were made on the *Li-Ir-O system*, the *Li-Ru-O system*, the *Li-Ir-Ru-O system*, and the *Na-Ru-O system*.

The common structural feature of examined compounds is the edge-sharing of AO_6 and MO_6 octahedra (A = Li; Na and M = Ir; Ru). The majority of compounds crystallises in the Li_2MO_3 structure type, which is characterised by a honeycomb structure. Single crystals were grown by the CVTR method and the solid-state reaction method. The growth systems were differentiated by their chemical composition and, in the case of CVTR growth, by their gaseous reactants involved in the growth process. Resting on the assumed transport reactions, for the gaseous reactants the temperature-dependent progress of the partial pressure $p(i)$ was investigated. Further, the temperature limit for reaching transport-effectiveness was determined ($p(i) \geq 10^{-5}$ atm [93]). In the *Li-Ir-O system*, the gaseous reactants LiOH(g) and IrO_3(g) exhibit a similar $p(i)$ behaviour and reach transport-effective values at $T \geq 1205$ K [52, 93]. In contrast, $p(RuO_3)$ reaches transport-effectiveness at $T \geq 1300$ K [93]. These minimum temperatures coincide with the optimum transport temperature T_{opt} = 1300 K as calculated on the basis of thermodynamic approaches for all Li_2MO_3 compounds (M = Ir; Ru). Hence, in the present work T_{opt} determined the experiment temperature. The investigations enable the comparison of growth results from systems with similar (*Li-Ir-O*) or different partial pressures (*Li-Ru-O* and *Li-Ir-Ru-O*) of its gaseous reactants at growth temperature.

At similar growth conditions, concerning temperature, temperature gradient, educts, time, and setup arrangement, larger single crystals of Li_2IrO_3 were yielded than of Li_2RuO_3. This observation might be explained by the higher $p(i)$ of LiOH(g) and IrO_3(g) than of RuO_3(g) at growth temperature. Li_3RuO_4 crystals grew along with Li_2RuO_3. The relatively small size of Li_3RuO_4 is interpreted to result from the growth temperature (1300 K) being lower than the calculated one (T_{opt} = 1365 K). In

the *Li-Ir-O system*, the simultaneous growth of α- and β-Li_2IrO_3 crystals was noted. In the *Li-Ir-Ru-O system*, the successful growth of $Li_2Ir_{1-x}Ru_xO_3$ crystals was yielded for $0 < x < 1$ and the composition was confirmed by elemental analysis. Within the setup, a compositional gradient between grown crystals was observed: The higher the distance between the Ir/Ru educt and the position of growth, the higher the relative amount of Ir. This indicates that the incorporation of Ir is favoured, which might be interpreted as a result of the higher $p(i)$ of IrO_3(g) compared to RuO_3(g) at growth temperature. Further, this difference in $p(i)$ might be enlarged with increasing distance and, hence, could lead to an increase of Ir with distance. However, these considerations cannot be supported by measured data on the availability of gaseous phases, since for the investigated growth systems no data have been reported so far.

Crystals of Li_2MO_3 compounds (M = Ir; Ru) were found in different morphologies: isometric, platy, and dendritic. In the *Li-Ir-O system*, the *Li-Ru-O system*, and the *Li-Ir-Ru-O system*, the formation of isometric crystals was observed to be independent on the time of growth. For isometric α-Li_2IrO_3 and Li_2RuO_3 crystals, a homogeneous distribution of Ir/Ru and O is shown. For isometric $Li_2Ir_{1-x}Ru_xO_3$ crystals, a compositional gradient with a small increase in incorporated relative Ru amount at the end of the crystal growth is found. The observation of graded $Li_2Ir_{1-x}Ru_xO_3$ crystals is explained by a different $p(i)$ of IrO_3(g) and RuO_3(g) at growth as discussed for graded crystals of $Zn_{1-x}Cd_xS$ [104]. The comparison of platy single crystals of α-Li_2IrO_3 and Li_2RuO_3 revealed differences in time and position of growth. Platy Li_2RuO_3 grew homogeneously at different distances to the Ru educt and independent on the growth duration. Accordingly to isometric Li_2RuO_3, this indicates constant and suitable growth conditions, which is also underlined by the corresponding calculated and conducted growth temperature. Contrastingly, platy α-Li_2IrO_3 only grew at the beginning of the experiment on the highest stair with largest distance to the Ir educt. These crystals are composed of a thin part at the point of attachment to the Al_2O_3 setup. Here, a relative Ir amount lower than at the remaining thicker part of the crystal was noted. In combination with the observation of the favoured early growth of platy α-Li_2IrO_3, this points to a lower availability of IrO_3(g) at the beginning of growth. This can be related to the $p(i)$ of IrO_3(g), which reaches transport-effective values at $T \geq 1205$ K, ergo significantly below the growth temperature. Hence, an early growth of platy Li_2IrO_3 might be favoured and is accompanied by the incorporation of a lower relative Ir amount compared to the remaining part of the crystal, which grew subsequently and at a higher temperature and, hence, a presumably higher $p(i)$ of IrO_3(g). The growth of dendritic α-Li_2IrO_3 crystals was observed at high Li concentrations in the experimental setup. During growth, the incorporated relative Ir amount decreased. This emphasises unbalanced growth conditions for dendritic crystals in the *Li-Ir-O system*. In contrast, in the *Li-Ru-O system*, the growth of dendritic but homogeneous Li_3RuO_4 crystals was preferred at a high concentration of Li. The homogeneous elemental distribution in Li_3RuO_4 crystals indicates constant growth conditions in experiments in the *Li-Ru-O system*.

Observations on the growth in the *Li-Ir-O system* and the *Li-Ru-O system* revealed an influence of growth temperature on the crystal symmetry. For honeycomb Li_2IrO_3, two modifications crystallised from the gaseous phase: α- and β-Li_2IrO_3 ($C2/m$ and *Fddd*, respectively). The evaluation of temperature-dependent growth attempts emphasised that α-Li_2IrO_3 is formed at lower temperatures than β-Li_2IrO_3. Based on crystal-growth investigations and thermal analysis, the phase boundary between both modifications can be determined to $\sim$ 1273 K. Thermal analysis revealed that the transformation from α- to β-Li_2IrO_3 at HT is significantly faster than the back-transformation from β- to α-Li_2IrO_3 at LT. The latter reaction is considered as a slowly proceeding one, which is kinetically inhibited. The slowly-proceeding back-transformation explains the presence of both modifications at RT at the end of growth experiments. Despite this difference in growth conditions, no difference in stoichiometry between both modifications was found by SC-XRD and EDX data. For α-Li_2IrO_3, the comparison of structural models reveals a dependence of site occupancy on the growth method. In contrast to samples obtained by the solid-state reaction method [90], crystals grown by the CVTR method show no shared occupancy between Ir and Li and, hence, present a more stable structural solution with a lower global instability index. For CVTR grown β-Li_2IrO_3 crystals, no shared occupancy was noted based on SC-XRD, which coincides with the structural investigations of flux-grown crystals [11]. In contrast to α- and β-Li_2IrO_3, for Li_2RuO_3 solely the RT phase ($P2_1/m$) could be determined in the present work. This structure is characterised by its Ru-Ru dimers. The proposed phase transition at 540 K to a HT stable non-dimerised $C2/m$ structure [76] could not be proven by thermal analysis. These observations coincide with the study of Wang et al. [130]. The comparison of SC-XRD data of Li_2RuO_3 ($P2_1/m$) do not note significant structural differences between samples from different synthesis methods applied in the present work and in the literature [76] (CVTR and solid-state reaction method, respectively). Further thermal analysis in the *Li-Ru-O system* showed that the thermal stability of Li_3RuO_4 is limited to $T < 1533$ K, where it decomposes into Li_2RuO_3 and Li_2O.

In the *Li-Ir-Ru-O system*, the structural investigation of $Li_2Ir_{1-x}Ru_xO_3$ compounds revealed a dependency of the crystal symmetry on the relative amount of Ir and on the temperature. Whilst the end members α-Li_2IrO_3 and Li_2RuO_3 are isostructural at HT and form a solid-solution series with $C2/m$ symmetry, the phases at RT are heterostructural and show $C2/m$ and $P2_1/m$ symmetry, respectively. Accordingly to the temperature-dependent behaviour of the end members, at a high relative Ir amount (Ir $\geq$ 0.55(2)), P-XRD measurements between 12 K and 310 K proved the $C2/m$ symmetry and, hence, a non-dimerised honeycomb structure, which does not undergo a phase transition. In the same temperature range, at a low relative Ir amount (Ir $\leq$ 0.13(3)), the $P2_1/m$ symmetry can be determined, which confirms the dimerised honeycomb structure and implies a phase transition between growth temperature and 310 K. Hence, the dimerisation is only favoured in structures with a low relative Ir amount. This observation is in accordance with the study of Lei et al. [67] and is explained by a slightly higher ionic radius of Ir^{4+} than of Ru^{4+}. Due to an ambiguous assignment of the crystal structures at a medium relative Ir amount, the composition limit between the stability areas of the non-dimerised

$C2/m$ and the dimerised $P2_1/m$ phase at RT is not clearly determinable. However, taking together results from the present work and results reported by Lei et al. [67], this limit is close to a relative Ir amount of $0.4 - 0.5$. Consequently, further structural investigations of $Li_2Ir_{1-x}Ru_xO_3$ crystals should be pursued for a reliable determination of the limit at RT. For those samples with $P2_1/m$ symmetry at RT, *i.e.* with a low relative Ir amount, temperature-dependent SC-XRD measurements should cover the range of $T \geq 310$ K to investigate the structural phase transition to the HT $C2/m$ phase. Here, a shift of phase transition temperature is expected with increasing relative Ir amount. Next to differences in $p(i)$ of IrO_3(g) and RuO_3(g), which point towards a complex growth process of $Li_2Ir_{1-x}Ru_xO_3$ at 1300 K, these structural investigations show that the composition-dependent phase transition further gives complexity to the subsequent cooling process of $Li_2Ir_{1-x}Ru_xO_3$.

CVTR growth experiments in the *Na-Ru-O system* showed that Na_2CO_3(s) is not the most suitable educt for this growth method. This is due to the complex gas transport reaction of Na_2CO_3: Close to its melting point at 1123 K [6, p. 1117], the decomposition of Na_2CO_3(s) to Na_2O(s) and CO_2(g) has been reported [81]. In the present work, DSC/TG measurements confirmed the decomposition reaction at around 1100 K. CVTR experiments revealed that evasive openings of the setup are required and enable the introduction of N_2(g) and the escape of CO_2(g) from the growth chamber, which prevents a possible back-reaction, and, hence, the growth of $Na_{3-x}Ru_4O_9$ crystals. However, due to the evasive openings, the escape of volatiles (RuO_3(g) and NaOH(g)) is possible during growth and led to a small amount and size of single crystals of $Na_{3-x}Ru_4O_9$. Because of the similar transport reactions of Li_2O(s) and Na_2O(s), a more suitable educt for the CVTR growth might be Na_2O(s). However, due to the high reactivity of Na_2O(s) [38, p. 168], it was not chosen for growth preparation in the present work. Further investigations in the *Na-Ru-O system* emphasised that the solid-state reaction method is more suitable for growth attempts starting from Na_2CO_3(s) and RuO_2(s). Using a specified experimental setup for this method, $Na_{3-x}Ru_4O_9$ crystals of larger size and amount were obtained, which is explained by the isolation of educts from the surroundings and, hence, the prevented escape of volatiles. Moreover, using this method, the growth of triclinic $Na_{27}Ru_{14}O_{48}$ crystals with high Na and Ru stoichiometric amounts was observed. For sodium ruthenates, SC-XRD data show differences in Na stoichiometry depending on the growth method ($Na_{3-x}Ru_4O_9$) or the occurrence of stacking faults ($Na_{27}Ru_{14}O_{48}$). In the case of $Na_{3-x}Ru_4O_9$ with a tunnel-like structure, the Na stoichiometric amount is higher for a sample grown by CVTR (Na = 2.55(8)) than for a sample grown by the solid-state reaction method (Na = 2.36(3)). Further, the anisotropic refinement of atomic displacement parameters resulted in elongated displacement ellipsoids of Na in the direction of the tunnels. This indicates a mobility of Na atoms and, hence, suggests conducting behaviour in $Na_{3-x}Ru_4O_9$.

In accordance with the results of growth investigations of the present work, an extended usage of the applied growth method to other growth systems is proposed for future works. Though, since the present work focussed on CVTR experiments including a platinum-group metal, which is transported via auto transport, this limitation would only include Os as a suitable candidate. However, the high

toxicity of its oxidic compound OsO_4 has to be taken into account. If the requirement of auto transport is neglected but the focus on platinum-group metals is maintained, the *Li-Rh-O system* should be investigated as a promising candidate. In the *Li-Rh-O system*, two modifications of $LiRhO_2$ and the Li_2RhO_3 compound have been reported in various works [9, 40, 126]. In trigonal $LiRhO_2$ ($R\bar{3}m$), the structure is characterised by alternating layers, which are composed of edge-sharing LiO_6 or RhO_6 octahedra and stacked along the *c*-axis [9]. In cubic $LiRhO_2$ ($Fd\bar{3}m$), mixed metal layers form a 3D network of edge-sharing LiO_6 and RhO_6 octahedra [40]. As for the discussed Li_2MO_3 compounds (M = Ir; Ru) with space group $C2/m$, the crystal structure of monoclinic Li_2RhO_3 ($C2/m$) is characterised by its edge-sharing RhO_6 octahedra, which form a 2D honeycomb structure [126]. In a manner consistent with the isostructural α-Li_2IrO_3 [90], a shared occupancy of Rh and Li atomic positions was reported for Li_2RhO_3 on the basis of P-XRD data [126]. Thus, the growth and structural investigation of the 2D honeycomb structure Li_2RhO_3 should be performed. For comparison, growth attempts should start from Li_2O(s) and Rh(s). At $T > 873$ K, the oxidation of Rh(s) to Rh_2O_3(s) has been reported [24], *i.e.* with Rh^{3+}. Since for the growth of Li_2RhO_3 the required oxidation state of Rh is +4, experiments should be performed in a stream of oxygen to increase the Rh oxidation state. For this investigation, a suitable furnace and an adjusted growth setup with openings for the introduction of O_2 would be necessary.

Appendix A

Li-Ir-O system

Table A.1: Compounds in the Li-Ir-O system including their space groups (SG), lattice parameters a, b, c, β, and ICSD Collection Codes.

Compound	SG	a / Å	b / Å	c / Å	β / °	Coll. Code
α-Li_2IrO_3 [90]	$C2/m$	5.1633(2)	8.9294(3)	5.1219(2)	109.759(3)	246025
β-Li_2IrO_3 [11]	$Fddd$	5.8903(2)	8.4261(3)	17.7924(7)		193972
γ-Li_2IrO_3 [77]	$Cccm$	5.9119(3)	5.4461(5)	17.836(1)		-
Li_8IrO_6 [63]	$R\bar{3}$	5.4151(6)	5.4151(6)	15.0584(37)		61217

Thermodynamic calculations

Table A.2: Calculated temperature-dependent values of the standard enthalpy and entropy of formation (ΔH_T^0 and ΔS_T^0), and heat capacity (C_p) of Li_2IrO_3. The temperature-dependent values for Li_2O(s) and IrO_2(s) were taken from Barin [6].

T / K	ΔH_T^0 / kJmol^{-1}	ΔS_T^0 / Jmol^{-1}K^{-1}
298	-888(20)	89(15)
500	-859(20)	118(15)
600	-852(20)	125(15)
700	-846(20)	131(15)
800	-840(20)	136(15)
900	-836(20)	141(15)
1000	-831(20)	146(15)
1100	-827(20)	150(15)
1200	-823(20)	154(15)
1300	-819(20)	158(15)
1368	-816(20)	161(15)

$$C_p = 131.67 + 0.03808\ T - 2950000\ T^{-2}\ /\ \text{Jmol}^{-1}\text{K}^{-1}\ (298\ \text{K} - 1368\ \text{K})$$

Table A.3: Calculated temperature-dependent values of the reaction enthalpy and entropy (ΔH_R and ΔS_R) of the assumed reaction 2 LiOH(g) + IrO_3 ⇔ Li_2IrO_3(s) + H_2O(g) + 0.5 O_2(g). The temperature-dependent values of the enthalpy and entropy of formation (ΔH_T^0 and ΔS_T^0) for LiOH(g), IrO_3(g), H_2O(g), and O_2(g) were taken from Barin [6], whereas the values for Li_2IrO_3 were calculated in the present work and are listed in appendix table A.2.

T / K	ΔH_R / kJmol^{-1}	ΔS_r / Jmol^{-1}K^{-1}
298	-675(30)	-433(25)
500	-674(30)	-477(25)
600	-682(30)	-496(25)
700	-691(30)	-513(25)
800	-701(30)	-528(25)
900	-711(30)	-541(25)
1000	-721(30)	-553(25)
1100	-732(30)	-563(25)
1200	-743(30)	-572(25)
1300	-754(30)	-580(25)
1368	-761(30)	-584(25)

Raman spectroscopic analysis

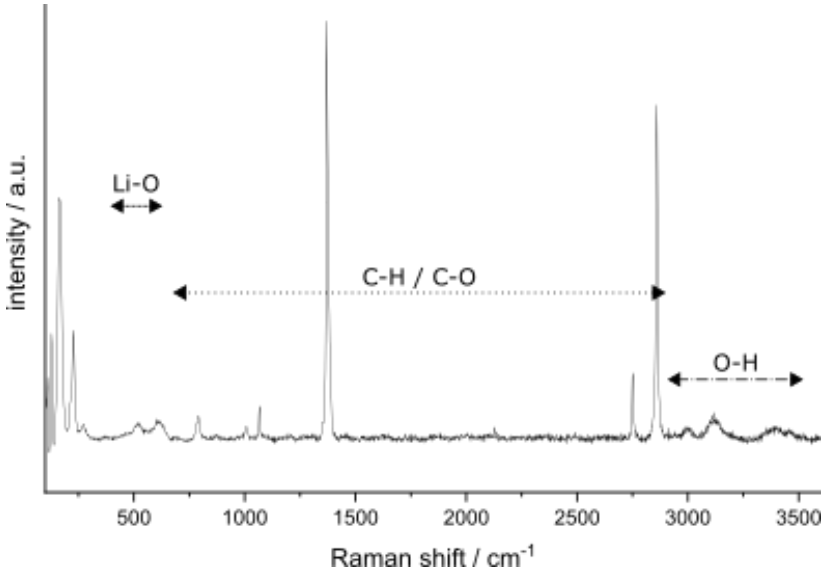

Figure A.1: In the Raman spectrum of the colourless single crystals, which form on the surface of Li_2IrO_3 crystals as reaction product of Li with ethanol, C_2H_5OH, and/or ethyleneglycol, $C_2H_4(OH)_2$, in air, different vibrational modes are found. Li-O, C-H, C-O and O-H vibrational modes are detected within their characteristic ranges of Raman shift.

Structural aspects

α-Li_2IrO_3, $C2/m$

Table A.4: Anisotropic atomic displacement parameters (ADPs) of α-Li_2IrO_3 of the present work. ADPs for Li atoms are restrained to exhibit an approximate isotropic behaviour.

Atom site	U_{11} / Å^2	U_{22} / Å^2	U_{33} / Å^2	U_{12} / Å^2	U_{13} / Å^2	U_{23} / Å^2
Ir1	0.0015(2)	0.0019(2)	0.0064(2)	0	0.00108(15)	0
Li2	0.05(2)	0.05(2)	0.05(2)	0	0.016(8)	0
Li3	0.011(5)	0.011(5)	0.011(5)	0	0.004(2)	0
Li4	0.014(7)	0.014(7)	0.014(7)	0	0.005(3)	0
O5	0.005(4)	0.006(4)	0.012(3)	0.0002(19)	0.004(3)	0.0002(18)
O6	0.004(4)	0.006(5)	0.009(4)	0	0.003(4)	0

Table A.5: Selected bond angles and average deviations in the α-Li_2IrO_3 structure of the present work.

Bond	Bond angle / °	Bond	Bond angle / °
O5-**Ir1**-O5	90.3(5)	O6-**Li3**-O6	96.0(12)
O5-Ir1-O5	85.1(4)	O6-Li3-O5	86.5(4)
O5-Ir1-O5	92.4(4)	O5-Li3-O5	92.2(11)
O5-Ir1-O6	92.1(4)	O6-Li3-O5	92.2(6)
O5-Ir1-O6	92.0(4)	O6-Li3-O5	92.5(6)
O5-Ir1-O6	90.5(4)	O5-Li3-O5	85.0(6)
O6-Ir1-O6	85.7(5)	O5-Li3-O5	90.1(7)
Average deviation	2.3°	Average deviation	2.85°
O5-**Li2**-O5	85.4(5)	O6-**Li4**-O5	93.5(4)
O5-Li2-O5	94.6(5)	O6-Li4-O5	86.5(4)
O5-Li2-O6	94.3(4	O5-Li4-O5	90.9(4)
O5-Li2-O4	85.7(4)	O5-Li4-O5	89.1(4)
Average deviation	4.3°	Average deviation	2.6°

Table A.6: Averaged bond lengths in Å and calculated bond valence sums (BVS) of α-Li_2IrO_3 of the present work, resulting in a global instability index of 0.032.

	Bond length / Å		Bond valence			Bond length / Å		Bond valence	
Ir1-O1	2.02(2)	x2	0.67(3)	x2	**Li3**-O1	2.14(2)	x2	0.16(1)	x2
-O1	2.02(1)	x2	0.67(2)	x2	-O1	2.18(2)	x2	0.15(1)	x2
-O2	2.03(1)	x2	0.65(1)	x2	-O2	2.12(2)	x2	0.17(1)	x2
		BVS	**3.978(49)**				**BVS**	**0.959(20)**	
Li2-O1	2.11(1)	x4	0.18(1)	x4	**Li4**-O1	2.18(1)	x4	0.15(1)	x4
-O2	2.12(2)	x2	0.17(1)	x2	-O2	2.08(2)	x2	0.19(1)	x2
		BVS	**1.044(13)**				**BVS**	**0.969(13)**	
O1- Ir1	2.02(2)	x1	0.67(3)	x1	**O2**- Ir1	2.03(1)	x2	0.65(1)	x2
- Ir1	2.02(1)	x1	0.67(2)	x1	-Li2	2.12(2)	x1	0.17(1)	x1
-Li2	2.11(1)	x1	0.18(1)	x1	-Li3	2.12(2)	x2	0.17(1)	x2
-Li3	2.14(2)	x1	0.16(1)	x1	-Li4	2.08(2)	x1	0.19(8)	x1
-Li3	2.18(2)	x1	0.15(1)	x1			**BVS**	**2.007(24)**	
-Li4	2.18(1)	x1	0.15(1)	x1					
		BVS	**1.969(35)**						

Table A.7: Structural model of α-Li_2IrO_3 published by Freund et al. [35] including lattice parameters (a, b, c, β), cell volume V, atomic positions with Wyckoff site symmetry, fractional coordinates (x, y, z), and isotropic atomic displacement parameters (U_{iso}).

α-Li_2IrO_3

Space group	$C2/m$
Z	4
a, b, c, β	5.1749(2) Å, 8.9359(2) Å, 5.1194(2) Å, 109.827(5)°
V	222.70(2) Å^3
T	293 K
Diffraction method	SC-XRD

Atom	Site	x	y	z	U_{iso} / Å^2
Ir1	4g	0.0000	0.3331(4)	0.0000	-
Li2	2a	0.0000	0.0000	0.0000	0.00633
Li3	4h	0.0000	0.809	0.5000	0.00633
Li4	2d	0.0000	0.5000	0.5000	0.00633
O5	8j	0.25(1)	0.321(5)	0.765(8)	0.3(1)
O6	4i	0.27(1)	0.0000	0.76(1)	0.3 (1)

Anisotropic Displacement Parameters of Ir1 / Å^2

U_{11}	0.019(7)
U_{22}	0.007(2)
U_{33}	0.028(3)
U_{12}	-
U_{13}	0.011(3)
U_{23}	-

Data collection

No. of measured reflections: 2415

Data reduction R_{int}: 5.76 %

Criterion for observed reflections: I > 2.0 σ(I)

No. of observed independent reflections: 83

No. of fitted parameters: 12

Table A.8: Structural model of α-Li_2IrO_3 published by O'Malley et al. [90] including lattice parameters (a, b, c, β), cell volume V, atomic positions with Wyckoff site symmetry, site occupancy factors (SOF), fractional coordinates (x, y, z), and isotropic atomic displacement parameters (B_{iso}).

α-Li_2IrO_3

Space group	$C2/m$
Z	4
a, b, c, β	5.1633(2) Å, 8.9294(3) Å, 5.1219(2) Å, 109.759(2)°
V	222.2(2) Å^3
T	293 K
Diffraction method	P-XRD
ICSD Code	246025

Atom	Site	SOF	x	y	z	B_{iso} / Å^2
Ir1	4g	0.902(2)	0.0000	0.3332(2)	0.0000	0.39(4)
Li1	4g	0.098(2)	0.0000	0.3332(2)	0.0000	0.39(4)
Li2	2a	0.804(3)	0.0000	0.0000	0.0000	0.39(4)
Ir2	2a	0.196(3)	0.0000	0.0000	0.0000	0.39(4)
Li3	4h	1	0.0000	0.809(6)	0.5000	0.39(4)
Li4	2d	1	0.0000	0.5000	0.5000	0.39(4)
O5	8j	1	0.252(4)	0.316(1)	0.759(2)	0.3
O6	4i	1	0.256(5)	0.0000	0.788(3)	0.3

Quality indicators of Rietveld refinement

R_{wp}: 0.198

R_{Bragg}: 0.05382

χ^2: 2.283

Table A.9: Averaged bond lengths in Å and calculated bond valence sums (BVS) of α-Li_2IrO_3 published by Freund et al. [35], resulting in a global instability index of 0.095.

	Bond length / Å		Bond valence			Bond length / Å		Bond valence	
Ir1-O1	2.05(5)	x2	0.62(9)	x2	**Li3**-O1	1.92(4)	x2	0.29(3)	x2
-O1	1.99(4)	x2	0.72(8)	x2	-O1	2.17(5)	x2	0.15(2)	x2
-O2	2.04(4)	x2	0.64(8)	x2	-O2	2.32(5)	x2	0.10(1)	x2
		BVS	**3.951(203)**				**BVS**	**1.089(58)**	
Li2-O1	2.15(4)	x4	0.16(2)	x4	**Li4**-O1	2.21(4)	x4	0.13(2)	x4
-O2	2.15(9)	x2	0.16(4)	x2	-O2	2.06(9)	x2	0.20(5)	x2
		BVS	**0.943(68)**				**BVS**	**0.933(77)**	
O1- Ir1	2.05(5)	x1	0.62(9)	x1	**O2**- Ir1	2.04(4)	x2	0.64(8)	x2
- Ir1	1.99(4)	x1	0.72(8)	x1	-Li2	2.15(9)	x1	0.16(4)	x1
-Li2	2.15(4)	x1	0.16(2)	x1	-Li3	2.32(5)	x2	0.10(1)	x2
-Li3	1.92(4)	x1	0.30(3)	x1	-Li4	2.06(9)	x1	0.20(5)	x1
-Li3	2.17(5)	x1	0.15(2)	x1			**BVS**	**1.826(127)**	
-Li4	2.21(4)	x1	0.13(2)	x1					
		BVS	**2.076(130)**						

Table A.10: Averaged bond lengths in Å and calculated bond valence sums (BVS) of α-Li_2IrO_3 published by O'Malley et al. [90]. Due to the shared occupancy of two atomic positions (Ir1:0.902/Li1:0.098; Li2:0.804/Ir2:0.196), the global instability index is calculated with weighted bond valence sums (BVS) of the respective interatomic bonds. For better understanding, these bonds are marked in red. Overall, this results in a global instability index of 0.158.

	Bond length / Å		Bond valence			Bond length / Å		Bond valence	
Ir1-O1	2.08(2)	x2	0.57(3)	x2	**Li1**-O1	2.08(2)	x2	0.19(1)	x2
-O1	1.97(1)	x2	0.77(2)	x2	-O1	1.97(1)	x2	0.26(1)	x2
-O2	2.01(1)	x2	0.68(2)	x2	-O2	2.01(1)	x2	0.23(1)	x2
		BVS	**4.02(63)**				**BVS**	**1.350(16)**	
Li2-O1	2.19(1)	x4	0.14(1)	x4	**Ir2**-O1	2.19(1)	x4	0.42(1)	x4
-O2	1.97(3)	x2	0.25(2)	x2	-O2	1.97(3)	x2	0.76(5)	x2
		BVS	**1.073(26)**				**BVS**	**3.196(77)**	
Li3-O1	1.88(3)	x2	0.33(3)	x2	**Li4**-O1	2.23(1)	x4	0.13(1)	x4
-O1	2.13(2)	x2	0.17(1)	x2	-O2	2.24(2)	x2	0.12(1)	x2
-O2	2.35(4)	x2	0.09(1)	x2			**BVS**	**0.750(14)**	
		BVS	**1.168(46)**						
O1- Ir1	2.08(2)	x1	0.57(3)	x1	**O1**-Li1	2.08(2)	x1	0.19(1)	x1
- Ir1	1.97(1)	x1	0.77(2)	x1	-Li1	1.97(1)	x1	0.26(1)	x1
-Li2	2.19(1)	x1	0.14(1)	x1	- Ir2	2.19(1)	x1	0.42(1)	x1
-Li3	1.88(3)	x1	0.33(3)	x1	-Li3	1.88(3)	x1	0.33(3)	x1
-Li3	2.13(2)	x1	0.17(1)	x1	-Li3	2.13(2)	x1	0.17(1)	x1
-Li4	2.23(1)	x1	0.13(1)	x1	-Li4	2.23(1)	x1	0.13(1)	x1
		BVS	**2.095(49)**				**BVS**	**1.488(36)**	
O2- Ir1	2.01(1)	x2	0.68(2)	x2	**O2**-Li1	2.01(1)	x2	0.23(1)	x2
-Li2	1.97(3)	x1	0.25(2)	x1	- Ir2	1.97(3)	x1	0.76(5)	x1
-Li3	2.35(4)	x2	0.09(1)	x2	-Li3	2.35(4)	x2	0.09(1)	x2
-Li4	2.24(2)	x1	0.12(1)	x1	-Li4	2.24(2)	x1	0.12(1)	x1
		BVS	**1.913(40)**				**BVS**	**1.516(55)**	

β-Li_2IrO_3, *Fddd*

Table A.11: Anisotropic atomic displacement parameters (ADPs) of β-Li_2IrO_3 of the present work.

Atom site	U_{11} / Å^2	U_{22} / Å^2	U_{33} / Å^2	U_{12} / Å^2	U_{13} / Å^2	U_{23} / Å^2
Ir1	0.00383(16)	0.00370(15)	0.00332(17)	0.000	0.000	-0.00018(17)
O1	0.0078(13)	0.0073(13)	0.0066(13)	0.0002(9)	0.000	0.000
O2	0.0035(11)	0.0042(10)	0.0045(11)	-0.0001(9)	0.0018(8)	0.0002(10)

Table A.12: Selected bond angles and average deviations of the β-Li_2IrO_3 structure of the present work.

Bond	Bond angle / °	Bond	Bond angle / °
O2-**Ir1**-O2	88.9(2)	O2-**Li2**-O2	95.3(8)
O2-Ir1-O2	92.81(16)	O2-Li2-O1	86.75(14)
O2-Ir1-O2	84.88(17)	O1-Li2-O1	91.2(7)
O2-Ir1-O1	91.76(15)	O2-Li2-O2	92.9(4)
O2-Ir1-O1	89.61(12)	O2-Li2-O2	85.3(4)
O2-Ir1-O1	92.73(12)	O1-Li2-O2	89.4(3)
O1-Ir1-O1	87.7(3)	O1-Li2-O2	92.4(4)
Average deviation	2.4°	Average deviation	2.85°
O2-**Li3**-O2	95.3(8)		
O2-Li3-O1	89.0(4)		
O2-Li3-O1	95.5(4)		
O2-Li3-O2	92.35(13)		
O1-Li3-O2	84.4(4)		
O1-Li3-O2	90.5(5)		
O2-Li3-O2	80.0(7)		
Average deviation	3.7°		

Table A.13: Averaged bond lengths in Å and calculated bond valence sums (BVS) of β-Li_2IrO_3 of the present work, resulting in a global instability index of 0.059.

	Bond length / Å		Bond valence			Bond length / Å		Bond valence	
Ir1-O1	2.06(1)	x2	0.60(1)	x2	**Li1**-O1	2.13(1)	x2	0.17(1)	x2
-O1	1.99(1)	x2	0.72(1)	x2	-O2	2.11(1)	x2	0.18(1)	x2
-O2	2.03(1)	x2	0.66(1)	x2	-O2	2.19(1)	x2	0.14(1)	x2
		BVS	**3.946(17)**				**BVS**	**0.968(12)**	
Li2-O1	2.11(1)	x4	0.18(1)	x4	**O1**- Ir1	2.06(1)	x4	0.60(1)	x4
-O2	2.17(1)	x2	0.15(1)	x2	-Li1	2.13(1)	x2	0.17(1)	x2
-O2	2.11(1)	x2	0.18(1)	x2	-Li2	2.11(1)	x2	0.18(1)	x2
		BVS	**1.001(13)**				**BVS**	**1.886(13)**	
O2- Ir1	2.03(1)	x1	0.66(2)	x1					
- Ir1	1.99(1)	x1	0.72(1)	x1					
-Li1	2.19(1)	x1	0.14(1)	x1					
-Li1	2.11(1)	x1	0.18(1)	x1					
-Li2	2.11(1)	x1	0.18(1)	x1					
-Li2	2.17(1)	x1	0.15(1)	x1					
		BVS	**2.014(15)**						

Table A.14: Structural model of β-Li_2IrO_3 published by Biffin et al. [11] including lattice parameters (a, b, c, β), cell volume V, atomic positions with Wyckoff site symmetry, fractional coordinates (x, y, z), and isotropic atomic displacement parameters (U_{iso}).

β-Li_2IrO_3

Space group	*Fddd*
Z	16
a, b, c	5.8903(2) Å, 8.4261(3) Å, 17.7924(7) Å
V	883.08(6) Å^3
T	100 K
Diffraction method	SC-XRD

Atom	Site	x	y	z	U_{iso} / Å^2
Ir	16*g*	0.125	0.125	0.70845(7)	0.0025(3)
Li1	16*g*	0.125	0.125	0.04167	0.00633
Li2	16*g*	0.125	0.125	0.875	0.00633
O1	16*e*	0.855(7)	0.125	0.125	0.002(5)
O2	32*h*	0.621(8)	0.3669(19)	0.0384(7)	0.002(3)

Quality indicators of refinement

$R(F^2) = 4.50\,\%$

$wR(F^2) = 5.24\,\%$

$R(F) = 2.42\,\%$

$\chi^2 = 0.318$

Data collection

No. of measured reflections: 3770

Data reduction R_{int}: 6.99 % (Criterion for observed reflections: I > 2.0 σ(I))

No. of observed independent reflections: 298

No. of fitted parameters: 9

Table A.15: Averaged bond lengths in Å and calculated bond valence sums (BVS) of β-Li_2IrO_3 published by Biffin et al. [11], resulting in a global instability index of 0.092.

	Bond length / Å		Bond valence			Bond length / Å		Bond valence	
Ir1-O1	2.01(3)	x2	0.69(5)	x2	**Li1**-O1	2.17(3)	x2	0.15(1)	x2
-O1	2.06(4)	x2	0.89(6)	x2	-O2	2.03(3)	x2	0.22(2)	x2
-O2	2.04(2)	x2	0.63(3)	x2	-O2	2.18(2)	x2	0.15(1)	x2
		BVS	**3.815(114)**				**BVS**	**1.020(34)**	
Li2-O1	2.11(1)	x4	0.17(1)	x4	**O1**- Ir1	2.01(3)	x4	0.69(5)	x4
-O2	2.15(3)	x2	0.16(2)	x2	-Li1	2.17(3)	x2	0.15(1)	x2
-O2	2.12(1)	x2	0.17(2)	x2	-Li2	2.11(1)	x2	0.18(1)	x2
		BVS	**1.012(30)**				**BVS**	**2.016(75)**	
O2- Ir1	2.04(2)	x1	0.63(3)	x1					
- Ir1	2.07(4)	x1	0.59(6)	x1					
-Li1	2.18(2)	x1	0.15(1)	x1					
-Li1	2.03(3)	x1	0.22(2)	x1					
-Li2	2.11(3)	x1	0.17(2)	x1					
-Li2	2.15(3)	x1	0.16(2)	x1					
		BVS	**1.916(69)**						

γ-Li_2IrO_3, *Cccm*

Table A.16: Structural model of γ-Li_2IrO_3 published by Modic et al. [77] including lattice parameters (a, b, c, β), cell volume V, atomic positions with Wyckoff site symmetry, fractional coordinates (x, y, z), and isotropic atomic displacement parameters (U_{iso}). Data taken from published crystallographic information file.

γ-Li_2IrO_3

Space group	*Cccm*
Z	16
a, b, c	5.9119(3) Å, 8.4461(5) Å, 17.836(1) Å
V	890.60(9) Å^3
Diffraction method	SC-XRD

Atom	Site	x	y	z	U_{iso} / Å^2
Ir1	8*k*	0.25	0.25	0.08353(7)	0.0069
Ir2	8*i*	0.5	0.5	0.16659(8)	0.0103
Li3	8*j*	0.0	0.5	0.33333	0.01
Li4	8*k*	0.75	0.25	0.25	0.01
Li6	8*k*	0.75	0.25	0.91667	0.01
Li5	4*c*	0.5	0.5	0.5	0.01
Li7	4*d*	0.5	0.0	0.0	0.01
O8	16*m*	0.716(4)	0.518(2)	0.0850(10)	0.016
O9	8*g*	0.719(9)	0.5	0.25	0.047
O11	8*l*	0.018(7)	0.271(5)	0.0	0.033
O12	16*m*	0.470(4)	0.258(3)	0.162(2)	0.030

Table A.17: Structural model of γ-Li_2IrO_3 published by Modic et al. [77] including lattice parameters (a, b, c, β), cell volume V, atomic positions with Wyckoff site symmetry, fractional coordinates (x, y, z), and isotropic atomic displacement parameters (U_{iso}). Data taken from published supplementary material.

γ-Li_2IrO_3

Space group	*Cccm*
Z	16
a, b, c	5.9119(3) Å, 8.4461(5) Å, 17.8363(10) Å
V	890.60(9) Å^3
T	300 K
Diffraction method	SC-XRD

Atom	Site	x	y	z	U_{iso} / Å^2
Ir1	8*k*	0.25	0.25	0.0836(2)	0.0124(4)
Ir2	8*i*	0.5	0.5	0.1670(3)	0.0206(6)
Li1	8*j*	0.0	0.5	0.3333	0.01
Li2	8*k*	0.75	0.25	0.25	0.0
Li3	8*k*	0.75	0.25	0.91667	0.01
Li4	4*c*	0.5	0.5	0.5	0.01
Li5	4*d*	0.5	0.0	0.0	0.01
O1	16*m*	0.77(1)	0.515(3)	0.087(4)	0.02(1)
O2	8*g*	0.72(2)	0.5	0.25	0.04(1)
O3	8*l*	0.00(1)	0.262(8)	0.0	0.006(9)
O4	16*m*	0.49(1)	0.262(6)	0.163(3)	0.006(9)

Table A.18: Structural model of γ-Li_2IrO_3 reported by Analytis [4] including lattice parameters (a, b, c, β), cell volume V, atomic positions with Wyckoff site symmetry, fractional coordinates (x, y, z), and isotropic atomic displacement parameters (U_{iso}). Data taken from crystallographic information file distributed by private communication.

γ-Li_2IrO_3 [4]

Space group	*Cccm*
Z	16
a, b, c	5.91250 Å, 8.44520 Å, 17.8400 Å
V	890.791 Å^3
Diffraction method	SC-XRD

Atom	Site	x	y	z	U_{iso} / Å^2
Ir1	8*k*	0.25	0.25	0.08362(19)	0.0124(3)
Ir2	8*i*	0.5	0.5	0.1670(3)	0.0206(6)
Li1	8*j*	0.0	0.5	0.3333	0.01279
Li2	8*k*	0.75	0.25	0.25	0.01279
Li3	8*k*	0.75	0.25	0.91667	0.01279
Li4	4*c*	0.5	0.5	0.5	0.01279
Li5	4*d*	0.5	0.0	0.0	0.01279
O1	16*m*	0.773(13)	0.515(3)	0.087(4)	0.027(10)
O2	8*g*	0.722(16)	0.5	0.25	0.04(1)
O3	8*l*	0.006(15)	0.262(8)	0.0	0.006(10)
O4	16*m*	0.487(14)	0.262(6)	0.163(3)	0.006(9)

Table A.19: Averaged bond lengths in Å and calculated bond valence sums (BVS) of γ-Li_2IrO_3 published by Modic et al. [77], resulting in a global instability index of 0.249. Data taken from published crystallographic information file.

	Bond length / Å		Bond valence			Bond length / Å		Bond valence	
Ir1-O8	1.97(2)	x2	0.76(3)	x2	**Ir2**-O8	1.94(2)	x2	0.76(3)	x2
-O11	2.03(3)	x2	0.64(5)	x2	-O9	1.97(3)	x2	0.64(5)	x2
-O12	1.91(3)	x2	0.89(7)	x2	-O12	1.91(3)	x2	0.89(7)	x2
		BVS	**4.601(135)**				**BVS**	**4.382(134)**	
Li3-O8	2.23(2)	x2	0.127(7)	x2	**Li4**-O9	2.12(1)	x2	0.171(2)	x2
-O9	2.23(4)	x2	0.13(1)	x2	-O12	2.28(3)	x2	0.110(9)	x2
-O12	2.19(3)	x2	0.14(1)	x2	-O12	2.04(3)	x2	0.21(2)	x2
		BVS	**0.794(26)**				**BVS**	**0.987(29)**	
Li5-O8	1.99(2)	x4	0.24(1)	x4					
-O11	2.29(4)	x2	0.11(1)	x2	**Li6**-O8	2.27(2)	x2	0.113(5)	x2
		BVS	**1.191(32)**		-O11	2.18(3)	x2	0.15(1)	x2
Li7-O8	2.27(2)	x4	0.115(7)	x4	-O12	2.17(3)	x2	0.15(1)	x2
-O11	1.94(4)	x2	0.28(3)	x2			**BVS**	**0.814(77)**	
		BVS	**1.019(47)**						
O8- Ir1	1.97(2)	x1	0.76(4)	x1	**O12**- Ir1	1.91(3)	x2	0.89(7)	x2
- Ir2	1.94(2)	x1	0.82(5)	x1	- Ir2	2.05(3)	x1	0.61(4)	x1
-Li3	2.23(2)	x1	0.127(7)	x1	-Li3	2.19(3)	x2	0.14(1)	x2
-Li5	2.27(2)	x1	0.113(5)	x1	-Li4	2.28(3)	x1	0.110(9)	x1
-Li6	1.99(2)	x1	0.244(13)	x1	-Li4	2.04(3)	x1	0.21(2)	x1
-Li7	2.27(2)	x1	0.115(7)	x1	-Li6	2.17(3)	x1	0.15(1)	x1
		BVS	**2.185(60)**				**BVS**	**2.116(89)**	
O9- Ir2	1.97(3)	x2	0.76(7)	x2	**O11**- Ir1	2.03(3)	x2	0.64(5)	x2
-Li3	2.23(4)	x2	0.13(1)	x2	-Li6	2.18(3)	x2	0.15(1)	x2
-Li4	2.12(1)	x2	0.171(2)	x2	-Li5	2.29(4)	x2	0.11(1)	x2
		BVS	**2.114(103)**		-Li7	1.94(4)	x2	0.28(3)	x2
							BVS	**1.966(79)**	

Table A.20: Averaged bond lengths in Å and calculated bond valence sums (BVS) of the structural model of γ-Li_2IrO_3 published by Modic et al. [77], resulting in a global instability index of 0.141. Data taken from published supplementary material.

	Bond length / Å		Bond valence			Bond length / Å		Bond valence	
Ir1-O8	1.99(3)	x2	0.72(5)	x2	**Ir2**-O8	2.15(6)	x2	0.48(8)	x2
-O11	2.10(4)	x2	0.53(6)	x2	-O9	1.97(8)	x2	0.76(2)	x2
-O12	2.01(4)	x2	0.69(8)	x2	-O12	2.01(5)	x2	0.68(10)	x2
		BVS	**3.898(231)**				**BVS**	**3.837(293)**	
Li3-O8	1.97(6)	x2	0.26(5)	x2	**Li4**-O9	2.12(1)	x2	0.171(5)	x2
-O9	2.22(9)	x2	0.13(3)	x2	-O12	2.19(42)	x2	0.14(16)	x2
-O12	2.01(5)	x2	0.13(2)	x2	-O12	2.11(44)	x2	0.18(21)	x2
		BVS	**1.033(82)**				**BVS**	**0.983(374)**	
Li5-O8	2.23(7)	x4	0.13(2)	x4					
-O11	2.21(7)	x2	0.13(2)	x2	**Li6**-O8	2.24(3)	x2	0.12(1)	x2
		BVS	**0.773(56)**		-O11	2.10(4)	x2	0.18(2)	x2
Li7-O8	2.07(6)	x4	0.20(4)	x4	-O12	2.10(40)	x2	0.18(20)	x2
-O11	2.01(7)	x2	0.23(4)	x2			**BVS**	**0.972(281)**	
		BVS	**1.248(92)**						
O8- Ir1	1.99(3)	x1	0.72(5)	x1	**O12**- Ir1	2.01(42)	x2	0.69(78)	x2
- Ir2	2.14(6)	x1	0.48(8)	x1	- Ir2	2.01(5)	x1	0.68(10)	x1
-Li3	1.97(7)	x1	0.26(5)	x1	-Li3	2.21(5)	x2	0.13(2)	x2
-Li5	2.24(3)	x1	0.123(8)	x1	-Li4	2.19(42)	x1	0.14(16)	x1
-Li6	2.23(7)	x1	0.13(2)	x1	-Li4	2.11(44)	x1	0.18(21)	x1
-Li7	2.07(7)	x1	0.20(4)	x1	-Li6	2.10(40)	x1	0.18(20)	x1
		BVS	**1.902(115)**				**BVS**	**2.006(852)**	
O9- Ir2	1.97(8)	x2	0.76(16)	x2	**O11**- Ir1	2.10(4)	x2	0.53(6)	x2
-Li3	2.22(9)	x2	0.13(3)	x2	-Li6	2.10(4)	x2	0.18(2)	x2
-Li4	2.12(1)	x2	0.171(5)	x2	-Li5	2.21(7)	x2	0.13(2)	x2
		BVS	**2.124(232)**		-Li7	2.01(7)	x2	0.23(4)	x2
							BVS	**1.793(102)**	

Table A.21: Averaged bond lengths in Å and calculated bond valence sums (BVS) of γ-Li_2IrO_3 reported by Analytis [4], resulting in a global instability index of 0.148. Data taken from crystallographic information file distributed via private communication.

	Bond length / Å		Bond valence			Bond length / Å		Bond valence	
Ir1-O1	1.99(3)	x2	0.72(5)	x2	**Ir2**-O1	2.16(7)	x2	0.46(9)	x2
-O3	2.08(6)	x2	0.57(10)	x2	-O2	1.98(6)	x2	0.75(13)	x2
-O4	1.99(7)	x2	0.71(31)	x2	-O4	2.01(5)	x2	0.68(9)	x2
		BVS	**4.013(243)**				**BVS**	**3.768(258)**	
Li1-O1	1.96(7)	x2	0.26(5)	x2	**Li2**-O2	2.12(1)	x2	0.17(1)	x2
-O2	2.22(7)	x2	0.13(3)	x2	-O4	2.20(7)	x2	0.14(3)	x2
-O4	2.22(5)	x2	0.13(2)	x2	-O4	2.09(7)	x2	0.18(3)	x2
		BVS	**1.055(86)**				**BVS**	**0.986(60)**	
Li4-O1	2.24(7)	x4	0.12(3)	x4					
-O3	2.21(7)	x2	0.13(2)	x2	**Li3**-O1	2.24(3)	x2	0.12(1)	x2
		BVS	**0.756(60)**		-O3	2.12(6)	x2	0.17(3)	x2
Li5-O1	2.06(7)	x4	0.20(4)	x4	-O4	2.11(7)	x2	0.18(3)	x2
-O3	2.01(7)	x2	0.23(4)	x2			**BVS**	**0.934(64)**	
		BVS	**1.272(100)**						
O1- Ir1	1.99(3)	x1	0.72(5)	x1	**O4**- Ir1	2.00(70)	x2	0.71(13)	x2
- Ir2	2.16(7)	x1	0.46(9)	x1	- Ir2	2.01(5)	x1	0.68(9)	x1
-Li1	1.96(7)	x1	0.26(5)	x1	-Li1	2.22(5)	x2	0.13(2)	x2
-Li4	2.24(3)	x1	0.12(1)	x1	-Li2	2.20(7)	x1	0.14(3)	x1
-Li3	2.24(7)	x1	0.12(3)	x1	-Li2	2.09(7)	x1	0.18(3)	x1
-Li5	2.06(7)	x1	0.20(4)	x1	-Li3	2.11(7)	x1	0.18(3)	x1
		BVS	**1.893(127)**				**BVS**	**2.023(17)**	
O2- Ir2	1.98(6)	x2	0.75(13)	x2	**O3**- Ir1	2.08(6)	x2	0.57(1)	x2
-Li1	2.22(7)	x2	0.13(3)	x2	-Li3	2.12(6)	x2	0.17(3)	x2
-Li2	2.12(1)	x2	0.17(1)	x2	-Li4	2.21(7)	x2	0.13(2)	x2
		BVS	**2.098(183)**		-Li5	2.01(7)	x2	0.23(4)	x2
							BVS	**1.841(149)**	

Table A.22: Selected bond angles (°) and averaged deviation of the γ-Li_2IrO_3 structure reported by Analytis [4]. Data taken from crystallographic information file distributed private communication.

Bond	Bond angle / °	Bond	Bond angle / °
O3-**Ir1**-O1	86(3)	O1-**Ir2**-O4	84(3)
O4-Ir1-O4	90(4)	O2-Ir2-O4	93(2)
O1-Ir1-O3	86(3)	O2-Ir2-O4	90(2)
O4-Ir1-O1	89(3)	O1-Ir2-O4	94(3)
O4-Ir1-O3	91(3)	O2-Ir2-O1	90(3)
O3-Ir1-O3	88(4)	O2-Ir2-O2	83(5)
O1-Ir1-O3	97(3)	O1-Ir2-O1	97(4)
Average deviation	2°	Average deviation	2.75°
O4-**Li1**-O1	84(2)	O2-**Li2**-O4	96(3)
O4-Li1-O2	89.7(19)	O2-Li2-O4	84(3)
O4-Li1-O2	92.6(19)	O4-Li2-O4	90(4)
O4-Li1-O1	94(2)	O4-Li2-O4	93(2)
O1-Li1-O1	87(5)	O4-Li2-O4	84(4)
O2-Li1-O1	89(3)		
O2-Li1-O2	96(4)		
Average deviation	3.4°	Average deviation	6°
O1-**Li3**-O4	89(3)	O3-**Li4**-O1	93.9(18)
O1-Li3-O3	86(3)	O3-Li4-O1	86(18)
O1-Li3-O3	96(3)	O1-Li4-O1	88(4)
O3-Li3-O4	87(3)	O1-Li4-O1	92(4)
O4-Li3-O4	95(3)		
O3-Li3-O3	91(4)		
Average deviation	2.66°	Average deviation	3.3°
O3-**Li5**-O1	85.8(18)		
O3-Li5-O1	94.2(18)		
O1-Li5-O1	98(5)		
O1-Li5-O1	92(5)		
Average deviation	5.5°		

Appendix B

Li-Ru-O system

Table B.1: Compounds in the Li-Ru-O system including their space groups (SG), lattice parameters a, b, c, α, β, γ, and ICSD Collection Codes.

Compound	SG	a / Å	b / Å	c / Å	α / β / γ	Coll. Code
Li_2RuO_3 [33]	$C2/c$	5.057	8.752	9.849	β = 99.86°	23409
Li_2RuO_3 [44]	$C2/c$	4.9116	8.7586	9.8544	β = 100.08°	202611
Li_2RuO_3 [60]	$C2/c$	4.9230(3)	8.7746(5)	9.8776(6)	β = 100.073(4)°	78721
Li_2RuO_3 [101]	$C2/c$	4.914(1)	8.763(2)	9.859(2)	β = 100.08(1)°	180367
Li_2RuO_3 [76]	$C2/m$	5.0466(3)	8.7649(2)	5.9417(3)	β = 124.495(4)°	-
Li_2RuO_3 [76]	$P2_1/m$	4.9210(2)	8.7829(2)	5.8941(2)	β = 124.342(2)°	-
$Li_{2.81}Ru_{1.04}O_4$ [2]	$P2/a$	5.1057(1)	5.8545(1)	5.1062(1)	β = 110.039(1)°	99333
$Li_{0.75}Ru_{0.25}O$ [43]	$P2/a$	5.084878(3)	5.87207(3)	5.12450(2)	β = 110.2130(4)°	243927
$LiRu_2O_4$ [48]	$Pnma$	9.13940(5)	2.80070(9)	11.0017(1)		290491
$Li_{0.9}RuO_2$ [30]	$Pnnm$	5.062(3)	4.967(4)	2.771(4)		48007
$Li_{1.4}RuO_3$ [60]	$C2/c$	4.9398(6)	8.6271(10)	9.9353(8)	β = 99.262(9)°	78722
$Li_{0.8}RuO_3$ [34]	$C2/c$	4.9274(22)	8.786(4)	9.8860(31)	β = 100.023(35)°	172179
$Li_{0.9}RuO_3$ [60]	$R\bar{3}$	5.1016(5)	5.1016(5)	14.0301(17)		78723
Li_7RuO_6 [82]	$P\bar{1}$	5.3654(1)	5.8584(1)	5.3496(1)	α = 117.182(1)°	155951
					β = 119.117(1)°	
					γ = 62.232(1)°	

Thermodynamic calculations

Table B.2: Calculated temperature-dependent values of the standard enthalpy and entropy of formation (ΔH_T^0 and ΔS_T^0), and heat capacity (C_p) of Li_2RuO_3. The temperature-dependent values for Li_2O(s) and RuO_2(s) were taken from Barin [6].

T / K	ΔH_T^0 / kJmol^{-1}	ΔS_T^0 / Jmol^{-1}K^{-1}
298	-944(20)	96(15)
500	-907(20)	133(15)
600	-899(20)	141(15)
700	-893(20)	147(15)
800	-888(20)	152(15)
900	-884(20)	156(15)
1000	-880(20)	160(15)
1100	-876(20)	163(15)
1200	-873(20)	167(15)
1300	-870(20)	170(15)
1400	-867(20)	173(15)

$$C_p = 146.42 + 0.02846\ T\ \text{-}4260000\ T^{-2}\ /\ \text{Jmol}^{-1}\text{K}^{-1}$$
$$298\ \text{K - }1400\ \text{K}$$

Table B.3: Calculated temperature-dependent values of the reaction enthalpy and entropy (ΔH_R and ΔS_R) of the assumed reaction 2 LiOH(g) + RuO_3 $\Leftrightarrow$ Li_2RuO_3(s) + H_2O(g) + 0.5 O_2(g). The temperature-dependent values of the enthalpy and entropy of formation (ΔH_T^0 and ΔS_T^0) for LiOH(g), RuO_3(g), H_2O(g), and O_2(g) were taken from Barin [6], whereas the values for Li_2IrO_3 were calculated in the present work and are listed in appendix table B.2.

T / K	ΔH_R / kJmol^{-1}	ΔS_R / Jmol^{-1}K^{-1}
298	-639(30)	-412(25)
500	-629(30)	-443(25)
600	-635(30)	-479(25)
700	-643(30)	-477(25)
800	-652(30)	-491(25)
900	-663(30)	-504(25)
1000	-674(30)	-516(25)
1100	-685(30)	-526(25)
1200	-696(30)	-536(25)
1300	-708(30)	-544(25)
1400	-719(30)	-552(25)

Table B.4: Calculated temperature-dependent values of the standard enthalpy and entropy of formation, ΔH_T^0 and ΔS_T^0, and heat capacity, C_p, of the solid compound Li_3RuO_4 based on equation 2.4 and the Neumann-Kopp law on page 29 from the sum of the respective values of its decomposition products Li_2O(s) and RuO_2(s) [13]. The temperature dependent values for Li_2O(s) and RuO_2(s) are listed in [6].

T / K	ΔH_T^0 / kJmol^{-1}	ΔS_T^0 / Jmol^{-1}K^{-1}
298	-1253(20)	115(15)
500	-1208(20)	160(15)
600	-1198(20)	170(15)
700	-1190(20)	178(15)
800	-1184(20)	184(15)
900	-1179(20)	189(15)
1000	-1174(20)	194(15)
1100	-1169(20)	199(15)
1200	-1165(20)	203(15)
1300	-1160(20)	208(15)
1400	-1156(20)	211(15)

$$C_p = 181.32 + 0.03729\ T\ \text{-}5185000\ T^{-2}\ /\ \text{Jmol}^{-1}\text{K}^{-1}$$
$$298\ \text{K - }1400\ \text{K}$$

Table B.5: Calculated temperature-dependent values of the reaction enthalpy and entropy, ΔH_R and ΔS_R, of the assumed total reaction 3 LiOH (g) + RuO_3(g) $\Leftrightarrow$ Li_3RuO_4(s) + 1.5 H_2O + 0.25 O_2(g) following the equations 2.7 and 2.6. Therefore, the necessary temperature dependent values of the enthalpy and entropy of formation, ΔH_T^0 and ΔS_T^0 for LiOH(g), RuO_3(g), H_2O(g) and O_2(g) are listed in [6], whereas the values for Li_3RuO_4 were calculated in the present work following equation 2.4 and are listed in appendix table B.4.

T / K	ΔH_R / kJmol^{-1}	ΔS_R / Jmol^{-1}K^{-1}
298	-835(30)	-510(25)
500	-868(30)	-593(25)
600	-840(30)	-598(25)
700	-847(30)	-597(25)
800	-858(30)	-614(25)
900	-870(30)	-628(25)
1000	-882(30)	-642(25)
1100	-895(30)	-654(25)
1200	-909(30)	-665(25)
1300	-922(30)	-676(25)
1400	-936(30)	-685(25)

Structural aspects

Li_2RuO_3

Table B.6: Structural model of Li_2RuO_3 ($C2/c$) reported by Ramesha et al. [101] including lattice parameters (a, b, c, β), atomic positions with Wyckoff site symmetry, fractional coordinates (x, y, z), and isotropic atomic displacement parameters (B_{iso}).

Li_2RuO_3

Space group	$C2/c$
Z	8
a,b,c,β	4.914(1) Å, 8.763(2) Å, 9.859(2) Å, 100.08(1)°
T	298 K
Diffraction method	P-XRD

Atom	Site	x	y	z	B_{iso} / Å^2
Ru1	8f	0.2471(2)	0.0828(1)	0.0029(1)	0.85(2)
Li1	4d	0.25	0.25	0.5	0.45(4)
Li2	4e	0	0.0837(1)	0.25	0.31(3)
Li3	4e	0	0.4154(2)	0.25	0.28(1)
Li4	4e	0	0.75	0.25	0.43(2)
O1	8f	0.1231(1)	0.2496(2)	0.1174(1)	1.02(2)
O2	8f	0.1231(1)	0.5852(2)	0.1174(1)	1.24(3)
O3	8f	0.1231(1)	0.9173(2)	0.1174(1)	0.84(1)

Table B.7: Structural model of Li_2RuO_3 ($C2/m$) reported by Miura et al. [76] including lattice parameters (a, b, c, β), atomic positions with Wyckoff site symmetry, and fractional coordinates (x, y, z).

Li_2RuO_3

Space group	$C2/m$
Z	2
a,b,c,β	5.0466(3) Å, 8.7649(2) Å, 5.9417(3) Å, 124.495(4)°
T	298 K
Diffraction method	P-ND

Atom	Site	x	y	z
Ru1	4g	0.0	0.3308(4)	0.0
Li1	2a	0.0	0.0	0.0
Li2	4h	0.0	0.3425(9)	0.5
Li3	2c	0.0	0.0	0.5
O1	8j	-0.0162(7)	0.1701(2)	0.2324(2)
O2	4i	0.4991(8)	0.0	0.2325(4)

Table B.8: Structural model of Li_2RuO_3 ($P2_1/m$) reported by Miura et al. [76] including lattice parameters (a, b, c, β), atomic positions with Wyckoff site symmetry, and fractional coordinates (x, y, z).

Li_2RuO_3

Space group	$P2_1/m$
Z	2
a, b, c, β	4.9210(2) Å, 8.7829(2) Å, 5.8941(2) Å, 124.342(2)°
T	298 K
Diffraction method	P-ND

Atom	Site	x	y	z
Ru1	$4f$	0.2737(6)	0.0766(2)	-0.0063(6)
Li1	$2e$	0.706(35)	0.25	-0.068(2)
Li2	$4f$	0.253(3)	0.0991(7)	0.493(3)
Li3	$2e$	0.772(4)	0.25	0.513(5)
O1	$4f$	0.7553(7)	0.0805(6)	0.2489(6)
O2	$4f$	0.7757(6)	0.0819(6)	0.7685(6)
O3	$2e$	0.7757(6)	0.25	0.2144(9)
O4	$2e$	0.255(1)	0.25	0.761(1)

Table B.9: Averaged bond lengths in Å and calculated bond valence sums (BVS) of Li_2RuO_3 ($C2/c$) published by Ramesha et al. [101], resulting in a global instability index of 0.183.

	Bond length / Å		Bond valence			Bond length / Å		Bond valence	
Ru1-O1	2.01(2)	x1	0.63(1)	x1	**O1**-Ru1	2.01(1)	x1	0.63(1)	x1
-O1	2.06(21)	x1	0.55(1)	x1	-Ru1	2.06(1)	x1	0.55(1)	x1
-O2	1.9(2)	x1	0.66(1)	x1	-Li1	1.99(1)	x1	0.24(1)	x1
-O2	2.06(2)	x1	0.54(1)	x1	-Li2	2.11(1)	x1	0.17(1)	x1
-O3	2.00(1)	x1	0.64(1)	x1	-Li3	2.11(1)	x1	0.17(1)	x1
-O3	1.99(1)	x1	0.66(1)	x1	-Li4	2.07(1)	x1	0.20(1)	x1
		BVS	**3.672(6)**				**BVS**	**1.960(4)**	
Li1-O1	1.99(1)	x2	0.24(1)	x2	**Li2**-O1	2.11(1)	x2	0.17(1)	x2
-O2	2.02(1)	x2	0.23(1)	x2	-O2	2.14(1)	x2	0.20(1)	x2
-O3	2.03(1)	x2	0.22(1)	x2	-O3	2.07(1)	x2	0.17(1)	x2
		BVS	**1.370(2)**				**BVS**	**1.082(2)**	
Li3-O1	2.11(1)	x2	0.17(1)	x2	**Li4**-O1	2.07(1)	x2	0.20(1)	x2
-O2	2.14(1)	x2	0.16(1)	x2	-O2	2.11(1)	x2	0.18(1)	x2
-O3	2.07(1)	x2	0.20(1)	x2	-O3	2.12(1)	x2	0.17(1)	x2
		BVS	**1.064(2)**				**BVS**	**1.083(1)**	
O2-Ru1	1.99(1)	x1	0.55(5)	x1	**O3**-Ru1	2.00(1)	x1	0.64(1)	x1
-Ru1	2.06(1)	x1	0.64(11)	x1	-Ru1	1.99(1)	x1	0.66(1)	x1
-Li1	2.02(1)	x1	0.18(3)	x1	-Li1	2.03(1)	x1	0.22(1)	x1
-Li2	2.07(1)	x1	0.20(2)	x1	-Li2	2.12(1)	x1	0.17(1)	x1
-Li3	2.14(1)	x1	0.16(1)	x1	-Li3	2.07(1)	x1	0.20(1)	x1
-Li4	2.11(1)	x1	0.18(1)	x1	-Li4	2.12(1)	x1	0.17(1)	x1
		BVS	**1.959(4)**				**BVS**	**2.052(4)**	

Table B.10: Averaged bond lengths in Å and calculated bond valence sums (BVS) of Li_2RuO_3 ($C2/m$) published by Miura et al. [76], resulting in a global instability index of 0.160.

	Bond length / Å		Bond valence			Bond length / Å		Bond valence	
Ru1-O1	2.01(1)	x2	0.63(1)	x2	**Li1**-O1	2.07(1)	x2	0.20(1)	x2
-O1	2.01(1)	x2	0.62(1)	x2	-O2	2.07(1)	x2	0.20(1)	x2
-O2	2.03(1)	x2	0.59(1)	x2	-O3	2.08(1)	x2	0.19(1)	x2
		BVS	**3.673(13)**				**BVS**	**1.177(3)**	
Li2-O1	2.16(1)	x2	0.15(1)	x2	**Li3**-O1	2.15(1)	x2	0.16(1)	x2
-O1	2.15(1)	x2	0.16(1)	x2	-O1	2.15(1)	x2	0.16(1)	x2
-O2	2.10(1)	x2	0.18(1)	x2	-O2	2.09(1)	x2	0.19(1)	x2
		BVS	**0.975(5)**				**BVS**	**1.006(3)**	
O1-Ru1	2.01(1)	x1	0.63(1)	x1	**O2**-Ru1	2.03(1)	x2	0.59(1)	x2
-Ru1	2.01(1)	x1	0.62(1)	x1	-Li1	2.08(1)	x1	0.19(1)	x1
-Li1	2.07(1)	x1	0.20(1)	x1	-Li2	2.10(1)	x2	0.18(1)	x2
-Li2	2.16(1)	x1	0.15(1)	x1	-Li3	2.09(1)	x1	0.19(1)	x1
-Li2	2.15(1)	x1	0.16(1)	x1			**BVS**	**1.917(9)**	
-Li3	2.15(1)	x1	0.16(1)	x1					
		BVS	**1.911(8)**						

Table B.11: Averaged bond lengths in Å and calculated bond valence sums (BVS) of Li_2RuO_3 ($P2_1/m$) published by Miura et al. [76], resulting in a global instability index of 0.206.

	Bond length / Å		Bond valence			Bond length / Å		Bond valence	
Ru1-O1	1.96(1)	x1	0.70(1)	x1	**Li2**-O1	2.03(1)	x1	0.22(1)	x1
-O1	1.93(1)	x1	0.76(1)	x1	-O1	2.21(2)	x1	0.14(1)	x1
-O2	2.02(1)	x1	0.60(1)	x1	-O2	2.14(2)	x1	0.16(1)	x1
-O2	2.08(1)	x1	0.51(1)	x1	-O2	2.16(1)	x1	0.15(1)	x1
-O3	2.04(1)	x1	0.58(1)	x1	-O3	2.11(2)	x1	0.17(1)	x1
-O4	2.04(1)	x1	0.58(1)	x1	-O4	2.03(2)	x1	0.22(1)	x1
		BVS	**3.725(20)**				**BVS**	**1.057(17)**	
Li1-O1	2.29(1)	x2	0.11(1)	x2	**Li3**-O1	2.12(1)	x2	0.17(1)	x2
-O2	1.90(1)	x2	0.31(1)	x2	-O2	2.10(1)	x2	0.18(1)	x2
-O3	2.24(1)	x1	0.13(1)	x1	-O2	2.13(1)	x1	0.17(1)	x1
-O4	1.80(1)	x1	0.41(2)	x1	-O2	2.01(1)	x1	0.23(1)	x1
		BVS	**1.373(21)**				**BVS**	**1.095(25)**	
O1-Ru1	1.90(10)	x1	0.70(1)	x1	**O2**-Ru1	2.02(1)	x2	0.60(1)	x2
-Ru1	1.97(1)	x1	0.76(1)	x1	-Ru1	2.08(1)	x1	0.51(1)	x1
-Li1	2.29(1)	x1	0.11(1)	x1	-Li1	1.90(1)	x2	0.31(1)	x2
-Li2	2.03(1)	x1	0.22(1)	x1	-Li2	2.14(1)	x1	0.16(1)	x1
-Li2	2.21(1)	x1	0.14(1)	x1	-Li2	2.16(1)	x1	0.15(1)	x1
-Li3	2.12(2)	x1	0.17(1)	x1	-Li3	2.10(1)	x1	0.18(1)	x1
		BVS	**2.097(19)**				**BVS**	**1.912(19)**	
O3-Ru1	2.04(1)	x2	0.58(1)	x2	**O4**-Ru1	2.04(1)	x2	0.58(1)	x2
-Li1	2.24(1)	x1	0.13(1)	x1	-Li1	1.80(1)	x1	0.41(1)	x1
-Li2	2.11(1)	x2	0.17(1)	x2	-Li2	2.03(1)	x2	0.22(1)	x2
-Li3	2.13(1)	x1	0.17(1)	x1	-Li3	2.01(1)	x1	0.23(1)	x1
		BVS	**1.791(17)**				**BVS**	**2.224(25)**	

Table B.12: Anisotropic atomic displacement parameters (ADPs) of Li_2RuO_3 ($P2_1/m$) of the present work.

Atom site	U_{11} / Å^2	U_{22} / Å^2	U_{33} / Å^2	U_{12} / Å^2	U_{13} / Å^2	U_{23} / Å^2
Ru1	0.00431(16)	0.00404(17)	0.00412(16)	-0.00027(5)	0.00271(11)	-0.00008(5)
Li1	0.005(3)	0.002(3)	0.013(4)	0 0.004(3)	0	
Li2	0.009(3)	0.010(3)	0.010(3)	0.0014(14)	0.006(3)	0.0003(13)
Li3	0.014(4)	0.010(4)	0.011(4)	0	0.008(3)	0
O1	0.0043(9)	0.0052(11)	0.0059(10)	-0.0015(6)	0.0025(8)	-0.0014(6)
O2	0.0056(9)	0.0054(11)	0.0062(9)	0.0013(6)	0.0036(8)	0.0018(6)
O3	0.0080(12)	0.0051(13)	0.0058(12)	0	0.0046(10)	0
O4	0.0063(12)	0.0046(13)	0.0066(12)	0	0.0042(10)	0

Table B.13: Averaged bond lengths in Å and calculated bond valence sums (BVS) of Li_2RuO_3 ($P2_1/m$) of the present work, resulting in a global instability index of 0.146.

	Bond length / Å		Bond valence			Bond length / Å		Bond valence	
Ru1-O1	1.97(2)	x1	0.70(1)	x1	**Li2**-O1	2.05(1)	x1	0.21(1)	x1
-O1	1.98(1)	x1	0.69(1)	x1	-O1	2.18(1)	x1	0.14(1)	x1
-O2	2.02(1)	x1	0.60(1)	x1	-O2	2.11(1)	x1	0.18(1)	x1
-O2	2.04(1)	x1	0.57(1)	x1	-O2	2.09(1)	x1	0.19(1)	x1
-O3	2.03(1)	x1	0.59(1)	x1	-O3	2.11(1)	x1	0.17(1)	x1
-O4	2.03(1)	x1	0.58(1)	x1	-O4	2.09(1)	x1	0.19(1)	x1
		BVS	**3.718(11)**				**BVS**	**1.076(7)**	
Li1-O1	2.15(1)	x2	0.16(1)	x2	**Li3**-O1	2.09(1)	x2	0.18(1)	x2
-O2	2.00(1)	x2	0.23(1)	x2	-O2	2.12(1)	x2	0.17(1)	x2
-O3	2.01(1)	x1	0.23(1)	x1	-O2	2.07(1)	x1	0.20(1)	x1
-O4	2.00(1)	x1	0.24(1)	x1	-O2	2.07(1)	x1	0.20(1)	x1
		BVS	**1.044(13)**				**BVS**	**1.101(8)**	
O1-Ru1	1.97(1)	x1	0.70(3)	x1	**O2**-Ru1	2.02(1)	x2	0.60(1)	x2
-Ru1	1.98(1)	x1	0.69(1)	x1	-Ru1	2.04(1)	x1	0.57(1)	x1
-Li1	2.15(1)	x1	0.16(1)	x1	-Li1	2.00(1)	x2	0.23(1)	x2
-Li2	2.04(1)	x1	0.21(1)	x1	-Li2	2.11(1)	x1	0.18(1)	x1
-Li2	2.18(1)	x1	0.14(1)	x1	-Li2	2.09(1)	x1	0.19(1)	x1
-Li3	2.09(1)	x1	0.18(1)	x1	-Li3	2.12(1)	x1	0.17(1)	x1
		BVS	**2.070(9)**				**BVS**	**1.943(9)**	
O3-Ru1	2.03(1)	x2	0.59(1)	x2	**O4**-Ru1	2.03(1)	x2	0.58(1)	x2
-Li1	2.01(1)	x1	0.23(1)	x1	-Li1	2.00(1)	x1	0.24(1)	x1
-Li2	2.11(1)	x2	0.17(1)	x2	-Li2	2.09(1)	x2	0.19(1)	x2
-Li3	2.07(1)	x1	0.20(1)	x1	-Li3	2.07(1)	x1	0.20(1)	x1
		BVS	**1.946(9)**				**BVS**	**1.968(10)**	

Li_3RuO_4

Table B.14: Structural model of $Li_{2.81(2)}Ru_{1.04(2)}O_4$ published by Alexander et al. [2] including lattice parameters (a, b, c, β), cell volume V, atomic positions with Wyckoff site symmetry and oxidation state, site occupancy factors (SOF), fractional coordinates (x, y, y), and isotropic atomic displacement parameters (B_{iso}).

$\mathbf{Li_{2.81(2)}Ru_{1.04(2)}O_4}$	
Space group	$P2/a$
Z	2
a, b, c, β	5.1057(1) Å, 5.8545(1) Å, 5.1062(1) Å, 110.039(1)°
V	143.689(6) Å^3
T	293 K
Diffraction method	P-ND
PDF	01-074-4149

Atom	Oxidation state	Site	SOF	x	y	z	B_{iso} / Å^2
Li1	1+	2e	0.951(8)	0.75	0.614(3)	0	0.013(2)
Ru1	5+	2e	0.010(2)	0.75	0.614(3)	0	0.013(2)
Li2	1+	2f	0.940(8)	0.75	0.883(3)	0.5	0.014(2)
Ru2	5+	2f	0.012(2)	0.75	0.883(3)	0.5	0.014(2)
Li3	1+	2f	0.917(8)	0.75	0.368(3)	0.5	0.0119(1)
Ru3	5+	2f	0.017(2)	0.75	0.368(3)	0.5	0.0119(1)
Ru4	5+	2e	1.0	0.25	0.8671(8)	0	0.0082(3)
O1	2-	4g	1.0	0.0181(6)	0.6400(3)	0.7555(6)	0.0089(3)
O2	2-	4g	1.0	0.5028(6)	0.1107(4)	0.2235(6)	0.0061(3)

Quality indicators of refinement

R_{wp}: 0.0569

GOF: 1.672

Table B.15: Structural model of Li_3RuO_4 published by Jacquet et al. [43] including lattice parameters (a, b, c, β), cell volume V, atomic positions with Wyckoff site symmetry and oxidation state, site occupancy factors (SOF), fractional coordinates (x, y, z), and isotropic atomic displacement parameters (B_{iso}).

Li_3RuO_4

Space group	$P2/a$
Z	2
a, b, c, β	5.08487(3) Å, 5.87207(3) Å, 5.12450(2) Å, 110.2130(4)°
V	143.5878 Å^3
T	298 K
GOF	2.20
Diffraction method	P-ND

Atom	Oxidation state	Site	SOF	x	y	z	B_{iso} / Å^2
Li1	1+	2e	1.0	0.75	0.616(2)	0	0.0059
Li2	1+	2f	1.0	0.75	0.879(2)	0.5	0.0059
Li3	1+	2f	1.0	0.75	0.389(2)	0.5	0.0059
Ru4	5+	2e	1.0	0.25	0.85775(16)	0	0.00028
O1	2-	4g	1.0	0.0178(7)	0.6356(5)	0.7578(5)	0.0104
O2	2-	4g	1.0	0.5029(7)	0.1136(5)	0.2263(7)	0.0104

Table B.16: Averaged bond lengths in Å and calculated bond valence sums (BVS) of Li_3RuO_4 published by Jacquet et al. [43], resulting in a global instability index of 0.08.

	Bond length / Å		Bond valence			Bond length / Å		Bond valence	
Li1-O5	2.14(1)	x2	0.16(1)	x2	**Li2**-O5	2.10(1)	x2	0.18(1)	x2
-O5	2.03(1)	x2	0.22(1)	x2	-O5	2.06(1)	x2	0.20(1)	x2
-O6	2.12(1)	x2	0.17(1)	x2	-O6	2.21(1)	x2	0.14(1)	x2
		BVS	**1.107(10)**				**BVS**	**1.039(9)**	
Li3-O5	2.11(1)	x2	0.18(1)	x2	**Ru4**-O5	1.90(1)	x2	0.99(1)	x2
-O5	2.06(1)	x2	0.20(1)	x2	-O5	2.06(1)	x2	0.66(1)	x2
-O6	2.22(1)	x2	0.13(1)	x2	-O6	1.99(1)	x2	0.79(1)	x2
		BVS	**1.012(8)**				**BVS**	**4.864(18)**	
O5- Li1	2.14(1)	x1	0.16(1)	x1	**O6**- Li1	2.12(1)	x1	0.17(1)	x1
-Li1	2.03(1)	x1	0.22(1)	x1	-Li2	2.06(1)	x1	0.20(1)	x1
-Li2	2.10(1)	x1	0.18(1)	x1	-Li2	2.21(1)	x1	0.14(1)	x1
-Li3	2.11(1)	x1	0.18(1)	x1	-Li3	2.22(1)	x1	0.13(1)	x1
-Li3	2.06(1)	x1	0.20(1)	x1	-Ru4	2.06(1)	x1	0.66(1)	x1
-Ru4	1.90(1)	x1	0.99(1)	x1	-Ru4	1.99(1)	x1	0.79(1)	x1
		BVS	**1.931(11)**				**BVS**	**2.080(13)**	

Table B.17: Averaged bond lengths in Å and calculated bond valence sums (BVS) of Li_3RuO_4 published by Alexander et al. [2]. Due to the shared occupancy of three atomic positions (Li1:0.951/Ru1:0.010; Li2:0.94/Ru2:0.012; Li3:0.917/Ru3:0.017), the global instability index is calculated with weighted bond valence sums of the respective interatomic bonds. For better understanding, these bonds are marked in red. Overall, this results in a global instability index of 0.13.

	Bond length / Å		Bond valence			Bond length / Å		Bond valence	
Li1-O5	2.15(1)	x2	0.16(1)	x2	**Ru1**-O5	2.15(1)	x2	0.51(1)	x2
-O5	2.04(1)	x2	0.21(1)	x2	-O5	2.04(1)	x2	0.69(2)	x2
-O6	2.13(1)	x2	0.16(1)	x2	-O6	2.13(1)	x2	0.53(2)	x2
		BVS	**1.067(14)**				**BVS**	**3.448(44)**	
Li2-O5	2.09(1)	x2	0.18(1)	x2	**Ru2**-O5	2.09(1)	x2	0.60(1)	x2
-O6	2.04(1)	x2	0.22(1)	x2	-O6	2.04(1)	x2	0.69(1)	x2
-O6	2.22(1)	x2	0.13(1)	x2	-O6	2.22(1)	x2	0.43(1)	x2
		BVS	**1.062(3)**				**BVS**	**3.430(10)**	
Li3-O5	2.21(1)	x2	0.13(1)	x2	**Ru3**-O5	2.21(1)	x2	0.43(2)	x2
-O5	2.04(1)	x2	0.21(1)	x2	-O5	2.04(1)	x2	0.68(1)	x2
-O6	2.15(1)	x2	0.16(1)	x2	-O6	2.15(1)	x2	0.52(1)	x2
		BVS	**1.003(10)**				**BVS**	**3.241(33)**	
Ru4-O5	1.93(1)	x2	0.93(1)	x2					
-O5	2.00(1)	x2	0.77(1)	x2					
-O6	1.97(1)	x2	0.82(1)	x2					
		BVS	**5.025(21)**						
O5-Li1	2.15(1)	x1	0.16(1)	x1	**O5**-Ru1	2.15(1)	x1	0.51(1)	x1
-Li1	2.04(1)	x1	0.21(1)	x1	-Ru1	2.04(1)	x1	0.69(2)	x1
-Li2	2.09(1)	x1	0.18(1)	x1	-Ru2	2.09(1)	x1	0.60(1)	x1
-Li3	2.21(1)	x1	0.13(1)	x1	-Ru3	2.21(1)	x1	0.43(2)	x1
-Li3	2.04(1)	x1	0.21(1)	x1	-Ru3	2.04(1)	x1	0.68(1)	x1
-Ru4	1.93(1)	x1	0.93(1)	x1	-Ru4	1.93(1)	x1	0.93(1)	x1
		BVS	**1.827(13)**				**BVS**	**3.833(31)**	
O6-Li1	2.13(1)	x1	0.16(1)	x1	**O6**-Ru1	2.13(1)	x1	0.53(2)	x1
-Li2	2.03(1)	x1	0.22(1)	x1	-Ru2	2.03(1)	x1	0.69(1)	x1
-Li2	2.22(1)	x1	0.13(1)	x1	-Ru2	2.22(1)	x1	0.43(1)	x1
-Li3	2.15(1)	x1	0.16(1)	x1	-Ru3	2.15(1)	x1	0.51(2)	x1
-Ru4	2.00(1)	x1	0.77(1)	x1	-Ru4	2.00(1)	x1	0.77(1)	x1
-Ru4	1.97(1)	x1	0.82(4)	x1	-Ru4	1.97(1)	x1	0.82(4)	x1
		BVS	**2.521(14)**				**BVS**	**3.739(29)**	

Table B.18: Structural model of Li_3RuO_4 of the present work including lattice parameters (a, b, c, β), cell volume V, atomic positions with Wyckoff site symmetry and oxidation state, site occupancy factors (SOF), fractional coordinates (x, y, z), and isotropic atomic displacement parameters (B_{iso}).

Li_3RuO_4

Space group	$P2/a$
Z	2
a, b, c, β	5.08279(24) Å,5.86653(24) Å, 5.12437(21) Å, 110.1909(27)°
V	143.410(11) Å^3
T	298 K
Diffraction method	P-XRD

Atom	Oxidation state	Site	SOF	x	y	z	B_{iso} / Å^2
Li1	1+	2e	1.0	0.75	0.632(15)	0	0.4658
Li2	1+	2f	1.0	0.75	0.876(15)	0.5	0.4658
Li3	1+	2f	1.0	0.75	0.4059(85)	0.5	0.4658
Ru4	5+	2e	1.0	0.25	0.85769(80)	0	0.02211
O1	2-	4g	1.0	0.0217(46)	0.6238(31)	0.7570(34)	0.82115
O2	2-	4g	1.0	0.5143(46)	0.1087(28)	0.2096(35)	0.82115

Quality indicators of Rietveld refinement

R_{wp}: 0.1023

GOF: 1.86

Table B.19: Averaged bond lengths in Å and calculated bond valence sums (BVS) of Li_3RuO_4 of the present work, resulting in a global instability index of 0.22.

	Bond length / Å		Bond valence			Bond length / Å		Bond valence	
Li1-O5	2.16(2)	x2	0.16(1)	x2	**Li2**-O5	2.13(7)	x2	0.16(3)	x2
-O5	2.05(7)	x2	0.21(4)	x2	-O5	2.07(6)	x2	0.19(3)	x2
-O6	2.06(6)	x2	0.20(4)	x2	-O6	2.33(2)	x2	0.10(1)	x2
		BVS	**1.128(75)**				**BVS**	**0.909(60)**	
Li3-O5	2.01(4)	x2	0.23(2)	x2	**Ru4**-O5	1.95(2)	x2	0.89(1)	x2
-O5	2.04(2)	x2	0.21(1)	x2	-O5	2.03(2)	x2	0.70(1)	x2
-O6	2.34(4)	x2	0.10(1)	x2	-O6	1.87(2)	x2	1.08(7)	x2
		BVS	**1.076(40)**				**BVS**	**5.343(125)**	
O5- Li1	2.16(2)	x1	0.16(1)	x1	**O6**- Li1	2.06(7)	x1	0.20(1)	x1
-Li1	2.05(7)	x1	0.21(1)	x1	-Li2	2.07(6)	x1	0.19(1)	x1
-Li2	2.13(6)	x1	0.16(1)	x1	-Li2	2.33(2)	x1	0.10(1)	x1
-Li3	2.01(4)	x1	0.23(1)	x1	-Li3	2.34(4)	x1	0.10(1)	x1
-Li3	2.04(2)	x1	0.21(1)	x1	-Ru4	2.03(2)	x1	0.70(1)	x1
-Ru4	1.94(2)	x1	0.88(4)	x1	-Ru4	1.87(2)	x1	1.08(7)	x1
		BVS	**1.857(69)**				**BVS**	**2.371(92)**	

Table B.20: Comparison of Ru-Ru distances between Li_3RuO_4 of the present work and of Alexander et al. [2]. The interaction types describe the paths of magnetic interaction between two Ru atoms in the crystal structure.

Interaction type	Ru-Ru distance / Å	
	Alexander et al. [2]	present work
Intrachain, direct-neighbour	2.990(5)	3.041(6)
Interchain, along [110] direction	4.999(9)	4.906(9)
Intrachain, next-neighbour	5.1057(1)	5.0828(3)
Interchain, along [001] direction	5.1062(1)	5.1244(3)

Appendix C

Li-Ir-Ru-O system

Thermodynamic calculations

Table C.1: Calculated temperature-dependent values of the standard enthalpy and entropy of formation (ΔH_T^0 and ΔS_T^0), heat capacity (C_p), and the reaction enthalpy and entropy (ΔH_R and ΔS_R) of $Li_2Ir_{1-x}Ru_xO_3$. The temperature-dependent values for Li_2O(s), IrO_2(s), and RuO_2(s) were taken from Barin [6].

$Li_2Ir_{1-x}Ru_xO_3$
x = 0.1

T / K	ΔH_T^0 / kJmol^{-1}	ΔS_T^0 / Jmol^{-1}K^{-1}	ΔH_R / kJmol^{-1}	ΔS_R / Jmol^{-1}K^{-1}
298	-894(20)	89(15)	-671(30)	-431(25)
500	-864(20)	119(15)	-670(30)	-474(25)
600	-856(20)	127(15)	-677(30)	-495(25)
700	-850(20)	133(15)	-686(30)	-510(25)
800	-845(20)	138(15)	-696(30)	-525(25)
900	-840(20)	143(15)	-706(30)	-538(25)
1000	-836(20)	147(15)	-717(30)	-549(25)
1100	-832(20)	151(15)	-727(30)	-559(25)
1200	-828(20)	155(15)	-738(30)	-568(25)
1300	-824(20)	159(15)	-749(30)	-576(25)
1400	-820(20)	163(15)	-760(30)	-583(25)

C_p = 133.2 + 0.037118 T -3081000 T^{-2} / Jmol^{-1}K^{-1}
298 K - 1400 K

$Li_2Ir_{1-x}Ru_xO_3$
x = 0.2

T / K	ΔH_T^0 / kJmol^{-1}	ΔS_T^0 / Jmol^{-1}K^{-1}	ΔH_R / kJmol^{-1}	ΔS_R / Jmol^{-1}K^{-1}
298	-899(20)	90(15)	-668(30)	-429(25)
500	-869(20)	121(15)	-665(30)	-470(25)
600	-851(20)	128(15)	-672(30)	-493(25)
700	-855(20)	134(15)	-681(30)	-506(25)
800	-850(20)	139(15)	-691(30)	-521(25)
900	-845(20)	144(15)	-701(30)	-534(25)
1000	-841(20)	148(15)	-712(30)	-545(25)
1100	-837(20)	153(15)	-723(30)	-555(25)
1200	-833(20)	157(15)	-734(30)	-564(25)
1300	-829(20)	161(15)	-745(30)	-573(25)
1400	-825(20)	164(15)	-756(30)	-580(25)

C_p = 134.6 + 0.036156 T -3212000 T^{-2} / Jmol^{-1}K^{-1}
298 K - 1400 K

$Li_2Ir_{1-x}Ru_xO_3$
x = 0.3

T / K	ΔH_T^0 / kJmol^{-1}	ΔS_T^0 / Jmol^{-1}K^{-1}	ΔH_R / kJmol^{-1}	ΔS_R / Jmol^{-1}K^{-1}
298	-905(20)	91(15)	-664(30)	-426(25)
500	-873(20)	122(15)	-661(30)	-467(25)
600	-866(20)	130(15)	-668(30)	-491(25)
700	-860(20)	136(15)	-676(30)	-502(25)
800	-855(20)	141(15)	-686(30)	-517(25)
900	-850(20)	146(15)	-796(30)	-530(25)
1000	-846(20)	150(15)	-707(30)	-542(25)
1100	-842(20)	154(15)	-718(30)	-552(25)
1200	-838(20)	158(15)	-729(30)	-561(25)
1300	-834(20)	162(15)	-740(30)	-569(25)
1400	-830(20)	166(15)	-751(30)	-576(25)

C_p = 136.1 + 0.035194 T -3343000 T^{-2} / Jmol^{-1}K^{-1}
298 K - 1400 K

$Li_2Ir_{1-x}Ru_xO_3$

x = 0.4

T / K	ΔH_T^0 / kJmol^{-1}	ΔS_T^0 / Jmol^{-1}K^{-1}	ΔH_R / kJmol^{-1}	ΔS_R / Jmol^{-1}K^{-1}
298	-910(20)	92(15)	-660(30)	-424(25)
500	-878(20)	124(15)	-656(30)	-463(25)
600	-871(20)	131(15)	-663(30)	-489(25)
700	-865(20)	137(15)	-672(30)	-499(25)
800	-859(20)	143(15)	-681(30)	-513(25)
900	-855(20)	147(15)	-692(30)	-526(25)
1000	-851(20)	151(15)	-702(30)	-538(25)
1100	-847(20)	155(15)	-713(30)	-548(25)
1200	-843(20)	159(15)	-724(30)	-557(25)
1300	-839(20)	163(15)	-735(30)	-565(25)
1400	-835(20)	167(15)	-747(30)	-573(25)

C_p = 137.6 + 0.034232 T -3474000 T^{-2} / Jmol^{-1}K^{-1}

298 K - 1400 K

$Li_2Ir_{1-x}Ru_xO_3$

x = 0.5

T / K	ΔH_T^0 / kJmol^{-1}	ΔS_T^0 / Jmol^{-1}K^{-1}	ΔH_R / kJmol^{-1}	ΔS_R / Jmol^{-1}K^{-1}
298	-916(20)	92(15)	-657(30)	-422(25)
500	-883(20)	125(15)	-651(30)	-460(25)
600	-875(20)	133(15)	-658(30)	-488(25)
700	-869(20)	139(15)	-667(30)	-495(25)
800	-864(20)	144(15)	-677(30)	-510(25)
900	-860(20)	149(15)	-687(30)	-523(25)
1000	-856(20)	153(15)	-698(30)	-534(25)
1100	-852(20)	157(15)	-708(30)	-544(25)
1200	-848(20)	161(15)	-720(30)	-554(25)
1300	-844(20)	164(15)	-731(30)	-562(25)
1400	-841(20)	168(15)	-742(30)	-569(25)

C_p = 139.0 + 0.03327 T -3605000 T^{-2} / Jmol^{-1}K^{-1}

298 K - 1400 K

$Li_2Ir_{1-x}Ru_xO_3$

x = 0.6

T / K	ΔH_T^0 / kJmol^{-1}	ΔS_T^0 / Jmol^{-1}K^{-1}	ΔH_R / kJmol^{-1}	ΔS_R / Jmol^{-1}K^{-1}
298	-921(20)	93(15)	-653(30)	-420(25)
500	-888(20)	127(15)	-647(30)	-457(25)
600	-880(20)	135(15)	-653(30)	-486(25)
700	-874(20)	141(15)	-662(30)	-491(25)
800	-869(20)	146(15)	-672(30)	-506(25)
900	-865(20)	150(15)	-682(30)	-519(25)
1000	-860(20)	154(15)	-693(30)	-531(25)
1100	-857(20)	158(15)	-704(30)	-541(25)
1200	-853(20)	162(15)	-715(30)	-550(25)
1300	-849(20)	165(15)	-726(30)	-558(25)
1400	-846(20)	169(15)	-738(30)	-566(25)

C_p = 140.5 + 0.032308 T -3736000 T^{-2} / Jmol^{-1}K^{-1}

298 K - 1400 K

$Li_2Ir_{1-x}Ru_xO_3$

x = 0.7

T / K	ΔH_T^0 / kJmol^{-1}	ΔS_T^0 / Jmol^{-1}K^{-1}	ΔH_R / kJmol^{-1}	ΔS_R / Jmol^{-1}K^{-1}
298	-927(20)	94(15)	-650(30)	-418(25)
500	-893(20)	128(15)	-642(30)	-453(25)
600	-885(20)	136(15)	-649(30)	-484(25)
700	-879(20)	142(15)	-657(30)	-488(25)
800	-874(20)	147(15)	-667(30)	-502(25)
900	-869(20)	152(15)	-677(30)	-515(25)
1000	-865(20)	156(15)	-688(30)	-527(25)
1100	-862(20)	159(15)	-699(30)	-537(25)
1200	-858(20)	163(15)	-710(30)	-546(25)
1300	-854(20)	167(15)	-722(30)	-555(25)
1400	-851(20)	170(15)	-733(30)	-562(25)

C_p = 142.0 + 0.031346 T -3867000 T^{-2} / Jmol^{-1}K^{-1}

298 K - 1400 K

$Li_2Ir_{1-x}Ru_xO_3$

x = 0.8

T / K	ΔH_T^0 / kJmol^{-1}	ΔS_T^0 / Jmol^{-1}K^{-1}	ΔH_R / kJmol^{-1}	ΔS_R / Jmol^{-1}K^{-1}
298	-933(20)	95(15)	-646(30)	-416(25)
500	-897(20)	130(15)	-638(30)	-450(25)
600	-890(20)	138(15)	-644(30)	-482(25)
700	-884(20)	144(15)	-652(30)	-484(25)
800	-879(20)	149(15)	-662(30)	-499(25)
900	-874(20)	153(15)	-672(30)	-512(25)
1000	-870(20)	157(15)	-683(30)	-523(25)
1100	-867(20)	161(15)	-694(30)	-534(25)
1200	-863(20)	164(15)	-705(30)	-543(25)
1300	-860(20)	168(15)	-717(30)	-551(25)
1400	-856(20)	171(15)	-728(30)	-559(25)

C_p = 143.5 + 0.030384 T -3998000 T^{-2} / Jmol^{-1}K^{-1}

298 K - 1400 K

$Li_2Ir_{1-x}Ru_xO_3$

x = 0.9

T / K	ΔH_T^0 / kJmol^{-1}	ΔS_T^0 / Jmol^{-1}K^{-1}	ΔH_R / kJmol^{-1}	ΔS_R / Jmol^{-1}K^{-1}
298	-938(20)	95(15)	-642(30)	-414(25)
500	-902(20)	131(15)	-633(30)	-446(25)
600	-894(20)	139(15)	-639(30)	-480(25)
700	-888(20)	145(15)	-648(30)	-480(25)
800	-883(20)	150(15)	-657(30)	-495(25)
900	-879(20)	155(15)	-668(30)	-508(25)
1000	-875(20)	158(15)	-678(30)	-519(25)
1100	-872(20)	162(15)	-690(30)	-530(25)
1200	-868(20)	166(15)	-701(30)	-539(25)
1300	-865(20)	169(15)	-712(30)	-548(25)
1400	-861(20)	172(15)	-724(30)	-555(25)

C_p = 144.9 + 0.029422 T -4129000 T^{-2} / Jmol^{-1}K^{-1}

298 K - 1400 K

Structural aspects

Table C.2: Transformed structural model of Li_2RuO_3 ($C2/m$) [76] by applying the linear transformation: -a, -b, a+c. Presented data includes lattice parameters (a, b, c, β) and atomic positions with Wyckoff site symmetry.

Li_2RuO_3

Space group	$C2/m$
Z	2
a, b, c, β	5.0466(3) Å, 8.7649(2) Å, 5.1777(3) Å, 108.952(4)°

Atom	Site	x	y	z
Ru1	4g	0.0	0.3308(4)	0.0
Li1	2a	0.0	0.0	0.0
Li2	4h	0.0	0.8425(9)	0.5
Li3	2c	0.0	0.0	0.5
O1	8j	0.2514(7)	0.3299(2)	0.7676(2)
O2	4i	0.2666(8)	0.0	0.7675(4)

Table C.3: Transformed structural model of Li_2RuO_3 ($P2_1/m$) of the present work by applying the linear transformation: -a, -b, a+c. Presented data including lattice parameters (a, b, c, β) and atomic positions with Wyckoff site symmetry.

Li_2RuO_3

Space group	$P2_1/m$
Z	4
a, b, c, β	4.9132(3) Å, 8.7686(6) Å, 5.1086(7) Å, 108.190(2)°

Atom	Site	x	y	z
Ru1	4f	-0.27917(5)	-0.07683(2)	-0.00402(3)
Li1	2e	-0.7752(15)	-0.25	-0.0084(11)
Li2	4f	0.2300(11)	-0.0931(8)	0.4920(8)
Li3	2e	-0.2521(17)	-0.25	0.5131(12)
O1	4f	-0.5027(6)	-0.0830(2)	0.2555(5)
O2	4f	-0.0051(6)	-0.0781(2)	0.7721(5)
O3	2e	-0.0425(7)	-0.25	0.2192(6)
O4	2e	0.4906(7)	-0.25	0.7656(6)

Table C.4: Refined lattice parameters a, b, c, and β of the $C2/m$ and $P2_1/m$ phases of $Li_2Ir_{1-x}Ru_xO_3$ with averaged Ru amount $\bar{x}_m$, including the GOF of the refinement with the structural model. The $P2_1/m$ phase was refined starting from the transformed structure. For $\bar{x}_m$ = 0.50(5); 0.69(4); 0.71(3) the P-XRD patterns could be refined with either the $C2/m$ or the $P2_1/m$ phase.

$\bar{x}_m$	Sample	Space group	a / Å	b / Å	c / Å	β / °	GOF
0.12(2)	V2T1S1	$C2/m$	5.1548(3)	8.8863(5)	5.1230(2)	109.694(3)	4.1
0.28(2)	V1T1S1	$C2/m$	5.1310(3)	8.8512(6)	5.1294(2)	109.533(3)	4.1
0.31(3)	V2T2S1	$C2/m$	5.1252(3)	8.8317(6)	5.1329(2)	109.510(3)	3.6
0.41(3)	V1T2S2	$C2/m$	5.1151(3)	8.8196(6)	5.1378(3)	109.440(5)	4.1
0.50(5)	V2T3xS2	$C2/m$	5.0747(3)	8.8522(7)	5.1330(3)	109.200(3)	2.9
0.50(5)	V2T3xS2	$P2_1/m$	5.0731(5)	8.8408(8)	5.1304(3)	109.159(5)	3.2
0.69(4)	V1T3xS1/2	$C2/m$	5.0403(3)	8.7977(6)	5.1371(3)	108.975(3)	3.8
0.69(4)	V1T3xS1/2	$P2_1/m$	5.0395(4)	8.7905(6)	5.1350(3)	108.942(4)	3.8
0.71(3)	V2T4xS2	$C2/m$	5.0536(4)	8.8120(5)	5.1313(2)	109.117(4)	2.8
0.71(3)	V2T4xS2	$P2_1/m$	5.0536(5)	8.8023(8)	5.1270(3)	109.041(6)	2.7
0.81(1)	V1T4xS3	$P2_1/m$	5.0187(6)	8.7740(9)	5.1286(4)	108.825(6)	2.7
0.93(1)	V2ToxS1	$P2_1/m$	4.9443(5)	8.7911(8)	5.1238(4)	108.284(5)	2.4

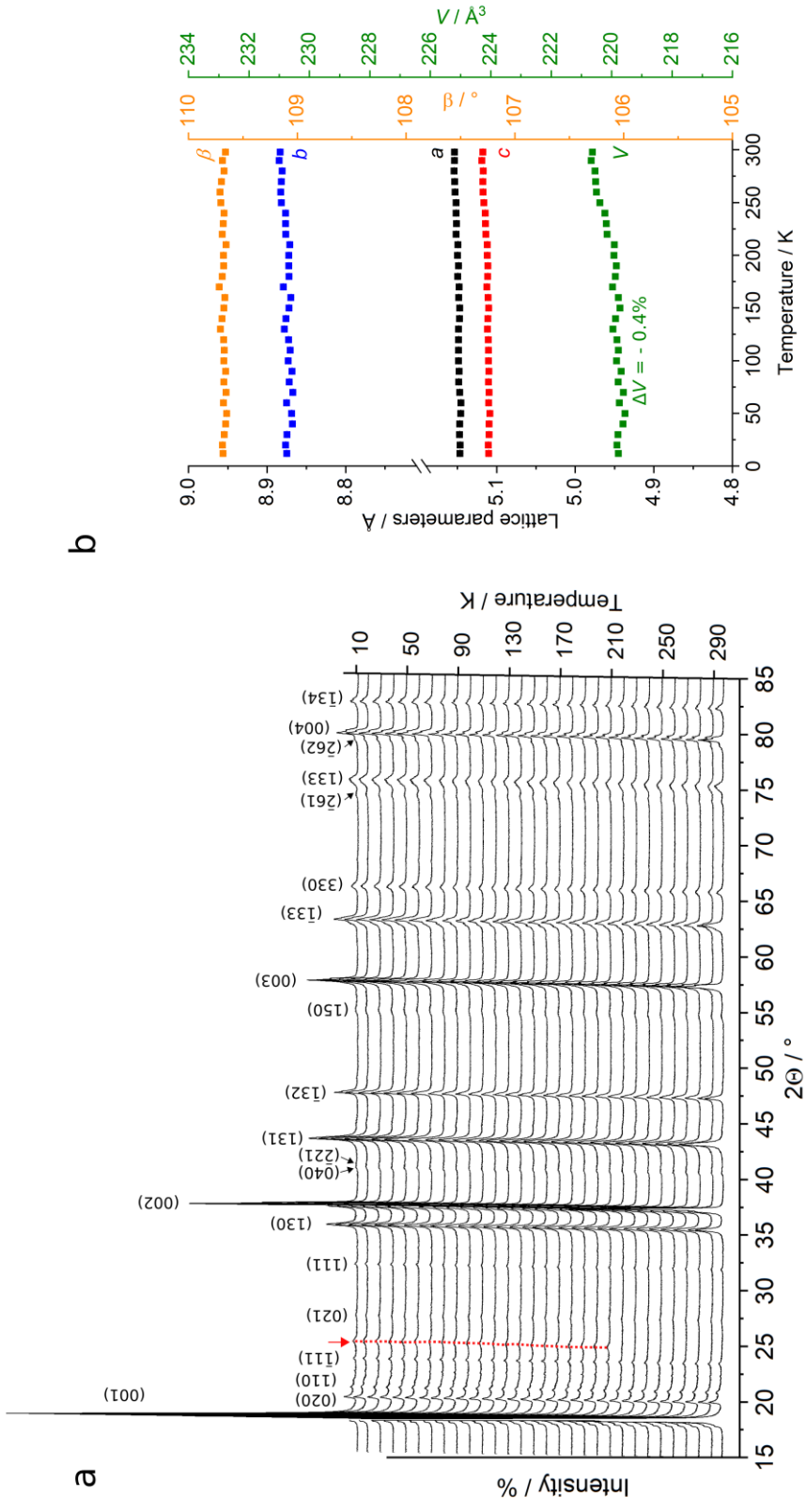

Figure C.1: Low-temperature behaviour of $Li_2Ir_{1-x}Ru_xO_3$ with $\bar{x}_m = 0.13(2)$ with space group $C2/m$ (sample V2T1S2). (a) Sequence of P-XRD measurements at temperatures between 298 K and 12 K. The strongest peaks of the $C2/m$ phase are indicated. The evolution of a phase impurity with 0.4 rel% intensity is marked in red. The dotted line gives a guide to the eye. (b) Progression of lattice parameters and cell volume with temperature. Error bars are smaller than symbols used.

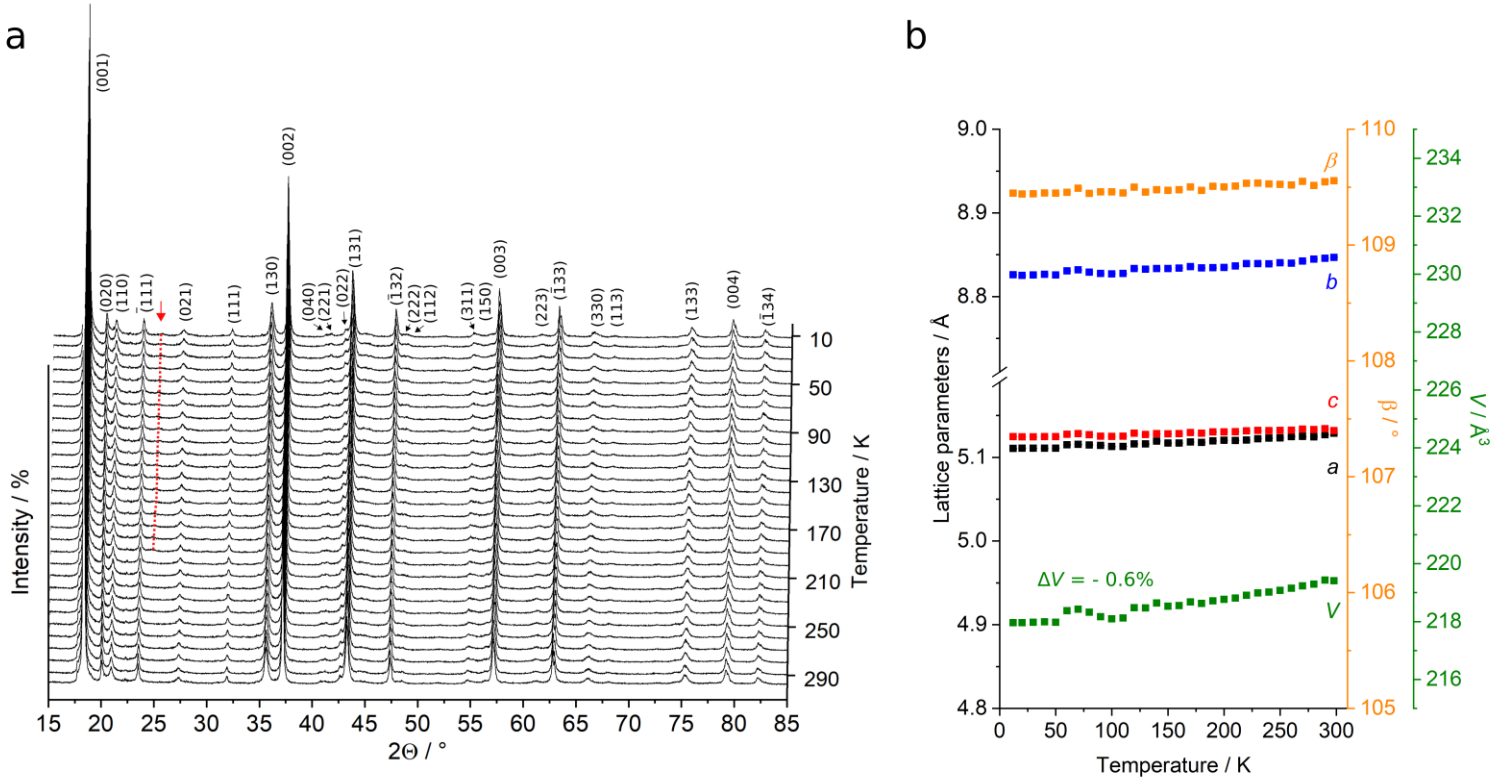

Figure C.2: Low-temperature behaviour of $Li_2Ir_{1-x}Ru_xO_3$ with $\bar{x}_m = 0.31(3)$ with space group $C2/m$ (sample V2T2S1). (a) Sequence of P-XRD measurements at temperatures between 298 K and 12 K. The strongest peaks of the $C2/m$ phase are indicated. The evolution of a phase impurity with 0.3 rel% intensity is marked in red. The dotted line gives a guide to the eye. (b) Progression of lattice parameters and cell volume with temperature. Error bars are smaller than symbols used.

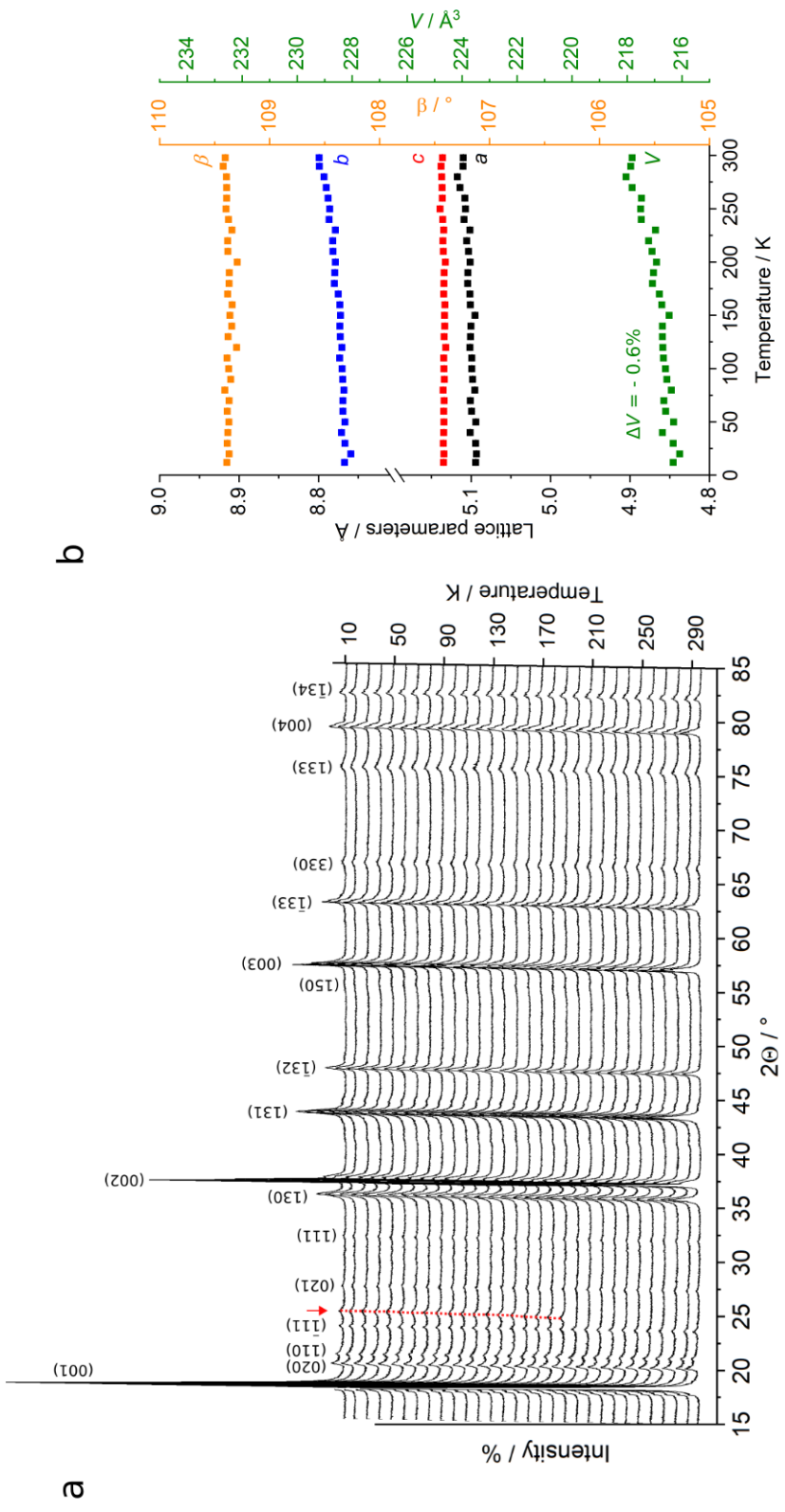

Figure C.3: Low-temperature behaviour of $Li_2Ir_{1-x}Ru_xO_3$ with $\bar{x}_m = 0.45(2)$ with space group $C2/m$ (sample V1T2S1). (a) Sequence of P-XRD measurements at temperatures between 298 K and 12 K. The strongest peaks of the $C2/m$ phase are indicated. The evolution of a phase impurity with 0.5 rel% intensity is marked in red. The dotted line gives a guide to the eye. (b) Progression of lattice parameters and cell volume with temperature. Error bars are smaller than symbols used.

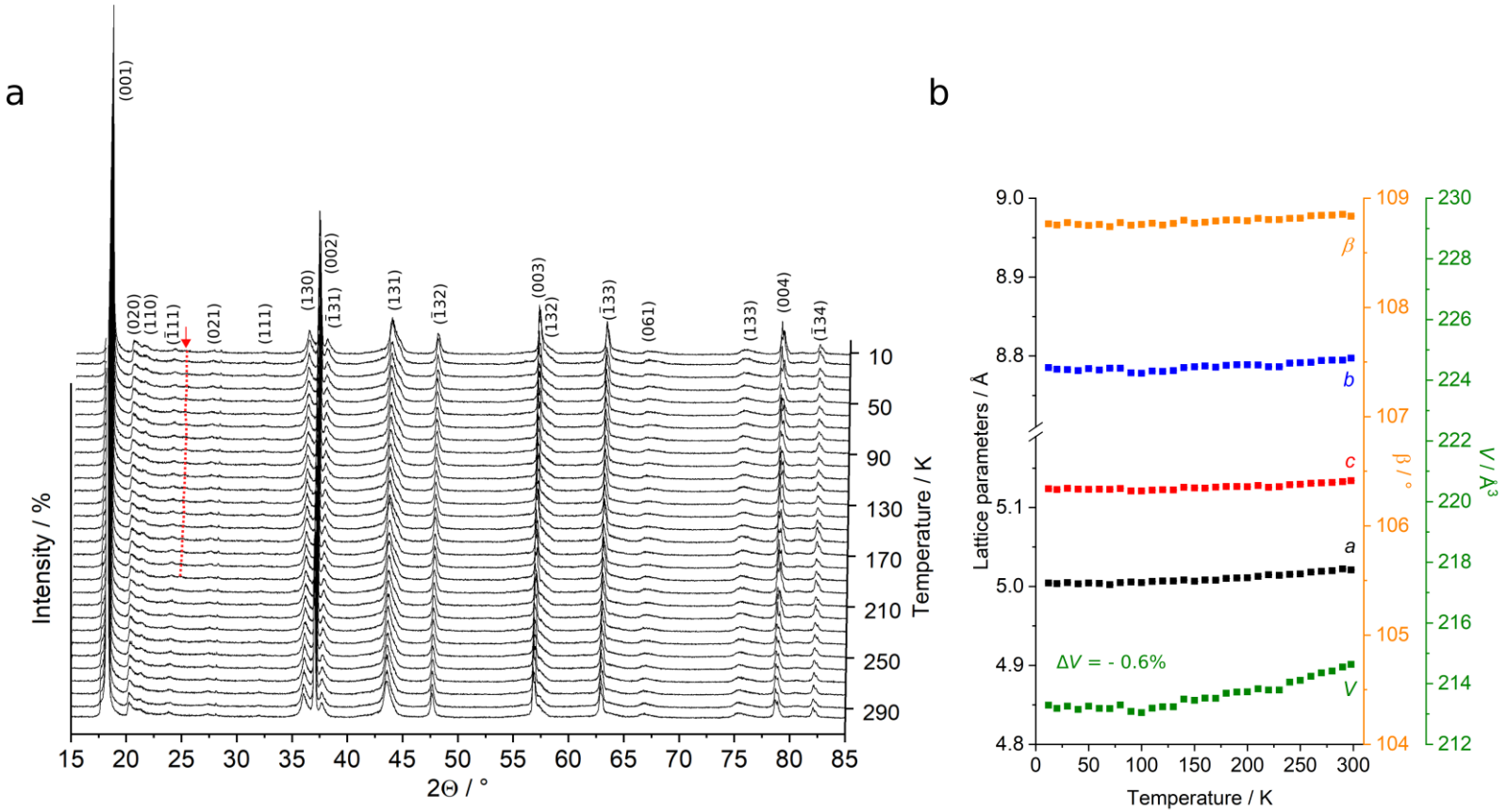

Figure C.4: Low-temperature behaviour of $Li_2Ir_{1-x}Ru_xO_3$ with $\bar{x}_m$ = 0.70(3) (sample V2T4xS1). (a) Sequence of P-XRD measurements at temperatures between 298 K and 12 K. The strongest peaks of the $C2/m$ phase are indicated. The evolution of a phase impurity with 0.2 rel% intensity is marked in red. The dotted line gives a guide to the eye. (b) Progression of lattice parameters and cell volume with temperature. Error bars are smaller than symbols used.

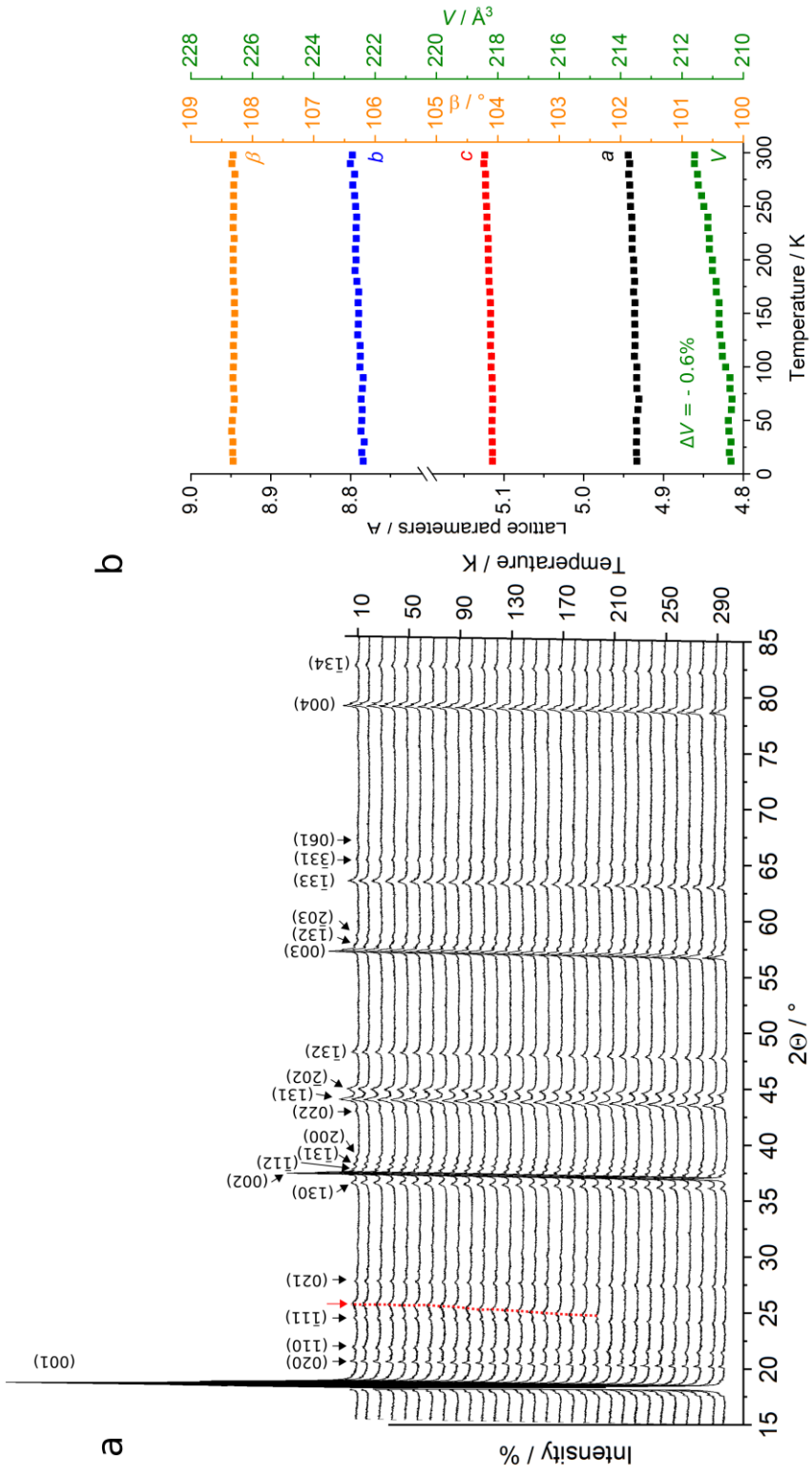

Figure C.5: Low-temperature behaviour of $Li_2Ir_{1-x}Ru_xO_3$ with $\bar{x}_m = 0.91(1)$ with space group $P2_1/m$ (sample V2ToxS2). (a) Sequence of P-XRD measurements at temperatures between 298 K and 12 K. The strongest peaks of the $P2_1/m$ phase are indicated. The evolution of a phase impurity with 1 rel% intensity is marked in red. The dotted line gives a guide to the eye. (b) Progression of lattice parameters and cell volume with temperature. Error bars are smaller than symbols used.

Appendix D

Na-Ru-O system

Table D.1: Compounds in the Na-Ru-O system including their space groups (SG), lattice parameters a, b, c, α, β, γ, and ICSD Collection Codes.

Compound	SG	a / Å	b / Å	c / Å	α / β / γ	Coll. Code
Na_2RuO_4 [78]	$P2_1/c$	10.65122(8)	7.01135(4)	10.82996(8)	β = 119.1978(4)°	157318
Na_2RuO_4 [78]	$P2_1/c$	10.68366(8)	7.02334(5)	10.85282(9)	β = 119.1884(5)°	157319
Na_2RuO_4 [78]	$P2_1/c$	10.721(6)	7.033(4)	10.871(6)	β = 119.10(4)°	413644
Na_2RuO_4 [117]	$P2_1/n$	10.7098(1)	7.0356(1)	10.9253(2)	β = 119.668(10)°	281692
Na_2RuO_3 [78]	$R\bar{3}$	3.12360(5)	3.12360(5)	16.0370(4)		97583
Na_2RuO_3 [78]	$C2/c$	5.4141(4)	9.3663(6)	10.8481(4)	β = 99.636(9)°	97584
$Na_{0.67}RuO_2$ [116]	$R\bar{3}m$	2.9298	2.9298	21.9127		170346
$NaRuO_2$ [116]	$R\bar{3}m$	3.0184(2)	3.0184(2)	16.4929(3)		170347
$NaRu_2O_4$ [103]	$Pnma$	9.2737(4)	2.8215(1)	11.1701(5)		172608
$Na_{0.94}Ru_2O_4$ [95]	$Pnma$	9.2641(7)	2.8249(3)	11.1496(7)		250424
Na_3RuO_4 [102]	$C2/m$	11.0295(6)	12.8205(7)	5.7028(3)	β = 109.908(3)°	153119
$Na_{2.1}Ru_4O_9$ [29]	$C2/m$	23.180(6)	2.831(2)	10.990(4)	β = 104.50(3)°	2095
$Na_{2.73}Ru_4O_9$ [103]	$C2/m$	23.246(1)	2.8411(1)	11.0394(6)	β = 104.766(5)°	172609
$Na_{2.7}Ru_4O_9$ (695K) [137]	$C2/m$	23.520 (11)	2.890(1)	10.953(6)	β = 104.55(3)°	-
$Na_{2.7}Ru_4O_9$ (450K) [137]	$P2/m$	23.311(2)	5.701(4)	11.057(7)	β = 104.39(4)°	-
$Na_{2.7}Ru_4O_9$ (300K) [137]	$P2/m$	23.342(2)	17.028 (16)	33.191(3)	β =104.43(7)°	-
$Na_{27}Ru_{14}O_{48}$ [3]	$P\bar{1}$	5.7763(4)	10.9910(9)	18.2042(13)	α = 88.517(4)°	261255
					β = 87.194(3)°	
					γ = 75.165(3)°	

Thermodynamic calculations

Table D.2: Calculated temperature-dependent values of the standard enthalpy and entropy of formation (ΔH_T^0 and ΔS_T^0), and heat capacity (C_p) of $Na_3Ru_4O_9$. The temperature-dependent values for RuO_2(s), γ-, and β-Na_2O(s) were taken from Barin [6].

T / K	ΔH_T^0 / kJmol^{-1}	ΔS_T^0 / Jmol^{-1}K^{-1}
298	-1953(20)	347
500	-1854(20)	446(15)
600	-1833(20)	467(15)
700	-1817(20)	483(15)
800	-1804(20)	496(15)
900	-1793(20)	507(15)
1000	-1783(20)	517(15)
1023	-1857(20)	503(15)
1100	-1850(20)	509(15)
1200	-1843(20)	517(15)
1300	-1835(20)	524(15)

$$C_p = 421.63 + 0.073335\ T\ \text{-}11530000\ T^{-2} \text{ / Jmol}^{-1}\text{K}^{-1} \text{ (298 K - 1023 K)}$$
$$C_p = 429.97 + 0.06234\ T\ \text{-}9640000\ T^{-2} \text{ / Jmol}^{-1}\text{K}^{-1} \text{ (102 3K - 1300 K)}$$

Table D.3: Calculated temperature-dependent values of the reaction enthalpy and entropy (ΔH_R and ΔS_R) of the assumed reaction 3 NaOH (g) + 4 RuO_3 (g) $\Leftrightarrow$ $Na_3Ru_4O_9$ (s) + 1.5 H_2O (g) + 2.25 O_2 (g) . The temperature-dependent values of the enthalpy and entropy of formation (ΔH_T^0 and ΔS_T^0) for NaOH(g), RuO_3(g), H_2O(g) and O_2(g) were taken from Barin [6], whereas the values for $Na_3Ru_4O_9$ were calculated in the present work and are listed in appendix table D.2.

T / K	ΔH_R / kJmol^{-1}	ΔS_R / Jmol^{-1}K^{-1}
298	-1410(30)	-1160(25)
500	-1386(30)	-1251(25)
600	-1405(30)	-1375(25)
700	-1430(30)	-1350(25)
800	-1458(30)	-1392(25)
900	-1489(30)	-1430(25)
1000	-1520(30)	-1464(25)
1100	-1630(30)	-1511(25)
1200	-1665(30)	-1541(25)
1300	-1700(30)	-1567(25)

Structural aspects

$Na_{3-x}Ru_4O_9$, $C2/m$

Table D.4: Averaged bond lengths in Å and calculated bond valence sums (BVS) of $Na_{2.55(8)}Ru_4O_9$ grown by the CVTR method, resulting in a global instability index of 0.143.

	Bond length / Å		Bond valence			Bond length / Å		Bond valence	
Ru1-O1	1.995(5)	x4	0.647(9)	x4	**Ru2**-O5	2.018(4)	x4	0.511(6)	x4
-O2	1.969(6)	x2	0.694(12)	x2	-O4	2.027(8)	x2	0.499(10)	x2
		BVS	**3.976(24)**				**BVS**	**3.043(19)**	
Ru3-O2	1.979(4)	x2	0.676(8)	x2	**Ru4**-O3	1.893(6)	x1	0.853(14)	x1
-O3	1.921(7)	x1	0.790(16)	x1	-O6	2.012(6)	x2	0.618(10)	x2
-O4	2.005(5)	x2	0.629(8)	x2	-O6	2.043(6)	x1	0.568(10)	x1
-O5	2.084(8)	x1	0.509(10)	x1	-O7	1.972(5)	x2	0.689(10)	x2
		BVS	**3.909(24)**				**BVS**	**4.034(26)**	
Ru5-O7	1.960(7)	x1	0.71(1)	x1	**O1**-Ru1	1.995(5)	x2	0.647(9)	x2
-O8	2.033(4)	x2	0.584(7)	x2	-Na1	2.391(6)	x2	0.198(3)	x2
-O8	2.056(7)	x1	0.549(11)	x1	-Na3	2.50(1)	x2	0.094(2)	x2
-O9	1.970(4)	x2	0.692(8)	x2	-Na4	2.30(2)	x1	0.057(3)	x1
		BVS	**3.816(23)**				**BVS**	**1.935(14)**	
O2- Ru1	1.969(6)	x2	0.694(12)	x2	**O5**- Ru2	2.018(4)	x2	0.511(6)	x2
-Ru3	1.979(6)	x2	0.676(8)	x2	-Ru3	2.084(8)	x1	0.509(10)	x1
-Na1	2.810(9)	x1	0.064(1)	x1	-Na3	2.458(8)	x2	0.106(2)	x2
-Na3	2.40(1)	x1	0.122(4)	x1	-Na4	2.05(2)	x1	0.111(5)	x1
		BVS	**2.231(17)**				**BVS**	**1.854(15)**	
O3-Ru3	1.911(7)	x1	0.79(2)	x1	**O4**-Ru2	2.027(8)	x1	0.499(10)	x1
-Ru4	1.893(6)	x1	0.85(1)	x1	-Ru3	2.005(5)	x2	0.629(8)	x2
-Na1	2.373(7)	x2	0.207(4)	x2	-Na2	2.452(6)	x2	0.128(2)	x2
		BVS	**2.058(22)**				**BVS**	**2.015(15)**	
O6-Ru4	2.012(6)	x2	0.618(10)	x2	**O8**-Ru2	2.033(4)	x2	0.584(7)	x2
-Ru4	2.043(6)	x1	0.568(10)	x1	-Ru3	2.056(7)	x2	0.549(11)	x2
-Na2	2.456(8)	x2	0.127(3)	x2	-Na2	2.485(7)	x2	0.153(3)	x2
		BVS	**2.058(17)**				**BVS**	**2.024(15)**	
O7-Ru4	1.972(5)	x2	0.689(10)	x2	**O9**-Ru5	1.970(4)	x2	0.692(8)	x2
-Ru5	1.959(7)	x1	0.713(14)	x1	-Na2	2.549(7)	x2	0.099(2)	x2
-Na1	2.635(7)	x1	0.102(2)	x1	-Na3	2.64(1)	x1	0.178(6)	x1
-Na2	2.765(8)	x1	0.055(1)	x1	-Na4	2.39(2)	x2	0.045(2)	x2
		BVS	**2.248(20)**				**BVS**	**1.850(13)**	
Na1-O1	2.391(6)	x2	0.204(3)	x2	**Na2**-O4	2.452(6)	x2	0.173(3)	x2
-O2	2.810(9)	x1	0.066(2)	x1	-O6	2.456(8)	x2	0.171(4)	x2
-O3	2.373(7)	x2	0.214(4)	x2	-O7	2.765(8)	x1	0.074(2)	x1
-O7	2.635(7)	x1	0.106(2)	x1	-O9	2.549(7)	x2	0.133(3)	x2
-O8	2.485(7)	x2	0.158(3)	x2					
		BVS	**1.324(9)**				**BVS**	**1.029(8)**	
Na3-O1	2.50(1)	x2	0.152(4)	x2	**Na4**-O1	2.30(2)	x1	0.26(2)	x1
-O2	2.40(1)	x1	0.197(6)	x1	-O5	2.05(2)	x1	0.51(3)	x1
-O5	2.46(8)	x2	0.170(4)	x2	-O9	2.39(2)	x2	0.202(10)	x2
-O9	2.26(1)	x1	0.288(9)	x1					
		BVS	**1.130(14)**				**BVS**	**1.169(32)**	

Table D.5: Anisotropic atomic displacement parameters (ADPs) of $Na_{2.55(8)}Ru_4O_9$ grown by the CVTR method. ADPs for Na3 and Na3a atoms were restrained to exhibit an approximate isotropic behaviour.

Atom site	U_{11} / Å^2	U_{22} / Å^2	U_{33} / Å^2	U_{23} / Å^2	U_{13} / Å^2	U_{12} / Å^2
Ru1	0.0029(5)	0.0201(6)	0.0066(6)	0.000	0.0012(4)	0.000
Ru2	0.0148(7)	0.0316(7)	0.0172(7)	0.000	0.0048(5)	0.000
Ru3	0.0057(4)	0.0270(5)	0.0086(5)	0.000	0.0007(3)	0.000
Ru4	0.0043(4)	0.0254(5)	0.0051(4)	0.000	0.0012(3)	0.000
Ru5	0.0045(4)	0.0197(5)	0.0063(4)	0.000	0.0015(3)	0.000
O1	0.018(4)	0.004(3)	0.012(4)	0.000	0.002(3)	0.000
O2	0.008(3)	0.014(3)	0.004(3)	0.000	0.002(3)	0.000
O3	0.007(3)	0.013(3)	0.013(3)	0.000	0.001(3)	0.000
O4	0.007(3)	0.012(3)	0.017(4)	0.000	0.010(3)	0.000
O5	0.011(3)	0.014(3)	0.012(4)	0.000	0.005(3)	0.000
O6	0.009(3)	0.017(3)	0.013(4)	0.000	0.002(3)	0.000
O7	0.009(3)	0.010(3)	0.011(3)	0.000	0.002(3)	0.000
O8	0.011(3)	0.011(3)	0.010(3)	0.000	0.007(3)	0.000
O9	0.017(4)	0.007(3)	0.015(4)	0.000	0.006(3)	0.000
Na1	0.007(2)	0.014(2)	0.016(2)	0.000	-0.0002(17)	0.000
Na2	0.003(3)	0.106(7)	0.007(3)	0.000	-0.002(2)	0.000
Na3	0.015(5)	0.155(16)	0.022(5)	0.000	0.006(4)	0.000
Na4	0.012(12)	0.051(18)	0.013(11)	0.000	0.007(8)	0.000

Table D.6: Averaged bond lengths in Å and calculated bond valence sums (BVS) of $Na_{2.36(3)}Ru_4O_9$ grown by solid-state reaction, resulting in a global instability index of 0.127.

	Bond length / Å		Bond valence			Bond length / Å		Bond valence	
Ru1-O1	1.984(2)	x4	0.667(3)	x4	**Ru2**-O5	2.010(2)	x4	0.523(4)	x4
-O2	1.973(2)	x2	0.686(4)	x2	-O4	2.027(3)	x2	0.500(4)	x2
		BVS	**4.093(9)**				**BVS**	**3.091(7)**	
Ru3-O2	1.975(2)	x2	0.683(3)	x2	**Ru4**-O3	1.904(2)	x1	0.827(5)	x1
-O3	1.895(3)	x1	0.848(6)	x1	-O6	2.004(2)	x2	0.631(3)	x2
-O4	2.007(2)	x2	0.627(3)	x2	-O6	2.053(2)	x1	0.553(3)	x1
-O5	2.103(3)	x1	0.484(4)	x1	-O7	1.974(2)	x2	0.685(3)	x2
		BVS	**3.953(9)**				**BVS**	**4.012(8)**	
Ru5-O7	1.957(3)	x1	0.717(5)	x1	**O1**-Ru1	1.984(2)	x2	0.667(3)	x2
-O8	2.030(2)	x2	0.589(2)	x2	-Na1	2.394(2)	x2	0.181(1)	x2
-O8	2.047(2)	x1	0.562(4)	x1	-Na3	2.450(4)	x2	0.090(1)	x2
-O9	1.968(2)	x2	0.696(3)	x2	-Na4	2.340(8)	x1	0.054(1)	x1
		BVS	**3.849(8)**				**BVS**	**1.928(5)**	
O2- Ru1	1.973(2)	x1	0.686(4)	x1	**O3**- Ru3	1.895(3)	x1	0.848(6)	x1
-Ru3	1.975(2)	x2	0.683(3)	x2	-Ru4	1.904(2)	x1	0.827(5)	x1
-Na3	2.437(5)	x1	0.093(1)	x1	-Na1	2.394(2)	x2	0.181(1)	x2
		BVS	**2.146(6)**				**BVS**	**2.036(8)**	
O4-Ru2	2.027(3)	x1	0.500(4)	x1	**O6**-Ru4	2.005(2)	x2	0.631(3)	x2
-Ru3	2.007(2)	x2	0.627(3)	x2	-Ru4	2.053(2)	x1	0.553(3)	x1
-Na2	2.466(2)	x2	0.124(1)	x2	-Na2	2.444(3)	x2	0.131(1)	x2
		BVS	**2.001(5)**				**BVS**	**2.077(5)**	
O5-Ru2	2.010(2)	x2	0.523(2)	x2	**O7**-Ru4	1.974(2)	x2	0.685(3)	x2
-Ru3	2.103(3)	x1	0.484(4)	x1	-Ru5	1.957(3)	x1	0.717(5)	x1
-Na3	2.540(3)	x2	0.070(1)	x2	-Na1	2.641(3)	x1	0.093(1)	x1
-Na4	2.065(6)	x1	0.114(2)	x1	-Na2	2.750(3)	x1	0.057(1)	x1
		BVS	**1.785(5)**				**BVS**	**2.237(7)**	
O8-Ru5	2.030(2)	x2	0.589(2)	x2	**O9**-Ru5	1.968(2)	x2	0.696(3)	x2
-Ru5	2.047(2)	x1	0.562(4)	x1	-Na2	2.549(3)	x2	0.099(1)	x2
-Na1	2.477(3)	x2	0.144(1)	x2	-Na3	2.236(5)	x1	0.160(2)	x1
					-Na4	2.374(6)	x2	0.050(1)	x2
		BVS	**2.029(5)**				**BVS**	**1.849(5)**	
Na1-O1	2.394(2)	x2	0.203(1)	x2	**Na2**-O4	2.466(2)	x2	0.167(1)	x2
-O3	2.394(2)	x2	0.202(1)	x2	-O6	2.444(3)	x2	0.177(1)	x2
-O7	2.641(3)	x1	0.104(1)	x1	-O7	2.750(3)	x1	0.077(1)	x1
-O8	2.477(3)	x2	0.162(1)	x2	-O9	2.549(3)	x2	0.133(1)	x2
		BVS	**1.238(3)**				**BVS**	**1.031(3)**	
Na3-O1	2.450(4)	x2	0.174(2)	x2	**Na4**-O1	2.340(8)	x1	0.234(5)	x1
-O2	2.437(5)	x1	0.180(2)	x1	-O5	2.065(6)	x1	0.492(8)	x1
-O5	2.540(3)	x2	0.137(1)	x2	-O9	2.373(6)	x2	0.214(4)	x2
-O9	2.236(5)	x1	0.311(4)	x1					
		BVS	**1.112(5)**				**BVS**	**1.154(11)**	

Table D.7: Anisotropic atomic displacement parameters (ADPs) of $Na_{2.36(3)}Ru_4O_9$ grown by solid-state reaction. ADPs for Na3 and Na3a atoms are restrained to exhibit an approximate isotropic behaviour.

Atom site	U_{11} / Å^2	U_{22} / Å^2	U_{33} / Å^2	U_{23} / Å^2	U_{13} / Å^2	U_{12} / Å^2
Ru1	0.00451(18)	0.0209(2)	0.00583(18)	0.000	0.00113(14)	0.000
Ru2	0.00635(18)	0.0238(2)	0.00873(19)	0.000	0.00299(15)	0.000
Ru3	0.00491(14)	0.02538(17)	0.00639(14)	0.000	0.00132(10)	0.000
Ru4	0.00475(14)	0.02398(17)	0.00611(14)	0.000	0.00173(10)	0.000
Ru5	0.00480(14)	0.01976(16)	0.00525(14)	0.000	0.00118(10)	0.000
O1	0.0169(12)	0.0053(11)	0.0118(12)	0.000	-0.0003(10)	0.000
O2	0.0101(11)	0.0113(11)	0.0083(11)	0.000	0.0016(9)	0.000
O3	0.0061(11)	0.0141(12)	0.0132(12)	0.000	0.0019(9)	0.000
O4	0.0097(12)	0.0138(12)	0.0205(13)	0.000	0.0081(10)	0.000
O5	0.0114(12)	0.0123(12)	0.0206(13)	0.000	0.0092(10)	0.000
O6	0.0080(11)	0.0114(12)	0.0181(13)	0.000	0.0004(10)	0.000
O7	0.0125(12)	0.0116(11)	0.0071(11)	0.000	0.0031(9)	0.000
O8	0.0142(12)	0.0071(11)	0.0080(11)	0.000	0.0055(9)	0.000
O9	0.0174(13)	0.0065(11)	0.0160(12)	0.000	0.0082(10)	0.000
Na1	0.0071(9)	0.0283(11)	0.0143(9)	0.000	0.0011(6)	0.000
Na2	0.0103(12)	0.131(3)	0.0097(12)	0.000	0.0016(9)	0.000
Na3	0.0125(19)	0.166(7)	0.0143(19)	0.000	0.0079(14)	0.000
Na4	0.007(3)	0.019(4)	0.007(3)	0.000	0.005(2)	0.000

Table D.8: Structural model of $Na_{2.1}Ru_4O_9$ published by Darriet [29] including lattice parameters (a, b, c, β), cell volume V, atomic positions with Wyckoff site symmetry and oxidation state, fractional coordinates (x, y, z), isotropic atomic displacement parameters (B_{iso}), and site occupancy factors (SOF).

$Na_{2.1}Ru_4O_9$, Darriet [29]

Space group	$C2/m$
Z	4
a, b, c, β	23.180(6) Å, 2.831(2) Å, 10.990(4) Å, 104.50(3)°
V	698.22 Å^3
T	298 K
Diffraction method	P-ND
R_1	0.074

Atom	Oxidation state	Site	x	y	z	B_{iso} / Å^2	SOF
Ru1	+3	2*a*	0.0	0.0	0.0	0.77	1.0
Ru2	+3	2*c*	0.0	0.0	0.5	0.93	1.0
Ru3	+3	4*i*	0.05824(4)	0.5	0.31121(9)	0.71	1.0
Ru4	+3	4*i*	0.21423(4)	0.5	0.37837(8)	0.76	1.0
Ru5	+3	4*i*	0.27111(4)	0	0.12923(8)	0.81	1.0
O1	-2	4*i*	-0.0561(4)	0.5	0.0145(9)	1.68	1.0
O2	-2	4*i*	0.0274(4)	0	0.1835(8)	0.98	1.0
O3	-2	4*i*	0.1343(4)	0.5	0.2869(8)	1.44	1.0
O4	-2	4*i*	0.0766(4)	0	0.4461(8)	0.93	1.0
O5	-2	4*i*	-0.0221(4)	0.5	0.3673(8)	1.12	1.0
O6	-2	4*i*	0.2040(4)	0	0.5008(8)	1.09	1.0
O7	-2	4*i*	0.2378(4)	0	0.2743(9)	1.93	1.0
O8	-2	4*i*	0.2131(4)	0.5	0.0430(8)	0.81	1.0
O9	-2	4*i*	0.3273(4)	0.5	0.1982(8)	1.13	1.0
Na1	+1	4*i*	0.1362(3)	0	0.1050(6)	2.53	0.95
Na2	+1	4*i*	0.1437(4)	0.5	0.6028(8)	2.6	0.76
Na3	+1	4*i*	0.0804(7)	0	0.8207(15)	2.63	0.39

Table D.9: Structural model of $Na_{2.73}Ru_4O_9$ published by Regan et al. [103] including lattice parameters (a, b, c, β), cell volume V, atomic positions with Wyckoff site symmetry and oxidation state, fractional coordinates (x, y, z), isotropic atomic displacement parameters (B_{iso}), and site occupancy factors (SOF).

$Na_{2.73}Ru_4O_9$, Regan et al. [103]

Apace group	$C2/m$
Z	4
a, b, c, β	23.246(1) Å, 2.8411(1) Å, 11.0394(6) Å, 104.766(5)°
V	705.01 Å^3
T	298 K
Diffraction method	SC-XRD
R_1	-

Atom	Oxidation state	Site	x	y	z	B_{iso} / Å^2	SOF
Ru1	+3	2*a*	0.0	0.0	0.0	0.0087(1)	1.0
Ru2	+3	2*c*	0.0	0.0	0.5	0.0087(1)	1.0
Ru3	+3	4*i*	0.0591(3)	0.5	0.3097(7)	0.0087(1)	1. 0
Ru4	+3	4*i*	0.2153(3)	0.5	0.3808(7)	0.0087(1)	1.0
Ru5	+3	4*i*	0.2720(3)	0.0	0.1299(6)	0.0087(1)	1.0
O1	-2	4*i*	-0.0600(4)	0.5	0.0113(8)	0.0073(2)	1.0
O2	-2	4*i*	0.0293(3)	0.0	0.1845(8)	0.0062(2)	1.0
O3	-2	4*i*	0.1339(4)	0.5	0.2788(8)	0.0162(2)	1.0
O4	-2	4*i*	0.0776(4)	0.0	0.4415(9)	0.0129(2)	1.0
O5	-2	4*i*	-0.0235(4)	0.5	0.3665(9)	0.0156(3)	1.0
O6	-2	4*i*	0.2015(4)	0.0	0.4959(8)	0.0047(2)	1.0
O7	-2	4*i*	0.2386(3)	0.0	0.2737(7)	0.0024(2)	1.0
O8	-2	4*i*	0.2114(4)	0.5	0.0436(9)	0.0141(2)	1.0
O9	-2	4*i*	0.3314(4)	0.5	0.2009(7)	0.0044(2)	1.0
Na1	+1	4*i*	0.1388(9)	0.0	0.1026(17)	0.0314(3)	1.0
Na2	+1	4*i*	0.1456(8)	0.5	0.6055(15)	0.0314(3)	1.0
Na3	+1	4*i*	0.0730(11)	0.0	0.8107(24)	0.0314(3)	0.73(4)

Table D.10: Bond valence calculations on the structure of $Na_{2.1}Ru_4O_9$ reported by Darriet [29]. The resulting global instability index is 0.305.

Atom	Average distance / Å	Valence	BVS
Ru1	1.9559(30)	3	3.630(30)
Ru2	2.0057(31)	3	3.174(26)
Ru3	1.9959(31)	3	3.330(29)
Ru4	1.9790(31)	3	3.444(29)
Ru5	1.9796(31)	3	3.422(29)
O1	2.2893(47)	-2	1.679(17)
O2	2.1089(56)	-2	1.752(18)
O3	2.1599(46)	-2	1.888(28)
O4	2.1918(37)	-2	1.811(19)
O5	2.2579(47)	-2	1.560(16)
O6	2.1874(41)	-2	1.821(18)
O7	2.2500(44)	-2	1.935(25)
O8	2.2106(38)	-2	1.826(18)
O9	2.2378(51)	-2	1.584(16)
Na1	2.4871(36)	1	1.113(11)
Na2	2.5225(40)	1	1.033(11)
Na3	2.4683(69)	1	1.066(23)

Table D.11: Bond valence calculations on the structure of $Na_{2.73(4)}Ru_4O_9$ reported by Regan et al. [103]. The resulting global instability index is 0.233.

Atom	Average distance / Å	Valence	BVS
Ru1	2.0033(30)	3	3.198(26)
Ru2	2.0347(33)	3	2.939(25)
Ru3	1.9970(40)	3	3.344(38)
Ru4	1.9985(37)	3	3.252(33)
Ru5	2.0150(37)	3	3.116(32)
O1	2.3086(71)	-2	1.645(21)
O2	2.0820(77)	-2	1.859(23)
O3	2.1661(75)	-2	1.789(34)
O4	2.2200(51)	-2	1.814(23)
O5	2.2226(66)	-2	1.620(20)
O6	2.1842(61)	-2	1.925(26)
O7	2.2457(61)	-2	1.897(26)
O8	2.1994(65)	-2	1.774(25)
O9	2.2535(73)	-2	1.600(24)
Na1	2.4438(68)	1	1.254(23)
Na2	2.5171(61)	1	1.035(17)
Na3	2.4279(100)	1	1.140(33)

Table D.12: Bond valence calculations on the structure of $Na_{2.1}Ru_4O_9$ reported by Darriet [29], but with differing oxidation states of Ru due to bond valence calculations of structural models of the present work. The resulting global instability index is 0.167.

Atom	Average distance / Å	Valence	BVS
Ru1	1.9559(30)	4	4.316(35)
Ru2	2.0057(31)	3	3.174(26)
Ru3	1.9959(31)	4	3.959(35)
Ru4	1.9790(31)	4	4.094(35)
Ru5	1.9796(31)	4	4.069(34)
O1	2.2893(47)	-2	1.908(20)
O2	2.1089(56)	-2	2.071(22)
O3	2.1599(46)	-2	2.184(33)
O4	2.1918(37)	-2	2.005(20)
O5	2.2579(47)	-2	1.637(18)
O6	2.1874(41)	-2	2.115(22)
O7	2.2500(44)	-2	2.268(29)
O8	2.2106(38)	-2	2.117(21)
O9	2.2378(51)	-2	1.819(18)
Na1	2.4871(36)	1	1.113(11)
Na2	2.5225(40)	1	1.033(11)
Na3	2.4683(69)	1	1.066(23)

Table D.13: Bond valence calculations on the structure of $Na_{2.73(4)}Ru_4O_9$ reported by Regan et al. [103], but with differing oxidation states of Ru due to bond valence calculations of structural models of the present work. The resulting global instability index is 0.177.

Atom	Average distance / Å	Valence	BVS
Ru1	2.0033(30)	4	3.802(31)
Ru2	2.0347(33)	3	2.939(25)
Ru3	1.9970(40)	4	3.976(45)
Ru4	1.9985(37)	4	3.866(39)
Ru5	2.0150(37)	4	3.705(38)
O1	2.3086(71)	-2	1.839(23)
O2	2.0820(77)	-2	2.182(27)
O3	2.1661(75)	-2	2.058(40)
O4	2.2200(51)	-2	2.017(25)
O5	2.2226(66)	-2	1.685(22)
O6	2.1842(61)	-2	2.221(30)
O7	2.2457(61)	-2	2.216(31)
O8	2.1994(65)	-2	2.038(29)
O9	2.2535(73)	-2	1.805(26)
Na1	2.4438(68)	1	1.254(23)
Na2	2.5171(61)	1	1.035(17)
Na3	2.4279(100)	1	1.140(33)

$Na_{27}Ru_{14}O_{48}$, $P\bar{1}$

Table D.14: Structural model of $Na_{27}Ru_{14}O_{48}$ published by Allred et al. [3] including lattice parameters (a, b, c, β), cell volume V, atomic positions with Wyckoff site symmetry and oxidation state, fractional coordinates (x, y, z), atomic displacement parameters (B_{iso}), site occupancy factors (SOF) and bond valence sums (BVS).

$a, b, c, \alpha, \beta, \gamma$	5.7763(4) Å, 10.9910(9) Å, 18.2042(13) Å, 88.517(4)°, 87.194(3)°, 75.165(3)°
V	1115.77(14) Å^3
R_{int}, R_1, GOF	0.0231, 0.0424, 1.067

Atom	Site	Oxidation state	x	y	z	B_{iso} / Å^2	SOF	BVS
Ru1	1*a*	3+	0.0	0.0	0.0	0.00702(13)	1.0	3.092(14)
Ru2	2*i*	5+	-0.25365(9)	0.23603(4)	-0.09699(3)	0.00818(11)	0.9829(8)	4.919(24)
Ru3	2*i*	5+	0.02618(9)	0.02984(4)	0.17102(3)	0.00806(11)	0.9829(8)	5.030(25)
Ru4	2*i*	5+	-0.21674(8)	0.26220(4)	0.07410(3)	0.00792(11)	0.9829(8)	5.008(27)
Ru5	1*g*	4+	0.0	-0.5	0.5	0.01183(15)	0.9483(8)	3.979(18)
Ru6	2*i*	5+	-0.14638(9)	-0.26813(5)	0.39345(3)	0.01029(11)	0.9483(8)	5.065(29)
Ru7	2*i*	5+	0.09865(9)	0.46267(5)	0.32944(3)	0.00927(11)	0.9483(8)	5.103(31)
Ru8	2*i*	5+	0.27277(10)	0.23148(5)	0.43750(3)	0.01098(12)	0.9483(8)	4.980(29)
Na1	2*i*	1+	0.1270(5)	0.4065(3)	0.15282(16)	0.0191(6)	1.0	1.169(8)
Na2	2*i*	1+	0.1483(5)	0.3656(3)	-0.04561(16)	0.0195(6)	1.0	1.099(7)
Na3	2*i*	1+	0.2664(5)	-0.1996(3)	0.27523(15)	0.0199(6)	1.0	1.184(8)
Na4	2*i*	1+	0.3950(6)	0.2027(3)	0.24601(18)	0.0277(11)	0.977(13)	1.107(7)
Na5	2*i*	1+	-0.4508(6)	0.5089(3)	0.18345(17)	0.0230(10)	0.977(13)	1.112(8)
Na6	2*i*	1+	-0.3981(5)	-0.0728(3)	0.15720(18)	0.0229(6)	1.0	1.161(7)
Na7	2*i*	1+	0.1232(5)	0.3149(3)	-0.22077(15)	0.0196(6)	1.0	1.297(8)
Na8	2*i*	1+	-0.0316(5)	0.0888(3)	0.33854(16)	0.0200(10)	0.951(12)	1.236(8)
Na9	2*i*	1+	-0.6238(5)	0.1408(3)	0.05018(18)	0.0242(6)	1.0	1.144(7)
Na10	2*i*	1+	0.1931(6)	-0.1156(3)	0.49410(19)	0.0332(7)	1.0	1.069(8)
Na11	2*i*	1+	0.5404(7)	-0.0204(3)	0.3527(3)	0.0482(11)	1.0	0.945(7)
Na12	2*i*	1+	0.4143(6)	-0.3739(3)	0.4245(2)	0.0348(8)	1.0	0.998(7)
Na13	2*i*	1+	0.6681(6)	0.3681(3)	0.3604(2)	0.0277(12)	0.861(13)	1.151 8)
Na14	1*e*	1+	0.5	0.5	0.0	0.0455(16)	1.0	1.183(6)
O1	2*i*	2-	0.0198(8)	-0.1506(4)	0.1743(2)	0.0123(8)	1.0	2.290(14)
O2	2*i*	2-	-0.4520(8)	0.2885(4)	-0.0057(2)	0.0111(8)	1.0	2.302(13)
O3	2*i*	2-	0.1260(8)	-0.3609(4)	0.3293(2)	0.0139(9)	1.0	2.189(14)
O4	2*i*	2-	-0.2191(7)	0.0679(4)	0.0839(2)	0.0085(8)	1.0	2.033(11)
O5	2*i*	2-	0.0471(8)	0.2014(4)	0.1429(2)	0.0127(8)	1.0	2.029(14)
O6	2*i*	2-	0.5628(9)	0.1792(5)	0.3873(3)	0.0228(11)	1.0	2.038(18)
O7	2*i*	2-	0.0149(7)	0.1813(4)	-0.0172(2)	0.0091(8)	1.0	1.939(10)
O8	2*i*	2-	0.5846(9)	-0.2120(5)	0.4660(3)	0.0210(10)	1.0	2.151(18)
O9	2*i*	2-	-0.1517(8)	0.4189(4)	0.0625(2)	0.0145(9)	1.0	2.019(15)
O10	2*i*	2-	-0.2587(7)	0.0447(4)	-0.0764(2)	0.0091(8)	1.0	1.875(10)
O11	2*i*	2-	-0.5243(8)	0.2705(4)	-0.1530(2)	0.0160(9)	1.0	1.944(14)
O12	2*i*	2-	0.0771(8)	0.2871(4)	0.3508(2)	0.0150(9)	1.0	2.146(14)
O13	2*i*	2-	0.0371(9)	-0.3248(4)	0.4916(2)	0.0174(9)	1.0	1.952(12)
O14	2*i*	2-	0.2825(8)	-0.5726(4)	0.4312(2)	0.0149(9)	1.0	1.924(11)
O15	2*i*	2-	0.2671(8)	0.0110(4)	0.2374(2)	0.0142(9)	1.0	2.001(14)
O16	2*i*	2-	0.8224(8)	-0.4599(4)	0.4101(2)	0.0142(9)	1.0	2.136(12)
O17	2*i*	2-	-0.1843(8)	0.3893(4)	-0.1163(3)	0.0152(9)	1.0	1.940(16)
O18	2*i*	2-	0.1910(10)	0.0805(4)	0.4401(3)	0.0200(10)	1.0	2.013(18)
O19	2*i*	2-	-0.2263(8)	0.0667(4)	0.2361(2)	0.0151(9)	1.0	2.052(15)
O20	2*i*	2-	-0.1187(10)	0.4831(5)	0.2573(3)	0.0216(11)	1.0	2.020(20)
O21	2*i*	2-	0.6327(9)	-0.2351(5)	0.3223(3)	0.0252(11)	1.0	1.983(19)
O22	2*i*	2-	-0.4672(9)	0.3050(4)	0.1394(3)	0.0182(10)	1.0	1.995(19)
O23	2*i*	2-	0.3720(10)	0.4140(5)	0.2736(3)	0.0230(11)	1.0	2.139(20)
O24	2*i*	2-	-0.0462(9)	-0.1228(4)	0.3861(3)	0.0191(10)	1.0	1.794(17)

Table D.15: Additional atomic positions with site occupancy factor (SOF) for modeling stacking faults at the Ru5 cluster in the crystal structure of $Na_{27}Ru_{14}O_{48}$ of the present work. The U_{iso} had to be restrained to prevent non-positive definite atomic positions.

Atom	Site	x	y	z	U_{iso} / Å^2	SOF
Ru5A	2*i*	-0.103(3)	-0.4869(12)	0.4982(7)	0.002	0.069(3)
Ru6A	2*i*	-0.360(3)	-0.2502(14)	0.4020(8)	0.002	0.054(3)
Ru7A	2*i*	-0.140(4)	0.484(2)	0.3272(12)	0.002	0.039(3)
Ru8A	2*i*	0.110(3)	0.2503(14)	0.4248(8)	0.002	0.058(3)

Table D.16: Structural model of $Na_{37.1(4)}Ru_{21}O_{72}$ of the present work including measurement details, lattice parameters (a, b, c, β), cell volume V, atomic positions with Wyckoff site symmetry and oxidation state, fractional coordinates (x, y, z), isotropic atomic displacement parameters (U_{iso}), site occupancy factors (SOF) and bond valence sums (BVS). The resulting global instability index is 0.142. The three additional atomic positions Ru6A-Ru8A describe the stacking faults.

$Na_{37.1(4)}Ru_{21}O_{72}$	
Space group	$P\bar{1}$
Z	1
$a, b, c, \alpha, \beta, \gamma$	5.7599(3)Å, 10.9872(7) Å, 27.6569(16) Å, 99.859(2)°, 89.390(2)°, 75.093(2)°
V	1663.64(17) Å^3
ρ_{calc}	4.232 g cm^{-3}
T	150(2) K
Radiation wavelength	0.71073 Å
Crystal information	
Colour/shape	black with metallic luster, rectangular
Size	0.037 mm x 0.039 mm x 0.122 mm
Growth conditions	growth at the outer rim of crucible, T_{max} = 950 °C, Na_2CO_3:RuO_2 1.02:1
Data collection	
Θ range	1.95° to 27.50°
Independent reflections	7565
R_{int}	0.0264
Data reduction	
Absorption correction	numerical
μ	5.028 mm^{-1}
F(000)	1962
Refined parameters	325
Final R-values with I > 2σ(I)	
R_1	0.0631
GOF on F^2	1.093

Structure solution and refinement: SHELXT-2014/5 [114] , SHELXL-2018/3 [115]

– continued from previous page

Atom	Site	Ox. state	x	y	z	U_{iso} / Å^2	SOF	BVS
Ru1	2*i*	3+	0.04064(14)	0.32793(7)	0.66716(3)	0.00323(18)	1.0	3.120(27)
Ru2	2*i*	5+	0.80188(14)	0.53081(7)	0.60150(3)	0.00294(18)	1.0	5.019(47)
Ru3	2*i*	5+	0.05502(16)	0.41612(8)	0.78138(3)	0.00504(18)	1.0	4.999(48)
Ru4	2*i*	5+	0.25993(14)	0.04044(7)	0.61777(3)	0.00203(18)	1.0	5.019(47)
Ru5	1*a*	4+	0.0	0.0	0.0	0.0070(2)	1.0	3.852(34)
Ru6	2*i*	5+	0.13395(16)	0.80673(8)	0.07181(3)	0.0050(2)	0.961(4)	5.021(48)
Ru6A	2*i*	5+	0.340(3)	0.7853(17)	0.0637(7)	0.005(4)	0.046(4)	-
Ru7	2*i*	5+	0.11624(16)	0.90232(8)	0.88712(3)	0.0048(3)	0.972(4)	5.160(49)
Ru7A	2*i*	5+	0.890(3)	0.9268(18)	0.8865(7)	0.005(4)	0.042(4)	-
Ru8	2*i*	5+	0.27751(16)	0.70987(8)	0.95984(3)	0.0045(2)	0.953(4)	5.014(48)
Ru8A	2*i*	5+	0.121(3)	0.7279(17)	0.9508(7)	0.005(4)	0.044(4)	-
Ru9	2*i*	5+	0.02431(14)	0.24185(7)	0.55306(3)	0.00282(18)	1.0	5.099(48)
Ru10	2*i*	5+	0.28897(16)	0.12496(8)	0.73164(3)	0.00510(18)	1.0	4.931(46)
Ru11	2*i*	5+	0.82131(14)	0.61555(8)	0.71598(3)	0.00455(18)	1.0	5.004(48)
Na1	2*i*	1+	0.4211(9)	0.0977(5)	0.9527(2)	0.0114(17)	0.87(2)	1.017(12)
Na2	2*i*	1+	0.1966(8)	0.5655(4)	0.51741(17)	0.0106(15)	0.98(2)	1.169(13)
Na3	2*i*	1+	0.4893(8)	0.2418(4)	0.44802(17)	0.0098(16)	0.94(2)	1.145(12)
Na4	2*i*	1+	0.9795(8)	0.5330(4)	0.89348(16)	0.0060(15)	0.92(2)	1.236(13)
Na5	2*i*	1+	0.9215(8)	0.8664(4)	0.56496(17)	0.0083(15)	0.94(2)	1.192(12)
Na6	2*i*	1+	0.1952(9)	0.6787(5)	0.63780(18)	0.0106(16)	0.93(2)	1.132(13)
Na7	2*i*	1+	0.4475(9)	0.3536(5)	0.56838(17)	0.0077(16)	0.90(2)	1.188(13)
Na8	2*i*	1+	0.7204(9)	0.7751(5)	0.14712(18)	0.0100(16)	0.91(2)	1.186(14)
Na9	2*i*	1+	0.5791(9)	0.8992(5)	0.7916(2)	0.0112(17)	0.89(2)	1.070(14)
Na10	2*i*	1+	0.5095(10)	0.8337(5)	0.6769(2)	0.0092(19)	0.78(2)	1.144(13)
Na11	2*i*	1+	0.4150(9)	0.4899(5)	0.70312(18)	0.0078(17)	0.86(2)	1.147(13)
Na12	2*i*	1+	0.1592(8)	0.7852(4)	0.77116(17)	0.0073(16)	0.91(2)	1.206(12)
Na13	2*i*	1+	0.4235(10)	0.6140(5)	0.8332(2)	0.0145(18)	0.91(2)	1.066(12)
Na14	2*i*	1+	0.8868(9)	0.9778(5)	0.69773(18)	0.0116(17)	0.92(2)	1.126(13)
Na15	2*i*	1+	0.6891(10)	0.0496(5)	0.5084(2)	0.0083(18)	0.78(2)	1.178(12)
Na16	2*i*	1+	0.6672(9)	0.1724(5)	0.6358(2)	0.0102(18)	0.85(2)	1.068(13)
Na17	2*i*	1+	0.9119(9)	0.0839(5)	0.8131(2)	0.0076(18)	0.80(2)	1.339(16)
Na18	2*i*	1+	0.8130(9)	0.6202(5)	0.00403(18)	0.0095(16)	0.89(2)	1.129(12)
Na19	2*i*	1+	0.5477(11)	0.4288(7)	0.9094(2)	0.019(2)	0.86(2)	0.977(12)
Na20	2*i*	1+	0.6333(10)	0.3082(5)	0.7758(2)	0.0139(18)	0.87(2)	1.179(13)
Na21	2*i*	1+	0.6810(9)	0.8196(5)	0.9081(2)	0.0089(17)	0.85(2)	1.172(13)
O1	2*i*	2-	0.2967(13)	0.3087(7)	0.7183(4)	0.0044(13)	1.0	1.840(20)
O2	2*i*	2-	0.8154(14)	0.4243(7)	0.7224(4)	0.0080(14)	1.0	2.023(21)
O3	2*i*	2-	0.0507(14)	0.2362(8)	0.7827(4)	0.0105(15)	1.0	2.323(28)
O4	2*i*	2-	0.0772(13)	0.5790(7)	0.7624(4)	0.0065(14)	1.0	2.007(26)
O5	2*i*	2-	0.5608(14)	0.6833(7)	0.7583(4)	0.0097(15)	1.0	1.973(28)
O6	2*i*	2-	0.4138(14)	0.7231(8)	0.0252(4)	0.0119(16)	1.0	2.202(26)
O7	2*i*	2-	0.1972(14)	0.5594(7)	0.9612(4)	0.0103(15)	1.0	2.087(30)
O8	2*i*	2-	0.5110(14)	0.9750(7)	0.5726(4)	0.0086(14)	1.0	2.056(28)
O9	2*i*	2-	0.7074(14)	0.0997(7)	0.0446(4)	0.0096(15)	1.0	1.953(21)
O10	2*i*	2-	0.2788(14)	0.1782(7)	0.5092(4)	0.0079(14)	1.0	2.176(29)
O11	2*i*	2-	0.7929(14)	0.4753(7)	0.8237(4)	0.0081(14)	1.0	2.011(29)
O12	2*i*	2-	0.5599(14)	0.1079(8)	0.7682(4)	0.0109(15)	1.0	1.942(27)
O13	2*i*	2-	0.3427(16)	0.7967(9)	0.1219(4)	0.0175(18)	1.0	1.928(30)
O14	2*i*	2-	0.2897(14)	0.4206(7)	0.8261(4)	0.0093(15)	1.0	2.010(28)
O15	2*i*	2-	0.0299(14)	0.6645(7)	0.0767(4)	0.0085(14)	1.0	1.855(29)
O16	2*i*	2-	0.8897(14)	0.7669(8)	0.7079(4)	0.0106(15)	1.0	1.952(31)
O17	2*i*	2-	0.1469(14)	0.0771(7)	0.8874(4)	0.0100(15)	1.0	2.234(26)
O18	2*i*	2-	0.3917(14)	0.8329(8)	0.8498(4)	0.0113(15)	1.0	2.210(30)
O19	2*i*	2-	0.9027(15)	0.8992(8)	0.8387(4)	0.0136(16)	1.0	2.095(31)
O20	2*i*	2-	0.5743(15)	0.6401(8)	0.9272(4)	0.0142(16)	1.0	2.044(28)

– continued from previous page

Atom	Site	Ox. state	x	y	z	U_{iso} / Å^2	SOF	BVS
O21	2*i*	2-	0.1931(13)	0.8884(7)	0.6248(4)	0.0061(14)	1.0	2.064(29)
O22	2*i*	2-	0.0606(13)	0.5016(7)	0.6553(4)	0.0042(13)	1.0	1.950(21)
O23	2*i*	2-	0.7904(13)	0.3470(7)	0.6152(4)	0.0045(13)	1.0	1.972(21)
O24	2*i*	2-	0.2655(13)	0.2300(7)	0.6109(4)	0.0051(13)	1.0	2.071(22)
O25	2*i*	2-	0.0435(13)	0.4181(7)	0.5503(4)	0.0071(14)	1.0	2.298(25)
O26	2*i*	2-	0.5418(14)	0.5447(8)	0.5623(4)	0.0107(15)	1.0	2.028(28)
O27	2*i*	2-	0.8813(14)	0.6745(7)	0.5886(4)	0.0100(15)	1.0	1.983(30)
O28	2*i*	2-	0.5943(13)	0.6147(7)	0.6613(4)	0.0073(14)	1.0	2.287(25)
O29	2*i*	2-	0.0231(14)	0.1527(7)	0.6779(4)	0.0083(14)	1.0	1.984(21)
O30	2*i*	2-	0.0020(14)	0.0759(7)	0.5699(4)	0.0099(15)	1.0	2.071(25)
O31	2*i*	2-	0.7833(14)	0.2439(7)	0.5095(4)	0.0075(14)	1.0	2.116(28)
O32	2*i*	2-	0.4916(14)	0.0403(7)	0.6706(4)	0.0080(14)	1.0	2.334(27)
O33	2*i*	2-	0.8304(14)	0.0082(7)	0.9394(4)	0.0077(14)	1.0	2.165(24)
O34	2*i*	2-	0.0891(13)	0.7343(7)	0.9011(4)	0.0066(14)	1.0	2.150(26)
O35	2*i*	2-	0.2171(14)	0.9771(7)	0.7438(4)	0.0088(15)	1.0	1.995(28)
O36	2*i*	2-	0.9637(14)	0.8245(7)	0.0050(4)	0.0098(15)	1.0	1.990(22)

Bibliography

[1] Ahrens, L. H. (1952). The use of ionization potentials Part 1. Ionic radii of the elements. *Geochim. Cosmochim. Acta*, 2(3):155–169.

[2] Alexander, A., Battle, P., Burley, J., Gallon, D. J., Grey, C. P., and Kim, S. (2003). Structural and magnetic properties of Li_3RuO_4. *J. Mater. Chem.*, 13(10):2612–2616.

[3] Allred, J., Wang, L., Khalifah, P., and Cava, R. J. (2011). $Na_{27}Ru_{14}O_{48}$: A new mixed-valence sodium ruthenate with magnetic heptameric plaquettes. *J. Solid State Chem.*, 184(1):44–51.

[4] Analytis, J. G. (2019). Private communication via E-mail, 03/09/19.

[5] Arkel, A. V., Spitsbergen, U., and Heyding, R. (1955). Note on the volatility of lithium oxide. *Can. J. Chem.*, 33(2):446–447.

[6] Barin, I. (1995). *Thermochemical Data of Pure Substances*. Wiley-VCH, Weinheim, Germany.

[7] Berkowitz-Mattuck, J. B. and Büchler, A. (1963). A transpiration study of lithium hydroxide. *J. Phys. Chem.*, 67(6):1386–1388.

[8] Bernath, P. F. (2005). *Spectra of* A*toms and* M*olecules, 2nd edition*. Oxford University Press, New York, USA.

[9] Bertaut, E. (1961). Sur l'isomorphisme d'oxydes ternaires de chrome et de rhodium trivalents. *J. Phys. Chem. Solids*, 21(1-2):118–119.

[10] Bette, S., Takayama, T., Kitagawa, K., Takano, R., Takagi, H., and Dinnebier, R. E. (2017). Solution of the heavily stacking faulted crystal structure of the honeycomb iridate $H_3LiIr_2O_6$. *Dalton Trans.*, 46(44):15216–15227.

[11] Biffin, A., Johnson, R., Choi, S., Freund, F., Manni, S., Bombardi, A., Manuel, P., Gegenwart, P., and Coldea, R. (2014a). Unconventional magnetic order on the hyperhoneycomb Kitaev lattice in β-Li_2IrO_3 : Full solution via magnetic resonant X-ray diffraction. *Phys. Rev. B*, 90(20):205116.

[12] Biffin, A., Johnson, R., Kimchi, I., Morris, R., Bombardi, A., Analytis, J., Vishwanath, A., and Coldea, R. (2014b). Noncoplanar and counterrotating incommensurate magnetic order stabilized by Kitaev interactions in γ-Li_2IrO_3. *Phys. Rev. Lett.*, 113(19):197201.

[13] Binnewies, M., Glaum, R., Schmidt, M., and Schmidt, P. (2012). *Chemical Vapor Transport Reactions*. Walter de Gruyter, Berlin/Boston, Germany/USA.

[14] Binnewies, M. and Milke, E. (2002). *Thermochemical data of elements and compounds*. Wiley-VCH, Weinheim, Germany.

[15] Binnewies, M., Schmidt, M., and Schmidt, P. (2017). Chemical vapor transport reactions - arguments for choosing a suitable transport agent. *Z. Anorg. Allg. Chem.*, 643(21):1295–1311.

[16] Bréger, J., Jiang, M., Dupré, N., Meng, Y. S., Shao-Horn, Y., Ceder, G., and Grey, C. P. (2005). High-resolution X-ray diffraction, DIFFaX, NMR and first principles study of disorder in the Li_2MnO_3-$Li[Ni_{0.5}Mn_{0.5}]O_2$ solid solution. *J. Solid State Chem.*, 178(9):2575–2585.

[17] Brown, I. (1992). Chemical and steric constraints in inorganic solids. *Acta Cryst. B*, 48(5):553–572.

[18] Brown, I. (2016). Accumulated table of Bond Valence parameters, version 2.2, McMaster University, Hamilton, Ontario, Canada.

[19] Bruker (2016). *APEX3 software suite*. Bruker AXS Inc., Madison, Wisconsin, USA.

[20] Bunsen, R. (1852). Vulkanische Exhalation. *J. prakt. Chem.*, 56:53.

[21] Bush, T., Catlow, C. R. A., and Battle, P. (1995). Evolutionary programming techniques for predicting inorganic crystal structures. *J. Mater. Chem.*, 5(8):1269–1272.

[22] Cao, G., McCall, S., Freibert, F., Shepard, M., Henning, P., and Crow, J. (1996). Observation of an anomalous quasi-one-dimensional behavior in $Na_2Ru_4O_{9-\delta}$ single crystals. *Phys. Rev. B*, 53(18):12215.

[23] Cao, G., Qi, T., Li, L., Terzic, J., Cao, V. S., Yuan, S., Tovar, M., Murthy, G., and Kaul, R. K. (2013). Evolution of magnetism in the single-crystal honeycomb iridates $(Na_{1-x}Li_x)_2IrO_3$. *Phys. Rev. B*, 88(22):220414.

[24] Carol, L. and Mann, G. (1990). High-Temperature Oxidation of Rhodium. *Oxid. Met.*, 34(1-2):1–12.

[25] Chaloupka, J., Jackeli, G., and Khaliullin, G. (2013). Zigzag magnetic order in the iridium oxide Na_2IrO_3. *Phys. Rev. Lett.*, 110(9):097204.

[26] Choi, S., Coldea, R., Kolmogorov, A., Lancaster, T., Mazin, I., Blundell, S., Radaelli, P., Singh, Y., Gegenwart, P., Choi, K., Cheong, S., Baker, P., Stock, C., and Taylor, J. (2012). Spin waves and revised crystal structure of honeycomb iridate Na_2IrO_3. *Phys. Rev. Lett.*, 108(12):127204.

[27] Coelho, A. (2012). *Topas Academic V5*. Coelho Software, Brisbane, Australia.

[28] Cottrell, A. (1997). *An introduction to metallurgy*. CRC Press, London, United Kingdom.

[29] Darriet, J. (1974). Structure Cristalline de la Phase Type 'Bronze de Ruthénium' $Na_{3-x}Ru_4O_9$. *Acta Cryst. B*, 30(6):1459–1462.

[30] Davidson, I. J. and Greedan, J. (1984). Neutron and X-ray powder diffraction study of Li_xRuO_2 and Li_xIrO_2: the crystal structure of $Li_{0.9}RuO_2$. *J. Solid State Chem.*, 51(1):104–117.

[31] Dhanaraj, G., Byrappa, K., Prasad, V., and Dudley, M. (2010). *Springer Handbook of Crystal Growth*. Springer, Berlin/Heidelberg, Germany.

[32] Dietrich, H. v. (1963). Die Kristallstruktur von Äthyl-Lithium. *Acta Cryst.*, 16(7):681–689.

[33] Dulac, J. (1970). Synthesis and crystallographic structure of a new ternary compound Li_2RuO_3. *C. R. Hebd. Seances Acad. Sci. B*, 270(3):223.

[34] Foo, M. L., Huang, Q., Lynn, J., Lee, W.-L., Klimczuk, T., Hagemann, I., Ong, N., and Cava, R. J. (2006). Synthesis, structure and physical properties of Ru ferrites: $BaMRu_5O_{11}$ (M= Li and Cu) and $BaM'_2Ru_4O_{11}$ (M'= Mn, Fe and Co). *J. Solid State Chem.*, 179(2):563–572.

[35] Freund, F., Williams, S., Johnson, R., Coldea, R., Gegenwart, P., and Jesche, A. (2016). Single crystal growth from separated educts and its application to lithium transition-metal oxides. *Sci. Rep.*, 6:35362.

[36] Gibbs, J. (1928). On the equilibrium of heterogeneous substances. *Longmanns, Green and Co, New York, USA*.

[37] Glauglitz, G. and Vo-Dinh, T. (2003). *Handbook of Spectroscopy*. Wiley-VCH, Weinheim, Germany.

[38] Gmelin, L. (1928). *Gmelins Handbuch der Anorganischen Chemie, 8. Auflage, System 21: Natrium*. Verlag Chemie GmbH, Weinheim/Berlin, Germany.

[39] Hermann, V., Altmeyer, M., Ebad-Allah, J., Freund, F., Jesche, A., Tsirlin, A. A., Hanfland, M., Gegenwart, P., Mazin, I., Khomskii, D., Valentí, R., and Kuntscher, C. (2018). Competition between spin-orbit coupling, magnetism, and dimerization in the honeycomb iridates: α-Li_2IrO_3 under pressure. *Phys. Rev. B*, 97(2):020104.

[40] Hobbie, K. and Hoppe, R. (1986). Über Oxorhodate der Alkalimetalle: β-$LiRhO_2$. *Z. Anorg. Allg. Chem.*, 535(4):20–30.

[41] Jackeli, G. and Khaliullin, G. (2009). Mott insulators in the strong spin-orbit coupling limit: from Heisenberg to a quantum compass and Kitaev models. *Phys. Rev. Lett.*, 102(1):017205.

[42] Jackeli, G. and Khomskii, D. (2008). Classical dimers and dimerized superstructure in an orbitally degenerate honeycomb antiferromagnet. *Phys. Rev. Lett.*, 100(14):147203.

[43] Jacquet, Q., Perez, A., Batuk, D., Van Tendeloo, G., Rousse, G., and Tarascon, J.-M. (2017). The $Li_3Ru_yNb_{1-y}O_4$ ($0 \leq y \leq 1$) system: Structural diversity and Li insertion and extraction capabilities. *Chem. Mater.*, 29(12):5331–5343.

[44] James, A. and Goodenough, J. B. (1988). Structure and bonding in lithium ruthenate, Li_2RuO_3. *J. Solid State Chem.*, 74(2):287–294.

[45] Jansen, M. and Hoppe, R. (1973). Zur Kenntnis der NaCl-Strukturfamilie: Neue Untersuchungen an Li_2MnO_3. *Z. Anorg. Allg. Chem.*, 397(3):279–289.

[46] Jenderka, M., Schmidt-Grund, R., Grundmann, M., and Lorenz, M. (2015). Electronic excitations and structure of Li_2IrO_3 thin films grown on ZrO_2:Y (001) substrates. *J. Appl. Phys.*, 117(2):025304.

[47] Jimenez-Segura, M.-P., Ikeda, A., Yonezawa, S., and Maeno, Y. (2016). Effect of disorder on the dimer transition of the honeycomb-lattice compound Li_2RuO_3. *Phys. Rev. B*, 93(7):075133.

[48] Jung, Y. H., Kim, D. K., and Hong, S.-T. (2013). Synthesis, structure, and electrochemical Li-ion intercalation of $LiRu_2O_4$ with $CaFe_2O_4$-type structure. *J. Power Sources*, 233:285–289.

[49] Karle, J. T. and Hauptman, H. (1956). A theory of phase determination for the four types of non-centrosymmetric space groups 1P222, 2P22, $3P_12$, $3P_22$. *Acta Cryst.*, 9(8):635–651.

[50] Katukuri, V. M., Yadav, R., Hozoi, L., Nishimoto, S., and Van Den Brink, J. (2016). The vicinity of hyper-honeycomb β-Li 2 IrO_3 to a three-dimensional Kitaev spin liquid state. *Sci. Rep.*, 6:29585.

[51] Khaliullin, G. (2005). Orbital order and fluctuations in Mott insulators. *Prog. Theor. Phys. Supp.*, 160:155–202.

[52] Kikuchi, T. (1976). Vapor pressure of lithium oxide and dissociation pressure of lithium hydroxide. Technical report, Japan Atomic Energy Research Inst., Tokai, Japan.

[53] Kim, H.-S., Lee, E. K.-H., and Kim, Y. B. (2016). Predominance of the Kitaev interaction in a three-dimensional honeycomb iridate: From *ab initio* to spin model. *Europhys. Lett.*, 112(6):67004.

[54] Kim, J.-W. and Lee, H.-G. (2001). Thermal and carbothermic decomposition of Na_2CO_3 and Li_2CO_3. *Metall. Mater. Trans. B*, 32(1):17–24.

[55] Kimber, S. A., Mazin, I., Shen, J., Jeschke, H. O., Streltsov, S. V., Argyriou, D. N., Valenti, R., and Khomskii, D. I. (2014). Valence bond liquid phase in the honeycomb lattice material Li_2RuO_3. *Phys. Rev. B*, 89(8):081408.

[56] Kimchi, I., Coldea, R., and Vishwanath, A. (2015). Unified theory of spiral magnetism in the harmonic-honeycomb iridates α-, β-, and γ-Li_2IrO_3. *Phys. Rev. B*, 91(24):245134.

[57] Kitaev, A. (2006). Anyons in an exactly solved model and beyond. *Ann. Phys.*, 321(1):2–111.

[58] Knacke, O. and Hesselmann, K. (1991). *Thermochemical properties of inorganic substances*. Springer, New York, USA.

[59] Knacke, O., Kubashewski, O., and Hesselmann, K. (1991). *Thermochemical data of pure substances, 2nd edition*, volume I and II. Springer, New York, USA.

[60] Kobayashi, H., Kanno, R., Kawamoto, Y., Tabuchi, M., Nakamura, O., and Takano, M. (1995). Structure and lithium deintercalation of $Li_{2-x}RuO_3$. *Solid State Ion.*, 82(1-2):25–31.

[61] Kobayashi, H., Kanno, R., Tabuchi, M., Kageyama, H., Nakamura, O., and Takano, M. (1997). Structure and charge/discharge characteristics of new layered oxides: $Li_{1.8}Ru_{0.6}Fe_{0.6}O_3$ and Li_2IrO_3. *J. Power Sources*, 68(2):686–691.

[62] Krizan, J. W., Roudebush, J. H., Fox, G. M., and Cava, R. J. (2014). The chemical instability of Na_2IrO_3 in air. *Mat. Res. Bull.*, 52:162–166.

[63] Kroeschell, P., Wolf, R., and Hoppe, R. (1986). Neue Vertreter der Li_8SnO_6-Familie: Li_8IrO_6, Li_8PtO_6 und Li_8CeO_6. *Z. Anorg. Allg. Chem.*, 536(5):81–91.

[64] Kumari, L. S., Wallace, M., Barnes, J., Tong, B., Ramirez, A., and Subramanian, M. (2016). Charge transfer instability in a mixed Ir/Rh honeycomb lattice in $Li_2Ir_{1-x}Rh_xO_3$ solid solution. *Solid State Sci.*, 61:232–238.

[65] Laligant, Y., Lacorre, P., and Rodríquez-Carvajal, J. (2001). Powder Structure Determination of Li_2PdO_3: A NaCl Structure Type with Turbostratic Effect. *Mater. Sci. Forum*, 378-381:632–637.

[66] Lang, G. (1966). Strukturvergleiche an ternären und quarternären Oxiden. *Z. Anorg. Allg. Chem.*, 348(5-6):246–256.

[67] Lei, H., Yin, W.-G., Zhong, Z., Hosono, H., et al. (2014). Structural, magnetic, and electrical properties of $Li_2Ir_{1-x}Ru_xO_3$. *Phys. Rev. B*, 89(2):020409.

[68] Liu, X., Berlijn, T., Yin, W.-G., Ku, W., Tsvelik, A., Kim, Y.-J., Gretarsson, H., Singh, Y., Gegenwart, P., and Hill, J. (2011). Long-range magnetic ordering in Na_2IrO_3. *Phys. Rev. B*, 83(22):220403.

[69] Mamak, M., Zavalij, P. Y., and Whittingham, M. S. (1998). Layered structure of lithium ethylene glycolate, $Li(OCH_2CH_2OH)$. *Acta Cryst. C*, 54(7):937–939.

[70] Manuel, P., Adroja, D., Lindgard, P.-A., Hillier, A., Battle, P., Son, W.-J., and Whangbo, M.-H. (2011). Neutron scattering and μSR investigations of quasi-one-dimensional magnetism in the spin = 3/2 compound Li_3RuO_4. *Phys. Rev. B*, 84(17):174430.

[71] Massa, W. (2007). *Kristallstrukturbestimmung, 7. Auflage*. Springer, Wiesbaden, Germany.

[72] Mehlawat, K., Sharma, G., and Singh, Y. (2015). Fragile magnetic order in the honeycomb lattice iridate Na_2IrO_3 revealed by magnetic impurity doping. *Phys. Rev. B*, 92(13):134412.

[73] Mehlawat, K. and Singh, Y. (2017). First-order magnetostructural transition in single crystals of the honeycomb lattice ruthenate Li_2RuO_3. *Phys. Rev. B*, 95(7):075105.

[74] Meyer, G. and Hoppe, R. (1976). Zum thermischen Verhalten von Li_3MnO_4. II. Über α-und β-Li_2MnO_3. *Z. Anorg. Allg. Chem.*, 424(3):257–264.

[75] Miura, Y., Sato, M., Yamakawa, Y., Habaguchi, T., and Ono, Y. (2009). Structural transition of Li_2RuO_3 induced by molecular-orbit formation. *J. Phys. Soc. Jpn.*, 78(9):094706–094706.

[76] Miura, Y., Yasui, Y., Sato, M., Igawa, N., and Kakurai, K. (2007). New-type phase transition of Li_2RuO_3 with honeycomb structure. *J. Phys. Soc. Jpn.*, 76(3):033705.

[77] Modic, K., Smidt, T. E., Kimchi, I., Breznay, N. P., Biffin, A., Choi, S., Johnson, R. D., Coldea, R., Watkins-Curry, P., McCandless, G. T., Chan, J. Y., Gandara, F., Islam, Z., Vishwanath, A., Shekhter, A., McDonald, R. D., and Analytis, J. G. (2014). Realization of a three-dimensional spin - anisotropic harmonic honeycomb iridate. *Nat. Comm.*, 5:4203.

[78] Mogare, K. M., Friese, K., Klein, W., and Jansen, M. (2004). Syntheses and crystal structures of two sodium ruthenates: Na_2RuO_4 and Na_2RuO_3. *Z. Anorg. Allg. Chem.*, 630(4):547–552.

[79] Momma, K. and Izumi, F. (2008). VESTA: a three-dimensional visualization system for electronic and structural analysis. *J. Appl. Cryst.*, 41(3):653–658.

[80] Mond, L., Langer, C., and Quincke, F. (1890). L. - Action of carbon monoxide on nickel. *J. Chem. Soc., Transactions*, 57:749–753.

[81] Motzfeldt, K. (1955). The thermal decomposition of sodium carbonate by the effusion method. *J. Phys. Chem.*, 59(2):139–147.

[82] Mühle, C., Karpov, A., Verhoeven, A., and Jansen, M. (2005). Crystal structures, dimorphism and lithium mobility of Li_7MO_6 (M = Bi, Ru, Os). *Z. Anorg. Allg. Chem.*, 631(12):2321–2327.

[83] Müller-Buschbaum, H. (2004). Zur Kristallchemie der Oxoplatinate. *Z. Anorg. Allg. Chem.*, 630(1):3–30.

[84] Müller-Buschbaum, H. (2005a). Zur Kristallchemie der Oxoiridate. *Z. Anorg. Allg. Chem.*, 631(6-7):1005–1028.

[85] Müller-Buschbaum, H. (2005b). Zur Kristallchemie der Oxopalladate. *Z. Anorg. Allg. Chem.*, 631(2-3):239–259.

[86] Müller-Buschbaum, H. (2006). Zur Kristallchemie der Oxoruthenate. *Z. Anorg. Allg. Chem.*, 632(10-11):1625–1659.

[87] Müller-Buschbaum, H. (2007). Zur Kristallchemie der Oxorhodate. *Z. Anorg. Allg. Chem.*, 633(9):1289–1306.

[88] Müller-Buschbaum, H. (2008). Zur Kristallchemie der Oxoosmate. *Z. Anorg. Allg. Chem.*, 634(12-13):2111–2124.

[89] Nitsche, R. (1968). Kristallzucht aus der Gasphase. In *Festkörper Probleme 8*, pages 42–73. Springer, Berlin/Heidelberg, Germany.

[90] O'Malley, M. J., Verweij, H., and Woodward, P. M. (2008). Structure and properties of ordered Li_2IrO_3 and Li_2PtO_3. *J. Solid State Chem.*, 181(8):1803–1809.

[91] Onoda, Y., Chung, S., Watanabe, A., and Mitsuhashi, T. (2000). Na^+ ion motion in $Na_{3-x}Ru_4O_9$: an NMR study of ^{23}Na line shape. *Solid State Ion.*, 136:365–370.

[92] Oppermann, H. and Okhotin, A. (1981). About the influence of convection on the transport velocity of chemical transport. *Adv. Space Res.*, 1(5):51–54.

[93] Oppermann, H., Schmidt, M., and Schmidt, P. (2005). Autotransport oder Selbsttransport - Systeme mit Gasphasentransporten unter dem eigenen Zersetzungsdruck. *Z. Anorg. Allg. Chem.*, 631(2-3):197–238.

[94] Palmer, D. and Palmer, S. (2017). *CrystalMaker version 9.2.9f1*. CrystalMaker Software Ltd, Oxfordshire, United Kingdom.

[95] Panin, R., Khasanova, N., Abakumov, A., Schnelle, W., Hadermann, J., and Antipov, E. (2006). Crystal structure and properties of the $Na_{1-x}Ru_2O_4$ phase. *Russ. Chem. Bull.*, 55(10):1717–1722.

[96] Panin, R. V., Khasanova, N. R., Abakumov, A. M., Antipov, E. V., Van Tendeloo, G., and Schnelle, W. (2007). Synthesis and crystal structure of the palladium oxides $NaPd_3O_4$, Na_2PdO_3 and $K_3Pd_2O_4$. *J. Solid State Chem.*, 180(5):1566–1574.

[97] Park, J., Tan, T.-Y., Adroja, D., Daoud-Aladine, A., Choi, S., Cho, D.-Y., Lee, S.-H., Kim, J., Sim, H., Morioka, T., Nojiri, H., Krishnamurthy, V. V., Manuel, P., Lees, M. R., Streltsov, S. V., Khomskii, D. I., and Park, J.-G. (2016). Robust singlet dimers with fragile ordering in two-dimensional honeycomb lattice of Li_2RuO_3. *Sci. Rep.*, 6:25238.

[98] Pauling, L. (1960). *The Nature of the Chemical Bond*, volume 260. Cornell University Press Ithaca, NY, USA.

[99] Perez, A. J., Batuk, D., Saubanère, M., Rousse, G., Foix, D., Mccalla, E., Berg, E. J., Dugas, R., HW van den Bos, K., Doublet, M.-L., Gonbeau, D., Abakumov, A. M., Van Tendeloo, G., and Tarascon, J.-M. (2016). Strong oxygen participation in the redox governing the structural and electrochemical properties of Na-rich layered oxide Na_2IrO_3. *Chem. Mater.*, 28(22):8278–8288.

[100] Pesin, D. and Balents, L. (2010). Mott physics and band topology in materials with strong spin-orbit interaction. *Nat. Phys.*, 6(5):376–381.

[101] Ramesha, K., Prakash, A., Sathiya, M., Madras, G., and Shukla, A. (2011). Synthesis and photocatalytic properties of $Ag[Li_{1/3}Ru_{2/3}]O_2$: A new delafossite oxide. *Mat. Sci. Eng. B*, 176(2):141–146.

[102] Regan, K., Huang, Q., and Cava, R. J. (2005). Isolated spin 3/2 plaquettes in Na_3RuO_4. *J. Solid State Chem.*, 178(6):2104–2108.

[103] Regan, K., Huang, Q., Lee, M., Ramirez, A., and Cava, R. J. (2006). Structure and magnetism of $NaRu_2O_4$ and $Na_{2.7}Ru_4O_9$. *J. Solid State Chem.*, 179(1):195–204.

[104] Reimers, P. (1969). The Preparation of Graded-Band-Gap Single Crystals of II–VI Compounds. *Phys. Stat. Sol.*, 35(2):707–716.

[105] Roisnel, T. and Rodríquez-Carvajal, J. (2001). WinPLOTR: A windows tool for powder diffraction pattern analysis. In *Proceedings of the EPDIC7, Barcelona, Spain*, volume 378, pages 118–123. Trans Tech Publications, Switzerland.

[106] Ruiz, A., Frano, A., Breznay, N. P., Kimchi, I., Helm, T., Oswald, I., Chan, J. Y., Birgeneau, R., Islam, Z., and Analytis, J. G. (2017). Correlated states in β-Li_2IrO_3 driven by applied magnetic fields. *Nat. comm.*, 8(1):1–6.

[107] Salinas-Sanchez, A., Garcia-Munoz, J., Rodriguez-Carvajal, J., Saez-Puche, R., and Martinez, J. (1992). Structural characterization of R_2BaCuO_5 (R = Y, Lu, Yb, Tm, Er, Ho, Dy, Gd, Eu and Sm) oxides by X-ray and neutron diffraction. *J. Solid State Chem.*, 100(2):201–211.

[108] Sayre, D. (1952). The squaring method: a new method for phase determination. *Acta Cryst.*, 5(1):60–65.

[109] Schäfer, H. (1964). *Chemical Transport Reactions*. Academic Press Inc., New York, USA.

[110] Schmidt, P. (2007). *Thermodynamische Analyse der Existenzbereiche fester Phasen- Prinzipien der Syntheseplanung in der anorganischen Festkörperchemie*. Habilitationsschrift, Technische Universität Dresden.

[111] Schmidt, P., Binnewies, M., Glaum, R., and Schmidt, M. (2013). *Advanced Topics on Crystal Growth*, chapter : Chemical vapor transport reactions - methods, materials, modeling. InTech, Rijeka, Croatia.

[112] Schwedes, B. and Hoppe, R. (1972). Über Oxobismutate. Zur Kenntnis von Na_3BiO_4 und Na_3SbO_4. *Z. Anorg. Allg. Chem.*, 393(2):136–148.

[113] Shaplygin, I. and Lazarev, V. (1980). New phases in a sodium-ruthenium-oxygen system. *Russ. J. Inorg. Chem*, 25(12):1837–1840.

[114] Sheldrick, G. (2014). SHELXT version-2014/5: Program for crystal structure solution. *University of Göttingen, Germany*.

[115] Sheldrick, G. (2018). SHELXS version-2018/3 and SHELXL version-2018/3: Programs for crystal structure solution and refinement. *University of Göttingen, Germany*.

[116] Shikano, M., Delmas, C., and Darriet, J. (2004a). $NaRuO_2$ and $Na_xRuO_2 \cdot y\,H_2O$: New Oxide and Oxyhydrate with Two Dimensional RuO_2 Layers. *Inorg. Chem.*, 43(4):1214–1216.

[117] Shikano, M., Kremer, R. K., Ahrens, M., Koo, H.-J., Whangbo, M.-H., and Darriet, J. (2004b). Synthesis and characterization of a magnetic semiconductor Na_2RuO_4 containing one-dimensional chains of Ru^{6+}. *Inorg. Chem.*, 43(1):5–7.

[118] Singh, Y. and Gegenwart, P. (2010). Antiferromagnetic Mott insulating state in single crystals of the honeycomb lattice material Na_2IrO_3. *Phys. Rev. B*, 82(6):064412.

[119] Singh, Y., Manni, S., Reuther, J., Berlijn, T., Thomale, R., Ku, W., Trebst, S., and Gegenwart, P. (2012). Relevance of the Heisenberg-Kitaev model for the honeycomb lattice iridates A_2IrO_3. *Phys. Rev. Lett.*, 108(12):127203.

[120] Soma, M. and Sato, H. (2006). Lithium ruthenates: Controlling dimensionality and topology of magnetic-ion arrangements. *J. Phys. Soc. Jpn.*, 75(12):124802.

[121] Son, W.-J., Manuel, P., Adroja, D., and Whangbo, M.-H. (2011). Density functional analysis of the magnetic structure of Li_3RuO_4: Importance of the Ru–O···O–Ru spin-exchange interactions and substitutional Ru defects at the Li sites. *Inorg. Chem.*, 50(19):9400–9405.

[122] STOE (2017). *WinXPOW version 3.11*. STOE & Cie GmbH, Darmstadt, Germany.

[123] Strobel, P. and Lambert-Andron, B. (1988). Crystallographic and magnetic structure of Li_2MnO_3. *J. Solid State Chem.*, 75(1):90–98.

[124] Takayama, T., Kato, A., Dinnebier, R., Nuss, J., Kono, H., Veiga, L., Fabbris, G., Haskel, D., and Takagi, H. (2015). Hyperhoneycomb iridate β-Li_2IrO_3 as a platform for Kitaev magnetism. *Phys. Rev. Lett.*, 114(7):077202.

[125] Terasaki, I., Abe, S., Yasui, Y., Okazaki, R., and Taniguchi, H. (2015). Ruthenium oxide as a thermoelectric material: unconventional thermoelectric properties of Li_2RuO_3. *J. Mater. Chem. C*, 3(40):10430–10435.

[126] Todorova, V. and Jansen, M. (2011). Synthesis, Structural Characterization and Physical Properties of a New Member of Ternary Lithium Layered Compounds - Li_2RhO_3. *Z. Anorg. Allg. Chem.*, 637(1):37–40.

[127] Trebst, S. (2017). Kitaev materials: Lecture Notes of the 48th IFF Spring School "Topological Matter - Topological Insulators, Skyrmions and Majoranas", Forschungszentrum Jülich. *arXiv*, 1701.07056v1.

[128] Urland, W. and Hoppe, R. (1972). Zur Kenntnis der Oxoplatinate Na_2PtO_2, Na_2PtO_3, K_2PtO_3 und Rb_2PtO_3. *Z. Anorg. Allg. Chem.*, 392(1):23–36.

[129] Van Arkel, A. and de Boer, J. H. (1925). Darstellung von reinem Titanium-, Zirkonium-, Hafnium- und Thoriummetall. *Z. Anorg. Allg. Chem.*, 148(1):345–350.

[130] Wang, J., Terzic, J., Qi, T., Ye, F., Yuan, S., Aswartham, S., Streltsov, S., Khomskii, D., Kaul, R. K., and Cao, G. (2014). Lattice-tuned magnetism of Ru^{4+} ($4d^4$) ions in single crystals of the layered honeycomb ruthenates Li_2RuO_3 and Na_2RuO_3. *Phys. Rev. B*, 90(16):161110.

[131] Wengert, S. and Nesper, R. (2000). Ba_3SiI_2, a double salt of barium iodide and the Zintl phase Ba_2Si. *J. Solid State Chem.*, 152(2):460–465.

[132] Wilke, K.-T. (1988). *Kristallzüchtung*. VEB Deutscher Verlag der Wissenschaften, Berlin, Germany.

[133] Williams, S., Johnson, R., Freund, F., Choi, S., Jesche, A., Kimchi, I., Manni, S., Bombardi, A., Manuel, P., Gegenwart, P., and Coldea, R. (2016). Incommensurate counterrotating magnetic order stabilized by Kitaev interactions in the layered honeycomb α-Li_2IrO_3. *Phys. Rev. B*, 93(19):195158.

[134] Wilson, A. (1976). Statistical bias in least-squares refinement. *Acta Cryst. A*, 32(6):994–996.

[135] Winter, S. M., Tsirlin, A. A., Daghofer, M., van den Brink, J., Singh, Y., Gegenwart, P., and Valenti, R. (2017). Models and materials for generalized Kitaev magnetism. *J. Phys. Condens. Matter*, 29(49):493002.

[136] Ye, F., Chi, S., Cao, H., Chakoumakos, B. C., Fernandez-Baca, J. A., Custelcean, R., Qi, T., Korneta, O., and Cao, G. (2012). Direct evidence of a zigzag spin-chain structure in the honeycomb lattice: A neutron and X-ray diffraction investigation of single-crystal Na_2IrO_3. *Phys. Rev. B*, 85(18):180403.

[137] Yogi, A., Sathish, C. I., Sim, H., Coak, M. J., Noda, Y., and Park, J.-G. (2018). Symmetry breaking and unconventional charge ordering in single crystal $Na_{2.7}Ru_4O_9$. *Phys. Rev. B*, 98(8):085113.

Erklärung

Ich versichere, dass ich die von mir vorgelegte Dissertation selbständig angefertigt, die benutzten Quellen und Hilfsmittel vollständig angegeben und die Stellen der Arbeit - einschließlich Tabellen, Karten und Abbildungen - , die anderen Werken im Wortlaut oder dem Sinn nach entnommen sind, in jedem Einzelfall als Entlehnung kenntlich gemacht habe; dass diese Dissertation noch keiner anderen Fakultät oder Universität zur Prüfung vorgelegen hat; dass sie - abgesehen von unten angegebenen Teilpublikationen - noch nicht veröffentlicht worden ist, sowie, dass ich eine solche Veröffentlichung vor Abschluss des Promotionsverfahrens nicht vornehmen werde. Die Bestimmungen der Promotionsordnung sind mir bekannt. Die von mir vorgelegte Dissertation ist von Prof. Dr. Petra Becker-Bohatý betreut worden.

Köln, 25. Januar 2021

- Linda Kerkhoff -